TECHNISCHE UNIVERSITÄT WIEN
Vienna University of Technology

Dissertation

Path integral methods for strong non-local correlations

Ausgeführt am Institut für Festkörperphysik
der Technischen Universität Wien

unter der Anleitung von

Prof. Dr. Karsten Held

von

Tin Ribic

Matrikelnummer: 00925829
Hollergasse 31, 1150 Wien

WIEN, Juni 26, 2018

Tin Ribic

Acknowledgments

Hiermit erkläre ich an Eides statt, dass ich die vorliegende Arbeit selbstständig verfasst und keine anderen als die angegebenen Quellen und Hilfsmittel verwendet habe.

_____

Tin Ribic

Deutsche Kurzfassung

Die vorliegende Arbeit beschäftigt sich mit effektiven Feynman-diagrammatischen Methoden für die Beschreibung starker elektronischer Korrelationseffekte in Festkörpern. Exakte numerische Lösungen für wechselwirkende Systeme mit mehr als ein paar Elektronen liegen weit außerhalb der Reichweite heute verfügbarer rechnerischer Ressourcen, wodurch Näherungsmethoden notwendig werden.

Effektive Feynman-diagrammatische Methoden wie die Dynamische Vertex Approximation werden oft auf einfache Referenzmodelle angewandt, welche numerisch behandelt werden können. Aus diesen Referenzmodellen werden diagrammatische Größen bestimmt und als Näherung für ihre jeweiligen Gegenstücke im eigentlichen System verwendet.

Bisher beschränkten sich derartige Methoden zumeist auf effektive Einteilchen- und Zweiteilchen-Diagramme. Diese Arbeit erweitert dieses Wissen um einen Ausdruck für n-Teilchen Vertices (Korrelatoren) für das Falicov-Kimball Modell für beliebige Zahlen n. Dreiteilchen-Diagramme für das Falicov-Kimball und Hubbard Modell wurden versuchsweise ausgewertet und zeigten relevante Korrekturen zu konventionellen Zweiteilchen-Rechnungen.

Zusätzlich wurde eine toplogische Klassifikation von Dreiteilchen-Diagrammen vorgenommen, wodurch ein Algorithmus zur Bestimmung des grundlegendsten Dreiteilchen-Diagramms, der vollständig irreduziblen Dreiteilchen-Vertex, angegeben werden konnte.

Schließlich wurde der Effekt von äußerer Selbstkonsistenz für das Hubbard Modell im *dual fermion* Zugang untersucht. Dadurch wird ein besseres Verständnis für die Wahl eines Referenzmodells ermöglicht. Wenig überraschend stellt man fest, dass die Wahl des Referenzmodells einen großen Einfluss auf die theoretische Beschreibung korrelierter Elektronensysteme hat.

Abstract

This thesis aims at furthering effective Feynman-diagramatic methods for describing correlation effects of electrons in solids. Exact solutions for interacting electron systems with more than a hand full of particles are far beyond the reach of numerical methods. Therefore, approximations are needed.

In this regard, effective Feynman-diagrammatic methods, such as the dynamical vertex approximation, use simple auxilliary models, which can be solved numerically. From these, diagramatic quantities are extracted which are used as approximations for their respective counterparts for the system of interest.

Hitherto, such methods were for the most part based on effective one- and two-particle diagrams. This thesis expands upon this by providing an expression for n-particle vertices (correlators) for arbitrary numbers of particles n in the Falicov-Kimball model. Three-particle diagrams for the Falicov-Kimball and Hubbard models are evaluated exploratively, showing relevant corrections to the conventional two-particle calculations.

Additionally, a systematic topological classification of three-particle diagrams is pursued, culiminating in an algorithm to calculate the most fundamental three-particle diagram: the fully irreducible three-particle vertex. Finally, the effect of the outer self-consistency for the Hubbard model within the dual fermion framework is investigated. This allows for understanding the influence of the auxilliary model better and shows how to update it iteratively. Maybe not surprisingly, the choice of auxilliary system has a strong influence on the theoretical description of correlated electron systems.

Contents

1. Introduction

Treating strong correlations in quantum lattice models is one of the most challenging problems in solid state theory. We know very well how to treat non-interacting systems, it is a (relatively speaking) simple matter of diagonalising the Hamiltonian, finding the eigenvalues and thus determining the behaviour of the system. While actually performing the diagonalisation of the Hamiltonian may be quite hard, the existence of a one-particle spectrum already constrains the possible dynamics of any system of non-interacting fermions. In fact, non-interacting quantum mechanics already provides us with a lot of insight. When materials now known as semiconductors started behaving in what was conceived to be a weird fashion [2, 3] and showed promise for applications [4], it took a while to work out a satisfying theoretical explanation for the observed phenomena [5]. Electrical engineering took its time before entering an age of rapid development after the basic elements of modern electronics were realised in 1948 [6]. The "effective one-particle" picture has served us well in understanding the foundations of what makes most of the modern world go round: semiconductor electronics. The difference between insulators and conductors can be explained in the band picture in the absence of exotic phenomena, with semiconductors being a special case of insulators. The quantum mechanical description together with the correct application of statistical physics was instrumentental in understanding semiconductors. With the problems resolved, electrical engineering and quantum physics parted ways, every field occupied with its own new and interesting challenges.

In theoretical solid state physics, many-particle effects became a focus of research. How many-body quantum systems ought to be treated was understood, but for interacting systems the computational effort scales exponentially with the number of particles and considered orbitals which up to this day makes an exact treatment impossible for all but the simplest models. Reasonable approximations [7–9], taking into account the relevant physics, yet still generating model descriptions which can be solved are needed [10]. One of the main problems of many-body systems is the huge number of degrees of freedom. In restricting oneself to only treating the collective density of all particles, this number can be reduced greatly. The Hohenberg-Kohn-theorem [11] and subsequent development of density functional theory [12–14] enabled us to calculate electronic properties of real materials and –with some caveats– even predict properties of newly synthesised materials. The density functional approach is an effective one-particle description as well as a mean-field theory and fails at describing strong correlation effects. However, the density-functional theory solution provides a reasonable starting point for constructing effective Hamiltonians for the description of low-energy excitations.

Such an effective Hamiltonian, the Hubbard model [15], is the most prototypical model Hamiltonian for correlations in solid-state physics. The Hubbard model seems innocent enough, consisting only of a kinetic and a local interaction term, both of which can be easily treated on their own. The combination of the two terms is believed to describe the effects responsible for the occurence of high-temperature superconductivity. Unfortunately, said model has proved to be quite resistant to attempts of solving it exactly and only the one-dimensional solution, which relies on a few pecularities of one-dimensional fermionic systems, is available [16–18], despite the high number of physicists who have embarked on this quest. Since exact solutions to interacting lattice problems proved to be elusive, the search for approximative treatments (of this already approximate model) commenced in full. It soon became apparent that Feynman-diagrammatic approaches are the method of choice for describing correlation effects in solids not only quantitatively, but also in intuitively understandable terms.

The advent of dynamical mean field theory (DMFT) [19] was a huge step forward for the description of interacting systems, as it solves a simple interacting problem – a local problem embedded into a bath which simulates the non-local degrees of freedom. The method can be employed with reasonable numerical effort and is physically intuitive – making it a key method of modern correlated-electron calculations. It is also applied together with density functional theory [20, 21]. DMFT, however, fails at describing non-local correlation effects, a direct consequence of being based on a local reference problem.

This work mostly deals with the possibilities for a theoretical description of strongly correlated electron systems beyond dynamical mean field theory. Multiple methods were developed to build upon the good description of local correlation effects within dynamical mean field theory. They seek to use diagrammatic methods to supplement the missing non-local effects. These methods include the dynamical vertex approximation [22], the dual fermion [23] as well as dual boson approach [24], the one-particle-irreducible approach [25], Trilex and Quadrilex [26, 27]. All these methods rely on diagrammatic quantities i.e. two-or-more particle vertices, extracted from local impurity problems, e.g. at DMFT convergence. These are subsequently employed as building blocks for constructing non-local vertices and self-energies. The precise relations between those methods are not yet fully understood and additional investigations on the quantitative differences between them are called for. In an attempt of reducing the complexity of the underlying problem and improving our understanding of the methods themselves, in this thesis they are mostly applied

to the Falicov-Kimball [28, 29] instead of the Hubbard model. The Falicov-Kimball model features reduced freedom in its dynamics, allowing for some analytical derivations, even for complicated diagrammatic expressions and thereby reducing the strain on computational ressources.

Within this thesis, diagrammatic methods are tested a tentative step beyond what was done before. The effects of higher order vertices for the Falicov-Kimball [30][1] and Hubbard [31][1] model are investigated. A classification of three-particle reducibility is pursued. Employing continuous-time quantum Monte Carlo data [32, 33], the effect of diagrammatic extensions of dynamical mean field theory on the underlying impurity is analysed.

The biggest hope in the field of strongly correlated electron physics is achieving a deep theoretical understanding of phenomena such as high-temperature superconductivity, which could potentially revolutionalise our power grid, or to use strong correlations for quantum computation applications. Whatever type of other seemingly weird behaviour may be discovered, human ingenuity is bound to ultimately find an application for it. As with most fundamental research, predicting exactly where the voyage is headed is impossible.

---

[1]Publications based on this Ph.D. thesis.

2. A brief summary of necessary aspects of quantum field theory

The aim of this section is to introduce briefly some of the concepts of quantum field theory and clarify notational conventions. A more thorough discussion can be found in [34], or in [35, 36]. We will restrict ourselves to fermions, as they are the main point of interest in the context of this work. The starting point will be the definition of Green's functions, which will then lead towards self-energies and vertices. These basic objects describe the propagation of particles through the system in question and allow us to calculate physical properties of our model systems, allowing for a connection with experiments performed on real systems. The utilisation of imaginary-time and, by extension, Matsubara-frequency objects will be introduced in the following. Subsequently, two-particle propagators will be investigated. A short discussion of transport-related physical observables and their description within a quantum field theoretical lattice models follows. The section closes with a short discussion of dynamical mean field theory and its possible extensions. Note that, while the notational convention mostly follows the one in [36], vertex functions are defined with a different sign, providing algebraic advantages in later parts of the thesis.

2.1. One-particle Green's function

The most basic object, one is typically interested in, is the one-particle Green's function, which is defined as:

$$\mathcal{G}_{i,j}(t) = i \left\langle \mathcal{T} c_i(t) c_j^\dagger(0) \right\rangle. \tag{1}$$

Here $c^\dagger$ and c are the (Heisenberg) creation and annihilation operators associated with the states described by the quantum numbers i and j in the subscripts and times 0 and t; i and j typically include site or wave vector k and spin indices, sometimes also band or orbital indices. $\mathcal{T}$ is the time ordering operator. The angled brackets denote a thermal averaging to arrive at an expectation value. Time translation invariance was implicitly assumed, setting the time of the creation operator to 0 and regarding only the difference in time, t. For practical reasons, usually one investigates the imaginary-time Greens function

$$G_{i,j}(\tau) = - \left\langle \mathcal{T} c_i(\tau) c_j^\dagger(0) \right\rangle. \tag{2}$$

A Wick rotation $t \to it = \tau$ was applied to transform the original Green's function to the equation above. The imaginary time Green's function has the advantage of being anti-periodic. Thus, its Fourier transform consists only of discrete frequencies, which is preferable for a numerical treatment. The time ordering leads to a discontinuity of the Green's function at $\tau = 0$ if $i = j$, where the value jumps from the occupation to minus the mean non-occupation.

$$p_i = \left\langle c_i^\dagger c_i \right\rangle \tag{3}$$

$$G_{i,i}(0_-) = \lim_{\epsilon \to 0} \left\langle c_i^\dagger(0) c_i(-\epsilon) \right\rangle = p_i \tag{4}$$

$$G_{i,i}(0_+) = \lim_{\epsilon \to 0} - \left\langle c_i(\epsilon) c_i^\dagger(0) \right\rangle = -(1 - p_i) \tag{5}$$

This means that one has to be careful about extracting the occupations of certain states from frequency-dependent Green's functions. Following the discussion of Fourier transformation, this issue will be addressed. The Green's function is calculated by performing a thermal averaging. This is done by using the weight $\exp -\beta \mathcal{H}$, β being the inverse temperature, and taking the trace over all possible states of the many body system. One can show that this means the Green's functions are anti-periodic in τ with anti-periodicity length β. This restricts the fermionic frequencies of the Fourier transform to:

$$\nu_n = \frac{(2n+1)\pi}{\beta}, \tag{6}$$

with n being an integer. The sign and normalisation factor convention for the transformations is given as:

$$G_{i,j}(\nu_n) = \int_0^\beta d\tau \, G_{i,j}(\tau) e^{i\nu_n \tau} \tag{7}$$

$$G_{i,j}(\tau) = \frac{1}{\beta} \sum_n G_{i,j}(\nu_n) e^{-i\nu_n \tau} \tag{8}$$

Including the factor $1/\beta$ in the reverse transformation and the choice of signs may seem strange to someone used to digital signal processing conventions, but it ensures that $G(\nu)$ has an algebraically appealing

representation. If one wants to know the mean occupation of a certain state i , which is given by p_i, straightforward summation of $G(\nu_n)$ will give

$$G_{i,i}(\tau = 0) = \frac{1}{\beta} \sum_n G_{i,i}(\nu_n). \tag{9}$$

This value corresponds neither to the mean occupation, nor to the negative mean non-occupation, but the mean value of the two:

$$G_{i,i}(\tau = 0) = \frac{1}{2} \left(p_i + (-1 + p_i) \right) = p_i - \frac{1}{2}. \tag{10}$$

Diagrammatic methods in quantum field theory often struggle when $G_{i,i}(\tau = 0)$ is required to be calculated, as the origin of these terms has to be traced back carefully to figure out which limiting value is required. Also, $G_{i,i}(\nu)$ behaves like $1/i\nu$ for large values of ν, which means that the series is not absolutely convergent. Typically, one tries to circumvent the problem of conditional convergence by subtracting $1/i\nu$ (the Green's function of a non-interacting state at zero energy relative to the Fermi energy) from the Green's function, which is known analytically to give half filling on its own. An alternative approach is to accept that $G_{i,i}(\tau = 0)$ describes the deviation from half-filling. Because it is known to be purely real, summing up just the real parts of the Fourier transform must give the same result as the full sum. Unlike the full sum, the real part on its own is absolutely convergent, so it can be summed up numerically in a meaningful way. Commonly, one also takes the Fourier transform of the Green's function in space, especially if dealing with a translationally invariant system, where the dependence on i and j reduces to a dependence on $j - i$:

$$G_k = \frac{1}{\sqrt{N}} \sum_j e^{-ikj} G_{0,j}. \tag{11}$$

Here $G_{0,j}$ is the original Green's function, which is assumed to be translationally invariant, N is the total number of lattice sites and 0, j and k are understood to be vectors of appropriate dimension, 0 being the vector of the origin. Just as we only investigated differences between times, we now only investigate differences between spatial positions.

2.2. Self-energy

Besides the Green's function, the quantity one is typically most interested in on the one-particle level is the self-energy, Σ. In terms of Feynman diagrams the self-energy is given by the sum of all one-particle-irreducible diagrams without outer legs. Physically, the self-energy gives the mean interaction a given electron feels from all the other ones in the system. The self-energy is responsible for a energy-shift of states as well as for a broadening of the spectral function. Roughly speaking, the real and imaginary part of the self energy are associated with these two effects. The Dyson equation relates the actual, full one-particle Green's function, the non-interacting referential Green's function, G^0, commonly also called bare Green's function, and the self-energy Σ to each other. In Matsubara-frequencies and k-space it reads

$$G_k(\nu) = G_k^0(\nu) + G_k^0(\nu)\Sigma_k(\nu)G_k(\nu). \tag{12}$$

A diagrammatic representation of the Dyson equation can be found in figure 1.
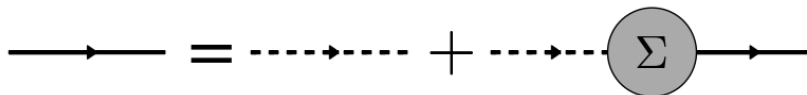
Figure 1: Diagrammatic representation of Dyson's equation. Full lines represent interacting Green's functions and dashed ones the non-interacting referential Green's functions.

The self-energy makes the introduction of the concept of irreducibility of diagrams necessary. A diagram is considered irreducible on the one-particle level if it cannot be separated into two disconnected parts by cutting a single (bare) propagator[1]. For the full propagator, all diagrams with an arbitrary number of such one-particle irreducible self-energies inserted between bare propagators contribute. The Dyson equation encodes this geometric series in an expression with the full Green's function on both sides of the equation.

---

[1] Note that the self-energy can be expressed in terms of either G_0 or G. One-particle reducibility does not depend on the choice of representation. However, if full propagators G are used, only so-called skeleton diagrams can be considered.

2.3. Two-particle Green's function

The two-particle Green's function is given by

$$\mathcal{G}^{(2)}_{i,j,k,l}(t_1, t_2, t_3) = \left\langle \mathcal{T} c_i(t_1) c_j^\dagger(t_2) c_k(t_3) c_l^\dagger(0) \right\rangle \tag{13}$$

One can immediately see that this object is much more complicated than the one-particle Green's function. As the two-particle Green's function connects two particles, it allows us to calculate not only occupations, but also conditional occupations. Conditional occupations tell us how probable it is to find a particle somewhere and another one somewhere else. Employing linear response theory, also physical susceptibilities can be expressed in terms of two-particle Green's functions or correlators.

We will again transform the Green's function to imaginary times, yielding:

$$G^{(2)}_{i,j,k,l}(\tau_1, \tau_2, \tau_3) = \left\langle \mathcal{T} c_i(\tau_1) c_j^\dagger(\tau_2) c_k(\tau_3) c_l^\dagger(0) \right\rangle \tag{14}$$

When trying to perform a Fourier-transform of the two-particle propagator, there is more freedom in how to choose the frequencies than in the one-particle case. The obvious way of proceeding is to transform every imaginary-time variable separately.

$$G^{(2)}_{i,j,k,l}(\nu_1, \nu_2, \nu_3) = \frac{1}{\beta} \int_0^\beta d\tau_1 \int_0^\beta d\tau_2 \int_0^\beta d\tau_3 e^{i(\nu_1\tau_1 - \nu_2\tau_2 + \nu_3\tau_3)} G^{(2)}_{i,j,k,l}(\tau_1, \tau_2, \tau_3) \tag{15}$$

If one performs the Fourier-transformation this way, all three frequencies the Green's function depends on are fermionic Matsubara frequencies. This notation corresponds to the diagram depicted in figure 2. Typically, other frequency conventions are preferred, for example particle-particle-notation (*pp*-notation), which is adapted by substituting:

$$\nu_2 \to \nu_2' \tag{16a}$$

$$(\nu_3 + \nu_1 - \nu_2) \to \omega' - \nu_2' \tag{16b}$$

$$\nu_1 \to \omega' - \nu_1' \tag{16c}$$

$$\nu_3 \to \nu_1' \tag{16d}$$

We introduced a bosonic Matsubara frequency ω'. Possible values for bosonic Matsubara frequencies are given by

$$\omega_n = \frac{(2n)\pi}{\beta}. \tag{17}$$

The diagrammatic representation of the two-particle Green's function in *pp*-notation is given in figure 3, dropping all primes $'$.
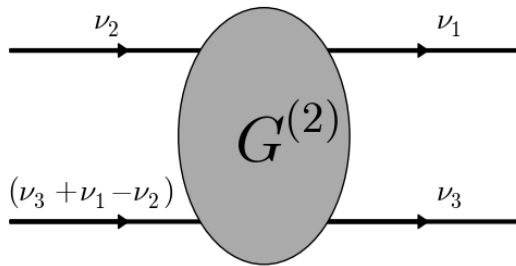
Figure 2: Diagrammatic representation of the two-particle Green's function $G^{(2)}$ with frequency notation taken straight from the Fourier transformation (15).
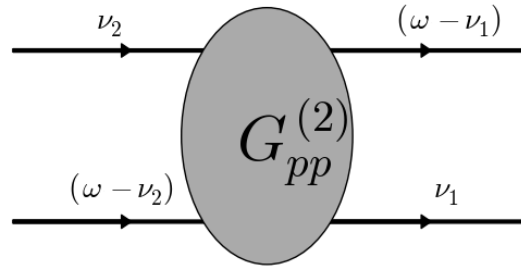
Figure 3: Diagrammatic representation of the two-particle Green's function $G^{(2)}$ adapting *pp*-notation.

Another useful notation is the particle-hole (*ph*) notation, which is epressed in terms of the particle-particle notation (*pp*) here.

$$\nu_{1,ph} = \nu_{1,pp} \tag{18a}$$

$$\nu_{2,ph} = \nu_{2,pp} \tag{18b}$$

$$\omega_{ph} = \omega_{pp} + \nu_{1,pp} + \nu_{2,pp} \tag{18c}$$

Note that both in figure 2 and 3, there are lines entering and leaving the bubble denoting the two-particle Green's function. These lines are denoted for clarity of the frequency convention, as they are already included in the definition of the two-particle Green's function. Also, the two-particle Green's function contains disconnected contributions. Disconnected contributions are terms which contain no new information and can already be determined with knowledge of the one-particle Green's function. In pp-notation, they are given by

$$^{\mathrm{disc}}_{\ \ pp}G^{(2)}_{i,j,k,l}(\nu_1,\nu_2,\omega) = \delta_{\omega,(\nu_1+\nu_2)}G_{i,j}(\nu_1)G_{k,l}(\nu_2) - \delta_{\nu_1,\nu_2}G_{i,l}(\nu_1)G_{k,j}(\omega-\nu_1). \tag{19}$$

Equation (19) describes the amplitude of two particles propagating trough the system without specifically noticing each other (Note however, that in the case of interacting systems some averaged interaction effects are already included in the self-energies of the two disconnected propagators). In the case of a non-interacting, non-disordered system, these disconnected terms actually constitute the whole two-particle Green's function. Anyhow, due to the second term, $\delta_{\nu_1,\nu_2}G_{i,l}(\nu_1)G_{k,j}(\omega-\nu_1)$, still some correlation effects can occur. While this term does cause correlations to occur, those are an intrinsic property of fermions and appear even for non-interacting systems, one aspect of this effect is commonly referred to as exchange hole for equal-time Green's functions.

Here it should be noted, that there is a lot of freedom in how to assign factors $1/\beta$ to the Fourier transformation and the definition of the Green's function (15) and (14), as well as in the choice of frequency conventions for the Fourier transformation. Unfortunately, there is a lot of conventions currently employed by different people and a generally accepted standard is not yet adopted[1], similar to the perpetual question about the sign of the Minkowski metric. In this thesis, the frequency notation from [36] is employed, but the sign of the two-particle vertex is changed.

2.4. Two-particle vertex

Once the connected part of the two-particle propagator is extracted by subtracting the disconnected contributions, what remains to be calculated is the full vertex, F. The full vertex is given by the connected propagator with the outer legs "amputated". That is, in terms of Feynman diagrams, any connected two-particle diagram has to have one-particle propagators as outermost elements and eliminating those outer legs is called amputation. Conducting the amputation in a basis in which the one-particle propagator is non-local is complicated, because the equations then become coupled, as given in equation (20)[2].

$$^{\mathrm{con}}G^{(2)}_{i,j,k,l} = \sum_{m,n,o,p} G_{i,m}G_{k,o}F_{m,n,o,p}G_{n,j}G_{p,l} \tag{20}$$

In equation (20), the indices i,j,k,l,m,n,o,p are assumed to encode all information about the propagation, including possible time variables. For continuous variables, the sum should be interpreted as an integral. Such an expression is not suited for the calculation of F. If, however, the one-particle propagator is local in a given variable,

$$G_{i,m} \propto \delta_{i,m} \cdot G_{i,i}, \tag{21}$$

the summation need not be performed and equation (20) simplifies to

$$^{\mathrm{con}}G^{(2)}_{i,j,k,l} = G_iG_kF_{i,j,k,l}G_jG_l, \tag{22}$$

which can be solved algebraically. One example of such occurrences are time-translation invariant systems, where the one-particle Green's function is always local in frequency space.

The methods designed to include non-local correlations on top of dynamical mean field theory described within this thesis build upon the full vertex or an irreducible one, as discussed in the following section, as input, therefore its numerical determination is of crucial importance.

2.5. Reducibility on the two-particle level

The concept of reducibility on the two-particle level is more diverse than in the case of a single particle. There are three separate ways in which diagrams contributing to the vertex can be separable: they can be particle-particle (pp), particle-hole (ph) or transverse particle-hole ($\overline{ph}$) separable. A diagram is called two particle-reducible if it can be split into two disconnected parts by cutting two one-particle propagators. A

---

[1]Note how I manage to lament the lack of a standard, refer to one and deviate from it for algebraic convenience at the same time.

[2]From here on, there is a deviation from the notation in [36], with the vertex picking up a relative sign. This results in all two-particle vertex functions (full as well as irreducible, as discussed later) having a relative sign.

diagram which is not separable in any of the three channels pp, ph or $\overline{ph}$ is called fully irreducible. Depending on which pairs of original outer legs remain connected, a reducible diagram can be categorised. A given two-particle diagram is either fully irreducible or reducible (separable) in exactly one channel [35](pp, ph or $\overline{ph}$). One can easily see that a given diagram can not be reducible in two different channels by investigating what would happen to it if both sets of cuts were performed on it. The diagram would first be disconnected into two diagrams with four outer legs each. Then in both parts one additional propagator would be cut, disconnecting them into a total of four diagrams with three outer legs each. For systems without spontaneous separate creation and annihilation of particles[1] (specifically excluding creation-annihilation pairs) such diagrams cannot exist. Note that reasonable physical theories should never allow for separate creation and annihilation events of fermions; Since Fermions carry half-integer spin, conservation of angular momentum is violated if the number of Fermions in the system changes by one. Only whole numbers can be absorbed by other particles changing their angular momentum. There is no such restriction on Bosons.
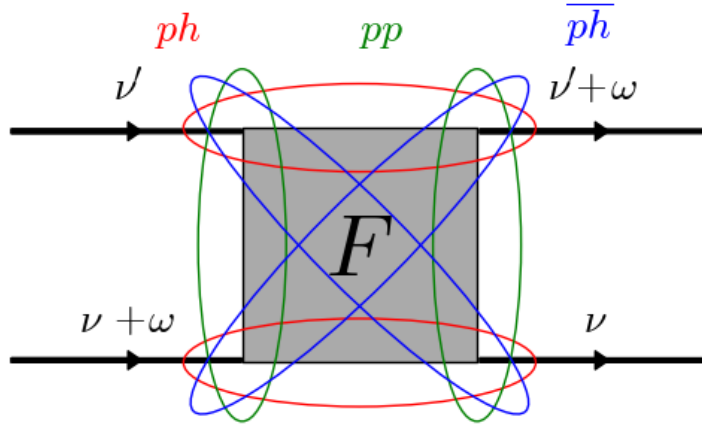
Figure 4: The pairs of outer legs which remain connected when a diagram reducible in a given channel (pp, pp, $\overline{ph}$) is cut are marked in the respective colour. Note that the frequencies were denoted in particle-hole notation.

In figure 4 the outer legs which remain connected if a separation of a reducible diagram is conducted are marked in the colours of the associated channels. The sum of all such diagrams reducible in a channel c is called Φ_c, the reducible vertex in the channel c, while the sum of the irreducible ones is called Γ_c. We have already established that any given diagram can be reducible in at most one channel. This also means that the intersection of the sets of diagrams included in any pair of reducible vertices Φ_c and $\Phi_{c'}$ is empty. Thus, we can subtract all reducible diagrams from the full vertex by subtracting all Φ_c without incurring any problems caused by overcounting. This can be formalised in terms of the parquet-equations

$$F = \Gamma_c + \Phi_c. \tag{23}$$

This equation holds for any of the three channels. Additionally, a fully irreducible vertex Λ can be expressed.

$$F = \Lambda + \sum_c \Phi_c. \tag{24}$$

Also, for the irreducible vertices,

$$\Gamma_c = \Lambda + \sum_{c' \neq c} \Phi_{c'}, \tag{25}$$

holds. The irreducible vertices can be calculated from the full vertex by means of Bethe-Salpeter equations.

$$F^{\nu,\nu',\omega} = \Gamma_{pp}^{\nu,\nu',\omega} + \frac{1}{2\beta} \sum_{\nu_1} F^{\nu,\nu_1+\omega,\nu'-\nu_1} G(\nu_1+\omega)G(\nu+\nu'-\nu_1)\Gamma_{pp}^{\nu+\nu'-\nu_1,\nu',\omega-\nu'+\nu_1} \tag{26}$$

$$F^{\nu,\nu',\omega} = \Gamma_{ph}^{\nu,\nu',\omega} - \frac{1}{\beta} \sum_{\nu_1} F^{\nu,\nu_1,\omega} G(\nu_1+\omega)G(\nu_1)\Gamma_{ph}^{\nu_1,\nu',\omega} \tag{27}$$

---

[1]This means tadpole diagrams vanish.

Equations (26) and (27) are the Bethe-Salpeter equations for the *pp* and *ph*-channels written in *ph*-notation. One immediately sees how the solutions to the Bethe-Salpeter equations fulfill the requirements on reducibility. The right hand side consists of the sum of all diagrams irreducible in the given channel Γ and all reducible ones. Any reducible diagram has a "leftmost" set of lines that can be cut to decompose it into two parts. This set of lines is given by the two Green's functions appearing explicitly in the equation. A diagram may be reducible in more than one way in a specific channel, but this is taken care of by the full vertex attached to the irreducible one, as it contains contributions reducible in the relevant channel as well as irreducible ones. Thus, this simple algebraic equation encodes the solution to a very complicated combinatoric problem, the decomposition of an infinite number of diagrams according to reducibility. As the $\overline{ph}$-irreducible vertex can be expressed via the *ph* one using the crossing symmetry (see section 3.1)

$$\Gamma_{\overline{ph}}^{\nu,\nu',\omega} = \Gamma_{ph}^{\nu,\nu+\omega,\nu'-\nu} \tag{28}$$

the corresponding Bethe-Salpeter equation has been omitted.

2.6. Physical observables

The ultimate goal of theoretical calculations in solids is always to describe experimentally observable physical phenomena. Experimental observables are always associated with Hermitian operators. If those operators are expressed in terms of creation and annihilation operators for particles, their expectation values can easily be expressed in terms of Green's functions. A typical one-particle operator which plays a role for the calculation of actual physical observables and material's behaviour is the charge density operator, another one is given by the current density operator. Thus, their equilibrium expectation values can be expressed using one-particle Green's functions. Kubo's Formula [37] provides relations between susceptibilities of a system and equilibrium correlators, which leads to expressions involving two-particle Green's functions, therefore two-particle quantities are of great interest in connecting theory and experiment in solid state physics.

Problems arising when going from a continuous real-space basis to a local-orbital description will be discussed here, especially concerning charge conservation and continuity equations on the subspaces spanned by the orbitals under consideration. A derivation of the electric current operator on a lattice is also provided with a more detailed discussion in appendix A.

2.6.1. Discrete charge densities

Defining a proper replacement for the continuous (non-relativistic) charge density operator $\rho(r)$

$$\rho(r) = q_c \left\langle c^\dagger(r) c(r) \right\rangle \tag{29}$$

with the creation and annihilation fields $c^\dagger$ and c at position r and q_c the elementary charge for the type of particles in question, on a discrete basis is straightforward. It is only defined on discrete points r_i in real space (typically lattice sites) and changes its dimension from a charge density to a charge.

$$\rho(r) \rightarrow q(r_i), \tag{30}$$

where r is a position in real space and $q(r_i)$ is the charge at position r_i. The operator associated with $q(r_i)$ is given by

$$q(r_i) = q_c \left\langle c_i^\dagger c_i \right\rangle \tag{31}$$

with $c^\dagger$ and c being creation and annihilation operators for the particles in questions. This charge operator is connected to a current operator through the equation of continuity.

2.6.2. Discrete current densities

An observable of great experimental interest is given by the electric current I through a system. For continuous systems, the current density for particles with a quadratic dispersion relation and mass m_c (in the absence of magnetic fields) is given by the expectation value of the current operator

$$j(r) = \frac{q_c i}{2m_c} \left\langle (\nabla c(r)) c^\dagger(r) - c(r)(\nabla c^\dagger(r)) \right\rangle, \tag{32}$$

again using the charge q_c. The complex unit is given by i and ∇ denotes the gradient operator, with brackets specifying what it acts on. It is well-known that the charge- and current density operators are coupled by the equation of continuity.

$$\partial_t \rho(r,t) = -\nabla \cdot j(r,t). \tag{33}$$

Equation (33) relates the time-derivative of the charge density and the divergence of the current-density. For the discrete case, a modified version of this equation takes its place, which looks similar to Kirchhoff's current law

$$\partial_t q(r_i, t) = -\sum_j I_{i,j}(t). \tag{34}$$

This establishes a connection between the time-derivative of the charge at position r_i and the currents $I_{i,j}$ from position r_i to position r_j. Notice how the currents are now dependent on two positions in space instead of one and are scalar, not vector quantities. Writing down a reasonable expression for the current density operator on a discrete basis turns out not to be fully trivial and is therefore carried out with some care in appendix A. Equation (34) can easily be reproduced from calculating the time derivative of $q(r_i)$ for a non-interacting Hamiltonian

$$\mathcal{H}_{NI} = \sum_i V_i c_i^\dagger c_i + \sum_{i,j} t_{i,j} c_i^\dagger c_j, \tag{35}$$

with hopping elements $t_{i,j}$, possibly including on-site potential-terms $t_{i,i}$. This yields the discrete continuity equation

$$\partial_t q_c \left\langle c_i^\dagger c_i \right\rangle = -i q_c \left\langle \sum_j t_{i,j} c_i^\dagger c_j - t_{j,i} c_j^\dagger c_i \right\rangle. \tag{36}$$

This equation has a very clear interpretation, and assignment of the terms is straightforward. Now, the challenge of defining a macroscopic current operator remains. The derivation is found in the appendix and yields

$$\vec{j} = \frac{1}{V} i q_c \sum_j t_{0,j} c_0^\dagger c_j r_j. \tag{37}$$

The volume of the unit cell, V was introduced. A Fourier transformation of equation (37) leads to the Peierls approximation for current densities:

$$\frac{1}{V} i q_c \sum_j t_{0,j} c_0^\dagger c_j r_j = \frac{1}{V} i q_c \sum_j \frac{1}{N} \sum_{k,k'} t_{0,j} c_k^\dagger c_{k'} e^{ik'r_j} r_j. \tag{38}$$

The factor r_j can be generated by differentiating $\exp(ik'r_j)$ by k'

$$\frac{1}{V} q_c \sum_j \frac{1}{N} \sum_{k,k'} t_{0,j} c_k^\dagger c_{k'} \partial_{k'} e^{ik'r_j}. \tag{39}$$

Now the summation over j is performed, yielding the Fourier Transform

$$\vec{j} = \frac{1}{V} q_c \sum_k \nabla_k \epsilon_k c_k^\dagger c_k. \tag{40}$$

2.7. Continuity and consistency

Having transformed the charge density and current density operator to their lattice counterparts, a little bit of reflection is in order. The current density has been derived for a non-interacting albeit otherwise general Hamiltonian. evaluating the time derivative of lattice charges for an interacting system can lead to problems under some circumstances. This will be elaborated on starting from the Hamiltonian for a interacting, periodic fermionic system in real space $\mathcal{H}_{RS}$.

$$\mathcal{H}_{RS} = \sum_i \int d^3r \Psi_i^\dagger(r) \left(V_i(r) - \hbar^2 \Delta/2m_i \right) \Psi_i(r) + 1/2 \sum_{i,j} \int d^3r d^3r' \Psi_i^\dagger(r) \Psi_j^\dagger(r') U_{i,j}(r,r') \Psi_j(r') \Psi_i(r). \tag{41}$$

$\Psi_i^{(\dagger)}(r)$ are the annihilation (creation) operators for the fermionic fields at position r and with the index i. The index should encompass any remaining degrees of freedom, e.g. from spin. Relativistic effects were neglected, V_i is some (periodic) potential, $U_{i,j}(r,r')$ gives the interaction between the fermions. Note how this Hamiltonian has only potential terms which are diagonal in real space, V_i is trivially diagonal, while the

interaction only has density-density like terms, making it diagonal as well. Such a Hamiltonian reproduces the current density operator from equation (32) (up to some indices) when taking the time derivative of the charge density operator. Any contributions from the potential terms to the commutator with $\Psi_i^\dagger(r)\Psi_i(r)$ cancel out exactly because they are diagonal in real space, leaving the current operator as a manifestly one-particle operator.

Now let us consider performing a transformation of the field operators and adapting a discrete basis set, for example one based on Wannier orbitals. The field operators $\Psi^\dagger$ are replaced according to

$$\Psi_\sigma^\dagger(r) = \sum_l b_{l,\sigma}^\dagger \Phi_{l,\sigma}^*(r) \tag{42a}$$

$$\Psi_\sigma(r) = \sum_l b_{l,\sigma} \Phi_{l,\sigma}(r) \tag{42b}$$

Here, $b_{l,\sigma}^{(\dagger)}$ are the new operators for states with indices l and spin-index σ and $\Phi_{l,\sigma}(r)$ is the associated wave function. Φ^* is its conjugate complex. In the following, we will combine the indices l, σ into a joint index l. Replacing all $\Psi^{(\dagger)}$ in $\mathcal{H}_{RS}$ then yields the representation of the Hamiltonian in the new basis. This new representation is of the form

$$\mathcal{H} = \sum_{i,j} H_{i,j} b_i^\dagger b_j + \frac{1}{2} \sum_{l,m,n,o} U_{l,m,n,o} b_l^\dagger b_m^\dagger b_n b_o \tag{43}$$

with

$$H_{i,j} = \int d^3r \, \Phi_i^*(r) \left(V(r) - \hbar^2 \Delta/2m \right) \Phi_j(r) \tag{44}$$

and

$$U_{l,m,n,o} = \int d^3r d^3r' \Phi_l^*(r) \Phi_m^*(r') U(r,r') \Phi_n(r') \Phi_o(r). \tag{45}$$

We can now see that the Hamiltonian is not necessarily diagonal in the interaction in this basis any longer. Thus, if discrete currents between the orbitals of this basis are calculated, the commutator of the corresponding charge operator $b_l^\dagger b_l$ with the Hamiltonian spawns terms of the structure $b^\dagger b^\dagger b b$, thus mixing in two-particle operator components into the current operator.

From this, we can see that problems can occur when incautiously changing into a discrete basis if only a finite number of basis states is considered, i.e. a projection onto a subspace is performed. The following potential pitfalls are especially problematic:

- Assuming, that charges are described only by diagonal, $b_l^\dagger b_l$ like terms. Neither is this charge localised at a single point-actually it is distributed according to the absolute square of the associated wave function in space.

- Neglecting the impact of $b_l^\dagger b_m$ like terms on the total charge distribution of the system. While such terms can only cause dipole or higher-order contributions to the charge distribution, they are not necessarily negligible. It might very well be possible to move around a lot of charge without adding or removing any.

- Neglecting the charge transport due to non-density-density like interaction terms $b_l^\dagger b_m^\dagger b_n b_o$ with $l, m \neq n, o$.

- Applying the equation of continuity to currents and charges, possibly with those two values being calculated based on different approximations. When projecting the system onto a subspace, the equation of continuity changes its form.

At the very least this should make us extremely cautious with regard to which approximations we apply to calculate charges and currents for an actual physical system. While the Hubbard and the Falicov-Kimball model do not display two-particle operator contributions to the currents because they are density-density like in their interaction term real space representations, but general multi-band Hubbard models need not, and generally do not, behave the same way. For a model with actual physical significance with non density-density like interaction, consider a DFT+DMFT treatment of a system where t_{2g} orbitals are considered within the DMFT calculation, as would be commonly done for the family of cuprates, exactly such non-diagonal interaction terms appear within the local problem, in the simplest case, in the form of a Kanamori-Hamiltonian.

We have to realise that restricting ourselves to solving our systems on subspaces only can—and in the general

case also will–lead to violations of exact conservation laws. This does not necessarily mean that all results obtained in such calculations are unphysical. The Peierls approximation is widely applied for a good reason, we just have to be wary about employing it without second thoughts[1].

2.8. Dynamical mean field theory and beyond

Since the exact diagrammatic treatment of an interacting system of any reasonable size is not feasible, approximations need to be developed in solid-state physics. Evaluating low-order diagrams, starting from Hartree and Hartree-Fock-like approaches proved successfull for weakly coupled systems. By restricting oneself to skeleton-diagrams only, such calculations could be performed self-consistently, thereby including higher-order contributions as well. However, such methods always come with the drawback of choosing, more or less arbitrarily, which diagrams to evaluate. While physical intuition allows for choosing diagrams which are suspected to be especially relevant for the processes one aims to describe, the remaining subjective freedom of choice is not fully satisfactory from a quantitative scientific point of view.

A conceptually different approach is the dynamical mean field theory [19,38,39] (DMFT). It aims to reduce the number of degrees of freedom instead of the expansion order in the interaction or types of Feynman-diagrams treated, thus ending up with an exactly, or at least numerically, solveable system. Within DMFT a single site embedded into a bath of non-interacting states, an Anderson impurity model (AIM), is treated. The bath states do not allow for direct transfer of electrons between them[2], this is only possible via the interacting site. The energies of the bath states and their hybridisations with the interacting site encode the structure of the lattice. For this system, the self-energy, which is always local by construction, is calculated and used as an approximation for the self-energy of the lattice. Therefore, DMFT approximates the one-particle irreducible vertex, the self-energy, of the full system by the counterpart of a local reference system. This approach works well for describing phenomena dominated by local correlation effects such as Mott-Hubbard transitions. It was shown that for infinite-dimensional systems or infinite coordination numbers, DMFT becomes exact [40,41]. DMFT has been successfully applied to different models, including the Hubbard and Falicov-Kimball model. Much effort was put into improving the methods for solving the local interacting problem [42,43]. Dynamical mean field theory was also used in combination with density functional theory, describing correlations in realistic materials, spawning the DFT+DMFT approaches [38, 44]. Nowadays DMFT is a well established and widely applied method of treating strongly correlated electron systems.

Anyhow, DMFT is limited to describing purely local correlation effects by construction. Unfortunately, many of the most intriguing and potentially useful phenomena in condensed matter physics are non-local in nature. Examples of interesting non-local physics include d-wave superconductivity and long-range ordering. Efforts at including non-local correlation effects in DMFT calculations were made by the treatment of clusters of sites, in cluster DMFT approaches [45–48], but these methods are limited with respect to the size of the clusters which can be treated and thus their resolution in k-space. Another set of promising methods are diagrammatic extensions of DMFT. These methods employ the good local results of DMFT as a basis, aiming at the inclusion of non-local correlations from this starting point. Diagrammatic extensions of DMFT include the dynamical vertex approximation ($D\Gamma A$) [22], the dual fermion (DF) [23] and one-particle irreducible ($1PI$) [25] approach, as well as the non-local expansion scheme [49]. A common feature of these methods is the use of local two-particle quantities calculated within DMFT or a related impurity problem, which are then connected via non-local propagators. From the resulting, non-local, two-particle quantities, non-local self-energy corrections are calculated. Depending on the parameter regime, the influence of those non-local self-energy corrections ranges from negligible to highly relevant for the overall behaviour of the system. Currently, such post-DMFT methods are a major point of interest in theoretical condensed matter physics.

---

[1]As pointed out by Karsten Held, a model Hamiltonian with only pair hopping but no single-particle hopping term is an interesting one to explore. While such a system physically should feature charge transport, the current will be trivially zero when calculated in the Peierls approximation.

[2]This is not a necessary prerequisite, but for any bath which includes inter-bathsite hopping, diagonalisation of the non-interacting bath-subspace yields an equivalent description for the impurity site.

3. General properties of two-particle vertices

This section is dedicated to a discussion of general features of vertices on the two-particle level. Specifically with regard to some approximations made on the vertices it can be of crucial importance to analyse which symmetries are broken and what the consequences can be. As computational power increases and we therefore are able to investigate more complicated objects, vertex-based approximation schemes are moving into the focus of research. These methods either attempt to build the vertices of a system from scratch, as it is the case within calculations based on the parquet-approximation, or use vertices taken from a DMFT calculation. From the local vertex these approaches extend the results beyond the scope of pure DMFT. Examples of the second kind of approximations are the dynamical vertex approximation [22], which uses fully irreducible vertices as an input, as well as the dual fermion [23] and one-particle irreducible approach [25], based on the full and one-particle irreducible[1] local vertices respectively.

3.1. Crossing Symmetry

The crossing symmetry is associated with the antisymmetry of fermions with regard to exchange of particles. This means that transport amplitudes into states with one pair of electrons exchanged have to pick up a relative sign, implying that whenever two incoming or outgoing particles of a vertex are exchanged, the sign has to change. For a translationally invariant system (cf. section 3.2), a vertex can be expressed in terms of three four-vectors k, k' and q. Below, the connected part of the two-particle Green's function, the full vertex with outer legs, is shown. All non-momentum indices, e.g. spin or orbit ones were assumed to be equal for the entering and leaving lines. The outer propagators were labeled in accordance with particle-hole notation. Next to it, the diagram with exchanged outgoing particles is given. Since both diagrams describe the same processes, the values of the vertex for those two sets of variables cannot be independent.
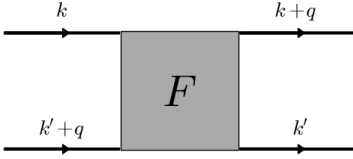
Figure 5: Diagrammatic representation of the full vertex with outer legs, adopting particle-hole notation
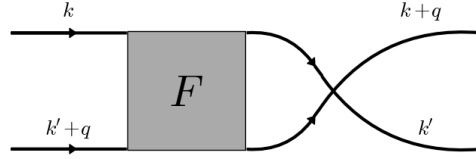
Figure 6: Diagrammatic representation of the full vertex with outer legs, exchanging the outgoing particles

In particle-hole notation, typically, one considers the scattering of a particle and a hole with four-momenta k and k', transferring a momentum of q. Note that time-translation invariance, as well as invariance under spatial transitions were assumed. If now the outgoing states are to be exchanged the conditions on the momenta are:

$$k \to k \tag{46a}$$
$$k' + q \to k' + q \tag{46b}$$
$$k + q \to k' \tag{46c}$$
$$k' \to k + q. \tag{46d}$$

These conditions are equivalent to:

$$k \to k \tag{47a}$$
$$k' \to k + q \tag{47b}$$
$$q \to k' - k. \tag{47c}$$

Thus, since the one-particle propagators, the outer legs, do not change, $F^{k,k',q}$ has to fulfill the condition

$$F^{k,k',q} = -F^{k,k+q,k'-k}. \tag{48}$$

An analogous exchange of the incoming particles yields:

$$F^{k,k',q} = -F^{k'+q,k',k-k'}. \tag{49}$$

---

[1]On the two-particle level, the one-particle irreducible and full vertex coincide.

While swapping both incoming and outgoing particles among each other results in the expression

$$F^{k,k',q} = F^{k'+q,k+q,-q}. \tag{50}$$

The crossing relations enforce the Pauli-exclusion principle, as one can easily see when setting

$$q = \pm(k' - k). \tag{51}$$

This leads to either two outgoing particles with momentum k' (in equation (48)) or two incoming ones with momentum k (in equation (49)). Inspection of the crossing symmetries shows that such a term can never contribute as the full vertex then has to be minus itself ($F^{k,k',k'-k} = -F^{k,k',k'-k}$ or $F^{k,k',k-k'} = -F^{k,k',k-k'}$) and thus assume the numerical value 0. This means that two-particle scattering amplitudes into (from) states with two identical particles do not exist. The crossing symmetry is an intrinsic property of fermions and does not depend on the properties of the system one is describing. It's a manifestation of the Pauli exclusion principle.

When building ladder diagrams in either of the particle hole channels as an approximation for the full vertex, the resulting vertex generally violates the crossing symmetry, unless both ph and $\overline{ph}$ ladder are taken into account symmetrically, for example within $D\Gamma A$.

3.2. Translation invariance

Typically, one investigates systems without explicit dependence on time. Furthermore, theoretical solid state physics commonly deals with systems displaying translation invariance in real space, as it is the case when periodic lattices are considered. In these cases, the dependence of the vertex on four times is reduced to a dependence on three time-differences. After a Fourier transform this quality manifests as conservation of energy – the sum of the frequencies of the particles entering the vertex has to be equal to the sum of all leaving ones. Equivalently, (lattice) momentum is conserved when the momenta of incoming and outgoing particles are equal when summed. The choice of frequency and momentum variables is not unique and a few different conventions exist. Two undoubtedly useful ways of assigning frequency arguments are certainly given by the ph and pp notation, yielding Bethe-Salpeter equations which are diagonal in their respective ω and q transfer-variables for the associated channel. Since frequency and momentum variables behave very similarily, they are often combined into four-momentum variables.

3.3. Symmetries in space

Commonly, one investigates systems with pointgroup symmetries in space. The consequences symmetries in space have on one-particle objects are typically more easily explained than for two-particles ones. Symmetries can allow us to save effort in calculations as well as memory. Formally, two points are equivalent if they can be mapped onto each other by use of the symmetry operators of the system. On a square lattice, the number of k-points which need to be considered can be reduced by a factor of 8, while on a cubic lattice it can be reduced by a factor 48. For a two-particle quantity in a translation-invariant system, not one, but three k-indices are required. This means that the numerical effort for determining those objects scales at least as the third power of k-points does (In fact, the memory requirements scale like the third power of k-points (n_k^3), while the number of operations for solving a Bethe-Salpeter scales even less favourably ($n_k^{3.373}$ - n_k^4, depending on the algoritm employed for the matrix inversion)). The symmetry reduction applies only once, tough. This is because, in the general case, the first k-vector to be chosen breaks the symmetry of the system for the choice of the remaining k-vectors. Formally, any symmetry transformation has to be applied to all three k-vectors which results in a reduced impact of the symmetry when the number of variables is increased. An unfortunate side-effect of the necessity of applying the same symmetry operation to all k-indices at once is the more complicated reconstruction procedure when one wants to access values which are not stored explicitly but can be determined by symmetry. Let us expatiate on the procedure involved by considering the example of three k-vectors a, b and c. We will assume that our data is symmetrised in a, that is to say that our vertex is only saved for a-values within the irreducible Brillouin zone $\mathcal{B}$ while the full grid for possible values of b and c is saved for every a. If we now want to reconstruct the value of the vertex for an a-value outside the irreducible Brillouin zone, we first need to find the symmetry operation $\mathcal{S}$ of the system which maps this value of a into the irreducible Brillouin zone:

$$\mathcal{S}(a) = \widetilde{a} \in \mathcal{B}. \tag{52}$$

The same symmetry operation needs to be applied to all three k-points, so we need to evaluate the original vertex at $\mathcal{S}(a)$. $\mathcal{S}(b)$ and $\mathcal{S}(c)$. For accessing a single value, this procedure is acceptable. From a computational viewpoint, it can cause complications, as will be discussed in section 3.4.

3.4. Computational challenges

Vertices have some challenging properties when it comes to a numerical treatment. First, they are huge objects. A single vertex, saved for a k-mesh of 4×4 points, with 16 values for the two fermionic frequencies and 8 bosonic ones without any spin degrees of freedom, assuming 16-byte complex numbers takes up 128Mb. While symmetries of the system have not been employed and most computers can treat such objects, we certainly cannot exceed the precision mentioned above by much. Increasing the precison to 6×6 k-points, with 24 fermionic and 12 bosonic frequencies already requires 4.8Gb.

Besides memory size, the high frequency properties of vertices manifest as another problem, as they typically contain structures which extend to arbitrary values of some frequencies, as long as at least some of them are small. Given below in figure 7 are two examplary plots of cuts through the full local DMFT vertex for $\omega = 0$ (in ph notation) for the Falicov-Kimball and also for the Hubbard model.
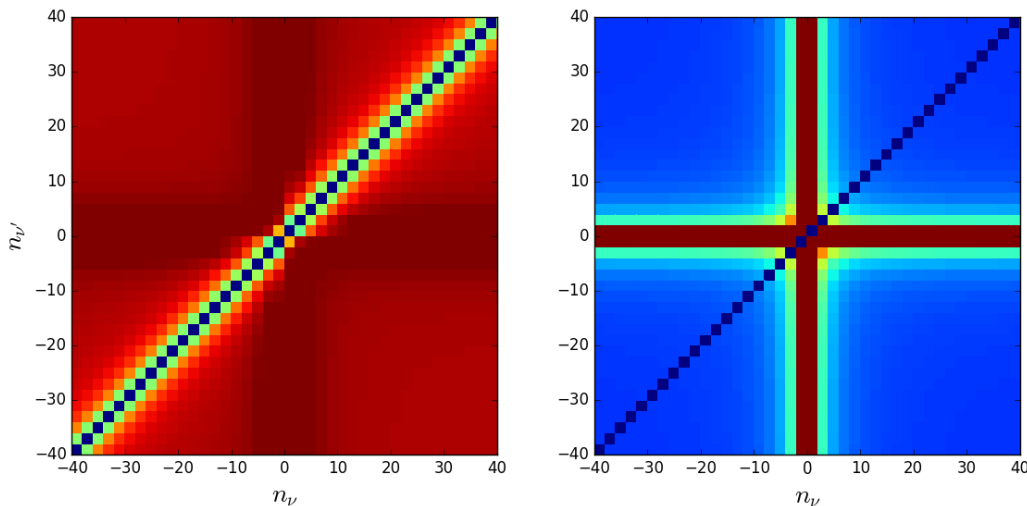
Figure 7: Examples of heatplots for the full vertex for $\omega = 0$ (in ph-notation) for the Hubbard model for interaction strength $U = 1$ and temperature $T = 0.125$ (left) and Falicov-Kimball model for interaction strength $U = 1$ and temperature $T = 0.06$ (right) at half-filling. n_ν and $n_{\nu'}$ denote fermionic Matsubara indices according to $\nu = T\pi n_\nu$ and go over all odd numbers.

One can easily recognise structures which extend to arbitrarily high frequency values. Both the HM's and FKM's vertex display cross-like structures, as well as some features along the main diagonal. Diagrammatically, such contributions are expected to appear [50], stemming from outer legs which are only connected to the remaining diagram via a single interaction line U. The main diagonal itself is zero due to the crossing symmetry for both models. While there is no special behaviour around the main diagonal in the FKM, in the HM there are additional structures around it. As a consequence of features of the vertices extending in frequency space and the infeasibility and futility of simply extending frequency ranges, approximate treatments of the vertex have been proposed. A promising attempt at controlling such features is the usage of kernel functions [50] as it is done in the *victory* package [51]. The vertex is only saved within a relatively small frequency range, but when it is needed outside this box, it is evaluated on the nearest boundary of the frequency box and the value is used as an approximation for the vertex where it is actually required.

As discussed before, in exploiting symmetries to reduce the amount of data which needs to be stored for a vertex, symmetry operations need to be applied to all arguments of the vertex at once. If one tries to optimise algorithms which solve the Bethe-Salpeter equations, this can become a huge problem, because the indices where the vertex is accessed can be at entirely different locations in memory. The Bethe-Salpeter equations in the pp and ph channels are preferably solved in their respective notations, where they are diagonal in their transfer momenta. This suggests the transfer momentum should be the slowest-moving variable. (leftmost index for C-arrays, rightmost index for FORTRAN-arrays) Unfortunately, the (bosonic) transfer momenta q within pp and ph notation are related by

$$q_{pp} = q_{ph} + k + k', \tag{53}$$

with k and k' being the (fermionic) non-transfer momenta which are the same between the two notations. When vertices stored according to the two conventions are to be added, incrementing the innermost variable

(usually k') leads to a change for one of the two q. As vertices can be quite large, the memory adress therefore changes rapidly, which impedes computational performance. For the *victory* package, the type of operation most of the CPU time is spent on is actually memory operations or communication if memory is distributed on many nodes[1]. This problem amplifies when a parallelisation of such a program is pursued, as each node needs to communicate with every other one.

3.5. Restriction to the two-particle level

Having discussed the computational challenges of treating vertices on the two-particle level, practical reasons for restricting oneself to pairs of particles are obvious. Besides our inability to computationally treat many-particle vertices, it has been argued that most of the systems one is typically interested in within the scope of solid-state theory are displaying two-particle interactions. Thus, one might assume that most relevant correlations are actually of two-particle nature. Additional arguments for a two-particle treatment are the ease of connecting two-particle quantities with physical susceptibilities via Kubo's formula and the huge success of a two-particle treatment of superconductivity within BCS-theory. Within the scope of this thesis, some explorations beyond the two-particle level were undertaken, testing the impact of higher order vertices [30, 31].

---

[1]Private communication with Anna Kauch

4. A closer look at the three-particle vertex

While the properties of the two-particle vertex are already quite well established and have been investigated closely [36, 52], the three-particle vertex is less well understood. There are obvious problems with the calculation of such objects for general systems, due to the huge number of degrees of freedom. Some calculations employing selected diagrams containing three-particle vertices have already been conducted as part of the present thesis [30, 31]. On the other hand, three-particle physics may be relevant in describing phenomena like interaction between excitons and electrons in solids[1].

The aim of this section is to give an overview of the features of three particle vertices in general, followed by an application of the gained knowledge to the fully local DMFT-vertices as derived in section 8.
We will start with a systematic classification of three-particle vertices, in terms of their (ir)reducibility. There are multiple possibilities of defining irredicibility and here an approach which is suitable to ladder diagramatics is presented. We will also restrict ourselves to systems with particle-number conservation. The notation will be chosen in agreement with figure 8. The indices a, b, ... are understood to be multi-indices carrying all necessary information about the involved incoming and outgoing states.
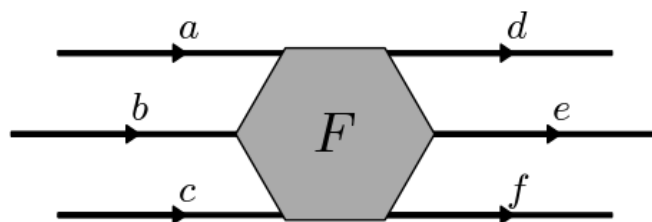
Figure 8: Notational convention for the three-particle vertex within this section. The external propagators are depicted for reasons of clarity only, they are not part of the vertex. The full vertex F contains all Feynman diagrams which connect all incoming and outgoing particle-lines.

4.1. One-particle reducible contributions

Unlike the two-particle vertex, the three-particle vertex is not precluded from containing one-particle reducible (1PR) contributions by conservation of particle number alone. A diagram is said to be 1PR if it can be disconnected into two two-particle diagrams by cutting a single one-particle propagator. The structure of 1PR contributions to the full vertex is very simple if one decides to work with "dressed" one-particle propagators already containing the self-energy. There is only one type of diagram which contributes to the three-particle vertex and is 1PR, see figure 9.
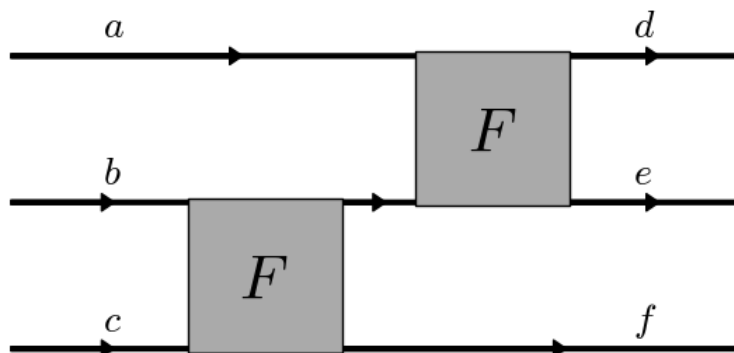
Figure 9: Here, we show all diagrams contributing to the three-particle vertex that are 1PR in the channel separating a, d, e from b, c, f. It can be written as a combination of two two-particle vertices and a Green's function line connecting them. The outer legs are shown for clarity.

---

[1] Other, arguably very relevant, three particle excitations are given by protons and neutrons which are bound states of three quarks. In the area of high-energy physics, some investigations have already been carried through on the three-particle level, considering a set of selected "reinbow" diagrams [53].

Since two-particle vertices are always one-particle irreducible, no overcounting problems arise for the diagrams shown in figure 9. There are 9 different channels in which a three-particle vertex can be 1PR as given in table 1.

a,b,d	a,b,e	a,b,f
c,e,f	c,d,f	c,d,e
a,c,d	a,c,e	a,c,f
b,e,f	b,d,f	b,d,e
b,c,d	b,c,e	b,c,f
a,e,f	a,d,f	a,d,e

Table 1: Systematic listing of all channels of one-particle reducibility for three-particle vertices. Each entry has two lines, the outer legs in every line remain connected to each other when the one-particle propagator is cut, while the connection between the legs of the upper and lower line is broken.

One might be surprised by the number of channels, as there are 10 different ways of grouping 6 elements into two sets of 3 elements. One of these 10 decompositions however is not possible. The missing decomposition is a,b,c and d,e,f. This sort of diagram cannot exist due to particle number conservation; corresponding diagrams would have to be separable into two-particle vertices with either 3 entering lines and 1 leaving line or 4 entering and no leaving lines and vice-versa–an impossibility due to conservation of particle number. We take note of the fact that a three-particle diagram can be reducible in one one-particle channel at most. If this were not the case, after the first cut, we would end up with two two-particle diagrams, one of which would have to be separable by cutting another one-particle propagator, while the other one would have to allow for a decomposition without a cut being performed, i.e. be disconnected. We already know that two-particle diagrams cannot be disconnected this way due to particle number conservation; two-particle vertices are always one-particle irreducible[1][2]. This means that no double-counting corrections are necessary when eliminating the 1PR contributions in table 1 from the full three-particle-vertex. In appendix D, the local one-particle irreducible three-particle vertex for the Falicov-Kimball model is derived.

4.2. Two-particle reducible contributions

There is a plethora of two-particle reducible (2PR) diagrams included in the full three-particle vertex. A three-particle diagram is considered 2PR if it can be disconnected into a three-particle and a two-particle diagram by cutting two internal one-particle propagators. The possibility of extracting an internal propagator with an self-energy insertion, thereby generating a one-particle diagram and a four-particle diagram is explicitly excluded. The number of channels increases dramatically compared to the two-particle level. In principle, there are 15 simple ways to be two-particle disconnected on the three-particle level, 6 pp-like ones and 9 ph-like ones. They are defined by which two outer legs can be disconnected from the remaining four by cutting two internal propagators. A table of all channels of 2PR diagrams is given below. We will refer to channels by the pair of outer legs which is separated from the rest.

a,b	d,e	a,d	b,d	c,d
c,d,e,f	a,b,c,f	b,c,e,f	a,c,e,f	a,b,e,f
a,c	d,f	a,e	b,e	c,e
b,d,e,f	a,b,c,e	b,c,d,f	a,c,d,f	a,b,d,f
b,c	e,f	a,f	b,f	c,f
a,d,e,f	a,b,c,d	b,c,d,e	a,c,d,e	a,b,d,e

Table 2: Systematic listing of all channels of two-particle reducibility for three-particle vertices. Each entry has two lines, the outer legs in every line remain connected to each other when two one-particle propagators are cut.

The structure of diagrams reducible in the pp-like channel separating d,e and a,b,c,f is given in figure 10. The major problem in attempting a systematic classification of 2PR three-particle diagrams comes from

---

[1] For systems with particle-number conservation.
[2] Because of this, the $1PI$ approach is relying on the same full vertex F as the DF approach which includes 1PR diagrams. Only on the three-particle vertex level the difference between them becomes more pronounced. This difference nontheless has consequences on the diagrams constructed from F in the different approaches, see section 5.3 and [25].
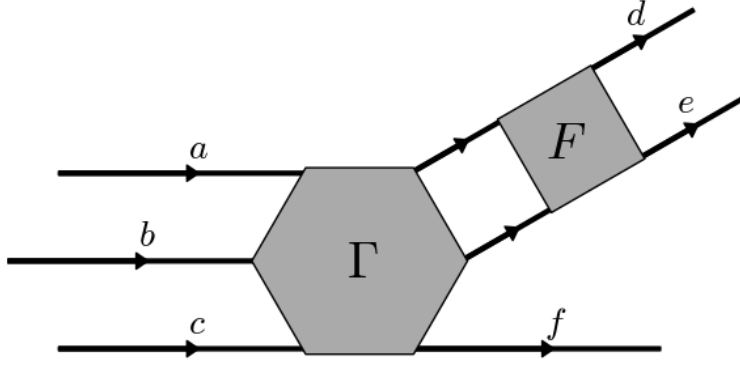
Figure 10: All diagrams contributing to the three-particle vertex and 2PR in the channel separating d, e from a, b, c, f

the diversity of combinations of reducibility. Just because a diagram is 2PR in a given channel does not necessarily cause it to be irreducible in the other ones, as it is the case for the two-particle vertex; there are some restricting features, however. A good example for the arising difficulties are all the diagrams of the structure depicted in figure 11. These diagrams additionally feature non-simultaneous reducibility, which is discussed in more detail in section 4.2.2.
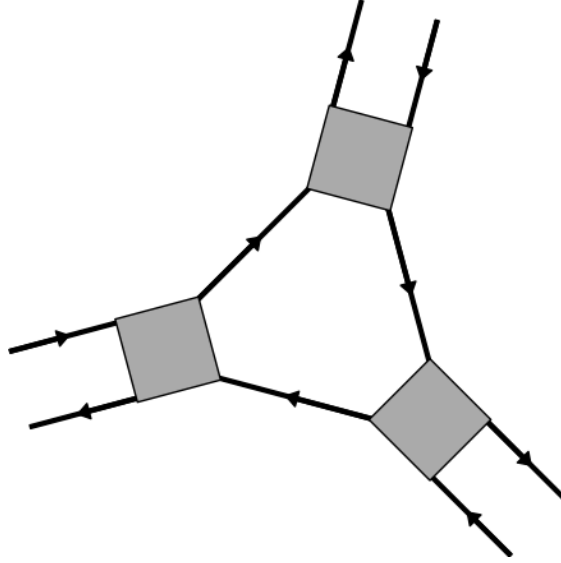
Figure 11: Diagrams of this structure are 2PR in three ph-like channels, but not necessarily simultaneously reducible in more than one. (i.e. cutting two lines disconnecting a two-particle part does not allow a subsequent cutting of two lines leading to another disconnected two-particle part)

To further our understanding of the structure of two-particle reducible contributions to the three-particle vertex, we investigate restrictions on reducibility. To this end, the standard argument against multiple reducibility is applied: Let us consider a diagram which is reducible in two different channels, i, j and k, l with

$$i, j, k, l \in \big\{ \{a, b, c, d, e, f\} \mid i \neq j, k \neq l, \{i, j\} \neq \{k, l\} \big\}. \tag{54}$$

This means that there are two sets of cuts disconnecting the diagram in specific manners. We imagine applying both sets of cuts. The first set disconnects the diagram into a two-particle diagram with two (i, j) of the original six outer legs and a three-particle diagram with the remaining four. The second set of cuts should now disconnect two more outer legs (k, l) from the rest. A problem might arise if both sets of cuts require cutting the same internal line as it would be the case with some diagrams of the structure depicted in figure 11, but this case will be treated separately in section 4.2.2. Excluding the 'shared cut' case, no

complications occur if i, j and k, l do not share an element. That is if,

$$\nexists m \mid m \in \{i, j\}, \, m \in \{k, l\}, \tag{55}$$

the diagrams are of the generalised structure depicted in figure 12. Note that the opposite case,

$$\exists m \mid m \in \{i, j\}, \, m \in \{k, l\} \tag{56}$$

leads to a contradiction, as will be shown in section 4.2.1. An analogous line of reasoning can be followed for the case of threefold two-particle reducibility, yielding similar results.
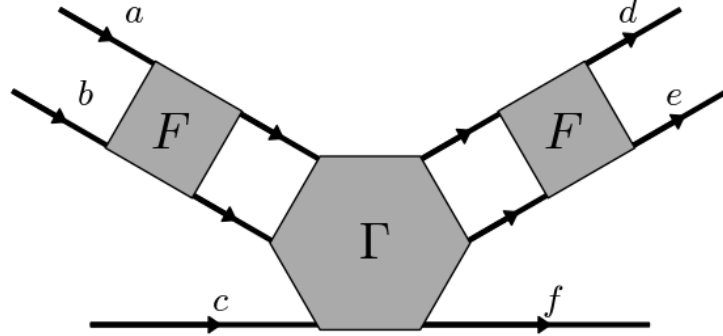
Figure 12: All diagrams contributing to the three-particle vertex and simultaneously 2PR in the channels separating both a, b and d, e

4.2.1. Incompatible channels

Let us now consider pairs of 2PR channels which share an external line to be disconnected, i.e. 56 holds, for example a, b and b, c. After the first set of cuts, we have disconnected our diagram into a two-particle and a three-particle part. If the second set of cuts is applied as well, one of the outer legs of the three-particle contribution as well as of the two particle contribution in our example a and c would have to be disconnected from their respective remaining diagrams. This can work neither for the two-particle nor for the three-particle part. It would mean that the diagramatic part starting from here a and c would till its cut from the rest of the diagram be a mere self-energy inclusion which is already contained in our skeleton diagrams in terms of the full, interacting Green's function. The implication is that a given diagram cannot be reducible in channels which share an element. We decide to call such channels incompatible with respect to two-particle reducibility. Each 2PR channel is incompatible with 8 and compatible with 6 other channels. In total, there are 45 distinct pairs of compatible channels as in figure 12 and 15 distinct sets of three compatible channels. There are 4 distinct types of pairs of compatible channels (incoming and outgoing pp-like, incoming pp and ph, outgoing pp and ph, as well as double ph with multiplicities 9, 9, 9 and 18 respectively). There are 2 types of triplets of reducibilities, pp-pp-ph and ph-ph-ph, appearing with multiplicities 9 and 6. Every two-particle channel appears in exactly three triplets.

Incompatible two-particle channels display additional behaviour hampering our attempts at finding fully irreducible three-particle vertices. Reducibility on the two-particle level can be masked. Consider a diagram of the structure depicted in figure 13. Obviously, the diagram is reducible in e, f, but would become reducible in d, e upon removing the e, f 2PR contribution. Such diagrams with masked two-particle reducibility are always 3PR as well, so taking some care in removing them is required to avoid overcounting issues when constructing the three-particle irreducible vertex[1].

---

[1] This masking issue already appears on the two-particle vertex level, but it is actually handled already by the Parquet formalism.
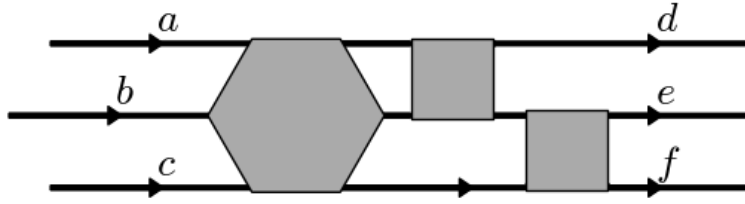
Figure 13: Reducibility in the e, f channel masking reducibility in the d, e channel. This diagram is reducible in e, f and irreducible in d, e but becomes reducible in d, e upon removing the d, e-reducible contribution.

4.2.2. Shared cuts

One can easily see that while the diagrams in figure 11 are 2PR in 3 different channels, they are not of the structure shown in figure 12. The issue of diagrams not simultaneously separable needs to be resolved. We start from a diagram which is 2PR in two compatible channels, but not simultaneously reducible in both. This can only happen if the first set of cuts somehow interferes with the other if both sets of cuts were to be applied. The only possibility of such an event occurring is when the same propagator would be cut by both sets of cuts. Without loss of generality, let us assume that the compatible channels in question are a, b and d, e. (If this condition is not fulfilled, we just relabel the external legs accordingly.) We now first conduct the cuts required to separate a and b from the remainder and end up with something akin to figure 14.
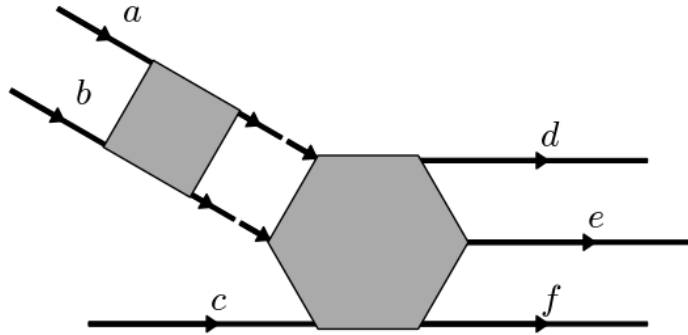
Figure 14: Remaining structure of "shared cut" diagram after disconnecting a, b.

Note that the directions of the one-particle propagators in figure 14 do not matter for our line of argument and are thus chosen arbitrarily. If the cuts required to disconnect d, e could simply be performed on the three-particle part, the diagram would be simultaneously separable in both channels and thus contained in the ones depicted already in figure 12. This means that at least one cut which is necessary to disconnect d, e is in some way interfered with by the first set of cuts. Let us first consider the (theoretical) possibility that one (or both) of the d, e cuts are located within the two-particle part of the disconnected diagrams in figure 14. A single cut within the two-particle part is not sufficient to disconnect any line from any other. A single cut within the three-particle part is neither sufficient to disconnect two external legs from the remaining ones, tough it is possible to disconnect the three-particle part into two two-particle pieces. Disconnecting d, e from c, f in the three-particle part, with each pair remaining connected to one of the legs originating from the a, b cut is the only way of achieving a separation of d, e from c, f. The problem with this sort of decomposition is, that such a diagram would not be 2PR in d, e in the first place, because performing only the d, e cuts would leave the original diagram fully connected (because after the first set of cuts the two-particle propagator with a, b cannot be disconnected by a single cut, acting as a chain-link for the diagram). The last remaining possibility is a "shared cut"-a single particle line which is included in both sets of cuts. In such a case only a single line is cut when disconnecting d, e after a, b, the remaining three-particle part after the a, b cuts being 1PR in a channel which allows disconnecting d, e from c, f. This implies that all diagrams which are 2PR but not simultaneously 2PR in two channels are actually of the

structure in figure 11 and actually 2PR–but not simultaneously 2PR–in exactly three compatible channels.

4.3. Three-particle reducible contributions

Even more complicated than the case of 1PR and 2PR diagrams, three-particle reducibility (3PR) offers a wide range of different channels and interplay with lower order reducibility. The channels can be labelled in accordance with the 1PR case, with one additional channel being introduced, the one disconnecting a, b, c from d, e, f, which is not prohibited due to particle number conservation any longer when cutting three single-particle propagators. The general structure of the reducible diagrams is given in figure 15.
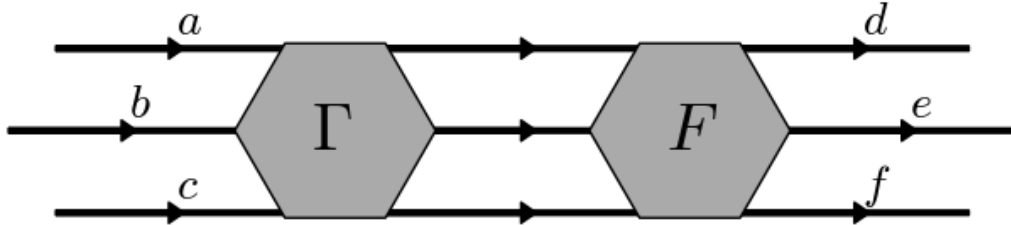
Figure 15: All diagrams contributing to the three-particle vertex and 3PR in the channel separating a, b, c from d, e, f can be written as an irreducible vertex Γ connected to the full three-particle vertex F by three one-particle Green's functions.

We also note that only diagrams which can be disconnected into two three-particle pieces are considered to be 3PR here. There is a possibility of disconnecting a three-particle diagram into a two-particle and a four-particle part by cutting three lines. This sort of decomposition is ignored for the sake of reducibility because it would relate the three-particle vertex to the four-particle one. Applying this sort of reducibility argument, all three-particle diagrams are reducible for a system with only quartic interaction (One example of such a quartic system is given by the Hubbard model, while the Falicov-Kimball model regarding only c-electron degrees of freedom and integrating out the f- degrees of freedom, as it is done in the scope of this thesis exhibits further contributions beyond the quartic one. Similarly, dual fermion, $1PI$ and $D\Gamma A$ diagramatics are not quartic unless all local (full vertices, $1PI$ vertices or fully irreducible vertices respectively) DMFT-vertices above the two-particle level vanish.). This is consistent with the definition of two-particle (ir)reducibility and in agreement with the treatment in [54], which disallows cutting a two-particle vertex into a one-particle and a three-particle diagram, essentially by choosing an internal propagator of the diagram and cutting it at both ends, thereby extracting a one-particle line. Also compare to three-particle reducibility concept from Trilex [26].

Note that the notion of an irreducible vertex becomes blurred when advancing from the two-particle to the three-particle level. At first glance, one might assume that Γ, as depicted in figure 15 contains all diagrams irreducible in the a, b, c-d, e, f channel. This assumption, however, would be wrong. Considering a diagram of the structure depicted in figure 16, it is clear that the two-particle insert has to be classified as a part of the full three-particle vertex[1]. If such 2PR contributions are considered within Γ an overcounting problem is the consequence. Therefore, in constructing a Bethe-Salpeter-like equation for the three-particle level, these 2PR contributions need to be explicitly taken into account.

An immediate consequence of the 2PR contributions between the 'proper' three-particle vertices as in figure 16 is that the two possible ways of constructing Bethe-Salpeter like equations are not fully equivalent; unlike the two particle level, the order of Γ and F matters and the irreducible vertex Γ depicted in figure 15 must irreducible in the three-particle particle $a, b, c - d, e, f$ channel, but also in the two-particle d, e; e, f and d, f channels. This is depicted in figure 16 Exchanging the order of Γ and F within the Bethe-Salpeter like equation would require another Γ irreducible in the three-particle particle $a, b, c - d, e, f$ channel and the two-particle a, b, b, c and a, c channels. Therefore, the Bethe-Salpeter like equations on the three-particle

---

[1]If we had two such two-particle insets, e.g. for the upper and lower two legs, we would get a three-particle reducible vertex.

Figure 16: Schematic representation of the issues arising from the interplay between two- and three-particle reducibility.

level are of the structure

$$
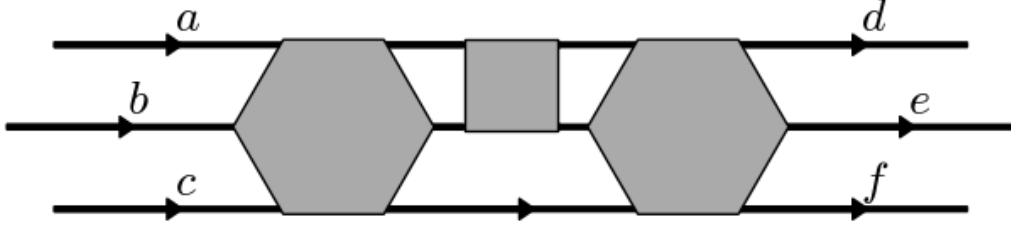F \begin{pmatrix} a & b & c \\ d & e & f \end{pmatrix} = \Gamma \begin{pmatrix} a & b & c \\ d & e & f \end{pmatrix} + \frac{1}{2} \sum_{1,2} \Gamma \begin{pmatrix} a & b & c \\ 1 & 2 & f \end{pmatrix} G(1)G(2) \, F \begin{pmatrix} 1 & 2 \\ d & e \end{pmatrix}
$$
$$
+ \frac{1}{2} \sum_{1,2} \Gamma \begin{pmatrix} a & b & c \\ d & 1 & 2 \end{pmatrix} G(1)G(2) \, F \begin{pmatrix} 1 & 2 \\ e & f \end{pmatrix} + \frac{1}{2} \sum_{1,2} \Gamma \begin{pmatrix} a & b & c \\ 1 & e & 2 \end{pmatrix} G(1)G(2) \, F \begin{pmatrix} 1 & 2 \\ d & f \end{pmatrix}
$$
$$
+ \frac{1}{6} \sum_{1,2,3} \Gamma \begin{pmatrix} a & b & c \\ 1 & 2 & 3 \end{pmatrix} G(1)G(2)G(3) \, F \begin{pmatrix} 1 & 2 & 3 \\ d & e & f \end{pmatrix}. \quad (57)
$$

for the ppp-like channel and

$$
F' \begin{pmatrix} a & b & c \\ d & e & f \end{pmatrix} = \Gamma \begin{pmatrix} a & b & c \\ d & e & f \end{pmatrix} + \frac{1}{2} \sum_{1,2} \Gamma \begin{pmatrix} a & b & c \\ 1 & 2 & f \end{pmatrix} G(1)G(2) \, F \begin{pmatrix} 1 & 2 \\ d & e \end{pmatrix}
$$
$$
+ \frac{1}{1} \sum_{1,2} \Gamma \begin{pmatrix} a & b & 2 \\ d & 1 & f \end{pmatrix} G(1)G(2) \, F \begin{pmatrix} 1 & c \\ e & 2 \end{pmatrix} + \frac{1}{1} \sum_{1,2} \Gamma \begin{pmatrix} a & b & 2 \\ 1 & e & f \end{pmatrix} G(1)G(2) \, F \begin{pmatrix} 1 & c \\ d & 2 \end{pmatrix}
$$
$$
+ \frac{1}{2} \sum_{1,2,3} \Gamma \begin{pmatrix} a & b & 3 \\ 1 & 2 & f \end{pmatrix} G(1)G(2)G(3) \, F' \begin{pmatrix} 1 & 2 & c \\ d & e & 3 \end{pmatrix}. \quad (58)
$$

for pph-like channels (The example is given for the $a, b, f - d, e, c$ channel specifically.). For above equations, the variables of the vertices were written as a matrix. The upper line of variables denotes incoming frequencies, the lower line denotes outgoing ones. Γ are the respective irreducible vertices. The terms coupling the irreducible three-particle vertex to the full two-particle vertex account for diagrams reducible in a two-particle channel excluded from Γ, but three-particle irreducible. Here, F' denotes the three-particle vertex that is $1PI$ with respect to the one-particle channel associated with the three-particle channel we are solving the Bethe-Salpeter like equation in. For the pph-like equation above, F' is given by[1]

$$
F' \begin{pmatrix} a & b & c \\ d & e & f \end{pmatrix} = F \begin{pmatrix} a & b & c \\ d & e & f \end{pmatrix} - \sum_{1} F \begin{pmatrix} a & b \\ f & 1 \end{pmatrix} G(1) F \begin{pmatrix} 1 & c \\ d & e \end{pmatrix}. \quad (59)
$$

This is because 1PR contributions in the channel associated with the 3PR channel need to be removed from the Bethe-Salpeter like equation as we prefer to work with dressed one-particle propagators which are difficult to categorise with respect to three-particle reducibility. Some self-energy diagrams can be cut into two parts by cutting three internal propagator lines[2]. A proper treatment of these contributions would call for additional classification of the self-energy and two-particle vertex with respect to three-particle reducibility. It seems advantageous to circumvent these issues by discarding potentially problematic diagrams in the first place.

For a solution of simplified three-particle ladder equations on the three-particle level for the Falicov-Kimball model see appendices E and F.

---

[1]In the case of the ppp-channel such 1PR contributions cannot occur.

[2]For quartic interaction, all Σ-diagrams except for Hartree- and Fock-term are 3PR while for models with higher order interactions only some are.

4.3.1. 3PR in more than one channel

A given diagram can be 3PR in any combination of two channels, there are no incompatible channels. Any diagram which is 3PR in more than one channel puts some restrictions on its decomposition. Let us investigate the possibilities of multiple reducibilities starting from a case as it is depicted in figure 15. We will discuss a diagram which is 3PR in more than one way. Without loss of generality, we can assume one of the channels to be the channel disconnecting a, b, c from d, e, f, as depicted (This channel is unique in being the only ppp-like channel, but the further discussion does not depend on that fact). For the second channel, we know for sure that applying the second set of cuts will further disconnect the groups of three outer legs each into a pair of legs and a single leg. For the following discussion, we will simply assume that the other channel is the one disconnecting b, c, f from a, d, e. Let us now discuss the possibilities of disconnecting a from b, c as well as f from d, e using three or less cuts starting from a configuration as it is given in figure 15. The two possibilities on how the diagram needs to be further decomposed are given in figure 17.
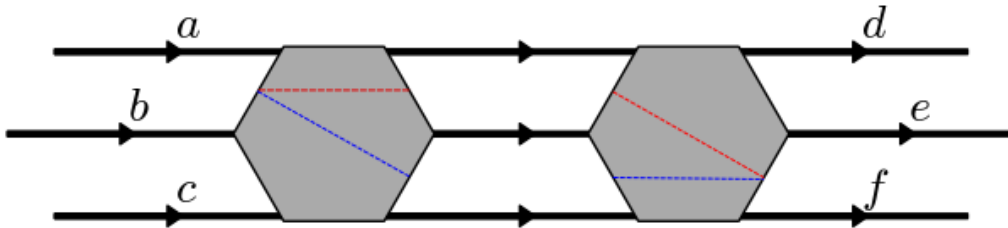
Figure 17: Possibilities of further decomposing a diagram with a, b, c already separated from d, e, f. The red and blue lines give the possibilities of further decompositions.

We can either disconnect a and one of the anonymous lines (for aesthetic reasons we choose the uppermost one, but they are equivalent) by performing two cuts and disconnecting a two-particle vertex from the remaining part of the left three-particle vertex. In this case, the right vertex needs to be disconnected by a single cut. This set of cuts is depicted schematically in figure 17 by red, dashed lines. The other possibility of multiple 3PR is depicted with blue, dashed lines. There is a further possibility of non-simultaneous reducibility, if both left and right vertex are one particle reducible. Then, by performing both tilted cuts (red and blue) as well as cutting the central line from the original decomposition, the diagram can be disconnected. We can gain valuable insights from the discussion. The constituent vertices of the first decomposition need to be 1PR and 2PR respectively for a diagram to be 3PR in more than one channel. This implies that by getting rid of all 1PR and 2PR contributions to the three-particle vertex prior to treating 3PR, we also preclude instances of multiple 3PR from occuring, reducing the combinatorical complexity in calculating the fully irreducible three-particle vertex. Algebraic solutions to simplified Bethe-Salpeter like equations for the three-particle case are given in the appendix E when only reducibility in a single three-particle channel is considered, as it should be done within three-particle ladder approximations.

4.4. Reconstruction of the vertex from irreducible vertices

If one wants to pursue a reconstruction of the full three-particke vertex based on the fully irreducible two-particle vertex, first a two-particle vertex is required. An approach in the spirit of $D\Gamma A$ on the three-particle level would thus require an already converged set of two-particle quantities. From these, it is possible to construct the auxilliary propagators V_{eff} and build three-particle ladders. Subsequently, 2PR and 1PR contributions can be reconstructed.

Such an approach could be used to update the two-particle vertex via an equation of motion, but this would require tremenduous computational ressources[1]. However, a restriction to ladders in a single three-particle channel is feasible and might uncover excitations which are of three-particle nature. First steps in this direction were undertaken in appendices E and F

4.5. Examplary low-order, fully irreducible contributions to the three-particle vertex

In this section, the lowest order (in the interaction) fully irreducible contributions to the three-particle vertex for a system with quartic interaction are derived. That is, the lowest order diagram which is irreducible in all

---

[1]Dynamical vertex approximation on the two-particle level has just recently become feasible in terms of computational ressources.

Figure 18: Six interaction points to be connected via propagator lines.

Figure 19: Interaction points after the first set of connections is established.

possible channels. The lowest order at which such terms can appear turns out to be 6. In the following, we will systematically derive the possible structures of such diagrams. To reduce the combinatorical complexity, we adopt a Hugenholtz-like diagramatic notation; the intera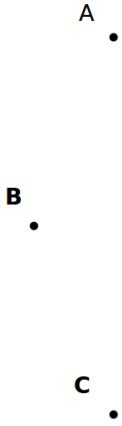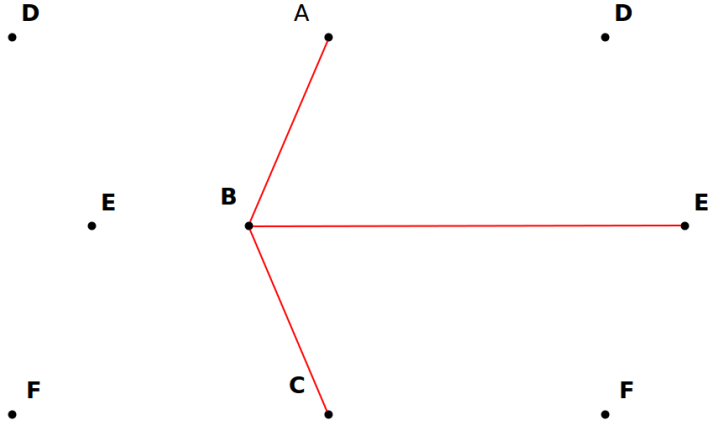ction is symmetrised with respect to outgoing and incoming lines. To avoid confusion, the diagramatic element corresponding to the interaction will be called interaction point[1]. Also, we will not care about directionality of the propagators at the moment. Due to the quartic interaction, each interaction point couples to exactly four propagator lines. Each propagator line couples to either two interaction points (if it is an internal line), or one interaction point (if it is an external line).

We first establish a lower boundary for the order of (one- and) two-particle irreducible, connected three-particle diagrams. Assume that the order of such a diagram was lower than 6. Since there are 6 external lines, at least one interaction point couples to at least 2 external lines. If an interaction point couples to 3 external lines, the diagram is 1PR – by cutting the fourth line connected to it, the diagram disconnects. We discard such contributions. If a point couples to two external lines, cutting the remaining two internal lines connected to it disconnects the diagram into two parts, it is therefore 2PR. We conclude that a connected three-particle diagram that is one- and two-particle irreducible has to be at least of order 6; each external line has to be connected to its own interaction point.

We now show that two interaction points cannot be connected by more than one line[2]. Assume that a pair of points is connected via a pair of lines. This pair of points is connected to the two external lines as well as to the remaining diagram by two lines–cutting the latter two lines disconnects the diagram and therefore it is 2PR.

We name the interaction points associated with (connected to) the external lines A,B,C,D,E and F. For aesthetical appeal we arrange them hexagonally as in figure 18. Without loss of generallity, we can assume that B is connected to A, C and E. (Point B has to be connected to exactly three other points and we can choose the names freely.) The resulting arrangement is depicted in figure 19.

Next we exclude any triangles-triplets of points which are mutually connected to each other. Assuming a diagram which contains a triangle, we can name the points forming it A, B and C. Relative to figure 19, this is achieved by connecting the points A and C. Once this is done, the remaining connections have to be performed as in figure 20[3]. Visual inspection of figure 20 immediately uncovers three-particle reducibility. We discard these diagrams as well.

If formation of triangles is not admissible, because it would cause the resulting diagrams to become 3PR, starting from figure 19, point A cannot be connected to C or E and therefore has to be coupled with D and F. Point C has to be connected D and F as well. In total, we end up with a diagram like figure 21, being the only type of sixth-order contribution to the fully irreducible three-particle vertex.

---

[1] The usual name for the diagramatic representation of an interaction would be (bare interaction) vertex, but "vertex qt would obviously be an ambiguous term in this context.

[2] This is only true if each interaction point is connected to an external line, for higher order terms it does not apply any longer.

[3] The choice of connecting A to D and C to F or A to F and C to D remains, but those diagrams are topologically equivalent.
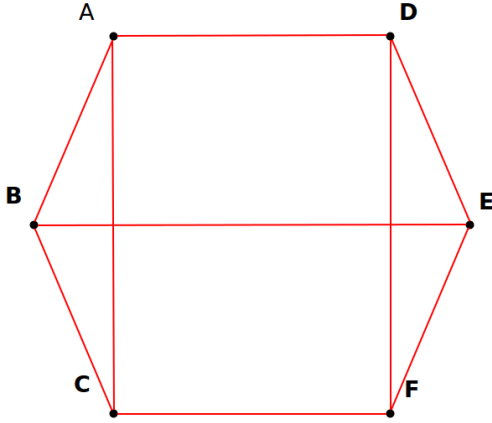
Figure 20: A low order three-particle diagram containing a triangle (in this case (ABC) and (DEF)) becomes three-particle reducible.
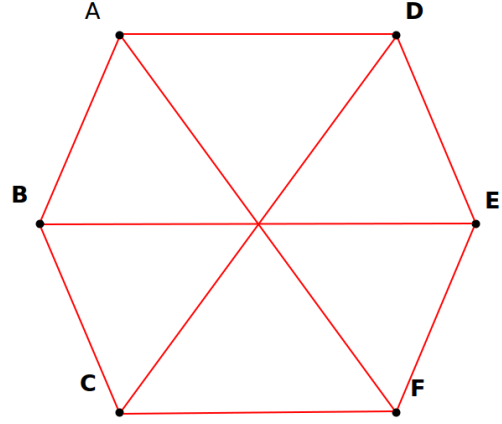
Figure 21: This diagram (and permutations thereof) is the only sixth (and lowest) order contribution to the three-particle vertex, which is fully (one-, two- and three-particle irreducible) irreducible.

4.6. Actual calculations on the three-particle level

Even assuming one has access to numerical data for local three-particle vertices, the question of what to do with it remains. The interpretation of self-energies has become quite clear in the quasiparticle-picture. On the two-particle level, the fluctuation-dissipation theorem allows us to associate physical susceptibilities with two-particle correlators. Moreover, a common argument why the calculation of two-particle properties might be sufficient to understand physical systems was given as follows: Most of the interactions we treat are of two-particle nature, thus we expect most of the relevant correlation effects to manifest on the two-particle level. We can exploratively evaluate some three-particle diagrams, as it is done in section 9 and compare their effect to the one of two-particle diagrams. Within theories such as dual fermion, this is straightforward. Selected diagrams can be considered as an error estimate if we truncate e.g. the DF theory at the two-particle level. If it turns out that the terms arising when explicitely taking into account three-particle quantities are of similar order of magnitude similar to the ones originating from the two-particle level, we are facing a major issue. Our original argument for truncating expansions, the two-particle nature of the interaction, is not valid any longer. While we could try constructing theories which are consistent on a three-particle level, implementing them and calculating results numerically, our calculations are probably just one explorative evaluation of some four-particle diagram away from being invalidated. In such cases it might be best to accept that our numerical calculations can qualitatively hint at processes which might be responsible for certain phenomena but not solve complicated correlated electron systems quantitatively.

4.7. Algorithm for hypothetical calculation of the fully irreducible three particle vertex

In this section, an algorithm for calculating the fully (one-, two-, and three-particle) irreducible three-particle vertex will be given. We will proceed as follows: first, all 1PR contributions will be removed, followed by any 2PR ones. With all remaining diagrams being one- and two-particle irreducible, it is possible to solve three-particle Bethe-Salpeter-like equations for all diagrams reducible exclusively in a single three-particle channel, with the new three-particle reducible channels being completely disjunct, i.e. not containing any common diagrams. Knowledge about the decomposition of the two-particle vertex will be required.

The 1PR contributions can be easily removed as their structure is known, see figure 9. No three-particle diagram can be 1PR in more than one channel, but some 1PR diagrams are 2PR as well. Also, for quartic interaction, the majority of the diagrams 1PR in a channel $ijk - lmn$ are also 3PR in the very same channel[1]. We can systematically remove all 1PR contributions by subtracting suitable combinations of full two-particle vertices connected by a single Green's function line. The 1PR vertex $\Phi_{1,abd-cef}$ in the channel

---

[1]Only if there are not enough internal lines to cut they are not 3PR.

$abd - cef$ is given by

$$\Phi_{1,abd-cef} \begin{pmatrix} a & b & c \\ d & e & f \end{pmatrix} = \sum_1 F \begin{pmatrix} a & b \\ d & 1 \end{pmatrix} G(1) F \begin{pmatrix} 1 & c \\ e & f \end{pmatrix}. \tag{60}$$

The 1PR vertices in all 9 one-particle channels can be subtracted from the full three-particle vertex F, yielding the fully one-particle irreducible three particle vertex Γ_1.

$$\Gamma_1 = F - \sum_{ijk-lmn} \Phi_{1,ijk-lmn} \tag{61}$$

The above summation is performed over all 9 1PR channels $ijk - lmn$.

Since any 1PR diagrams were already removed from the full vertex, we have to take care not to subtract 1PR diagrams which are also 2PR a second time when removing the 2PR diagrams. This means that we will establish Bethe-Salpeter-like equations for all one-particle irreducible diagrams. When doing so, not only do we need to remove all 1PR diagrams from the underlying set of diagrams, but also all the two-particle-reducible ones based on expanding 1PR diagrams.

We will discuss the procedure of removing such diagrams for the $ab - de - cf$ and $ad - be - cf$ sets of compatible channels. For a given set of compatible two-particle channels, every 1PR channel either (class 1 1PR channel) disconnects the entering and leaving lines into two sets of "unpaired" variables, where no variables belonging to the same two-particle channel are on the same end of the diagram, or (class 2 1PR channel) into two sets of an "unpaired" variable and two "paired" ones. For the $ab - de - cf$ set of channels, the completely "unpaired" (class 1) 1PR channels are given by $adc - bef$, $adf - bce$, $ace - bdf$ and $aef - bcd$. Any diagram 1PR in a completely "unpaired" channel is irreducible in all three two-particle channels. For the remaining channels, the 1PR, yet two-particle irreducible (in all three two-particle channels) contribution is given by the corresponding two-particle irreducible vertices, connected by a single one-particle Green's function. These 1PR contributions will be missing from our irreducible vertices, so any reducible diagrams built upon this irreducible basis need to be removed from the set of all diagrams for the Bethe-Salpeter-like equation to make sense.

Before turning to these class 1 1PR diagrams, we discuss the contributions from reducible diagrams built upon the 1PR diagrams made up from irreducible two-particle vertices, as depicted in figure 22 (class 2). To this basis diagram, full two-particle vertices F can be connected to ab, de and cf to recover all 2PR diagrams in the corresponding channels. Connecting the additional F to ab or de yields all reducible two-particle vertices. Obviously, the resulting diagrams are all still one-particle reducible and were therefore already removed in the first step, when removing the 1PR diagrams. Then further connecting another F to cf yields a diagram of the structure in figure 11, with all three vertices being full two-particle vertices and the outer variables being grouped as ab, de and cf. For this reason we need to remove these diagrams from the basis set of 2PR diagrams (the left hand side of our Bethe-Salpeter like equation). Note that this triangular diagram can be generated as a reducible contribution based on any class 2 1PR diagram (of which there are either 5 or 6 for the $ph - ph - ph$ and $pp - pp - ph$ cases respectively). The issue arises because the decomposition of such diagrams into two-particle irreducible and reducible parts is not unique, i.e. there is more than one diagram one can end up with, depending on the order in which reducible contributions in the different channels are removed. Had we not manually taken care of these diagrams, an overcounting issue would have been the consequence.

Now we proceed by investigating the behaviour of the class 1 1PR diagrams. To these diagrams, we connect any combination of either one, two or three full two-particle vertices. Attaching a single two-particle vertex yields a triangle-diagram again, this time with one pairing of variables as in the two-particle channel. Therefore, also all triangles with one pair of variables fitting our two-particle channels need to be removed from the l.h.s. of the equation. Connecting two full two-particle vertices to the class 1 1PR term yields butterfly-like structures as depicted in figure 23. The "external" vertices have pairs of associated variables and there are three possible configurations of variables to be distributed between the external legs. Finally, the option of attaching all three vertices remains, generating diagrams which are reducible in all three two-particle channels.

Triangle diagrams can be uniquely labeled by a set of compatible two-particle channels they are associated with. For $ph - ph - ph$ like sets of decompositions, two possible orientations for the inner line exist, which
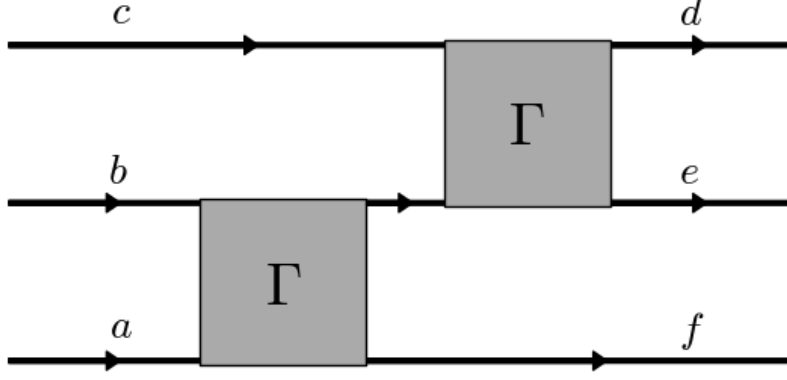
Figure 22: 1PR (class 2in the channel $abf - cde$) contribution to the two-particle $ab - de - cf$ irreducible vertex. The Γs are pp-irreducible two-particle vertices.

need to be taken into account. The $ad - be - cf$-triangle diagrams $T_{ad-be-cf}$ are given by

$$
T_{ad-be-cf} \begin{pmatrix} a & b & c \\ d & e & f \end{pmatrix} = \sum_{1,2,3} G(1)G(2)G(3) \times
$$

$$
\left(-F \begin{pmatrix} a & 1 \\ d & 2 \end{pmatrix} F \begin{pmatrix} b & 2 \\ e & 3 \end{pmatrix} F \begin{pmatrix} c & 3 \\ f & 1 \end{pmatrix} - F \begin{pmatrix} a & 1 \\ d & 2 \end{pmatrix} F \begin{pmatrix} b & 3 \\ e & 1 \end{pmatrix} F \begin{pmatrix} c & 2 \\ f & 3 \end{pmatrix} \right). \quad (62)
$$

For $pp - pp - ph$ cases there is only one possible orientation for the inner propagators and the triangle diagrams are given by

$$
T_{ad-bc-ef} \begin{pmatrix} a & b & c \\ d & e & f \end{pmatrix} = \sum_{1,2,3} G(1)G(2)G(3) F \begin{pmatrix} a & 1 \\ d & 2 \end{pmatrix} F \begin{pmatrix} b & c \\ 1 & 3 \end{pmatrix} F \begin{pmatrix} 2 & 3 \\ e & f \end{pmatrix}. \quad (63)
$$

The diagrams with Butterfly-like structure as depicted in figure 23 can be labelled by the pair of channels they are reducible in. They can be constructed based on triangle diagrams. The $ab - de$ Butterfly diagrams B_{ab-de} are given by

$$
B_{ab-de} \begin{pmatrix} a & b & c \\ d & e & f \end{pmatrix} = \frac{1}{2} \sum_{1,2} G(1)G(2) F \begin{pmatrix} a & b \\ 1 & 2 \end{pmatrix} \times
$$

$$
\left(T_{ac-bf-de} \begin{pmatrix} 1 & 2 & c \\ d & e & f \end{pmatrix} + T_{af-bc-de} \begin{pmatrix} 1 & 2 & c \\ d & e & f \end{pmatrix} \right), \quad (64)
$$

and the $ad - be$ ones by

$$
B_{ad-be} \begin{pmatrix} a & b & c \\ d & e & f \end{pmatrix} = \frac{1}{1} \sum_{1,2} G(1)G(2) F \begin{pmatrix} a & 2 \\ 1 & d \end{pmatrix} \times
$$

$$
\left(T_{ac-be-df} \begin{pmatrix} 1 & b & c \\ 2 & e & f \end{pmatrix} + T_{af-be-cd} \begin{pmatrix} 1 & b & c \\ 2 & e & f \end{pmatrix} \right). \quad (65)
$$

It is in turn possible to express all of the diagrams generated from attaching three full vertices to both sides of a class 1 1PR diagram, H, in terms of the butterfly diagrams

$$
H_{ab-cf-de} \begin{pmatrix} a & b & c \\ d & e & f \end{pmatrix} = \frac{1}{1} \sum_{1,2} G(1)G(2) F \begin{pmatrix} c & 1 \\ 2 & f \end{pmatrix} B_{ab-de} \begin{pmatrix} a & b & 2 \\ d & e & 1 \end{pmatrix}. \quad (66)
$$

To determine all 2PR contributions to the one-particle irreducible three-particle vertex, we resolve the
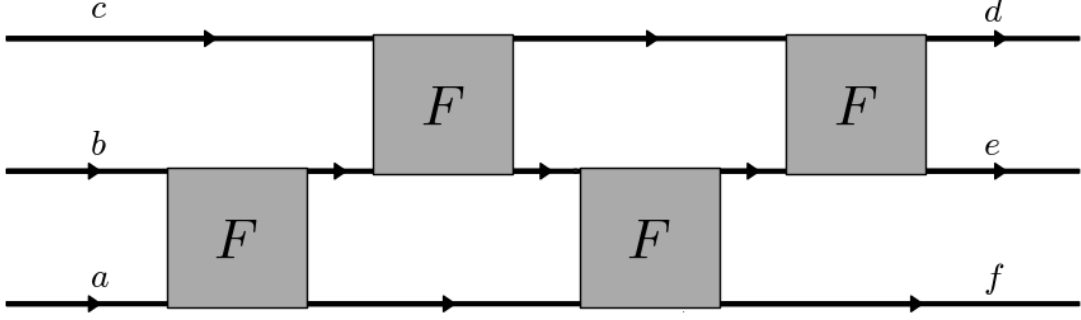
Figure 23: 2PR diagrams in the channels ab and de built by attaching two-particle vertices F upon the class 1 1PR diagrams in either the $acd - bef$, $ace - bdf$, $adf - bce$ or $aef - bcd$ channel. This kind of diagram is called butterfly-diagram, because it can be deformed into a butterfly with 2PR wings connected via a body consisting of two full two-particle vertices.

Bethe-Salpeter like equations

$$
\Gamma_1 \begin{pmatrix} a & b & c \\ d & e & f \end{pmatrix} - \text{"} \sum_{T,B,H} \text{"} = \Gamma' \begin{pmatrix} a & b & c \\ d & e & f \end{pmatrix} + \frac{1}{2} \sum_{1,2} \Gamma' \begin{pmatrix} a & b & c \\ 1 & 2 & f \end{pmatrix} G(1)G(2) \, F \begin{pmatrix} 1 & 2 \\ d & e \end{pmatrix}
$$

$$
+ \frac{1}{2} \sum_{1,2} \Gamma' \begin{pmatrix} 1 & 2 & c \\ d & e & f \end{pmatrix} G(1)G(2) \, F \begin{pmatrix} a & b \\ 1 & 2 \end{pmatrix} + \frac{1}{1} \sum_{1,2} \Gamma' \begin{pmatrix} a & b & 1 \\ d & e & 2 \end{pmatrix} G(1)G(2) \, F \begin{pmatrix} c & 2 \\ 1 & f \end{pmatrix}
$$

$$
+ \frac{1}{4} \sum_{1,2,3,4} \Gamma' \begin{pmatrix} 1 & 2 & c \\ 3 & 4 & f \end{pmatrix} G(1)G(2)G(3)G(4) \, F \begin{pmatrix} a & b \\ 1 & 2 \end{pmatrix} F \begin{pmatrix} 3 & 4 \\ d & e \end{pmatrix}
$$

$$
+ \frac{1}{2} \sum_{1,2,3,4} \Gamma' \begin{pmatrix} 1 & 2 & 3 \\ d & e & 4 \end{pmatrix} G(1)G(2)G(3)G(4) \, F \begin{pmatrix} a & b \\ 1 & 2 \end{pmatrix} F \begin{pmatrix} c & 4 \\ 3 & f \end{pmatrix}
$$

$$
+ \frac{1}{2} \sum_{1,2,3,4} \Gamma' \begin{pmatrix} a & b & 1 \\ 3 & 4 & 2 \end{pmatrix} G(1)G(2)G(3)G(4) \, F \begin{pmatrix} c & 2 \\ 1 & f \end{pmatrix} F \begin{pmatrix} 3 & 4 \\ d & e \end{pmatrix}
$$

$$
+ \frac{1}{4} \sum_{1,2,3,4,5,6} \Gamma' \begin{pmatrix} 1 & 2 & 3 \\ 4 & 5 & 6 \end{pmatrix} G(1)G(2)G(3)G(4)G(5)G(6) \, F \begin{pmatrix} a & b \\ 1 & 2 \end{pmatrix} F \begin{pmatrix} 4 & 5 \\ d & e \end{pmatrix} F \begin{pmatrix} c & 6 \\ 3 & f \end{pmatrix}. \quad (67)
$$

for $pp - pp - ph$ like separation (given for the $ab - de - cf$ case here) and

$$
\Gamma_1 \begin{pmatrix} a & b & c \\ d & e & f \end{pmatrix} - \text{"} \sum_{T,B,H} \text{"} = \Gamma' \begin{pmatrix} a & b & c \\ d & e & f \end{pmatrix} + \frac{1}{1} \sum_{1,2} \Gamma' \begin{pmatrix} 1 & b & c \\ 2 & e & f \end{pmatrix} G(1)G(2) \, F \begin{pmatrix} a & 2 \\ 1 & d \end{pmatrix}
$$

$$
+ \frac{1}{1} \sum_{1,2} \Gamma' \begin{pmatrix} a & 1 & c \\ d & 2 & f \end{pmatrix} G(1)G(2) \, F \begin{pmatrix} b & 2 \\ 1 & e \end{pmatrix} + \frac{1}{1} \sum_{1,2} \Gamma' \begin{pmatrix} a & b & 1 \\ d & e & 2 \end{pmatrix} G(1)G(2) \, F \begin{pmatrix} c & 2 \\ 1 & f \end{pmatrix}
$$

$$
+ \frac{1}{1} \sum_{1,2,3,4} \Gamma' \begin{pmatrix} 1 & 3 & c \\ 2 & 4 & f \end{pmatrix} G(1)G(2)G(3)G(4) \, F \begin{pmatrix} a & 2 \\ 1 & d \end{pmatrix} F \begin{pmatrix} b & 4 \\ 3 & e \end{pmatrix}
$$

$$
+ \frac{1}{1} \sum_{1,2,3,4} \Gamma' \begin{pmatrix} a & 1 & 3 \\ d & 2 & 4 \end{pmatrix} G(1)G(2)G(3)G(4) \, F \begin{pmatrix} b & 2 \\ 1 & e \end{pmatrix} F \begin{pmatrix} c & 4 \\ 3 & f \end{pmatrix}
$$

$$
+ \frac{1}{1} \sum_{1,2,3,4} \Gamma' \begin{pmatrix} a & 1 & 3 \\ b & 2 & 4 \end{pmatrix} G(1)G(2)G(3)G(4) \, F \begin{pmatrix} c & 2 \\ 1 & f \end{pmatrix} F \begin{pmatrix} 3 & 4 \\ d & e \end{pmatrix}
$$

$$
+ \frac{1}{1} \sum_{1,2,3,4,5,6} \Gamma' \begin{pmatrix} 1 & 3 & 5 \\ 2 & 4 & 6 \end{pmatrix} G(1)G(2)G(3)G(4)G(5)G(6) \, F \begin{pmatrix} a & 2 \\ 1 & d \end{pmatrix} F \begin{pmatrix} b & 4 \\ 3 & e \end{pmatrix} F \begin{pmatrix} c & 6 \\ 5 & f \end{pmatrix}. \quad (68)
$$

for $ph - ph - ph$ like separation (given for the $ad - be - cf$ case here). They provide a complete decomposition of the one-particle irreducible three-particle vertex in terms of reducibility in compatible two-particle channels. here Γ' denote the vertices two-particle-irreducible in all of the compatible channels associated with the

equation (ab, de and cf for the first case and ad, be and cf for the second) and are different quantities in the equations above. The sums over T, B, H are to include all triangle diagrams which share at least one two-particle channel with the Bethe-Salpeter like equation, all butterfly diagrams reducible in two channels appearing in the equation and the H diagrams with all three channels being compatible. There are 9 equations equivalent to the first one and 6 equivalent to the second. For each triplet of compatible chanels, the last line in the equations above gives the sum of all diagrams 2PR in all three of them. Those sets of diagrams are completely disjunct, i.e. no diagram can be reducible in all three channels of more than one triplet. We define the vertices reducible exclusively in the triplets for the two exemplary cases given above:

$$
\Phi'_{ab,de,cf} \begin{pmatrix} a & b & c \\ d & e & f \end{pmatrix} =
$$
$$
\frac{1}{4} \sum_{1,2,3,4,5,6} \Gamma' \begin{pmatrix} 1 & 2 & 3 \\ 4 & 5 & 6 \end{pmatrix} G(1)G(2)G(3)G(4)G(5)G(6) \, F \begin{pmatrix} a & b \\ 1 & 2 \end{pmatrix} F \begin{pmatrix} 4 & 5 \\ d & e \end{pmatrix} F \begin{pmatrix} c & 6 \\ 3 & f \end{pmatrix}
$$
$$
+ T_{ab,de,cf} \begin{pmatrix} a & b & c \\ d & e & f \end{pmatrix} + H_{ab,de,cf} \begin{pmatrix} a & b & c \\ d & e & f \end{pmatrix}. \quad (69)
$$

$$
\Phi'_{ad,be,cf} \begin{pmatrix} a & b & c \\ d & e & f \end{pmatrix} =
$$
$$
\frac{1}{1} \sum_{1,2,3,4,5,6} \Gamma' \begin{pmatrix} 1 & 3 & 5 \\ 2 & 4 & 6 \end{pmatrix} G(1)G(2)G(3)G(4)G(5)G(6) \, F \begin{pmatrix} a & 2 \\ 1 & d \end{pmatrix} F \begin{pmatrix} b & 4 \\ 3 & e \end{pmatrix} F \begin{pmatrix} c & 6 \\ 5 & f \end{pmatrix}
$$
$$
+ T_{ad,be,cf} \begin{pmatrix} a & b & c \\ d & e & f \end{pmatrix} + H_{ad,be,cf} \begin{pmatrix} a & b & c \\ d & e & f \end{pmatrix}. \quad (70)
$$

Those quantities can be safely subtracted from the full vertex without incurring any overcounting issues. Also, we define the vertices 2PR exclusively in pairs of compatible two-particle channels:

$$
\Phi'_{ab,de} \begin{pmatrix} a & b & c \\ d & e & f \end{pmatrix} =
$$
$$
\frac{1}{4} \sum_{1,2,3,4} \Gamma' \begin{pmatrix} 1 & 2 & c \\ 4 & 5 & f \end{pmatrix} G(1)G(2)G(3)G(4)G(5)G(6) \, F \begin{pmatrix} a & b \\ 1 & 2 \end{pmatrix} F \begin{pmatrix} 4 & 5 \\ d & e \end{pmatrix} + B_{ab,de} \begin{pmatrix} a & b & c \\ d & e & f \end{pmatrix}. \quad (71)
$$

$$
\Phi'_{ad,be} \begin{pmatrix} a & b & c \\ d & e & f \end{pmatrix} =
$$
$$
\frac{1}{1} \sum_{1,2,3,4} \Gamma' \begin{pmatrix} 1 & 3 & c \\ 2 & 4 & f \end{pmatrix} G(1)G(2)G(3)G(4)G(5)G(6) \, F \begin{pmatrix} a & 2 \\ 1 & d \end{pmatrix} F \begin{pmatrix} b & 4 \\ 3 & e \end{pmatrix} + B_{ad,be} \begin{pmatrix} a & b & c \\ d & e & f \end{pmatrix}. \quad (72)
$$

In this context exclusively 2PR in a pair of channels includes all diagrams 2PR in their respective pairs of channels, but irreducible in the third compatible channel. The exclusively reducible vertices in pairs of channels $\Phi'_{ij,kl}$ are related to the vertices containing all 2PR diagrams in a pair of channels $\Phi_{ij,kl}$[1] via

$$
\Phi_{ij,kl} = \Phi'_{ij,kl} + \Phi'_{ij,kl,mn}, \quad (73)
$$

with ij, kl, mn being any triplet of compatible channels. The vertices exclusively 2PR in pairs of channels do not share any diagrams with each other (if a diagram is reducible in three different two particle channels it is instead included in $\Phi'_{ij,kl,mn}$ and no three-particle diagram can be 2PR in more than 3 channels.), nor with the vertices exclusively reducible in any triplet of compatible channels, so all of them can safely be subtracted from the full vertex.

Unfortunately, we cannot directly extract the vertex exclusively 2PR in a single channel from any of the Bethe -Salpeter like equations above, because each 2PR-channel appears in two triplets of compatible channels and information from both of the associated Bethe-Salpeter like equations is required to exclude all undesireable diagrams, i.e. those already included in some $\Phi'_{ij,kl}$ or $\Phi'_{ij,kl,mn}$. For example, the Γ'

---

[1]Note that we restrict ourselves exclusively to one-particle irreducible vertices for the treatment of 2PR. That is there are further 2PR diagrams that are 1PR but these have already been subtracted.

calculated from equation (67) still contains contributions reducible in df or ce.

We define new, simpler Bethe-Salpeter like equations

$$\Gamma_1 \begin{pmatrix} a & b & c \\ d & e & f \end{pmatrix} - \text{"}\sum_T\text{"} = \Gamma_{de} \begin{pmatrix} a & b & c \\ d & e & f \end{pmatrix} + \frac{1}{2}\sum_{1,2}\Gamma_{de} \begin{pmatrix} a & b & c \\ 1 & 2 & f \end{pmatrix} G(1)G(2) \, F \begin{pmatrix} 1 & 2 \\ d & e \end{pmatrix}, \quad (74)$$

as well as

$$\Gamma_1 \begin{pmatrix} a & b & c \\ d & e & f \end{pmatrix} - \text{"}\sum_T\text{"} = \Gamma_{ad} \begin{pmatrix} a & b & c \\ d & e & f \end{pmatrix} + \frac{1}{1}\sum_{1,2}\Gamma_{ad} \begin{pmatrix} 1 & b & c \\ 2 & e & f \end{pmatrix} G(1)G(2) \, F \begin{pmatrix} a & 2 \\ 1 & d \end{pmatrix}. \quad (75)$$

For the pp (74) and ph-cases (75) respectively, above equations provide decompositions into all diagrams reducible and irreducible in a single two-particle channel. The summations on the respective left hand sides are to be performed over all triangles including the channel in question. The reducible contributions

$$\Phi_{de} \begin{pmatrix} a & b & c \\ d & e & f \end{pmatrix} = \frac{1}{2}\sum_{1,2}\Gamma_{de} \begin{pmatrix} a & b & c \\ 1 & 2 & f \end{pmatrix} G(1)G(2) \, F \begin{pmatrix} 1 & 2 \\ d & e \end{pmatrix} + \text{"}\sum_T\text{"} \quad (76)$$

and

$$\Phi_{ad} \begin{pmatrix} a & b & c \\ d & e & f \end{pmatrix} = \frac{1}{1}\sum_{1,2}\Gamma_{ad} \begin{pmatrix} 1 & b & c \\ 2 & e & f \end{pmatrix} G(1)G(2) \, F \begin{pmatrix} a & 2 \\ 1 & d \end{pmatrix} + \text{"}\sum_T\text{"} \quad (77)$$

are not exclusively reducible in their respective channels. We have to remove any contributions which also appear in reducible contributions we have already calculated to arrive at exclusively reducible vertices Φ':

$$\Phi'_{de} = \Phi_{de} - \Phi'_{ab,de} - \Phi'_{de,cf} - \Phi'_{ab,de,cf} - \Phi'_{af,de} - \Phi'_{de,bc} - \Phi'_{af,de,bc} - \Phi'_{ac,de} - \Phi'_{de,bf} - \Phi'_{ac,de,bf} \quad (78)$$

and

$$\Phi'_{ad} = \Phi_{ad} - \Phi'_{ad,be} - \Phi'_{ad,cf} - \Phi'_{ad,be,cf} - \Phi'_{ad,bf} - \Phi'_{ad,ce} - \Phi'_{ad,bf,ce} - \Phi'_{ad,bc} - \Phi'_{ad,ef} - \Phi'_{ad,bc,ef}. \quad (79)$$

Once these quantities have been calculated, all of the Φ' can simply be subtracted from the full three-particle vertex, removing all two-particle reducible contributions and yielding the fully one and two-particle irreducible three-particle vertex $\Gamma_{1,2}$

$$\Gamma_{1,2} = \Gamma_1 - \sum_{ij}\Phi'_{ij} - \sum_{\langle ij,kl\rangle}\Phi'_{ij,kl} - \sum_{\langle ij,kl,mn\rangle}\Phi'_{ij,kl,mn}, \quad (80)$$

where the summations are performed over all channels of two-particle reducibility ij, all distinct pairs of channels $\langle ij, kl\rangle$ and all triplets of channels $\langle ij, kl, mn\rangle$.

With all 2PR diagrams removed, the 3PR ones still remain to be removed. That is, $\Gamma_{1,2}$ now contains all three-particle diagrams which are one- and two-particle irreducible, yet there are still 3PR contributions remaining. However, the task of removing such diagrams is made simpler by taking into account the discussion in section 4.3.1, reminding us that any diagram reducible in more than one three-particle channel is also reducible in at least one two-particle channel (and such contributions have already been subtracted in $\Gamma_{1,2}$). Thus, by just determining the reducible contributions to $\Gamma_{1,2}$ in all 10 three-particle channels and subtracting them, we obtain the fully irreducible three particle vertex.

We have another look at the Bethe-Salpeter like equation (58) and compare two ways of writing it down:

$$F' \begin{pmatrix} a & b & c \\ d & e & f \end{pmatrix} = \Gamma_r \begin{pmatrix} a & b & c \\ d & e & f \end{pmatrix} + \frac{1}{2}\sum_{1,2}\Gamma_r \begin{pmatrix} a & b & c \\ 1 & 2 & f \end{pmatrix} G(1)G(2) \, F \begin{pmatrix} 1 & 2 \\ d & e \end{pmatrix}$$

$$+ \frac{1}{1}\sum_{1,2}\Gamma_r \begin{pmatrix} a & b & 2 \\ d & 1 & f \end{pmatrix} G(1)G(2) \, F \begin{pmatrix} 1 & c \\ e & 2 \end{pmatrix} + \frac{1}{1}\sum_{1,2}\Gamma_r \begin{pmatrix} a & b & 2 \\ 1 & e & f \end{pmatrix} G(1)G(2) \, F \begin{pmatrix} 1 & c \\ d & 2 \end{pmatrix}$$

$$+ \frac{1}{2}\sum_{1,2,3}\Gamma_r \begin{pmatrix} a & b & 3 \\ 1 & 2 & f \end{pmatrix} G(1)G(2)G(3) \, F' \begin{pmatrix} 1 & 2 & c \\ d & e & 3 \end{pmatrix} \quad (81)$$

and

$$F'\begin{pmatrix} a & b & c \\ d & e & f \end{pmatrix} = \Gamma_l \begin{pmatrix} a & b & c \\ d & e & f \end{pmatrix} + \frac{1}{2}\sum_{1,2} F\begin{pmatrix} a & b \\ 1 & 2 \end{pmatrix} G(1)G(2)\,\Gamma_l \begin{pmatrix} 1 & 2 & c \\ d & e & f \end{pmatrix}$$

$$+ \frac{1}{1}\sum_{1,2} F\begin{pmatrix} b & 2 \\ 1 & f \end{pmatrix} G(1)G(2)\,\Gamma_l \begin{pmatrix} a & 1 & c \\ d & e & 2 \end{pmatrix} + \frac{1}{1}\sum_{1,2} F\begin{pmatrix} b & 2 \\ 1 & f \end{pmatrix} G(1)G(2)\,\Gamma_l \begin{pmatrix} a & 1 & c \\ d & e & 2 \end{pmatrix}$$

$$+ \frac{1}{2}\sum_{1,2,3} F'\begin{pmatrix} a & b & 3 \\ 1 & 2 & f \end{pmatrix} G(1)G(2)G(3)\,\Gamma_l \begin{pmatrix} 1 & 2 & c \\ d & e & 3 \end{pmatrix}, \quad (82)$$

where we have defined 'left' and 'right' irreducible vertices Γ_l and Γ_r. Both of them are irreducible in the three-particle (and one-particle) $abf - cde$ channel. While Γ_r is additionally irreducible in cd, ce and de, Γ_l is additionally irreducible in ab, af and bf. For getting the fully irreducible three-particle vertex in all channels we still need all 3PR, yet one- and two-particle irreducible diagrams from above equations. All of the three-particle reducible vertex contributions are given by the terms where F' couples to the respective Γ. We insert the expression for F' extracted from one of the equations into the three-particle-reducible part of the other, recovering the reducible vertex Φ:

$$\Phi\begin{pmatrix} a & b & c \\ d & e & f \end{pmatrix} = \frac{1}{4}\sum_{1,2,3,4,5,6} \Gamma_r \begin{pmatrix} a & b & 3 \\ 1 & 2 & f \end{pmatrix} G(1)G(2)G(3)\,\cdot$$

$$\left[F'\begin{pmatrix} 1 & 2 & 6 \\ 4 & 5 & 3 \end{pmatrix} + F\begin{pmatrix} 1 & 2 \\ 4 & 5 \end{pmatrix} \delta_{3,6} G^{-1}(3) + 2\,F\begin{pmatrix} 1 & 6 \\ 4 & 3 \end{pmatrix} \delta_{2,5} G^{-1}(2) + 2\,F\begin{pmatrix} 2 & 6 \\ 5 & 3 \end{pmatrix} \delta_{1,4} G^{-1}(1) \right.$$

$$\left. + 2\,\delta_{1,4}\,\delta_{2,5}\,\delta_{3,6}\,G^{-1}(1)\,G^{-1}(2)\,G^{-1}(3) \right] G(4)G(5)G(6)\,\Gamma_l \begin{pmatrix} 4 & 5 & c \\ d & e & 6 \end{pmatrix}. \quad (83)$$

The quantity in the squared brackets can be calculated easily and will be abbreviated as effective vertex V_{eff}. From the reducible vertex, we want to remove all 1PR and 2PR contributions. There are no 1PR contributions currently included. One can easily verify that any 1PR contributions to either Γ_l or Γ_r immediately lead to 2PR contributions to Φ. We therefore remove the remaining 8 1PR terms in Γ_l and Γ_r, keeping in mind that they are two-particle irreducible in some channels. For Γ_r the remaining 1PR terms, Γ_r^{1PR}, are given by

$$\Gamma_r^{1PR} = \sum_1 G(1)\cdot\left(F\begin{pmatrix} a & b \\ d & 1 \end{pmatrix} \Gamma\begin{pmatrix} 1 & c \\ e & f \end{pmatrix} + F\begin{pmatrix} a & b \\ 1 & e \end{pmatrix} \Gamma\begin{pmatrix} 1 & c \\ d & f \end{pmatrix} + \right.$$

$$F\begin{pmatrix} b & 1 \\ e & f \end{pmatrix} \Gamma\begin{pmatrix} a & c \\ d & 1 \end{pmatrix} + F\begin{pmatrix} 1 & b \\ f & d \end{pmatrix} \Gamma\begin{pmatrix} a & c \\ 1 & e \end{pmatrix} + F\begin{pmatrix} a & c \\ 1 & f \end{pmatrix} \Gamma\begin{pmatrix} 1 & b \\ d & e \end{pmatrix} +$$

$$\left. F\begin{pmatrix} 1 & a \\ e & f \end{pmatrix} \Gamma\begin{pmatrix} b & c \\ d & 1 \end{pmatrix} + F\begin{pmatrix} 1 & a \\ f & d \end{pmatrix} \Gamma\begin{pmatrix} b & c \\ e & 1 \end{pmatrix} + F\begin{pmatrix} b & c \\ 1 & f \end{pmatrix} \Gamma\begin{pmatrix} a & 1 \\ d & e \end{pmatrix} \right). \quad (84)$$

Colours were used to denote inseperable outer legs of the two-particle Γ, i.e. $\Gamma\begin{pmatrix} a & b \\ c & d \end{pmatrix}$ is the ph-irreducible vertex, $\Gamma\begin{pmatrix} a & b \\ c & d \end{pmatrix}$ the $\overline{ph}$ one and the pp-irreducible vertex is given by $\Gamma\begin{pmatrix} a & b \\ c & d \end{pmatrix}$. We remove any 1PR terms from Γ_l and Γ_r.

$$\Gamma_l' = \Gamma_l - \Gamma_l^{1PR} \quad (85)$$

$$\Gamma_r' = \Gamma_r - \Gamma_r^{1PR} \quad (86)$$

The last task remaining in determining a proper $\Gamma_{abf-cde}$ is either removing all ab, af and bf-reducible terms from Γ_r' or all cd, ce and de ones from Γ_l' (which is equivalent), yielding Γ_{eff}.

$$\Gamma_r'\begin{pmatrix} a & b & c \\ d & e & f \end{pmatrix} = \Gamma_{eff}\begin{pmatrix} a & b & c \\ d & e & f \end{pmatrix} + \frac{1}{2}\sum_{1,2} F\begin{pmatrix} a & b \\ 1 & 2 \end{pmatrix} G(1)G(2)\,\Gamma_{eff}\begin{pmatrix} 1 & 2 & c \\ d & e & f \end{pmatrix}$$

$$+ \frac{1}{1}\sum_{1,2} F\begin{pmatrix} b & 2 \\ 1 & f \end{pmatrix} G(1)G(2)\,\Gamma_{eff}\begin{pmatrix} a & 1 & c \\ d & e & 2 \end{pmatrix} + \frac{1}{1}\sum_{1,2} F\begin{pmatrix} b & 2 \\ 1 & f \end{pmatrix} G(1)G(2)\,\Gamma_{eff}\begin{pmatrix} a & 1 & c \\ d & e & 2 \end{pmatrix} \quad (87)$$

$$\Gamma'_l \begin{pmatrix} a & b & c \\ d & e & f \end{pmatrix} = \Gamma_{eff} \begin{pmatrix} a & b & c \\ d & e & f \end{pmatrix} + \frac{1}{2} \sum_{1,2} \Gamma_{eff} \begin{pmatrix} a & b & c \\ 1 & 2 & f \end{pmatrix} G(1)G(2) \, F \begin{pmatrix} 1 & 2 \\ d & e \end{pmatrix}$$

$$+ \frac{1}{1} \sum_{1,2} \Gamma_{eff} \begin{pmatrix} a & b & 2 \\ d & 1 & f \end{pmatrix} G(1)G(2) \, F \begin{pmatrix} 1 & c \\ e & 2 \end{pmatrix} + \frac{1}{1} \sum_{1,2} \Gamma_{eff} \begin{pmatrix} a & b & 2 \\ 1 & e & f \end{pmatrix} G(1)G(2) \, F \begin{pmatrix} 1 & c \\ d & 2 \end{pmatrix} \quad (88)$$

With Γ_{eff} available, we are able to express the exclusively 3PR vertex, $\Phi'_{abf-cde}$, as

$$\Phi'_{abf-cde} \begin{pmatrix} a & b & c \\ d & e & f \end{pmatrix} = \frac{1}{4} \sum_{1,2,3,4,5,6} \Gamma_{eff} \begin{pmatrix} a & b & 3 \\ 1 & 2 & f \end{pmatrix} G(1)G(2)G(3)$$

$$V_{eff} \begin{pmatrix} 1 & 2 & 6 \\ 4 & 5 & 3 \end{pmatrix} G(4)G(5)G(6) \, \Gamma_{eff} \begin{pmatrix} 4 & 5 & c \\ d & e & 6 \end{pmatrix}. \quad (89)$$

Applying above procedure for all 10 channels (actually only the *pph* and *ppp* case are independent), all remaining reducible contributions to $\Gamma_{1,2}$ can be elliminated, yielding the fully irreducible three-particle vertex Λ

$$\Lambda = \Gamma_{1,2} - \sum_{\langle ijk-lmn \rangle} \Phi'_{ijk-lmn}. \quad (90)$$

The summation is again performed over all 10 channels of three-particle reducibility.

Summary of reducibility on the three-particle level

- A connected three-particle diagram is 1PR if it can be cut into two disconnected two-particle parts, each with three of the original six outer legs by removing a single internal one-particle propagator. There are 9 cannels of one-particle reducibility. The channels are labeled by the pair of triplets of outer legs which remain connected to each other when performing the cut. A diagram can be 1PR in one channel at most.

- A connected three-particle diagram is 2PR if it can be cut into two disconnected parts, a three-particle and a two-particle one, by removing two internal one-particle propagators. The three-particle part remains connected to four of the original six outer legs and the two-particle part to the remaining two outer legs. There are 15 channels of two-particle reducibility. The channels are labeled by the pair of outer legs which is disconnected from the remaining diagram. Two-particle channels are coined "compatible" if a single diagram can be reducible in all of them. There are 30 pairs of compatible channels and 10 triplets of compatible channels. A diagram is said to be simultaneously 2PR in $n \in \{2, 3\}$ channels if it can be disconnected into n two-particle parts with the corresponding pairs of the outer legs and a remaining three-particle part by removing $2n$ internal one-particle propagators. A diagram can be 1PR and 2PR in two-particle channels which disconnect a pair of outer legs that remains together in the 1PR decomposition.

- A connected three-particle diagrams is 3PR if it can be cut into two three-particle parts each of which remains connected to three external legs by removing three internal one-particle propagators. There are 10 different channels of three-particle reducibility. The channels are labeled by the pair of triplets of outer legs which remain connected to each other when disconnecting the diagram. A given diagram can be 3PR in more than one channel. If a diagram is 3PR in more than one channel, it is also 2PR. A diagram can be 1PR and 3PR, but only in the channels which are labeled the same.

5. Functional integral based non-local expansions

Aiming to expand upon the great success of DMFT, functional integral based methods have proven themselves as valuable tools. They allow for formally exact expansions of DMFT by providing us with a controlled method of introducing a DMFT impurity problem and coupling the impurities associated with the different sites of the lattice. All the methods described in the following share some common features. They all start from the action formalism for a lattice model, adding and subtracting a bath-hybridisation-term, thereby introducing a DMFT impurity problem for every lattice site and non-local terms proportional to the difference between kinetic and hybridisation term. Depending on which expansion scheme one decides to use, this is followed up by different numbers of Hubbard-Stratonovich and Legendre transformations acting on different parts of the new system. The discussion of the different schemes will be conducted starting from the action formalism in imaginary time and following the route towards the one-particle-irreducible approach [25] with other methods being introduced when their derivations start deviating from the $1PI$ one. The imaginary-time dependent action representation of the grand partition function for a (for the moment) general lattice problem with local interaction is given by

$$Z\left[\eta^{\dagger};\eta\right] = \int \mathcal{D}\left[c_i^{\dagger};c_i\right] e^{-S_l\left[c^{\dagger},c\right]+\int_0^{\beta} d\tau\left(\eta_i^{\dagger}c_i+c_i^{\dagger}\eta_i\right)}. \tag{91}$$

The fermionic degrees of freedom are described by Grassmann fields $c^{(\dagger)}$ which are τ-dependent. The caligraphic $\mathcal{D}$ implies that all degrees of freedom are to be integrated over and the index i stands for the different lattice sites. Possible orbital- or spin degrees of freedom are not written expilicitly and implicitly assumed to be summed over. We introduced (time-dependent) source fields $\eta^{(\dagger)}$, allowing us to express Green's functions of the system as functional derivatives of Z with respect to them. The physical grand partition function is recovered by evaluating at $\eta^{(\dagger)} = 0$. The action of the lattice model is given by

$$S_l = \sum_i \int_0^{\beta} d\tau \left(c_i^{\dagger}\frac{d}{d\tau}c_i + U\left[c_i^{\dagger};c_i\right]\right) + \sum_{i,j} \int_0^{\beta} d\tau\, t_{i,j}c_i^{\dagger}c_j. \tag{92}$$

Our only assumption about S_l so far is that the interaction is purely local. Local potential (quadratic) terms can be included in the interaction term or as diagonal terms in the hopping term. We rewrite the imaginary-time dependent actions in terms of Grassmann fields depending on (fermionic) Matsubara frequencies. The convention for the Fourier transform is chosen as:

$$o\left(\nu\right) = \frac{1}{\sqrt{\beta}} \int_0^{\beta} d\tau e^{i\nu\tau} o\left(\tau\right), \tag{93a}$$

$$o^{\dagger}\left(\nu\right) = \frac{1}{\sqrt{\beta}} \int_0^{\beta} d\tau e^{-i\nu\tau} o^{\dagger}\left(\tau\right). \tag{93b}$$

$$o\left(\tau\right) = \frac{1}{\sqrt{\beta}} \sum_{\nu} e^{-i\nu\tau} o\left(\nu\right), \tag{94a}$$

$$o^{\dagger}\left(\tau\right) = \frac{1}{\sqrt{\beta}} \sum_{\nu} e^{i\nu\tau} o^{\dagger}\left(\nu\right). \tag{94b}$$

The factors $1/\sqrt{\beta}$ were chosen in a manner so as to easily recover the well-known $1/(i\nu - \epsilon)$-expression for the Green's function in the non-interacting case. The local action takes a very similar form, though with all occuring fermionic fields now being dependent on Matsubara-frequencies instead of imaginary times. Again, we drop the Matsubara index ν for $c_i^{(\dagger)}$

$$S_l = \sum_{i,\nu} \left(-i\nu c_i^{\dagger}c_i + U\left[c_i^{\dagger};c_i\right]\right) + \sum_{i,j,\nu} t_{i,j}c_i^{\dagger}c_j \tag{95}$$

For the kinetic part of the action, a Fourier transform to k-space is performed, which results in a diagonalisation with respect to k-values in the $c^{(\dagger)}$ and the dispersion relation replacing the hopping amplitudes.

$$S_l = \sum_{i,\nu} \left(-i\nu c_i^{\dagger}c_i + U\left[c_i^{\dagger};c_i\right]\right) + \sum_{k,\nu} \varepsilon_k c_k^{\dagger}c_k \tag{96}$$

Usually, Feynman-diagramatic methods are based on an expansion in orders of the interaction term with respect to a non-interacting reference system. As we are interested in extending the good treatment of

purely local correlations within DMFT, we construct a system where the reference is the DMFT solution. To this end, a (frequency-dependent) local hybridisation function Δ is added and subtracted in the action as a quadratic term in the Grassmann fields $c^{(\dagger)}$.

$$S_l = \sum_{i,\nu} \left(-i\nu c_i^\dagger c_i + U \left[c_i^\dagger; c_i \right] + \Delta c_i^\dagger c_i \right) + \sum_{k,\nu} (\varepsilon_k - \Delta) c_k^\dagger c_k \tag{97}$$

Note that the hybridisation function was added as local term in real space and subtracted as a local term in k-space, which is possible because it is a constant with respect to both k and r-space, being only Matsubara-frequency dependent.

5.1. The non-local expansion scheme

In the following, a short introduction to a diagramatic expansion of an interacting lattice problem which is equivalent to the non-local expansion scheme (NLES) [49] will be given. The starting point is the action (97), which is already decomposed into a local and a non-local part. The underlying idea is to use the local, yet interacting, system as a reference system and to construct a diagramatic expansion scheme around its solution. The building blocks of the diagramatic theory are the (connected) n-particle Green's functions of the local reference problem and the perturbative, non-local, term $\varepsilon_k - \Delta$. Diagramatically, the Green's functions are denoted as ellipses for one-particle Green's functions $G^{(1)}$ and as polygons with $2n$ edges for higher-order Green's functions $G^{(n)}$. The non-local terms are denoted as lines. In figure 24, the Green's function building blocks of the NLES are shown. Note the subscript C used in the figure–it is possible to base the NLES either on full Green's functions or on the fully connected ones. If using full ones, additional bookkeeping is required, as diagrams with more than one Green's function element have to be precluded from obtaining contributions where both Green's functions are associated with the same lattice site. Employing connected Green's functions as building blocks, the distinction becomes unnecessary and the diagramatics more intuitive.
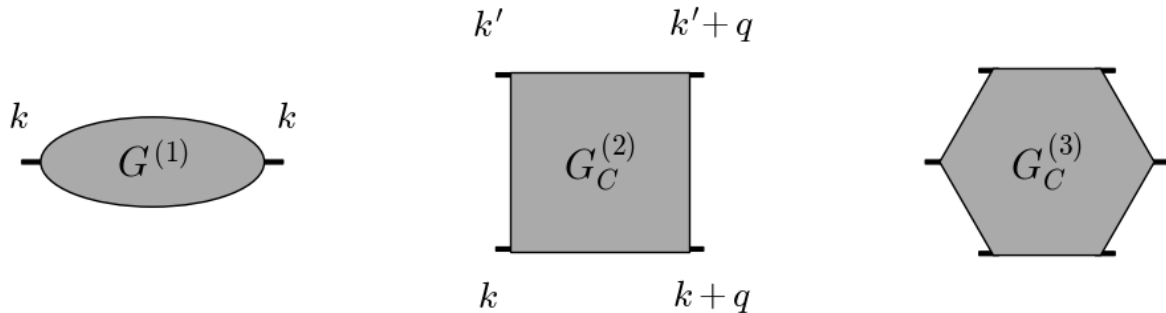
Figure 24: Local Green's function building blocks of the non-local expansion scheme. Note that the Green's functions scatter between all states fulfilling conservation of momentum equally due to being totally local. For the three-particle Green's function, no k-indices are denoted and higher order Green's functions are not shown.

Summing up a finite number of diagrams is not expected to give reliable results. Instead, consideration of certain classes of diagrams to infinite order is the preferred approach for correlated electron systems. Within the NLES, it is possible to calculate effective Green's functions and non-local terms in the spirit of the random phase approximation. The equations describing said dressing of Green's function and non-local term are depicted diagramatically in figure 25.
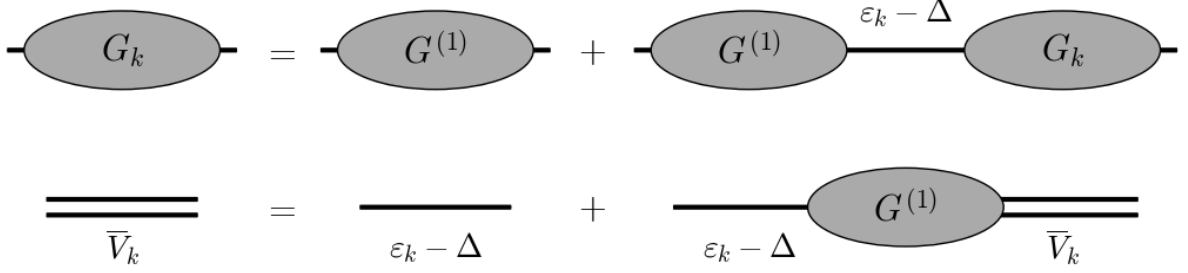
Figure 25: Dressing the one-particle Green's function and the non-local term in the spirit of random-phase approximation yields two Dyson-like equations.

Algebraically, the equations to dress the Green's function and non-local term read:

$$G_k(\nu, k) = G^{(1)}(\nu) + G^{(1)}(\nu)\left(\varepsilon_k - \Delta(\nu)\right) G_k(\nu, k), \tag{98}$$

$$V_k(\nu, k) = \left(\varepsilon_k - \Delta(\nu)\right) + \left(\varepsilon_k - \Delta(\nu)\right) G^{(1)}(\nu) V_k(\nu, k). \tag{99}$$

Those equations can be solved to yield:

$$G_k(\nu, k) = \frac{G^{(1)}(\nu)}{1 - G^{(1)}(\nu)\left(\varepsilon_k - \Delta(\nu)\right)} = \frac{1}{\left(G^{(1)}(\nu)\right)^{-1} + \Delta(\nu) - \varepsilon_k}, \tag{100}$$

$$V_k(\nu, k) = \frac{\left(\varepsilon_k - \Delta(\nu)\right)}{1 - \left(\varepsilon_k - \Delta(\nu)\right) G^{(1)}(\nu)} = \frac{G_k(\nu, k) - G^{(1)}(\nu)}{\left(G^{(1)}(\nu)\right)^2}. \tag{101}$$

If the hybridisation function is chosen in accordance with DMFT, these quantities can be identified as the k-resolved Green's function within the DMFT approximation

$$G_k = \frac{1}{i\nu - \Sigma_{DMFT} + \mu - \varepsilon_k}, \tag{102}$$

as well as a fully non-local term V_k, which is proportional to the dual-fermion Green's function $\overline{G} = G_k - G^{(1)}$ (115), albeit divided by an additional factor $\left(G^{(1)}\right)^2$. If V_k is used diagramatically to connect local, connected Green's functions, the division by $\left(G^{(1)}\right)^2$ amputates the external legs of the connected Green's functions, thus yielding vertex functions. The beauty of the NLES originates from avoiding any dual degrees of freedom–the interpretation of the diagramatics is quite straightforward.

5.2. The dual fermion approach

The dual fermion approach [23] relies on a Hubbard-Stratonovich transformation to decouple the local and non-local degrees of freedom in the action (97). The transformation introduces new, dual degrees of freedom to remove the non-local part of the action. We start from the expression

$$Z\left[\eta^\dagger; \eta\right] = \int \mathcal{D}\left[c_i^\dagger; c_i\right] e^{-S_l[c^\dagger, c] + \sum_{\nu, k}\left(\eta_k^\dagger c_k + c_k^\dagger \eta_k\right)}. \tag{103}$$

The action is explicitly split into a part local in real space (loc) and a part local in k-space:

$$\mathcal{S}_l = \mathcal{S}_{loc} + \mathcal{S}_k \tag{104}$$

$$\mathcal{S}_k = \sum_{k, \nu}(\varepsilon_k - \Delta)c_k^\dagger c_k \tag{105}$$

The term $\exp(-\mathcal{S}_k)$ ist now to be expressed in terms of another Grassmann integral

$$e^{-\sum_{k, \nu}(\varepsilon_k - \Delta)c_k^\dagger c_k} = \prod_{k, \nu} b^{-2}(k, \nu) \int \mathcal{D}\left[\zeta_k^\dagger; \zeta_k\right] e^{\sum_{k, \nu}\left[\zeta_k^\dagger \zeta_k b^2(k, \nu) + b(k, \nu)(\varepsilon_k - \Delta)^{1/2}\left(\zeta_k^\dagger c_k + c_k^\dagger \zeta_k\right)\right]}. \tag{106}$$

With an–up to this point arbitrary–function b. It turns out to be convenient to include a factor $(\varepsilon_k - \Delta)^{-1/2}$ into b.

$$b(k, \nu) = (\varepsilon_k - \Delta)^{-1/2} f(k, \nu), \tag{107}$$

43

recasting above expression into

$$e^{-\sum_{k,\nu}(\varepsilon_k - \Delta)c_k^\dagger c_k} = \prod_{k,\nu}(\varepsilon_k - \Delta)f^{-2}(k,\nu)\int \mathcal{D}\left[\zeta_k^\dagger; \zeta_k\right] e^{\sum_{k,\nu}\left[\zeta_k^\dagger \zeta_k(\varepsilon_k - \Delta)^{-1}f^2(k,\nu) + f(k,\nu)\left(\zeta_k^\dagger c_k + c_k^\dagger \zeta_k\right)\right]}. \quad (108)$$

If (108) is inserted into expression (97), the resulting action is one consisting of local DMFT impurity problems whose degrees of freedom couple linearly not only to the source fields $\eta^{(\dagger)}$, but also the dual degrees of freedom $\zeta^{(\dagger)}$. This allows for the local problems to be integrated out, which–in principle–generates infinitely many[1] local Green's functions coupling to the source fields and dual degrees of freedom. In practice, however, the local n-particle Green's functions cannot be calculated up to infinite order and the expressions have to be truncated. Since f can be chosen freely, it makes sense to render the diagramatics of the resulting dual system as simple as possible by a suitable choice. Specifically,

$$f(k,\nu) = \left(G^{(1)}(\nu)\right)^{-1} \quad (109)$$

ensures that the non-interacting reference propagator of the dual system is totally non-local. To see this is actually the case, the local problems need to be integrated out:

$$Z_{loc}\left[\eta^\dagger; \eta\right] = Z_{loc}\left[0; 0\right] \cdot e^{\sum_{n=1}^\infty 1/(n!)^2 G_C^{(n)}\left(\eta\eta^\dagger\right)^{"n"}} \quad (110)$$

Here, $G_C^{(n)}$ denotes the connected part of the local n-particle Green's function, an implicit summation over all frequency-degrees of freedom is assumed (affecting both the $G_C^{(n)}$ and the $\eta^{(\dagger)}$). The symbolic exponent "n" is a reminder that n pairs of source fields appear together with the Green's function. For calculating expectation values, constant prefactors do not matter, so Z_{loc} as well as the product over all $(\varepsilon_k - \Delta)f^{-2}(k,\nu)$ can be dropped. Since the actions for all local impurity problems are integrated out, we end up with multiple copies of Green's functions coupling to source fields at different sites. If all lattice sites are equivalent and thus the Green's functions are not position-dependent, a Fourier transform from real to k-space leaves us with the Green's functions connecting all states which obey conservation of momentum equally. Specifically, the quadratic part in the source fields is given by the one-particle Green's function:

$$\sum_{k,\nu} G^{(1)}(\nu)\eta_k \eta_k^\dagger \quad (111)$$

We note that the local impurity fields do not couple to $\zeta^{(\dagger)}$ but to $\left((G)^{(1)}\right)^{-1}\zeta^{(\dagger)}$. Thus, the contribution from the local impurities to the quadratic part of the action for the dual fermions is given by

$$-\sum_{k,\nu}\left(G^{(1)}(\nu)\right)^{-1}\zeta_k^\dagger \zeta_k. \quad (112)$$

Together with the term

$$\sum_{k,\nu}\left(G^{(1)}(\nu)\right)^{-2}(\varepsilon_k - \Delta)^{-1}\zeta_k^\dagger \zeta_k. \quad (113)$$

obtained from the Hubbard-Stratonovich transformation, the quadratic part of the action for dual fermions can be algebraically calculated to be

$$\sum_{k,\nu}\left(G_k(k,\nu) - G^{(1)}(\nu)\right)^{-1}\zeta_k^\dagger \zeta_k. \quad (114)$$

Thus, the bare propagator for the dual fermions $\widetilde{G}$ is given by

$$\widetilde{G} = G_k - G^{(1)}, \quad (115)$$

which is a purely non-local quantity if the DMFT self-consistency condition is fullfilled. With the non-interacting dual Green's function determined, what remains to be done is to calculate the interaction terms. The expansion in equation (110) contains connected Green's functions of the local reference problems

---

[1]On one hand, there are infinitely many fermionic Matsubara-frequencies, on the other hand for an actually continuous hybridisation function Δ, even the local impurity problems have infinitely many degrees of freedom. This corresponds to an infinitely extended lattice.

coupling to $\left(G^{(1)}\right)^{-1}\zeta^{(\dagger)}$ in an exponent. Formally, this is equivalent to an interaction term. The inverse one-particle Green's functions in the coupling lead to an amputation of the outer legs, thus generating interaction terms of the structure

$$\sum_{n=2}^{\infty}(-1)^n\frac{1}{(n!)^2}F^{(n)}\left(\zeta^{\dagger}\zeta\right)^{"n"}. \tag{116}$$

Again, the n-particle vertex functions of the local impurity problems scatter equally between all states obeying conservation of momentum. The total action for the dual fermion problem becomes

$$\mathcal{S}_{dual}\left[\zeta^{\dagger};\zeta\right]=-\sum_{k,\nu}\left(\widetilde{G}\right)^{-1}\zeta_k^{\dagger}\zeta_k-\sum_{n=2}^{\infty}(-1)^n\frac{1}{(n!)^2}F^{(n)}\left(\zeta^{\dagger}\zeta\right)^{"n"}. \tag{117}$$

The resulting lattice problem for the dual fermions is peculiar in a few ways, which will be discussed in the following.

Unlike typical models for interacting fermions, the interaction term is not just quartic, but appears up to infinite orders, i.e. interaction terms with any power of $\zeta^{\dagger}\zeta$ appear. These interaction terms are also automatically antisymmetrised with respect to exchange of two equivalent fermionic fields, meaning that one ends up with Hugenholtz diagrams in describing dual fermions. All of the local correlations described within DMFT are already included in the non-interacting dual reference system. The bare dual propagator is totally non-local, which means that any local closed loop gives zero contribution. Together with the purely local interaction terms, many diagrams' contributions trivially cancel out. The complete non-locality of dual propagators is lost once a dual self-energy is included in a calculation, for example within a self-consistent calculation in dual space.

Usually, two sets of approximations are employed within practical dual-fermion calculations. First of all, the interaction terms in dual space are usually restricted to $n=2$ particle vertices. For some parameter regions in the Hubbard model, the effects of three-particle corrections were found to be of low impact [55], but this need not be a general trend [30, 31]. Even with the interaction order restricted to 2, the dual fermion lattice problem remains an interacting one and is hard to treat. The high-frequency behaviour of the dual propagators is, however, better suited for a numerical treatment, as they decay like $1/\nu^2$ instead of $1/\nu$ for regular fermions, with the fermionic Matsubara frequency ν. This way, absolute convergence of all fermionic summations is ensured. The expansion into local vertices and non-local propagators provides the dual fermion formalism with two limits where its diagramatic perturbation series is expected to converge well. On one hand, in the non-interacting limit, the vertex functions become small, providing a small parameter. On the other hand, for large values of U, the problem can be rescaled and effectively approaches an atomic-limit problem, where the non-local Green's functions provide a small parameter. Obviously, the problem of selecting diagrams one wishes to include into a perturbation expansion, remains. The choice of diagrams which were actually employed range from simple second-order diagrams [23], over ladder-approaches [23, 55] and elaborate diagramatic Monte-Carlo calculations [56]. Mappings between the solution to the dual fermion problem and the lattice fermion problem exist, which can be most easily derived by following through a differentiation of the action-integral with respect to the kinetic energy ε_k. The self-energy for the real fermions is connected to the self-energy of the dual fermions $\widetilde{\Sigma}$ via the relation [23]

$$\Sigma_{real}(k,\nu)=\Sigma_{DMFT}(\nu)+\frac{\widetilde{\Sigma}(k,\nu)}{1+G^{(1)}(\nu)\widetilde{\Sigma}(k,\nu)}. \tag{118}$$

This mapping equation has sparked heated discussions and deserves discussion in greater detail. A derivation is given in figure 27.

5.2.1. Two diagramatic interpretations of the dual fermion approach and discussion of one-particle irreducibility

There are two points in the derivation of the dual fermion action where, in principle, a diagramatic expansion can be performed. Usually, the dual problem is treated after integrating out the local degrees of freedom. Combinatorically, this problem is easier to treat, but it comes at the disadvantage that the real fermions are no longer actual degrees of freedom of the system in question, making a diagramatic interpretation of the corrections for the real fermions harder. The building blocks for the two possible expansions of the dual-fermion problem, called I and II, in terms of Feynman-diagrams are shown in figure 26. The full dual Green's functions have to be the same, whether problem I or II is solved exactly, but the dual self energies are different because the reference-propagators are chosen differently. In practice, problem II is simpler to treat (Actually problem I is just a very complicated way of expressing the original real-fermion
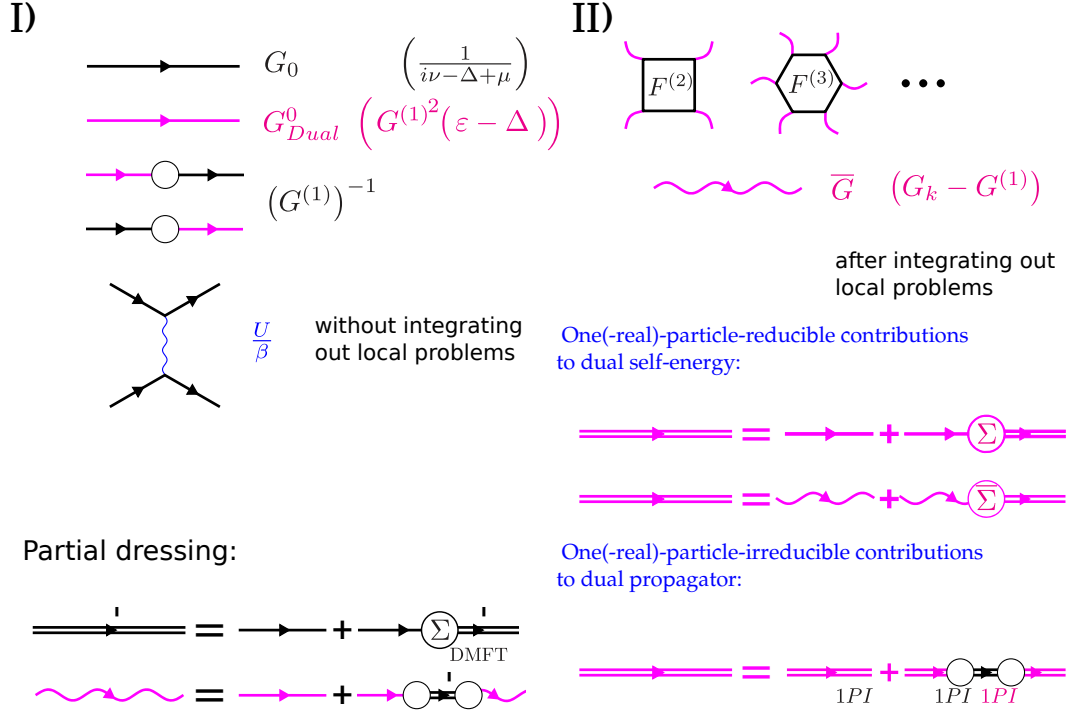
Figure 26: Building blocks of the diagramatic expansions for the dual fermion problem before (I) and after (II) integrating out the local degrees of freedom. The bare black propagator G_0 is the bare local propagator of the referential DMFT problems (This quantity is different from the bare lattice propagator). The bare purple propagator G^0_{Dual} is the bare propagator for the dual fermions resulting only from the quadratic term in the action introduced by the Hubbard-Stratonovich transformation. Small black circles denote the terms coupling dual to real fermions and vice-versa. The interaction terms of the original lattice problem are given by blue, wiggly lines. They connect to real fermion propagators exclusively. The quantities in both approaches are related by the partial dressing relations. Wiggly, purple propagators $\overline{G}$ are the usual dual propagators based on the quadratic term in the Hubbard-Stratonovich transformation and the quadratic term in the dual fermions appearing due to integrating out the local DMFT problems. The local DMFT Green's function (denoted as primed double black lines) is given by the bare Green's function dressed by the DMFT self-energy. Also shown are the Dyson equations coupling the different bare dual propagators and their respective self-energies Σ_{Dual} and $\overline{\Sigma}$ to the full dual propagator (two purple lines). Finally, a relation coupling the dual propagator with the dual propagator that is one-particle-irreducible with respect to real fermions and the real fermion propagator one-particle-irreducible with respect to dual fermions is given.

lattice problem Feynman-diagramatically), due to reduced combinatorical complexity and the favourable convergence properties of $\overline{G}$. In the following, our aim is to use the consistency of the dual Green's functions to express the self energy for the real fermions from I in terms of the dual self energy $\overline{\Sigma}$ from II. The necessary steps in the derivation are depicted in figure 27.
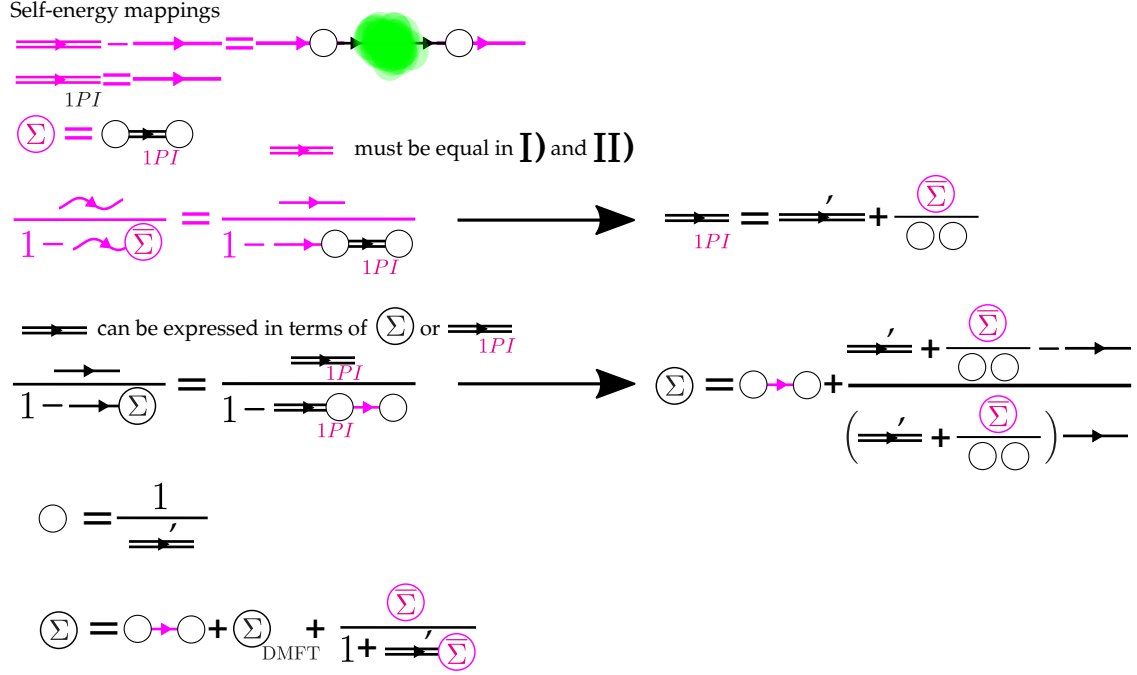

Figure 27: Diagramatic representation of the steps in the derivation of the mapping from $\overline{\Sigma}$ to the self energy of the real fermions Σ.

In expressing the self-energy of the real fermions, some preliminary observations are made first. We realise that in the diagramatic theory I, dual propagators can only couple to small black circles and thus to bare real propagators. It is therefore immediately clear that any non-trivial diagram contributing to the dual propagator is one-particle reducible with respect to the real fermions. For any such diagram, a cut can be performed immediately after the first or before the last black circle, disconnecting it into two parts. From this, we can also infer that the self-energy for the dual fermions $\overline{\Sigma}$ consists of all diagrams contributing to the real-fermion propagator and one-particle irreducible with respect to the dual fermions with two small black circles attached-obviously any diagram in $\overline{\Sigma}$ must also be included in the real propagator with circles attached, while the condition on one-particle irreducibility is an inherent property of the self-energy.

The full propagator for the dual fermions has to be the same whether we choose to adapt description I or II, and thus we can set the dual propagator expressed in terms of $\overline{\Sigma}$ and Σ_{Dual} equal. We already know that Σ_{Dual} equals the real-fermion propagator one-particle-irreducible with respect to the dual fermions. We also know that the full propagator for the real fermions can be expressed either in terms of the real self-energy or in terms of the real (dual) propagators one-particle-irreducible with respect to dual (real) fermions. After algebraic manipulations, the self-energy for the real fermions within diagramatic theory I can be expressed as

$$\Sigma = (G^{(1)})^{-1}\left((G^{(1)})^2(\varepsilon_k - \Delta)\right)(G^{(1)})^{-1} + \Sigma_{DMFT} + \frac{\overline{\Sigma}}{1 + G^{(1)}\overline{\Sigma}}. \tag{119}$$

A discussion of the different terms is in order here. The first term can be simplified to read $\varepsilon_k - \Delta$. The effect of this term on the Green's function is straightforward, replacing the hybridisation function from the local problem by the kinetic energy within the lattice model[1]. The DMFT self-energy encodes all purely

---

[1] Remember that the bare propagator for the real fermions within diagramatic theory I was defined as the Green's function of the associated Anderson impurity problem without interaction terms. This term is usually not included in the definition of the self-energy.

local interaction effects and appears without renormalisations. Including only those two contributions, one recovers the DMFT expressions for the one-particle Green's functions. The final term gives the corrections to the self-energy due to non-local correlation effects. The dual self-energy $\overline{\Sigma}$ is renormalised by a factor including it, as well as the local real-fermion Green's function. When thinking about the properties diagramatic theory II inherited from theory I this can be explained. Obviously, Σ_{Dual} contains contributions one-particle reducible with respect to real fermions-as it has been discussed, it contains such diagramms exclusively. The real fermions do not appear as degrees of freedom in theory II any longer and therefore the classification in terms of real-fermion one-particle-reducibility cannot be performed directly. However, any diagram within theory II can be translated into equivalent expressions within theory I.

The bare interaction terms of the dual diagramatic theory II are given by the fully connected vertices of the real fermions within DMFT. Those full n-particle vertices, however, for $n > 2$ contain contributions which are one-particle reducible with respect to the real fermions [25,35]. If two parts of a $\overline{\Sigma}$-diagram are linked by a vertex with $n > 2$, some of its contributions are one-particle reducible with respect to the real fermions. On the level of diagramatic theory II, there is no systematic way of precluding these contributions from appearing. However, as all impurity problems were integrated out locally, a Dyson-like equation for $\overline{\Sigma}$ can be written:

$$\overline{\Sigma} = \overline{\Sigma}_{1\text{PI}} + \overline{\Sigma}_{1\text{PI}}\, G^{(1)}\, \overline{\Sigma} \tag{120}$$

Here, $\overline{\Sigma}_{1\text{PI}}$ denotes the part of $\overline{\Sigma}$ irreducible with respect to real fermions if expressed within theory I. Any reducible contributions have to arise from a part of a full local n-particle vertex which decomposes into an m-particle vertex and a $(n - m + 1)$-particle vertex connected by a single local Green's function $G^{(1)}$. If the single Green's function were to be removed, both halves of the remaining diagram would constitute legitimate contributions to the dual self-energy. Solving equation (120) for $\overline{\Sigma}_{1\text{PI}}$, one recovers exactly the correction to the self-energy due to non-local correlations within DF.

Note however, that (120) is actually an exact relation that holds for the exact $\overline{\Sigma}_{1\text{PI}}$. When taking a closer look at the usual implementations of the dual fermion approach, truncating at the two-particle vertex level, one realises that such reducible contributions to the self-energy are a-priori precluded from appearing since the two-particle local vertex does not have any one-particle-reducible contributions. Also, when calculating corrections to the self-energy from diagrams such as the one depicted in figure 43, no reducible terms appear. Therefore, in such cases the mapping (118) is superfluous, introducing a systematic error, consistent with the numerical results found in [56].

5.3. The one Particle Irreducible approach

Realising the problems arising from reducible contributions to self-energies in dual fermion calculations, the one-particle-irreducible approach ($1PI$) was developed [25]. It specifically deals with the issue of one-particle reducibility already on the level of expanding the action in terms of vertices, albeit at the cost of a slightly unwieldy theory, encompassing more degrees of freedom than would be the case in a more straightforward dual fermion calculation. A Legendre transformation of the action is performed, formulating a theory in a new set of variables. The starting point for the derivation of the $1PI$ theory is a dual fermion action, however with the function f chosen differently from before:

$$f = 1. \tag{121}$$

The resulting expression for the partition function becomes:

$$Z\left[\eta^{\dagger}, \eta\right] = -\int \mathcal{D}\left[\zeta^{\dagger}; \zeta\right] e^{\sum_i W_l[\eta_i^{\dagger} + \zeta_i^{\dagger}, \eta_i + \zeta_i] + \sum_{k,\nu} \frac{\zeta_k^{\dagger}\zeta_k}{\varepsilon_k - \Delta}} \tag{122}$$

By performing a linear shift in the Grassmann fields

$$\zeta_i^{(\dagger)} \to \zeta_i^{(\dagger)} - \eta_i^{(\dagger)}, \tag{123}$$

the dependence of the local generating functional W on the source fields $\eta^{(\dagger)}$ can be eliminated.

$$Z\left[\eta^{\dagger}, \eta\right] = \int \mathcal{D}\left[\zeta^{\dagger}; \zeta\right] e^{\sum_i W_l[\zeta_i^{\dagger}, \zeta_i] + \sum_{k,\nu} \frac{\left(\zeta_k^{\dagger} - \eta_k^{\dagger}\right)\left(\zeta_k - \eta_k\right)}{\varepsilon_k - \Delta}}. \tag{124}$$

In a next step, the local generating functionals will be Legendre transformed to arrive at one-particle irreducible functionals.

5.3.1. The one particle irreducible generating functional

To remove all one-particle reducible contributions to the connected propagators–or equivalently, the n-particle vertex–a systematic way of building all 1PR diagrams and subtracting them is required. This goal can be achieved by performing a Legendre transform on the generating functional W. The generating functional can be expanded in terms of n-particle (fully connected) Green's functions

$$W\left[\eta^\dagger, \eta\right] = \ln(Z_0) + \sum_{n=1}^{\infty} \frac{(-1)^n}{(n!)^2} \sum_{a,\dots,z} G_C^{(n)}(a, \dots, z)\eta_z^\dagger\dots\eta_a, \tag{125}$$

where the indices $a\dots z$ encompass all degrees of freedom of the system in question. The constant term $\ln(Z_0)$ can be safely ignored for calculations of expectation values. New fields $\Phi^{(\dagger)}$ are introduced as follows

$$\Phi_a = -\delta_{\eta_a^\dagger} W \tag{126a}$$

$$\Phi_a^\dagger = \delta_{\eta_a} W \tag{126b}$$

Assuming that the one-particle Green's function is diagonal in the indices and truncating on the level of three-particle Green's functions, the explicit expressions for $\Phi^{(\dagger)}$ are given by

$$\Phi_a = G^{(1)}(a)\eta_a - \frac{1}{2}\sum_{b,c,d} G_C^{(2)}(d,c,b,a)\eta_b\eta_c^\dagger\eta_d + \frac{1}{12}\sum_{b,c,d,e,f} G_C^{(3)}(f,e,d,c,b,a)\eta_b\eta_c^\dagger\eta_d\eta_e^\dagger\eta_f \tag{127a}$$

$$\Phi_a^\dagger = G^{(1)}(a)\eta_a^\dagger - \frac{1}{2}\sum_{b,c,d} G_C^{(2)}(a,b,c,d)\eta_b^\dagger\eta_c\eta_d^\dagger + \frac{1}{12}\sum_{b,c,d,e,f} G_C^{(3)}(a,b,c,d,e,f)\eta_b^\dagger\eta_c\eta_d^\dagger\eta_e\eta_f^\dagger \tag{127b}$$

Note that the factors taking care of overcounting changed from $(n!)^2$ to $n!(n-1)!$ which is due to the n equivalent terms arising from the functional derivation. One can easily see the nature of the fields $\Phi^{(\dagger)}$, they include all possible diagrams which can be appended to an external leg of a given diagram. This means that by appending them to an one-particle irreducible core diagram, a whole class of one-particle reducible diagrams can be recovered. The $\Phi^{(\dagger)}$ fields are the natural variables of the $1PI$ functional Γ, recovered as the Legendre transform of W:

$$\Gamma\left[\Phi^\dagger, \Phi\right] = W\left[\eta^\dagger, \eta\right] + \sum_a \Phi_a^\dagger\eta_a + \eta_a^\dagger\Phi_a \tag{128}$$

Expressed in terms of the $\eta^\dagger$ fields, Γ, up to the three-particle order is given by:

$$\Gamma\left[\Phi^\dagger, \Phi\right] = \ln(Z_0) - \sum_a G^{(1)}(a)\eta_a^\dagger\eta_a + \frac{1}{4}\sum_{a,b,c,d} G_C^{(2)}(a,b,c,d)\eta_d^\dagger\eta_c\eta_b^\dagger\eta_a$$

$$- \frac{1}{36}\sum_{a,b,c,d,e,f} G_C^{(3)}(a,b,c,d,e,f)\eta_f^\dagger\eta_e\eta_d^\dagger\eta_c\eta_b^\dagger\eta_a + 2\sum_a G^{(1)}(a)\eta_a^\dagger\eta_a$$

$$- \sum_{a,b,c,d} G_C^{(2)}(a,b,c,d)\eta_d^\dagger\eta_c\eta_b^\dagger\eta_a + \frac{1}{6}\sum_{a,b,c,d,e,f} G_C^{(3)}(a,b,c,d,e,f)\eta_f^\dagger\eta_e\eta_d^\dagger\eta_c\eta_b^\dagger\eta_a. \tag{129}$$

The next–and slightly tedious–step is to replace the dependency on $\eta^{(\dagger)}$ by $\Phi^{(\dagger)}$. The most straightforward way to achieve this goal is to express $\eta^{(\dagger)}$ in terms of $\Phi^{(\dagger)}$ and higher-order terms in $\eta^{(\dagger)}$ by algebraic transformations of equations (127) and subsequent orderwise insertion of the recovered expressions. The resulting expression for Γ is

$$\Gamma\left[\Phi^\dagger, \Phi\right] = \ln(Z_0) + \sum_a \frac{1}{G^{(1)}(a)}\Phi_a^\dagger\Phi_a + \frac{1}{4}\sum_{a,b,c,d} F^{(2)}(a,b,c,d)\Phi_d^\dagger\Phi_c\Phi_b^\dagger\Phi_a$$

$$- \frac{1}{36}\sum_{a,b,c,d} F^{(3)}(a,b,c,d,e,f)\Phi_f^\dagger\Phi_e\Phi_d^\dagger\Phi_c\Phi_b^\dagger\Phi_a$$

$$+ \frac{1}{4}\sum_{a,b,c,d,e,f,g} F^{(2)}(a,b,c,g)G^{(1)}(g)F^{(2)}(g,d,e,f)\Phi_f^\dagger\Phi_e\Phi_d^\dagger\Phi_c\Phi_b^\dagger\Phi_a \tag{130}$$

The advantage of Γ in comparison to W is that it is expanded in terms of one-particle irreducible vertices instead of the fully connected ones. Thereby, the issue of one-particle irreducible contributions to self-energies

can be circumvented altogether. To employ this to our advantage, the integrand as well as the integration variables need to be expressed in terms of the new $\Phi^{(\dagger)}$ variables. The inverse Legendre transformation, expressing $\eta^{(\dagger)}$ in terms of $\Phi^{(\dagger)}$ is given by

$$\eta_a = \delta_{\Phi_a^\dagger} \Gamma \tag{131a}$$

$$\eta_a^\dagger = -\delta_{\Phi_a} \Gamma \tag{131b}$$

5.3.2. Rewriting the lattice action in terms of 1PI quantities

Starting from the functional integral representation of Z in equation (124), W is replaced by Γ, employing equation (128) as well as (131)

$$Z\left[\eta^\dagger, \eta\right] = \int \mathcal{D}\left[\zeta^\dagger; \zeta\right] e^{\sum_i \Gamma[\Phi_i^\dagger, \Phi_i] - \sum_i \Phi_i^\dagger \delta_{\Phi_i^\dagger}\left(\Gamma[\Phi_i^\dagger, \Phi_i]\right) + \sum_i \delta_{\Phi_i}\left(\Gamma[\Phi_i^\dagger, \Phi_i]\right)\Phi_i}$$
$$e^{\sum_{k,\nu} \dfrac{\left(-\delta_{\Phi_k}(\Gamma[\Phi_i^\dagger, \Phi_i]) - \eta_k^\dagger\right)\left(\delta_{\Phi_k^\dagger}(\Gamma[\Phi_i^\dagger, \Phi_i]) - \eta_k\right)}{\varepsilon_k - \Delta}} . \tag{132}$$

In addition to transforming the integrand, the integration variables need to be transformed, which is accomplished by including the inverse of the determinant of the transformation matrix M in the integrand.

$$M_{ab} = \delta_{\Phi_a^{(\dagger)}} \zeta_b^{(\dagger)}. \tag{133}$$

In this context, the determinant is taken over the (infinite-dimensional) space spanned by all possible indices a, b, including site, spin, orbital and all remaining degrees of freedom. Instead of the determinant, the exponential function of the logarithm of the determinant can be included in the integrand.

$$Z\left[\eta^\dagger, \eta\right] = \int \mathcal{D}\left[\Phi^\dagger; \Phi\right] e^{\sum_i \Gamma[\Phi_i^\dagger, \Phi_i] - \sum_i \Phi_i^\dagger \delta_{\Phi_i^\dagger}\left(\Gamma[\Phi_i^\dagger, \Phi_i]\right) + \sum_i \delta_{\Phi_i}\left(\Gamma[\Phi_i^\dagger, \Phi_i]\right)\Phi_i}$$
$$e^{\sum_{k,\nu} \dfrac{\left(-\delta_{\Phi_k}(\Gamma[\Phi_i^\dagger, \Phi_i]) - \eta_k^\dagger\right)\left(\delta_{\Phi_k^\dagger}(\Gamma[\Phi_i^\dagger, \Phi_i]) - \eta_k\right)}{\varepsilon_k - \Delta} - \ln\left(\det(M[\Phi^\dagger, \Phi])\right)} . \tag{134}$$

The resulting action has desireable, as well as undesireable features. All of the terms in the first line of equation (134) are easily evaluated and do not cause trouble. Expanding $\ln \det(M)$ is not fully trivial, but can be approached in a controlled manner. The term quadratic in $\delta_{\Phi^{(\dagger)}}(\Gamma) \pm \eta^{(\dagger)}$ is bad, because it couples the source fields to products of the fields $\Phi^{(\dagger)}$ of arbitrary order, implying that infinitely many Green's functions for the $\Phi^{(\dagger)}$ fields are required for calculating the Green's function of the original fermions. To battle this issue, another Hubbard-Stratonovich transformation is performed, introducing new fields $\Psi^{(\dagger)}$.

$$e^{\sum_{k,\nu} \dfrac{\left(-\delta_{\Phi_k}(\Gamma[\Phi_i^\dagger, \Phi_i]) - \eta_k^\dagger\right)\left(\delta_{\Phi_k^\dagger}(\Gamma[\Phi_i^\dagger, \Phi_i]) - \eta_k\right)}{\varepsilon_k - \Delta}} =$$
$$\prod C^{-2} \int \mathcal{D}\left[\Psi^\dagger; \Psi\right] e^{-\sum_{k,\nu} C^2 \Psi_k^\dagger \Psi_k + \dfrac{C}{\sqrt{\varepsilon_k - \Delta}}\left(\left(-\delta_{\Phi_k}(\Gamma[\Phi_i^\dagger, \Phi_i]) - \eta_k^\dagger\right)\Psi_k + \Psi_k^\dagger\left(\delta_{\Phi_k^\dagger}(\Gamma[\Phi_i^\dagger, \Phi_i]) - \eta_k\right)\right)} \tag{135}$$

Here, C can be chosen arbitrarily, though

$$C = \sqrt{\varepsilon_k - \Delta} \tag{136}$$

turns out to be algebraically convenient. For calculation of Green's functions, the constant factor in front of the integral does not matter and it is therefore dropped.

$$Z\left[\eta^\dagger, \eta\right] = \int \mathcal{D}\left[\Phi^\dagger; \Phi; \Psi^\dagger; \Psi\right] e^{\sum_i \Gamma[\Phi_i^\dagger, \Phi_i] - \sum_i \Phi_i^\dagger \delta_{\Phi_i^\dagger}\left(\Gamma[\Phi_i^\dagger, \Phi_i]\right) + \sum_i \delta_{\Phi_i}\left(\Gamma[\Phi_i^\dagger, \Phi_i]\right)\Phi_i}$$
$$e^{-\sum_{k,\nu}(\varepsilon_k - \Delta)\Psi_k^\dagger \Psi_k + \left(-\delta_{\Phi_k}(\Gamma[\Phi_i^\dagger, \Phi_i]) - \eta_k^\dagger\right)\Psi_k + \Psi_k^\dagger\left(\delta_{\Phi_k^\dagger}(\Gamma[\Phi_i^\dagger, \Phi_i]) - \eta_k\right) - \ln\left(\det(M[\Phi^\dagger, \Phi])\right)} \tag{137}$$

This action depends on two sets of degrees of freedom, the $\Phi^{(\dagger)}$ and $\Psi^{(\dagger)}$ fields. In above notation, the source fields couple to the $\Psi^{(\dagger)}$ fields only. A linear shift of the $\Psi^{(\dagger)}$ fields

$$\Psi^{(\dagger)} \to \Psi^{(\dagger)} + \Phi^{(\dagger)} \tag{138}$$

allows not only for a more symmetric notation, but also removes the terms with $\Phi^{(\dagger)}$ coupling to $\delta_{\Phi^{(\dagger)}}\Gamma$. The resulting expression for the action is then given by

$$Z\left[\eta^{\dagger},\eta\right] = \int \mathcal{D}\left[\Phi^{\dagger};\Phi;\Psi^{\dagger};\Psi\right] e^{\sum_i \Gamma[\Phi_i^{\dagger},\Phi_i] - \sum_{k,\nu}(\varepsilon_k - \Delta)\left(\Psi_k^{\dagger} + \Phi_k^{\dagger}\right)\left(\Psi_k + \Phi_k\right)}$$

$$e^{-\delta_{\Phi_k}\left(\Gamma[\Phi_i^{\dagger},\Phi_i]\right)\Psi_k + \Psi_k^{\dagger}\delta_{\Phi_k^{\dagger}}\left(\Gamma[\Phi_i^{\dagger},\Phi_i]\right) - \eta_k^{\dagger}\left(\Psi_k + \Phi_k\right) - \left(\Psi_k^{\dagger} + \Phi_k^{\dagger}\right)\eta_k - \ln\left(\det(M[\Phi^{\dagger},\Phi])\right)}. \quad (139)$$

Let us now turn towards a discussion of the properties of $\exp(-\ln\det(M[\Phi^{\dagger},\Phi]))$. A first important observation is that the terms arising from the determinant are all completely local. The determinant consists of terms which are complex numbers and of even orders of products of the fields $\Phi^{\dagger}$ with complex prefactors. The numbers are inconsequential for the calculation of expectation values (though their contribution is most readily obtained). The matrix M can be written in block-form as

$$M = \begin{pmatrix} \delta_{\Phi}\delta_{\Phi^{\dagger}}\Gamma & -\delta_{\Phi}\delta_{\Phi}\Gamma \\ \delta_{\Phi^{\dagger}}\delta_{\Phi^{\dagger}}\Gamma & -\delta_{\Phi^{\dagger}}\delta_{\Phi}\Gamma \end{pmatrix} \quad (140)$$

Obviously, the only number-valued terms surviving the functional derivation are the inverse Green's functions along the main diagonal of M. All other terms contain Grassmann fields and the one-particle Green's function was assumed to be diagonal in the a-indices, precluding non-diagonal one-particle terms from arising. If each row of the matrix M is multiplied by the one-particle Green's function evaluated for the index a, the determinant is multiplied by the product of all these Green's functions. Therefore, the determinant of M can be written as

$$\det(M) = \prod_a \left(G_a^{(1)}\right)^{-2} \det \begin{pmatrix} G^{(1)}\delta_{\Phi}\delta_{\Phi^{\dagger}}\Gamma & -G^{(1)}\delta_{\Phi}\delta_{\Phi}\Gamma \\ G^{(1)}\delta_{\Phi^{\dagger}}\delta_{\Phi^{\dagger}}\Gamma & -G^{(1)}\delta_{\Phi^{\dagger}}\delta_{\Phi}\Gamma \end{pmatrix} \quad (141)$$

The product in front of the new matrix $M' = G^{(1)}M$ can be separated due to the logarithm and contributes to the action as a constant and therefore mostly irrelevant number-valued term. All number-valued terms remaining in M' are 1 and come to lie on the diagonal. Symbolically, it can be written as

$$M'_{a,b} = \delta_{a,b} \pm G^{(1)}(a)\delta_{\Phi_a^{(\dagger)}}\delta_{\Phi_b^{(\dagger)}}\sum_{n=2}^{\infty}\frac{(-1)^n}{(n!)^2}F_{1PI}^{(n)}\left(\Phi^{\dagger}\Phi\right)^{"n"}. \quad (142)$$

Here, $F_{1PI}^{(n)}$ denotes the $1PI$ n-particle vertex. For diagonaliseable matrices A we have

$$\det\left(e^A\right) = e^{\text{Tr}(A)}, \quad (143)$$

therefore

$$\ln\det\left(e^A\right) = \text{Tr}(A), \quad (144)$$

and if we assume $A = \ln B$

$$\ln\det\left(B\right) = \text{Tr}(\ln B). \quad (145)$$

This allows us to express the contribution from M' to the action via

$$M' = \mathbf{1} + D \quad (146)$$

with

$$D = \pm G^{(1)}(a)\delta_{\Phi_a^{(\dagger)}}\delta_{\Phi_b^{(\dagger)}}\sum_{n=2}^{\infty}\frac{(-1)^n}{(n!)^2}F_{1PI}^{(n)}\left(\Phi^{\dagger}\Phi\right)^{"n"}. \quad (147)$$

D can also be written in block-form

$$D = \begin{pmatrix} G^{(1)}(a)\delta_{\Phi_a}\delta_{\Phi_b^{\dagger}}\Gamma & -G^{(1)}(a)\delta_{\Phi_a}\delta_{\Phi_b}\Gamma \\ G^{(1)}(a)\delta_{\Phi_a^{\dagger}}\delta_{\Phi_b^{\dagger}}\Gamma & -G^{(1)}(a)\delta_{\Phi_a^{\dagger}}\delta_{\Phi_b}\Gamma \end{pmatrix} = \begin{pmatrix} D^I & D^{II} \\ D^{III} & D^{IV} \end{pmatrix} \quad (148)$$

This allows us to expand the logarithm[1]

$$\ln\left(M'\right) = -\sum_{n=1}^{\infty}(-1)^n\frac{D^n}{n}. \quad (149)$$

---

[1] Due to the nature of Grassmann numbers, the series expansion for the logarithm is even guaranteed to converge for a finite-size matrix D where all entries are Grassmann valued. For infinite dimensional matrices, divergent number-valued prefactors can appear for some combinations of Grassmann numbers.

Let us investigate the contributions up to order of expansion D^2 to the action. To do so, first the subblocks of D are expressed

$$D_{ab}^I = \sum_{c,d} G^{(1)}(a)F^{(2)}(c,d,a,b)\Phi_d^\dagger\Phi_c - \sum_{c,d,e,f} \frac{1}{4}G^{(1)}(a)F_{1PI}^{(3)}(c,d,e,f,a,b)\Phi_f^\dagger\Phi_e\Phi_d^\dagger\Phi_c + ... \quad (150)$$

$$D_{ab}^{II} = \sum_{c,d} G^{(1)}(a)\frac{1}{2}F^{(2)}(a,c,b,d)\Phi_d^\dagger\Phi_c^\dagger - \sum_{c,d,e,f} \frac{1}{6}G^{(1)}(a)F_{1PI}^{(3)}(c,d,a,e,b,f)\Phi_f^\dagger\Phi_e^\dagger\Phi_d^\dagger\Phi_c + ... \quad (151)$$

$$D_{ab}^{III} = -\sum_{c,d} G^{(1)}(a)\frac{1}{2}F^{(2)}(c,a,d,b)\Phi_d\Phi_c + \sum_{c,d,e,f} \frac{1}{6}G^{(1)}(a)F_{1PI}^{(3)}(c,d,e,a,f,b)\Phi_f\Phi_e\Phi_d^\dagger\Phi_c + ... \quad (152)$$

$$D_{ab}^{IV} = \sum_{c,d} G^{(1)}(a)F^{(2)}(c,d,b,a)\Phi_d^\dagger\Phi_c - \sum_{c,d,e,f} \frac{1}{4}G^{(1)}(a)F_{1PI}^{(3)}(c,d,e,f,b,a)\Phi_f^\dagger\Phi_e\Phi_d^\dagger\Phi_c + ... \quad (153)$$

Where the expansion was performed only up to third order in $1PI$ vertices. The trace of the first-order summand in the expansion of the logarithm gives

$$\text{Tr}(D) = 2 \cdot \left(\sum_{a,c,d} G^{(1)}(a)F^{(2)}(c,d,a,a)\Phi_d^\dagger\Phi_c - \sum_{a,c,d,e,f} \frac{1}{4}G^{(1)}(a)F_{1PI}^{(3)}(c,d,e,f,a,a)\Phi_f^\dagger\Phi_e\Phi_d^\dagger\Phi_c \right), \quad (154)$$

where two equivalent contributions arise from the traces of D^I and D^{IV}. Diagramatically, the interpretation of these terms (and also those which would arise from expansion up to higher order in the local $1PI$ vertices) is clear. A single pair of entering and leaving lines of the n-particle vertex is connected via a local one-particle Green's function. Such purely local correction terms to the vertices are not a-priori expected within a theory where all of the purely local correlation effects should be treated within the DMFT problem. For the moment, we acknowledge and accept the existence of these terms and turn our attention towards the calculation of the trace of the second order term arising from the expansion of the logarithm.

$$D^2 = \begin{pmatrix} D^I D^I + D^{II} D^{III} & D^I D^{II} + D^{II} D^{IV} \\ D^{III} D^I + D^{IV} D^{III} & D^{III} D^{II} + D^{IV} D^{IV} \end{pmatrix} \quad (155)$$

The terms contributing to the trace of D^2 are therefore

$$\text{Tr}\left(D^2\right) = \text{Tr}\left(D^I D^I + D^{II} D^{III}\right) + \text{Tr}\left(D^{III} D^{II} + D^{IV} D^{IV}\right) \quad (156)$$

For the term of interest, $-Tr(D^2)/2$ the contributions are therefore given by

$$-\frac{1}{2}\text{Tr}\left(D^I D^I\right) = -\frac{1}{2}\sum_{a,c,d,b,e,f} G^{(1)}(a)F^{(2)}(c,d,b,a)\Phi_d^\dagger\Phi_c G^{(1)}(b)F^{(2)}(e,f,a,b)\Phi_f^\dagger\Phi_e +$$

$$\frac{1}{4}\sum_{a,c,d,b,e,f,g,h} G^{(1)}(a)F^{(2)}(c,d,b,a)\Phi_d^\dagger\Phi_c G^{(1)}(b)F_{1PI}^{(3)}(e,f,g,h,a,b)\Phi_h^\dagger\Phi_g\Phi_f^\dagger\Phi_e -$$

$$\frac{1}{32}\sum_{a,c,d,e,f,b,g,h,i,j} G^{(1)}(a)F_{1PI}^{(3)}(c,d,e,f,b,a)\Phi_f^\dagger\Phi_e\Phi_d^\dagger\Phi_c G^{(1)}(b)F_{1PI}^{(3)}(g,h,i,j,a,b)\Phi_j^\dagger\Phi_i\Phi_h^\dagger\Phi_g \quad (157)$$

$$-\frac{1}{2}\text{Tr}\left(D^{II} D^{III}\right) = +\frac{1}{8}\sum_{a,c,d,b,e,f} G^{(1)}(a)F^{(2)}(a,c,b,d)\Phi_d^\dagger\Phi_c^\dagger G^{(1)}(b)F^{(2)}(e,b,f,a)\Phi_f\Phi_e -$$

$$\frac{1}{24}\sum_{a,c,d,b,e,f,g,h} G^{(1)}(a)F^{(2)}(a,c,b,d)\Phi_d^\dagger\Phi_c^\dagger G^{(1)}(b)F_{1PI}^{(3)}(e,f,g,b,h,a)\Phi_h\Phi_g\Phi_f^\dagger\Phi_e -$$

$$\frac{1}{24}\sum_{a,c,d,b,e,f,g,h} G^{(1)}(a)F_{1PI}^{(3)}(c,d,a,e,b,f)\Phi_f^\dagger\Phi_e^\dagger\Phi_d^\dagger\Phi_c G^{(1)}(b)F^{(2)}(g,b,a,h)\Phi_h\Phi_g +$$

$$\frac{1}{72}\sum_{a,c,d,e,f,b,g,h,i,j} G^{(1)}(a)F_{1PI}^{(3)}(c,d,a,e,b,h)\Phi_f^\dagger\Phi_e^\dagger\Phi_d^\dagger\Phi_c G^{(1)}(b)F_{1PI}^{(3)}(g,h,i,b,j,a)\Phi_j\Phi_i\Phi_h^\dagger\Phi_g \quad (158)$$

$$-\frac{1}{2}\operatorname{Tr}\left(D^{IV}D^{IV}\right) = -\frac{1}{2}\operatorname{Tr}\left(D^{I}D^{I}\right). \tag{159}$$

$$-\frac{1}{2}\operatorname{Tr}\left(D^{III}D^{II}\right) = -\frac{1}{2}\operatorname{Tr}\left(D^{II}D^{III}\right) \tag{160}$$

Actually, the expansion of the trace can be performed in a diagramatic way as well if the correct building blocks are recognised and utilised. Hints on which elements are required can be extracted from the first expansion orders. Up to the 3-particle vertex order, they are depicted in figure 28.
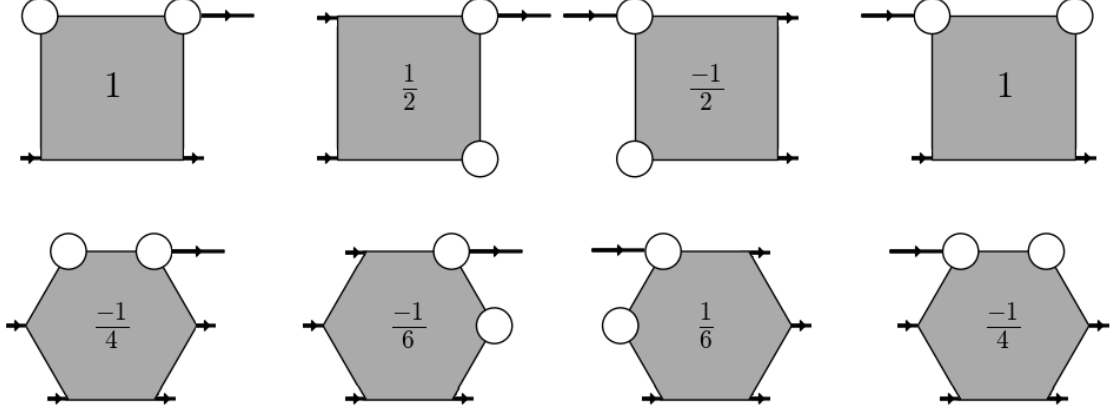

Figure 28: Diagramatic building blocks for the calculation of the contribution towards the $1PI$ action from the expansion of $\ln(M')$. Only the terms up to the order of the three-particle vertex are shown. Regular $2n$-gons denote the n-particle $1PI$ vertex. The fractional numbers denote the weight of the vertices in the diagramatic theory. Outer legs of the vertices with small arrows are to be associated with $\Phi^{(\dagger)}$ depending on whether they are incoming or outgoing. White circles denote the actual degrees of freedom for the construction of the determinant. Long outer arrows denote one-particle local propagators $G^{(1)}$. One needs to build all topologically distinct "vacuum diagrams", i.e. those which do not feature any unsaturated white circles.

With the diagramatic expression for the expansion of the determinant established, we turn our attention towards deriving a diagramatic theory for the full $1PI$ problem. The first step to this end consists of calculating the non-interacting reference Green's functions for the $\Phi^{(\dagger)}$ and $\Psi^{(\dagger)}$ fields. To do so, all quadratic contributions to the action are required. From equation (139), the quadratic terms are given by

$$-S_{quad}\left[\Phi^{\dagger};\Phi;\Psi^{\dagger};\Psi\right] = \sum_{k,\nu}\left(\frac{1}{G^{(1)}}-(\varepsilon_k-\Delta)\right)\left(\Psi_k^{\dagger}+\Phi_k^{\dagger}\right)\left(\Psi_k+\Phi_k\right)-\frac{1}{G^{(1)}}\Psi_k^{\dagger}\Psi_k \tag{161}$$

Therefore, the quadratic part of the exponent of equation (139) can be written as

$$\left(\Phi^{\dagger},\Psi^{\dagger}\right)\begin{pmatrix}\frac{1}{G^{(1)}}-(\varepsilon_k-\Delta) & \frac{1}{G^{(1)}}-(\varepsilon_k-\Delta) \\ \frac{1}{G^{(1)}}-(\varepsilon_k-\Delta) & -(\varepsilon_k-\Delta)\end{pmatrix}\begin{pmatrix}\Phi \\ \Psi\end{pmatrix}. \tag{162}$$

The bare Green's function is then given by the inverse of above matrix:

$$\mathbf{G_0} = \begin{pmatrix}G_k-G^{(1)} & G^{(1)} \\ G^{(1)} & -G^{(1)}\end{pmatrix}. \tag{163}$$

The cautious reader may point out that the contribution to the quadratic part of the action stemming from the expansion of the functional determinant was neglected. This implies that those one-particle insets need to be included explicitly in the resulting diagramatic theory in the end. For the moment however, let us turn towards an investigation of the interaction terms appearing in the $1PI$ action. The expansion of Γ beyond quadratic terms yields the following interaction terms for the $\Phi^{(\dagger)}$-fields

$$\Gamma_{int}\left[\Phi^{\dagger};\Phi\right] = \sum_{n=2}^{\infty}\frac{(-1)^n}{(n!)^2}F_{1PI}^{(n)}\left(\Phi^{\dagger}\Phi\right)^{"n"}. \tag{164}$$
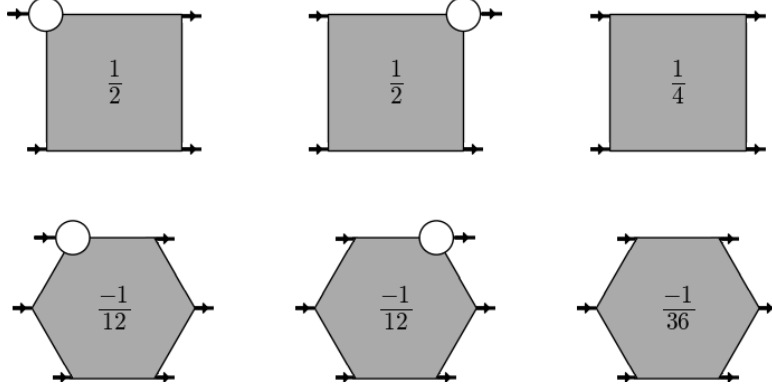
Figure 29: Diagramatic representation of the interaction terms up to third order in the vertices within $1PI$. The interaction vertices couple to $\Phi^{(\dagger)}$ at outer legs without a white circle and to $\Psi^{(\dagger)}$-fields where a white circle is present. Four types of propagators exist; black lines not connecting to any white circles ($\Phi^\dagger\Phi$), those starting or terminating at a white circle ($\Psi^\dagger\Phi$ and $\Phi^\dagger\Psi$ respectively), as well as those connecting two white circles ($\Psi^\dagger\Psi$). An interaction term can connect to a single $\Psi^{(\dagger)}$-field at most. Note the similarities to the building blocks of the expansion of $\ln(D)$.

For $\Phi^{(\dagger)}$ and $\Psi^{(\dagger)}$-fields coupling to each other we recover

$$\Psi^\dagger \delta_{\Phi^\dagger}\left(\Gamma_{int}\left[\Phi^\dagger;\Phi\right]\right) = \sum_{n=2}^\infty \frac{(-1)^n}{n!(n-1)!}F_{1PI}^{(n)}\Psi^\dagger\Phi\left(\Phi^\dagger\Phi\right)^{"n-1"}, \tag{165}$$

$$-\delta_\Phi\left(\Gamma_{int}\left[\Phi^\dagger;\Phi\right]\right)\Psi = \sum_{n=2}^\infty \frac{(-1)^n}{n!(n-1)!}F_{1PI}^{(n)}\Phi^\dagger\Psi\left(\Phi^\dagger\Phi\right)^{"n-1"}. \tag{166}$$

We can identify the interaction terms arising within $1PI$ as the one-particle irreducible, local n-particle vertices, coupling to the either only $\Phi^{(\dagger)}$ fields or to $\Phi^{(\dagger)}$ fields and a single $\Psi^{(\dagger)}$ field. The diagramatic representation of the interaction terms appearing in the $1PI$ approach are given in figure 29. Let us consider the first and second-order contributions to the self-energies of the $1PI$-fermions. Those can be calculated using standard Feynman-diagramatic methods. To the first order (in the interaction expansion, i.e. including local vertices up to arbitrary order in principle), only the two-particle vertex $\Phi^\dagger\Phi$-component of the self-energy is non-vanishing. This is because the local interaction vertices couple to one $\Psi^{(\dagger)}$ field at most and local $\Phi^\dagger\Phi$ Green's functions vanish. Higher-order vertices require at least one local $\Phi^\dagger\Phi$ Green's function loop, which vanishes when summed over. Of the two-particle vertex contributions, only the contributions to the $\Phi^\dagger\Phi$ self-energy with a local $\Phi^\dagger\Psi$ or $\Psi^\dagger\Phi$ Green's function loop do not vanish. The explicit expression for the term is

$$\Sigma_{2,\Psi_d^\dagger\Psi_c} = -2\sum_{a,b}F^{(2)}(a,b,c,d)G^{(1)}(b,a). \tag{167}$$

The one-particle Green's function $G^{(1)}$ stems from the expectation values of $\Psi_c^\dagger\Phi_b$ and $\Phi_c^\dagger\Psi_b$, which are equal and cancel the factor $1/2$ from equations (165) and (166). Another factor 2 arises from the two possible choices of contraction in the $\Psi^\dagger\Phi\Phi^\dagger\Phi$ and $\Phi^\dagger\Psi\Phi^\dagger\Phi$ terms. This term exactly cancels the 2-particle contribution to $\text{Tr}(D)$ (the first part of the right hand side of equation (154)) when taking into account that $G^{(1)}$ is diagonal in its indices a,b. Also note that the third-order vertex term in $\text{Tr}(D)$ (which is of first order in the $1PI$ interaction) vanishes because of a locally closed $\Phi^\dagger\Phi$ Green's function[1]

For the second order contributions to the self energy, a few different terms need to be considered. First, the case where both vertex functions are located at the same lattice site is considered. A second-order term has at least 6 $\Phi^{(\dagger)}$ and at most 2 $\Psi^{(\dagger)}$ fields, if it is constructed out of two-particle vertices. (Higher order vertices bring along more $\Phi^{(\dagger)}$ fields, but the number of $\Psi^{(\dagger)}$ fields remains unchanged.) Out of these (at least) 6 $\Phi^{(\dagger)}$, at most 2 can be contracted with $\Psi^{(\dagger)}$, leaving 4 $\Phi^{(\dagger)}$. The two fields the self-energy is to be evaluated for need not be contracted, but this leaves a pair of $\Phi^{(\dagger)}$, whose local Green's function vanishes. Therefore, this term does not contribute to any self-energy. However, if two vertices, say an n and an m-particle vertex, located at the same site are connected by a local $\Psi^\dagger\Phi$ and a $\Phi^\dagger\Psi$ contraction, i.e.

---

[1] There is an option of contracting higher order vertices with a single local propagator, generating corrections to lower-order vertices. These diagrams cancel the three-particle (and higher order which would appear were the expansion continued) terms in equation (154).

two local Green's functions $G^{(1)}$, this generates a local correction to the $n + m - 2$-particle vertex. These corrections exactly cancel the terms from $\text{Tr}(D^2)$.

Let us turn our attention towards a term with two vertices at different sites. Obviously, these vertices cannot be connected by local propagators and a self-energy term has to be constructed by connecting them via non-local propagators, yielding the same self-energy terms one would get from a dual fermion calculation, albeit with $1PI$ vertices instead of full ones[1].

Where the one-particle irreducible approach really shines is in calculating self-energy corrections in a ladder approximation when truncating at the two-particle vertex level. This is because it includes additional diagrams in comparison to the dual fermion approach (To be exact, it contains all local self-energy diagrams arising from one-particle reducible contributions to the three-particle vertex coupling to the two-particle ladder.).

Beyond a one-shot calculation, additional care is required when performing $1PI$ calculations. If a self-consistent solution for the $1PI$-fermions is pursued, there are four self-energy components to keep track of ($\Phi^\dagger\Phi$, $\Psi^\dagger\Phi$, $\Phi^\dagger\Psi$ and $\Psi^\dagger\Psi$, though $\Psi^\dagger\Phi$ and $\Phi^\dagger\Psi$ are not independent.) and the nice cancellation properties between the expansion of $\ln(D)$ and local terms in the interaction are lost once the $1PI$ propagators include self-energies.

An additional practical difficulty arises when one wants to go beyond the two-particle vertex level, as extracting the $1PI$ contribution to the vertices from numerical data adds a post-processing step which is not trivial. On the three-particle level, the one-particle reducible contributions can be handled (cf. 4.1).

---

[1] Two n-particle $1PI$ vertices have to be connected by $n-1$ non-local propagators, the terms where a vertex has a locally closed loop are cancelled by the expansion of D.

6. Falicov-Kimball model

The Falicov-Kimball model [28] (FKM) is a very interesting model Hamiltonian for three reasons:

- It describes a very simple interacting system. Such systems are very hard to treat theoretically and numerically, but also show a plethora of interesting behaviour.

- It does not have a trivial solution, despite the very limited number of degrees of freedom. Some very simple models like the atomic limit of the Hubbard model show well understood but essentially boring behaviour, despite their interacting nature. The Falicov-Kimball model exhibits phase transitions.

- Being a non-trivial system, it still allows for some analytic derivations. In certain cases an astonishing amount of calculations can be done analytically, allowing for more insights regarding the behaviour of the results, as well as reducing the strain on computational ressources.

The Falicov-Kimball model's more prestigious sibling, the Hubbard model, is believed to describe the relevant physics of high-temperature superconductors. Because of the many possible applications, a lot of effort is put into researching the Hubbard model. Most of the research has to be conducted relying on numerical solutions and approximations. The FKM has many features in common with the Hubbard model. A big advantage when investigating the FKM with vertex methods is that the associated dynamical mean field theory problem can be solved exactly. Additionally, vertices can be expressed in closed form within DMFT. Some of the usually very hard numerical problems therefore can be avoided for the Falicov-Kimball model. This way the behaviour of the solutions is also very well controlled; if quantities diverge, usually a denominator can be identified as the cause. Since the introduction of the model [28] a lot of progress has been made on understanding its behaviour (for a review, see [29]). In total, the Falicov-Kimball shows interesting behaviour that can be investigated with modest computational effort and is easier to interpret because analytical solutions are available. Also, newly developed methods actually meant to treat more complicated systems can be applied to the FKM where the implications about the approximations and limitations of the methods might be understood more thoroughly. An example is the application of advanced Quantum Monte-Carlo (QMC) methods to the dynamical mean field theory problem associated with the FKM [33]. While an analytical solution is obtainable, seemingly making the task futile, the analytic calculation actually provides an excellent benchmark for which solution the QMC should converge towards.
The Hamiltonian for the spin-less FKM can be written as:

$$\mathcal{H}_{FC} = -t \sum_{\langle i,j \rangle} c_i^\dagger c_j + \varepsilon_f \sum_i f_i^\dagger f_i + U \sum_i f_i^\dagger f_i c_i^\dagger c_i - \mu \sum_i (f_i^\dagger f_i + c_i^\dagger c_i). \tag{168}$$

There are two types of electrons on a discrete lattice, f-electrons, for which there is no hopping term and mobile c-electrons which hop with an amplitude t between neighbouring lattice sites. The sum over all indices i includes all lattice sites, while $\langle i, j \rangle$ includes all pairs of nearest-neighbouring sites. The local terms include the chemical potential for both species of particles and an interaction term U, which is typically repulsive; ε_f denotes an on-site potential for the f-electrons; c and f are the annihilation, $c^\dagger$ and $f^\dagger$ the annihilation operators for c and f electrons.
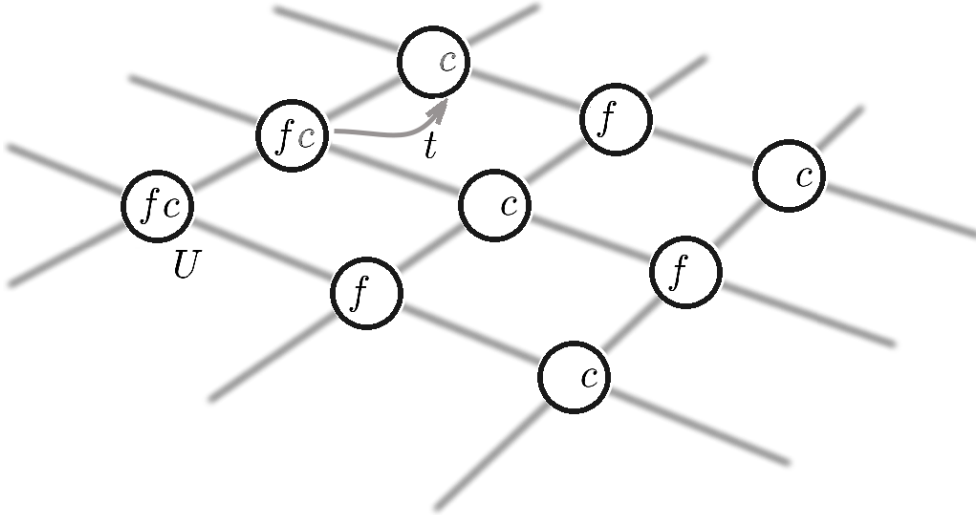
Figure 30: Schematic representation of the Falicov-Kimball Hamiltonian with c-electrons moving with hopping amplitude t and c and f electrons repelling each other with interaction strength U.

Originally, the model was introduced by Falicov and Kimball [28] hoping to be able to describe the semiconductor-to-metal transition for SmB_6. While the model fails at describing the Kondo physics relevant for f-electron systems, it displays a phase transition towards checkerboard-ordering of the c- and f-electrons on a quadratic lattice, which is of great theoretical interest. Also, the mobility of the c-electrons decreases, leading to a transition towards a non-conducting state. Since these phenomena show some similarity to the processes in the cuprate family of high-temperature superconductors, better understanding of the driving physics would be most valuable.

We will mostly concern ourselves with extensions of dynamical mean field theory (DMFT) for the Falicov-Kimball model. It is worth mentioning that the Falicov-Kimball model can be solved exactly within DMFT, up to the computational evaluation of numerical expressions. Specifically, no local solver is required, eliminating the usual DMFT-bottleneck.

Last and from a purely physical point of view probably also least, Feynman-diagrammatic methods can be applied to the Falicov-Kimball model straightforwardly and are quite simple to manage. Especially the combinatoric complexity of diagrams is vastly reduced compared to models such as the Hubbard Hamiltonian. This makes the FKM a good entry-level problem for people starting with path integral methods in solid-state theory.

6.1. Symmetries of the Falicov-Kimball model

For the FKM, conserved quantities can be found, some of which greatly reduce the computational effort needed to treat the problem numerically. Obviously, the total number of c-, as well as f-electrons is a conserved quantity. This is a common feature to all models which allow neither creation, annihilation nor transformation of particles.

More interestingly, the number of f-electrons at each lattice site is conserved. This has a massive impact on the structure of exact eigenfunctions to the Hamiltonian: Since each site can be either occupied or unoccupied by an f-electron, we can prepare a state by acting with a set of $f^\dagger$ operators associated with the set of sites S on the FKM-vacuum $|0\rangle$.

$$|\Psi_S\rangle = \prod_{i \in S} f_i^\dagger |0\rangle \tag{169}$$

This state then acts as an effective one-particle potential for the c-electrons. In principle, we can calculate the eigenvalues and eigenvectors of the resulting c-Hamiltonian and act with the corresponding creation operators on $|\Psi_S\rangle$, generating Eigenstates to the Hamiltonian. This procedure generates a full set of Eigenfunctions, each of which can be written as a single Slater determinant. Two immediate consequences of the conservation of local f-occupations are that any Green's function requiring non-local f propagation immediately vanishes and the applicability of classical Monte-Carlo approaches [57, 58] for the distributions of f-electrons within the FKM.

One can easily show that the total momentum (k-vector) of c and f electrons is conserved, which is a

consequence of the spatially homogeneous, tough local, interaction. On the other hand, one can see that the sum of the momenta of all c-electrons is not a conserved quantity on its own. This can be shown by explicit calculation, but also understood intuitively. For almost all configurations of f-electrons[1], the effective potential in which the c-electrons move is highly inhomogeneous, which means the momenta are not conserved. The f-electrons can be regarded as particles of infinite mass, allowing any momentum to be transfered to them without changing their energy.

6.2. Long range order

The ground state of the FKM displays long range order, as has been shown by Kennedy and Lieb [59]. Apart from the half-filled case, where a checkerboard-ordered ground state alternating between f-filled and f-empty sites, is found, for other rational fillings, exact statements about the ground state are known [60–62]. Obviously DMFT, being a theory describing local correlations, is unable to properly treat all properties of these states, which makes non-local extensions necessary. Diagrammatic extensions of DMFT allowed for the numerical calculation of critical exponents for the transition towards the charge-density wave [63]. Also, systematic expansions based on the dual fermion and one-particle irreducible approach allowed for calculation of momentum-dependent self-energies which support the notion of appearing long range order [64]. Besides diagrammatic extensions of DMFT, there are so-called cluster expansions of DMFT [45, 65, 66]. These usually employ a moderate number of lattice sites, which are embedded within a DMFT bath. Cluster expansions offer a lot of freedom in choosing the structure of the cluster. Unfortunate choices of the cluster can be compared to loaded questions; they preclude ordering incompatible with the cluster from appearing. Cluster studies of the Falicov-Kimball model show how crucial the choice of a suitable cluster can be [46, 47].

Within the scope of this thesis, we will be dealing with diagramatic extensions of DMFT mostly. These methods use the well established good description of purely local correlations within DMFT as a foundation, reintroducing non-local efects by means of Feynman diagrams, employing diagrammatic quantities extracted from the DMFT calculation as building blocks. Such methods are conceptually very different from diagrammatic methods [54], seeking to build diagrammatic corrections starting from bare propagators, though they share some similarities. The Falicov-Kimball model suits itself well as a test-bed for such methods, as the vertices are well-accessible.

---

[1]There are exactly two f configurations which are spatially homogeneous. Any periodic configurations still violate the conservation of c-momentum.

7. Two-particle vertices for the Falicov-Kimball model

For almost all interacting systems which are physically interesting, an analytical solution is not feasible, not even a complete one on the level of two particles. Thus, the vertices for these systems must be calculated numerically, which makes the interpretation of the results difficult. In this respect, the Falicov-Kimball model shows the remarkable quality of allowing closed-form expressions for purely local vertices for the c-electrons to be written down in terms of one-particle objects within a DMFT calculation, with the f-electrons being understood to be integrated out, as it was done in the master's thesis [67] and the present thesis. While these vertices do not exhibit all the features one would expect from a fully interacting model like the Hubbard model, they provide a middle ground between the atomic limit and the Hubbard model, with features simple enough to be treated without resorting to numerical methods while at the same time not being trivial, making the Falicov-Kimball model an ideal candidate as reference system for vertex and diagrammatic methods. This chapter aims to give an overview of these vertex objects on the two-particle level.

7.1. Full local vertex

The full local vertex for the c-electrons of the Falicov-Kimball model within a DMFT calculation can be shown [67] to be of the structure

$$F^{\nu\nu'\omega} = \beta(\delta_{\omega,0} - \delta_{\nu,\nu'})a(\nu)a(\nu' + \omega) \tag{170}$$

in particle-hole notation, a being defined as

$$a(\nu) = \sqrt{\frac{1}{p_1 p_2 U^2}}(\Sigma(\nu) - U)\Sigma(\nu). \tag{171}$$

Here, p_1 is the probability of a site being occupied by an f-electron and $p_2 = 1 - p_1$ the complementary probability. The constants and Σ are defined in accordance with the discussion of DMFT for the Falicov-Kimball model in [67]. The cross diagonal structure ($\delta_{\omega,0} - \delta_{\nu,\nu'}$) and factorisation of the vertex allows for an analytical extraction of all local vertices irreducible in a given channel Γ_c and, by extension, the fully irreducible one, Λ. Of course, a closed form expression for the vertices is preferable to purely numerical values as the structure can be understood more easily. The value of the vertex in the limit of large frequencies approaches $\pm\beta p_1 p_2 U^2$ instead of the usual U typical of the Hubbard model. This is a consequence of the c-electrons never interacting directly; there always have to be mediating f-electrons. The corresponding diagram is given by figure 31.
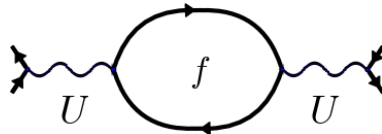

Figure 31: The diagram which constitutes the full vertex in the limit of large frequencies

In Matsubara-frequency space, only two planes, described by the conditions $\omega = 0$ and $\nu = \nu'$, have non-zero entries for the vertices of the Falicov-Kimball model. Schematically, this is shown in figure 32.
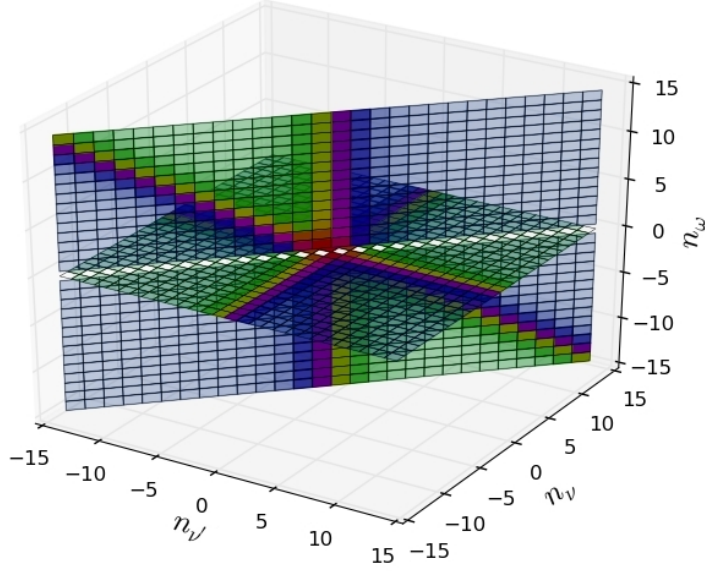
Figure 32: schematic representation of the non-zero entries for the full vertex in Matsubara-Space, adopting particle-hole notation

The main features of the full vertex can be seen. There is only an amplitude when either $\omega = 0$ or $\nu = \nu'$, but not both. The "empty line" where both $\omega = 0$ and $\nu = \nu'$ is required to be 0 by symmetry, as shown in section 3.1. Also, the limiting cases can be investigated, showing that there is a positive and a negative limiting value.

7.2. Particle-particle irreducible vertex

From the full vertex, it is possible to determine the particle-particle irreducible one by solving the according Bethe-Salpeter equation. The result is relatively well known [29]. The solution to the equation is trivial to find as the reduced frequency structure of the vertices leads to a reduction of the summation over all internal degrees of freedom to a summation of two terms, which can even be shown to be identical by employing the crossing symmetry. A closed form expression for the pp-irreducible vertex is given by:

$$\Gamma_{pp}^{\nu\nu'\omega} = \beta(\delta_{\omega,0} - \delta_{\nu,\nu'}) \frac{a(\nu)a(\nu'')}{1 + G(\nu)a(\nu)G(\nu'')a(\nu'')}, \tag{172}$$

with G being the local DMFT Green's function. To shorten the expression, $\nu'' = \nu' + \omega$ was introduced. The expression is simple to evaluate, but the factorisation property of the full vertex is gone for Γ_{pp}. Otherwise it shares the high frequency behaviour as well as the frequency structure of the full vertex.

This vertex is interesting especially when investigating Anderson-localisation of c-electrons. Anderson localisation is a consequence of constructive interference between paths that begin and end on the same site, thus increasing the amplitude of the particle remaining in the same place. While in a sufficiently disordered medium most propagators suffer from wildly fluctuating phases, for the local propagator the effect is mitigated by a certain class of paths which are ensured to have the same phase; two paths which start and end terminate at the same site and pass the same intermediate site in reverse order are guaranteed to have the same phase.

With Anderson-localisation being an effect reducing the conductivity, it may come as a surprise that the dominant contributions to superconductivity are also associated with pp-processes.

Anderson localisation and superconductivity are commonly described within a particle-particle ladder approximation. In order to avoid overcounting of diagrams the ladder has to be constructed starting from the local particle-particle irreducible vertex.

7.3. Particle-hole irreducible vertex

The BS equation in the particle-hole channel can be solved analytically, albeit taking more effort than in the pp case. Here, the factorisation of the full vertex plays an important role in the derivation. Unfortunately, the resulting expression for Γ_{ph} is obscure and little known, but it has been calculated by Shvaika as well [68]. The $\omega = 0$ and $\nu = \nu'$ planes are not equivalent for Γ_{ph} any more, nor do they need to be. For $\omega \neq 0$ the BS equation can be straightforwardly solved. For the $\omega = 0$ plane, the factorisation of the full vertex can be employed to separate the dependencies on the variables ν and $\nu' + \omega$, from where one can extract Γ_{ph} by means of a general ansatz solution. The vertex is given by

$$\Gamma_{ph}^{\nu\nu'\omega} = \beta\delta_{\omega,0}C^2\frac{a(\nu)a(\nu'')}{(1+(G(\nu)a(\nu))^2)(1+(G(\nu'')a(\nu''))^2)} - \beta\delta_{\nu,\nu'}\frac{a(\nu)a(\nu'')}{1+G(\nu)a(\nu)G(\nu'')a(\nu'')}. \tag{173}$$

The shorthand notation $\nu'' = \nu' + \omega$ was, again, employed and the constant factor C^2 introduced reads

$$C^2 = \left(1 - \sum_{\nu_1}\frac{(G(\nu_1)a(\nu_1))^2}{1+(G(\nu_1)a(\nu_1))^2}\right)^{-1}. \tag{174}$$

One can see that the $\nu = \nu'$ part of Γ_{ph} is the same as for Γ_{pp}, therefore also sharing the high frequency behaviour as well. Interestingly, the high frequency behaviour for the $\omega = 0$ part can be rather different as it is renormalised by the factor C^2.

There have been investigations about divergencies in the irreducible vertices of the Hubbard as well as the Falicov-Kimball model [64,67,69,70]. The availability of closed form expressions for the vertex means that tracking the origin of the divergencies becomes much simpler. Typically, just a denominator has to be examined. Besides the divergencies appearing for singular frequencies, it is possible that the factor C^2 leads to a global divergence of the $\omega = 0$ part of Γ_{ph}. For a quadratic lattice with $t = 0.25$, a heatmap of the values βC^2 assumes is given in figure 33.
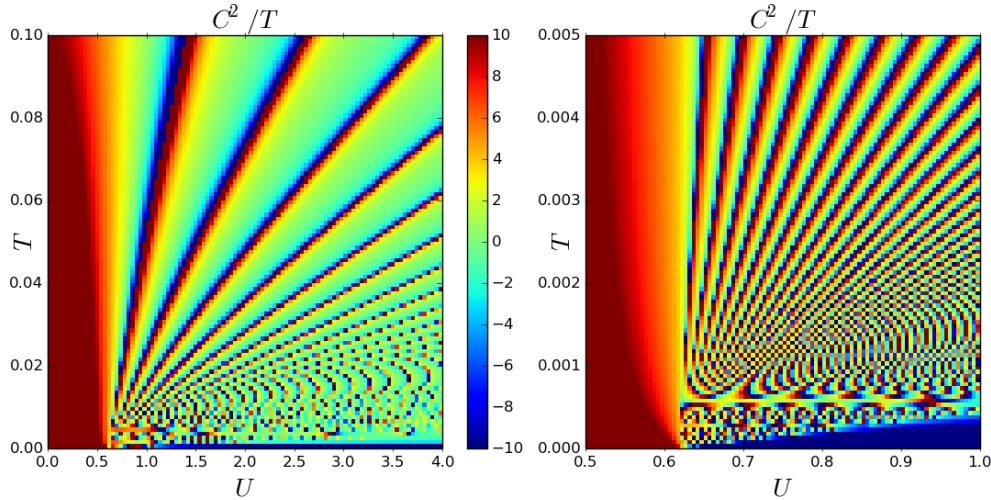

Figure 33: Heatplot of the value of C^2/T as a function of interaction U and temperature T on a quadratic lattice with $t = 0.25$. Note how the divergency lines converge towards one point in phase space. Due to finite resolution for the calculation, Moiré patterns appear where the lines lie very dense. The normalisation by T was introduced to make the plot more readable.

The particle-hole irreducible vertex is employed in calculations for charge susceptibilities. Also, one can show that the particle-hole ladders built in standard one-shot dual fermion and $1PI$ implementations are equivalent to the particle-hole ladder approximation for real fermions.

Let us remark finally that the transverse particle-hole irreducible vertex can be calculated from Γ_{ph} by applying the corresponding crossing symmetry.

$$\Gamma_{\overline{ph}}^{\nu\nu'\omega} = -\Gamma_{ph}^{\nu(\nu+\omega)(\nu'-\nu)} \tag{175}$$

This means that a separate discussion of $\Gamma_{\overline{ph}}$ would be redundant.

7.4. Fully irreducible vertex

The fully irreducible vertex, Λ, can be expressed in terms of the reducible vertices in all other channels and the full vertex via the Parquet equation. Since the Parquet equation is purely algebraic and does not contain any elements which are not present in the BS-equations as well, no new divergent features can arise. The Parquet equation is given by

$$\Lambda = F - \sum_c \Phi_c \tag{176}$$

where the sum goes over all channels c and Φ_c is the sum of all diagrams reducible in the channel c. Alternatively, the Parquet equation can also be expressed in terms of irreducible vertices

$$\Lambda = \sum_c \Gamma_c - (n-1) F, \tag{177}$$

Where all reducible vertices have been replaced by the difference of the full vertex and the irreducible vertex in the according channel, this results in the subtraction of the number of channels, n, times F. The explicit evaluation of this thesis yields

$$\Lambda^{\nu\nu'\omega} = \beta(\delta_{\omega,0} - \delta_{\nu,\nu'})a(\nu)a(\nu'')\left(C^2 \frac{1}{(1+(G(\nu)a(\nu))^2)(1+(G(\nu'')a(\nu''))^2)} \right.$$
$$\left. + 2\frac{G(\nu)a(\nu)G(\nu'')a(\nu'')}{1+G(\nu)a(\nu)G(\nu'')a(\nu'')} \right) \tag{178}$$

Obviously, the fully irreducible vertex shares most of the features of the vertices reducible in the different channels. Its high frequency behaviour is renormalised by C^2, not just for $\omega = 0$, but also for $\nu = \nu'$, with the contributions to those two planes stemming from the ph and $\overline{ph}$-irreducible vertex respectively. This object is the input required for dynamical vertex approximation calculations, where it is assumed that the local Λ extracted from DMFT is a good approximation for the fully irreducible vertex of the full lattice problem. By building different kinds of ladder-like diagrams out of Λ, one hopes to recover a fully momentum-dependent full vertex. Unfortunately, the dynamical vertex approximation cannot be straightforwardly applied to the Falicov-Kimball model, as it depends on the equation of motion to calculate self-energies. In the Falicov-Kimball model, we usually only investigate vertices between c-electrons and these do not enter the equation of motion. Instead, the mixed fc-vertices are necessary.

8. n-particle vertices for the Falicov-Kimball model

Having derived a closed form expression for the fully local two-particle vertex of the Falicov-Kimball model, one can try to generalise the concept and find fully local vertices for an arbitrary number of particles n within DMFT. In this section, the fully connected n-particle propagator will be derived, yielding the according vertex by amputation of the external one-particle propagators. To this end, the known Green's function will be subjected to algebraic transformations first. After achieving an advantageous shape, the terms will be interpreted and an inductive proof of the interpretation's consistency will be given. Finally, the remaining disconnected contributions will be singled out and eliminated. A more conservative, yet ultimately equivalent, approach is given in the appendix C. An early version of this section was used as a starting point for writing the corresponding part of [30].

8.1. Algebraic modifications of the Green's function

We will start by writing down the full n-particle Green's function. It is given by the mean value of the Green's functions for f-occupation $\overline{G}$ and non-occupation $\underline{G}$, weighted by the respective probabilities p_1 and p_2, which can be calculated from Wick's theorem, since in both cases, be the f state unoccupied or occupied, a non-interacting system is treated, the interaction U can be included in the on-site potential for the c-electrons when treating the f-occupied case.

$$G^{(n)}(a,b,c,\ldots,d,e,f,\ldots) = \delta^{abc\ldots}_{def\ldots}\left[p_1\left(\overline{G}(a)\overline{G}(b)\overline{G}(c)\ldots\right) + p_2\left(\underline{G}(a)\underline{G}(b)\underline{G}(c)\ldots\right)\right] \tag{179}$$

Here, $G^{(n)}$ is the n-particle Green's function written down in particle-frequencies $a,b,c,\ldots$ for entering electrons and $d,e,f,\ldots$ for leaving ones. Points ... imply a continuation until the correct number n of frequencies or terms is reached. Time-translation-invariance was not used in defining the frequencies to allow for a more symmetric notation, where each entering and leaving particle has its own frequency from $a,b,c,\ldots$ or $d,e,f,\ldots$ respectively. $\delta^{abc\ldots}_{def\ldots}$ is the generalised Kronecker delta. We can see that keeping track of the incoming frequencies is sufficient, as the term within the brackets is not dependent on them.
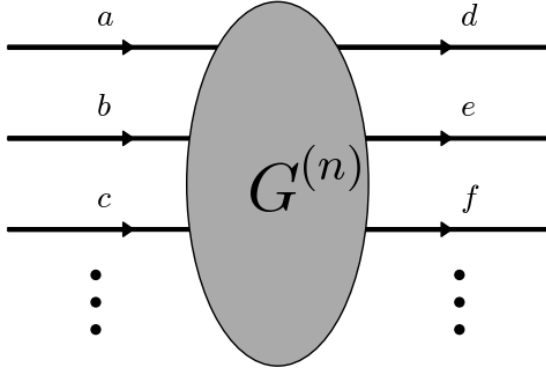

Figure 34: Diagrammatic representation of the n-particle Green's function $G^{(n)}$ keeping track of incoming and outgoing frequencies
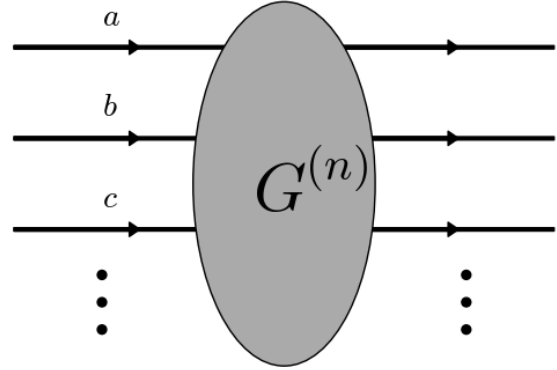
Figure 35: Diagrammatic representation of the n-particle Green's function $G^{(n)}$ with only the incoming frequencies being explicitly denoted

Having written down the n-particle Green's function, the connected parts need to be extracted. To do so, all the disconnected contributions have to be subtracted from the propagator. Typically, this is a combinatoric problem which grows very fast with the order n. Fortunately, the Falicov Kimball model allows for a systematic decomposition of the Green's function, with the combinatoric issues being reduced to an algebraic problem. We note that the component Green's functions $\overline{G}$ and $\underline{G}$ can be rewritten in the following manner:

$$\overline{G}(a) = p_1\overline{G}(a) + p_2\overline{G}(a) + p_2\underline{G}(a) - p_2\underline{G}(a) = G^{(1)}(a) + p_2\left(\overline{G}(a) - \underline{G}(a)\right) \tag{180a}$$

$$\underline{G}(a) = p_1\underline{G}(a) + p_2\underline{G}(a) + p_1\overline{G}(a) - p_1\overline{G}(a) = G^{(1)}(a) - p_1\left(\overline{G}(a) - \underline{G}(a)\right) \tag{180b}$$

If one inserts these expressions into equation (179), 2 times 2^n terms which have to be added up are obtained when multiplying the binomials, the first factor of 2 originating from the f-occupied and non-occupied case and the remaining 2^n originating from replacing either all $\underline{G}$ or $\overline{G}$ by a binomial for all n factors. Inspection of the products shows that each summand contains either a one-particle Green's function $G^{(1)}(a)$ or $(\overline{G}(a) - \underline{G}(a))$ for a given frequency a as a factor. We also note that two terms with identical decompositions and functional dependence, albeit with different constant factors exist, stemming from the two terms in the original n-particle Green's function. The terms come with multiplicative factors of $p_1(p_2)^l$ and $p_2(-p_1)^l$ respectively, with l being the total number of $(\overline{G} - \underline{G})$ factors in the term. We define

$$\mathcal{F}_l = p_1(p_2)^l + p_2(-p_1)^l. \tag{181}$$

and establish that $G^{(n)}$ can be written as:

$$G^{(n)} = \sum_{l=0}^{n} \sum_{P_l^n} \mathcal{F}_l \left(\overline{G} - \underline{G}\right)^{"l"} G^{(1)"n-l"}, \tag{182}$$

where all frequencies have been omitted, noting only how many factors of which nature occur. The quotation marks in the exponent acknowledge this condensed notation. Here, P_l^n denotes all possible permutations of grouping n elements (frequencies) into a set of l one-particle-connected and a set of $n - l$ one-particle disconnected elements. To avoid the extra summation we introduce the shorthand notation

$$G^{(n)} = \sum_{l=0}^{n} \binom{n}{l} \mathcal{F}_l \left(\overline{G} - \underline{G}\right)^{"l"} G^{(1)"n-l"}, \tag{183}$$

where the binomial coefficients are understood to take care of the number of all possible permutations of frequencies between the types of terms.

8.2. First part of diagrammatic decomposition

Taking a look at the expression for the n-particle Greens function in equation (183), it is clear that we would like to interpret the factors $G^{(1)}$ as one-particle Green's functions. This raises the question of what $\left(\overline{G} - \underline{G}\right)^{"l"}$ represents. The concept of one-particle disconnectedness ($1PD$) is introduced to allow for a systematic answer. Diagrams where a single particle line is not connected to any other are called one-particle disconnected in the frequency of that particle's propagator. For example, all the diagrams included in $G^{(n)}$ which are one-particle disconnected with respect to the particle with frequency a are given by

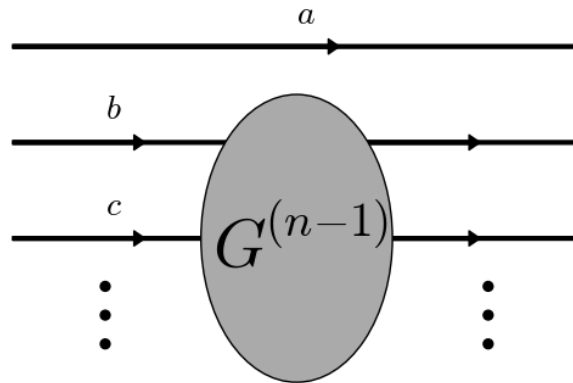$$\delta_{def...}^{abc...} G^{(1)}(a) G^{(n-1)}(b, c, ...). \tag{184}$$

Figure 36: All the diagrams contributing to the n-particle Green's function and one-particle disconnected in the frequency a

Obviously no diagram which is one-particle disconnected can be fully connected, so we can subtract them from our full propagator, tough care has to be taken to avoid overcounting. To illustrate the issue, imagine the diagrams included in figure 36. One can safely subtract them from the n-particle Green's function.

The problem arises when trying to do the same thing for all diagrams one-particle disconnected in the frequency b, as some of those diagrams were already subtracted in the first step, particularly the diagrams $1PD$ both in a and b have already been taken care of. If one could somehow obtain the contribution to the propagator which is not $1PD$ in any frequency, but not necessarily fully connected, the task of subtracting all $1PD$ diagrams from $G^{(n)}$ could be accomplished easily. We now claim that this one-particle connected propagator, $T^{(n)}$ is given by:

$$T^{(n)}(a,b,c,...,d,e,f,...) = \delta^{abc...}_{def...} \mathcal{F}_n \big(\overline{G}(a) - \underline{G}(a)\big)\big(\overline{G}(b) - \underline{G}(b)\big)\big(\overline{G}(c) - \underline{G}(c)\big)... \tag{185}$$

For the two-particle level, one can easily show that $T^{(2)}$ is really given by

$$T^{(2)}(a,b,d,e) = \delta^{a,b}_{d,e} \mathcal{F}_2 \big(\overline{G}(a) - \underline{G}(a)\big)\big(\overline{G}(b) - \underline{G}(b)\big) = p_1 p_2 \delta^{a,b}_{d,e} \big(\overline{G}(a) - \underline{G}(a)\big)\big(\overline{G}(b) - \underline{G}(b)\big). \tag{186}$$

We also know that $G^{(n)}$ can be written as in equation (183). We now separate the last summand and write:

$$G^{(n)} = \sum_{l=0}^{n-1} \binom{n}{l} \mathcal{F}_l \left(\overline{G} - \underline{G}\right)^{"l"} G^{(1)^{"n-l"}} + \mathcal{F}_n \left(\overline{G} - \underline{G}\right)^{"n"} \tag{187}$$

If equation (185) holds for all $l < n$, then what we have written in equation (187) is nothing but the sum of all $1PD$ diagrams and some remainder, all possible combinations of $1PD$ diagrams are included in the sum:

$$G^{(n)} = \sum_{l=0}^{n-1} \binom{n}{l} T^{(l)} G^{(1)^{"n-l"}} + \mathcal{F}_n \left(\overline{G} - \underline{G}\right)^{"n"} \tag{188}$$

Then, this remainder has to be exactly the sum of all one-particle connected diagrams in the n-particle propagator. What remains to be done is extracting the fully connected contribution. For the moment let us turn our attention to some features of $T^{(n)}$:

- $T^{(0)} = 1$
  On the zero-particle level one can not meaningfully talk about connectedness. The "connected" contribution to the expectation value of the number 1 is 1.

- $T^{(1)} = 0$
  There is no such thing as a diagram with only one entering and leaving line which is at the same time one-particle connected, there is nothing to be connected to.

- for odd numbers l at half-filling $p_1 = p_2 = 1/2$, $T^{(l)} = 0$. This also implies that the fully connected propagator and by extension the vertex have to vanish as will be discussed in the next section.

- on the two- and three-particle level, T is equal to the fully connected propagator, as on these levels, no disconnected diagrams without at least one one-particle propagator exist.

8.3. Second part of diagrammatic decomposition

Having already obtained the one-particle connected contributions to the n-particle propagators, the disconnected parts consisting of products of propagators of higher order in the number of particles need to be eliminated. The fully connected part of the n-particle Green's function will be called $C^{(n)}$. We start by noting that only products of lower-order connected propagators have to be subtracted, as any $1PD$ contributions have already been taken care of.

$$C^{(n)} = T^{(n)} - \sum_i \prod_j C^{(n_{i,j})} \tag{189}$$

Where the sum goes over all possible decompositions of the propagator into two or more lower-order fully connected ones. This has important consequences for the structure of $C^{(n)}$, since $T^{(n)} \propto \left(\overline{G} - \underline{G}\right)^{"n"}$. If all the lower order $C^{(l)} \propto \left(\overline{G} - \underline{G}\right)^{"l"}$ as well, we are subtracting terms which are equivalent except for a global factor, leaving $C^{(n)} \propto \left(\overline{G} - \underline{G}\right)^{"n"}$.

$$C^{(n)} = \mathcal{C}_n \big(\overline{G} - \underline{G}\big)^{"n"} \tag{190}$$

This leaves only the factor $\mathcal{C}_n$ to be determined. We will systematically find all distributions of n entering particles into groups of two or more particles. To do so, we start by investigating a specific entering line,

for example the one belonging to the frequency a. This line can be fully connected to any number of other lines between 1 and $n-2$. All the other lines can be interconnected in any fashion, as long as they are never $1PD$. Thus these disconnected diagrams can be written as terms of the shape:

$$C^{(l)} \cdot T^{(n-l)} = \mathcal{C}_l\big(\overline{G} - \underline{G}\big)^{"l"} \mathcal{F}_{n-l}\big(\overline{G} - \underline{G}\big)^{"n-l"} = \mathcal{C}_l \mathcal{F}_{n-l}\big(\overline{G} - \underline{G}\big)^{"n"} \tag{191}$$

To add all of them up, one needs to take care of the number of possible choices for fully connecting $l-1$ frequencies to a. We have already selected a, so only $n-1$ frequencies are left. From them, we select $l-1$ frequencies. Thus, the total sum of all terms which still need to be eliminated from $T^{(n)}$ to arrive at $C^{(n)}$ is given by

$$C^{(n)} = T^{(n)} - \sum_{l=2}^{n-2} \binom{n-1}{l-1} C^{(l)} T^{(n-l)} \tag{192}$$

which can be simplified to yield

$$\mathcal{C}_n = \mathcal{F}_n - \sum_{l=2}^{n-2} \binom{n-1}{l-1} \mathcal{C}_l \mathcal{F}_{n-l} \tag{193}$$

We note that no problem arises in equation (192) when we get rid of the factors $\big(\overline{G} - \underline{G}\big)^{"n"}$ because they appear in all terms equally-since all the terms have the same dependence on the frequencies, the exact permutation does not matter and we can interpret the binomial coefficients as numbers instead of a rule for taking all possible permutations of the frequencies involved. We arrive at equation (193), which gives us a simple iterative expression for calculating the fully connected contribution to the n-particle propagator. We immediately see that for half-filling and odd numbers n, $\mathcal{C}_n$ has to vanish: $\mathcal{F}_j$ is zero for all odd j, eliminating half the terms to be subtracted from $\mathcal{F}_n$ (which is also 0) immediately. The other terms are products of $\mathcal{F}_j$ for even j and $\mathcal{C}_{n-j}$ where $n-j$ has to be odd. If all odd $j < n$ have vanishing $\mathcal{C}_j$, all these terms vanish as well. Thus a proof by induction is constructed.

8.4. Numerical investigation of $\mathcal{C}_n$

With an exact recursion relation available, which allows us to calculate the prefactors for the n-particle vertex with modest numerical effort, we will now investigate the behaviour of the factor $\mathcal{C}_n$ for two different f-fillings $p_1 = 0.5$ and $p_1 = 0.25$. One might expect the factors to vanish with increasing n, just as $\mathcal{F}_n$ does. The asymptotic behaviour will be investigated, finding a simple closed expression for it. Provided in the following are plots of $\mathcal{C}_n$ and $\mathcal{F}_n$ for small values of n.
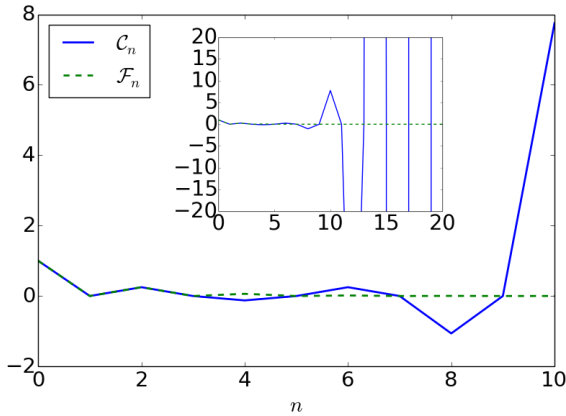

Figure 37: $\mathcal{C}_n$ and $\mathcal{F}_n$ up to $n = 10$ for $p_1 = 0.5$ with an inlay showing the values up to $n = 20$. Note how the odd-numbered factors have to vanish exactly.
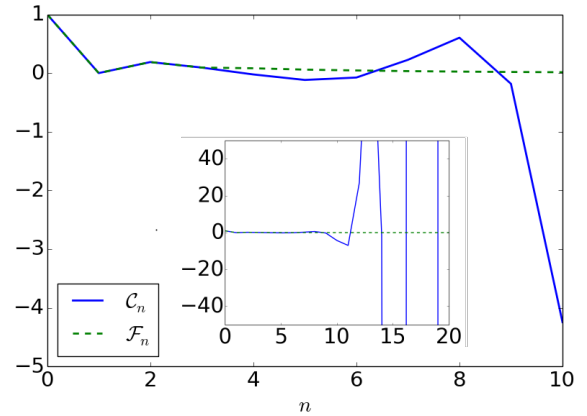
Figure 38: $\mathcal{C}_n$ and $\mathcal{F}_n$ up to $n = 10$ for $p_1 = 0.25$ with an inlay showing the values up to $n = 20$. Note the different onset of the oscillations.

In figures 37 and 38 we see that both $\mathcal{C}$ and $\mathcal{F}$ start out behaving quite well, up to $n \sim 7$, no problems arise, it seems as if the higher order vertices might converge towards zero, then one can observe that $\mathcal{C}$ not only starts increasing in absolute value, but also oscillating. For methods based on the expansion of local DMFT problems into different orders of correlators, wildly fluctuating factors are highly undesireable. Especially if expansions are truncated on the two-particle level, as it is usually done for the dual-fermion and

one-particle-irreducible methods, caution about what types of terms are neglected is required. To estimate the influence of high order diagrams, C_n was calculated up to $n = 200$, in hope of finding some asymptotic behaviour. The logarithmic plots are given in figures 39 and 40.
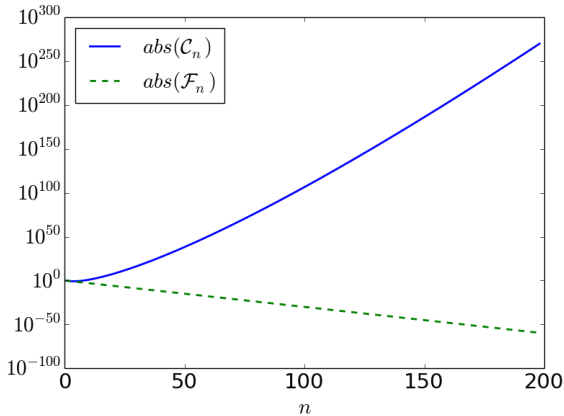

Figure 39: Logarithmic plot of the absolute values of $\mathcal{C}_n$ and $\mathcal{F}_n$ up to $n = 200$ for $p_1 = 0.5$.
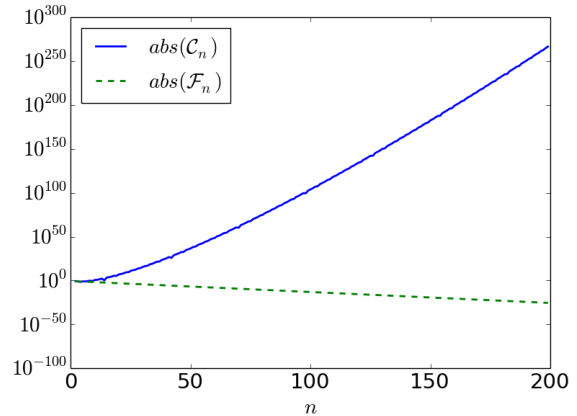
Figure 40: Logarithmic plot of the absolute values of $\mathcal{C}_n$ and $\mathcal{F}_n$ up to $n = 200$ for $p_1 = 0.25$.

Both for $p_1 = 0.5$ and 0.25, $\mathcal{C}$ diverges quite badly. As no asymptote can be found in the logarithmic plots, worse than exponential divergence is implied. The divergence is certainly a consequence of the many combinatoric possibilities of partitioning the n-particle propagator into disconnected contributions. From the recursion relation (193) and the strongly rising behaviour of $\mathcal{C}$ we might speculate that the final term in the sum is dominating the behaviour of $\mathcal{C}$. A plot showing the ratio of the last summand contributing to $\mathcal{C}$ and the factor itself at half filling $p_1 = 0.5$ itself is given in figure 41. The associated plot for $p_1 = 0.25$ is less informative, but still given in figure 42.
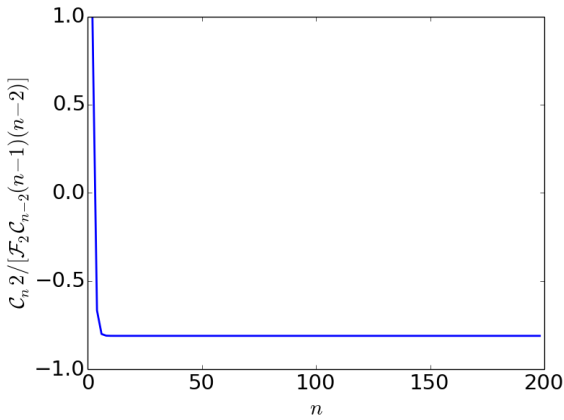

Figure 41: Ratio of $\mathcal{C}_n$ and the last summand removing disconnected contributions from it at half filling $p_1 = 0.5$.
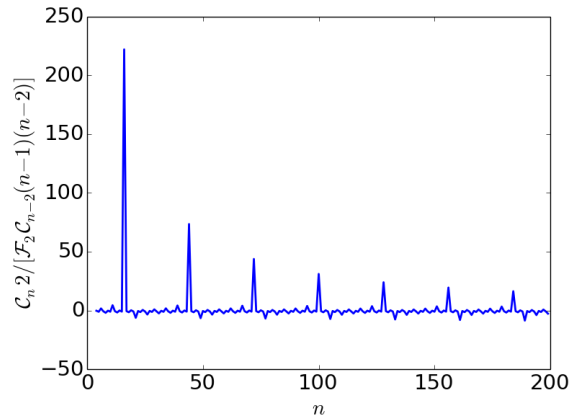
Figure 42: Ratio of $\mathcal{C}_n$ and the last summand removing disconnected contributions from it at quarter filling $p_1 = 0.25$.

8.4.1. Evaluation of r at half-filling

We can easily see that the ratio r in figure 41 seems to converge towards a constant value at half filling, which we can evaluate numerically.

$$r \cong \frac{2\,\mathcal{C}_n}{\mathcal{C}_{n-2}\,\mathcal{F}_2\,(n-1)(n-2)} \approx -0.81 \tag{194}$$

Assuming this relation holds exactly, it is possible to calculate an explicit expression for $\mathcal{C}$ for even n when $p_1 = 0.5$. (Remember that it vanishes exactly for odd n in this case.)

$$\mathcal{C}_n \approx \sqrt{\frac{\mathcal{F}_2 r}{2}}^{\,n} (n-1)!\, q, \tag{195}$$

with a multiplicative factor q. The factor r can be calculated analytically[1] We can insert this expression into the recursion relation (193):

$$\sqrt{\frac{\mathcal{F}_2 r}{2}}^{\,n} (n-1)!\, q = \left(\frac{1}{2}\right)^n - \sum_{l=2\,|\,l\equiv 0(2)}^{n-2} \binom{n-1}{l-1} \sqrt{\frac{\mathcal{F}_2 r}{2}}^{\,l} (l-1)!\, q \left(\frac{1}{2}\right)^{(n-l)} \tag{196}$$

For large values of n we can obviously neglect $(1/2)^n$. Then, we can divide by q and compensate one of the terms in the denominator of the binomial coefficient by $(l-1)!$, while $(n-1)!$ appears on the left and right hand side of the equation equally and can therefore also be elliminated.

$$\sqrt{\frac{\mathcal{F}_2 r}{2}}^{\,n} = - \sum_{l=2\,|\,l\equiv 0(2)}^{n-2} \frac{1}{(n-l)!} \sqrt{\frac{\mathcal{F}_2 r}{2}}^{\,l} \left(\frac{1}{2}\right)^{(n-l)} \tag{197}$$

As a next step, we introduce a new summation variable $u = n - l$, for which we then allow the summation to run up to infinity instead of $n-2$.

$$\sqrt{\frac{\mathcal{F}_2 r}{2}}^{\,n} = -\sqrt{\frac{\mathcal{F}_2 r}{2}}^{\,n} \sum_{u=2\,|\,u\equiv 0(2)}^{\infty} \frac{1}{(u)!} \sqrt{\frac{\mathcal{F}_2 r}{2}}^{\,-u} \left(\frac{1}{2}\right)^{u} \tag{198}$$

$$1 = -\left(\cosh\left(\frac{1}{2}\sqrt{\frac{2}{\mathcal{F}_2 r}} \right) - 1 \right) \tag{199}$$

$$0 = \cosh\left(\frac{1}{2}\sqrt{\frac{2}{\mathcal{F}_2 r}} \right) \tag{200}$$

We can insert $\mathcal{F}_2 = 1/4$ and use the known zeros of the cosh function

$$\frac{(2l+1)i\pi}{2} = \frac{1}{2}\sqrt{\frac{8}{r}} \tag{201}$$

with $l \in \mathbb{Z}$

$$r = \frac{-8}{(2l+1)^2 \pi^2} \tag{202}$$

Since the largest absolute value of r will dominate expression (195), we can restrict ourselves to

$$r = \frac{-8}{\pi^2} \approx -0.810569, \tag{203}$$

in excellent agreement with (194).

---

[1]This approach was proposed by Georg Rohringer.

9. Calculation of dual fermion corrections employing a local three-particle vertex for the Falicov-Kimball model

In an attempt to estimate the impact of higher-order correlators on one-particle quantities, dual-fermion theory was applied, employing a three-particle vertex in addition to the usual two-particle quantities [30]. The ingredients to be used are the local three-particle vertex from section 8 as well as a choice on which diagrams to include into the calculation. To generate a self-energy term, two legs of a vertex need to remain free while the others are saturated by Green's functions. We decided to connect the four remaining legs of the vertex via a ph-ladder of two-particle vertices, yielding the diagram in figure 43. The diagram was chosen because ph-fluctuations are expected to dominate the behaviour of the system and the construction ensures that divergencies in the two-particle ladder (which lead to diverging self-energies for the dual fermions already on the two-particle vertex level) also cause divergent three-particle vertex corrections.
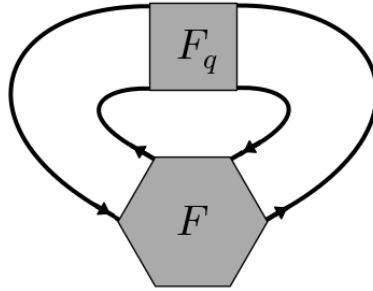

Figure 43: Correction to the local Σ_{DF} of the dual fermions including a three-particle vertex.

Actually, this type of dual-fermion diagram was already proposed in [23] as a contribution to the self-energy, but no values were given there. In [55] its effect on the leading eigenvalue of the dual Bethe-Salpeter equations is stated to be small in the Hubbard model at half-filling, but the self-energy data is not given explicitly. Since the local DMFT three-particle vertex vanishes at half-filling for the FKM, our calculation was performed at quarter-filling $p_1 = 0.25$. The three-particle vertex, being a purely local interaction term, scatters equally into all states obeying conservation of momentum. Remaining degrees of freedom have to be summed over. The self-energy correction term becomes

$$\Sigma_{DF}^3(\nu) = -\frac{1}{4} \sum_{\nu_1,\nu_2,\omega,k_1,k_2,q} F^{(3)}(\nu,\nu_1,\nu_2+\omega,\nu,\nu_1+\omega,\nu_2) \overset{\sim}{\chi}_q^{\nu_1,\nu_1+\omega} F_{k_1,k_2,q}^{\nu_1,\nu_2,\omega} \overset{\sim}{\chi}_q^{\nu_2,\nu_2+\omega}. \tag{204}$$

Here, dual susceptibilities $\overset{\sim}{\chi}_q$ were introduced. They consist of the product of two dual Green's functions whose momenta differ by q. In principle, F denotes the full dual two-particle vertex. We replace it by a ph-ladder approximation F_q. Furthermore, we can establish that the contribution to the self-energy from the ph and $\overline{ph}$ ladders is equal. This allows us to treat both of them using the ph ladder only and including a factor 2. However, in doing so, we overcount the diagrammatic contribution included in both ladders, i.e. the local DMFT two-particle vertex. Correctly taking into account all these factors, we end up with the expression

$$\Sigma_{DF}^3(\nu) = -\frac{1}{2} \sum_{\nu_1,\nu_2,\omega,k_1,k_2,q} F^{(3)}(\nu,\nu_1,\nu_2+\omega,\nu,\nu_1+\omega,\nu_2)$$

$$\overset{\sim}{\chi}_q^{\nu_1,\nu_1+\omega} \left(F_q^{\nu_1,\nu_2,\omega} - \frac{1}{2} F^{(2)\,\nu_1,\nu_2,\omega} \right) \overset{\sim}{\chi}_q^{\nu_2,\nu_2+\omega}, \tag{205}$$

which is then to be evaluated numerically. In the following, self-energy results are shown and discussed.
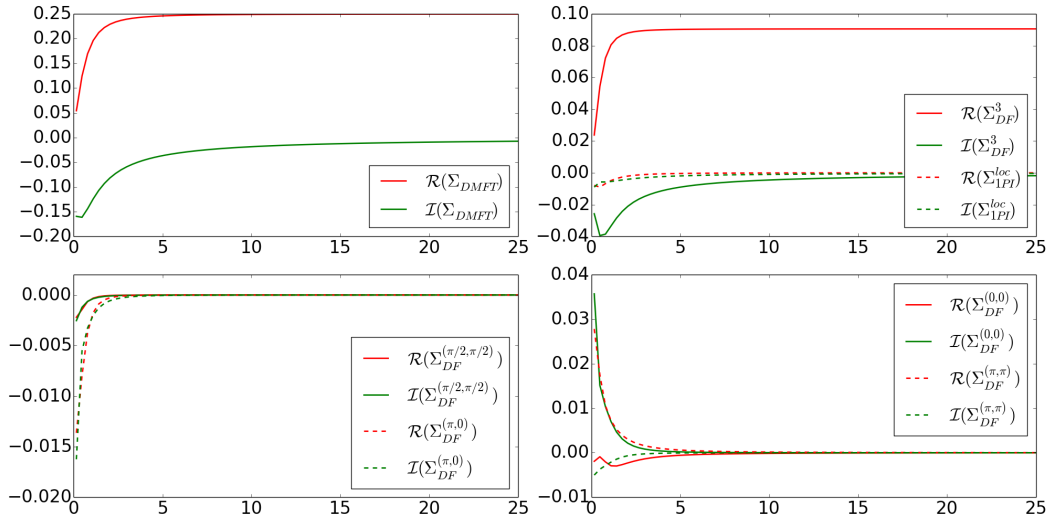
Figure 44: Upper left: Self-energy within DMFT. Upper right: Contribution to the self-energy of the dual fermions due to the term in equation 205 and correction to the local self-energy within a *ph*-ladder approximation in $1PI$. Lower right: Self-energy correction for the dual fermions within *ph*-ladder approximation for two k-points near the Fermi surface. Lower left: Self-energy corrections for the dual fermions for the center and corner of the Brillouin zone within a *ph*-ladder approximation. Data is given for a square lattice with $t = 0.25$, $U = 1$, $\mu = 0.2$ and $T = 0.05$ at quarter f-filling $p_1 = 0.25$.

Unlike typical ladder-type DF corrections on the two-particle level, this specific contribution from the combined two- and three-particle vertices is local and thus momentum-independent for the dual fermions. For this reason, a comparison to the similar, local, self-energy correction term appearing within $1PI$ calculations using a two-particle vertex makes sense. That is, diagramatically, the $1PI$ approach generates the self-energy corrections stemming from one-particle reducible contributions to the three-particle vertex already on the two-particle vertex level. When self-consistent calculations are performed, the diagrams included by the different methods in different expansion orders become harder to compare. It is worthwhile to point out that the argument given in [25] about the lack of one-particle reducible contributions to the dual self-energy still applies for all diagrams of the structure in figure 43. While the question whether the dual self-energy mapping in equation (118) should be employed remains, at least no weird situation arises where some, but not all one-particle reducible diagrams are considered explicitely.

The data presented in figure 44 was calculated for a square lattice for a hopping value of $t = 0.25$ with parameter values of $U = 1$ and $\mu = 0.2$ at a temperature $T = 0.05$. The chemical potential was chosen such that the filling by c-electrons is close to 0.5. The rationale behind this choice was to ensure that the Fermi-surface for c-electrons of the resulting system is similar as for the well-investigated half-filled case, allowing for comparisons of the results. Note that, for the data shown, no mapping of the dual self-energy was performed. The corrections due to the three-particle vertex turn out to be larger than those originating from two-particle vertices only for these parameters. The high-frequency limit of the corrections is a real constant, implying a change of the Hartree-term and thus a change of the f-filling perceived by the c-electrons. The ratio of two-particle to three-particle corrections casts some doubt on the two-particle truncation of the DF expansion.

With the the corrections to the self energy due to the three-particle vertex–somewhat surprisingly–even dominating the two-particle ones, a similar study was performed for the Hubbard model at half-filling [31].

10. Parquet dual fermion for the Falicov-Kimball model

Diagramatic techniques for strongly correlated quantum systems are intuitive, but suffer from uncontrolled freedom in the choice of the considered diagrams. The evaluation of low-order diagrams, while controlled for weak interactions, is limited in its applicability. If one is confident to know which type of fluctuations dominates the behaviour of the system, a ladder approximation in the corresponding channel is justified. But this knowledge has to originate from somewhere. Parquet-based methods on the other hand, offer an unbiased set of diagrams. They build upon the fully irreducible, two-particle vertex Λ, which is then used as a basis for reconstructing the full vertex through the Bethe-Salpeter and Parquet equations. What is needed is an approximation for Λ. The arguably simplest approximation is setting $\Lambda = U$, i.e. equal to the bare interaction, which is known as parquet approximation.

More recently, better approximations for Λ became possible. That is, one can obtain Λ from a local impurity problem, e.g. calculated at DMFT self-consistency. In practice, one first calculates the full local vertex, inverts the local Bethe-Salpeter equations and employs the parquet equation to obtain Λ. From this local Λ one builds a non-local full vertex from the non-local Bethe-Salpeter equations. Such an approach is called dynamical vertex approximation (DΓA) [22], it neglects all non-local contributions to the fully irreducible vertex. From the non-local full vertex, a non-local self-energy is obtained, which can be done for example by applying the Schwinger-Dyson equation of motion, or via a flow equation as it is done in Functional renormalisation group approaches [71].

Typically, Parquet-based schemes suffer from a lack of computer memory and communication speed because they have to store multiple non-local vertex objects depending on three frequencies and momenta[1] and the parquet equation mixes essentially all components. This means that one needs to work with finite frequency and momentum boxes. In this respect, additional complications arise from finite frequency boxes for the treated vertices because the BS-equations "reach out" and require for the update of the vertex, components of vertices in a larger frequency box [51]. Thus, each iteration reduces the frequency box where the results are reliable successively–if no countermeasures are taken. An early attempt at controling this issue consisted of implementing periodic boundary conditions for the frequencies of the vertex in analogy to the k-vectors[2]. More recently, kernel-approximations were applied, to extend the edges of the frequency box, trying to capture the non-trivial high frequency features of vertices [50,51]. For the Falicov-Kimball model, countermeasures to the shrinking frequency box are easily implemented. The problem originates from the choice of form for the frequency box. Subsection (10.2) is dedicated to the discussion of this issue. A combination of dual-fermion and parquet approximation seems most promising for the treatment of the Falicov Kimball model. Firstly, the bare interaction of the dual fermions is already given by the full local DMFT vertex F_{loc}, which implies that the purely local correlations are already encoded in low-order DF diagrams. Also, the local propagators for the dual fermions are typically small, further justifying the parquet approximation with interaction F_{loc}, though the non-locality is not perfect if pursuing a self-consistent solution. Also, the fast decay of dual propagators with the frequency is advantageous for the convergence of the full vertex constructed out of F_{loc}. Additionally, the special frequency structure of vertices within the FKM allows us to easily circumvent the "shrinking frequency box problem" by reformulating the BS equations.

For actual numerical calculations the victory program package [51] was modified. Later, a program dedicated especially to the Falicov-Kimball model was developed, taking full advantage of its symmetries.

10.1. Workflow of a parquet based dual fermion implementation

A good starting point for a dual fermion calculation, at least at higher temperatures, is the local vertex of a converged local solution for a DMFT problem. Based on this, the dual fermion problem is defined as discussed in section 5.2, using purely non-local propagators $\widetilde{G}_0 = G_k - G^{(1)}$ as non-interacting reference Green's functions for the dual fermions whose interaction is given by the local vertices. Our parquet based dual fermion implementation now employs what is essentially the parquet approximation for the dual fermions. That is, we approximate Λ by the local dual fermion interaction F_{loc} also known as the local vertices of the impurity problem. The Bethe-Salpeter and parquet equations then yield the full, non-local vertex for the dual fermions, from which a dual self-energy can be extracted. This self-energy modifies the propagators which connect the local impurity vertices, which in turn affects the full dual vertex from which the self-energy is to be calculated. Eventually, an agreement between the two expressions must be reached, which is equivalent to achieving self-consistency when iterating the two steps. From the dual self-energies, k-resolved corrections to the self-energies for the real fermions are extracted, which in turn allows us to

---

[1] See section 3.4 for the actual memory requirements for non-local vertices.
[2] This is arguably a problematic approximation.

update the DMFT bath, iterating the whole procedure until it converges. The workflow is illustrated in figure 45.
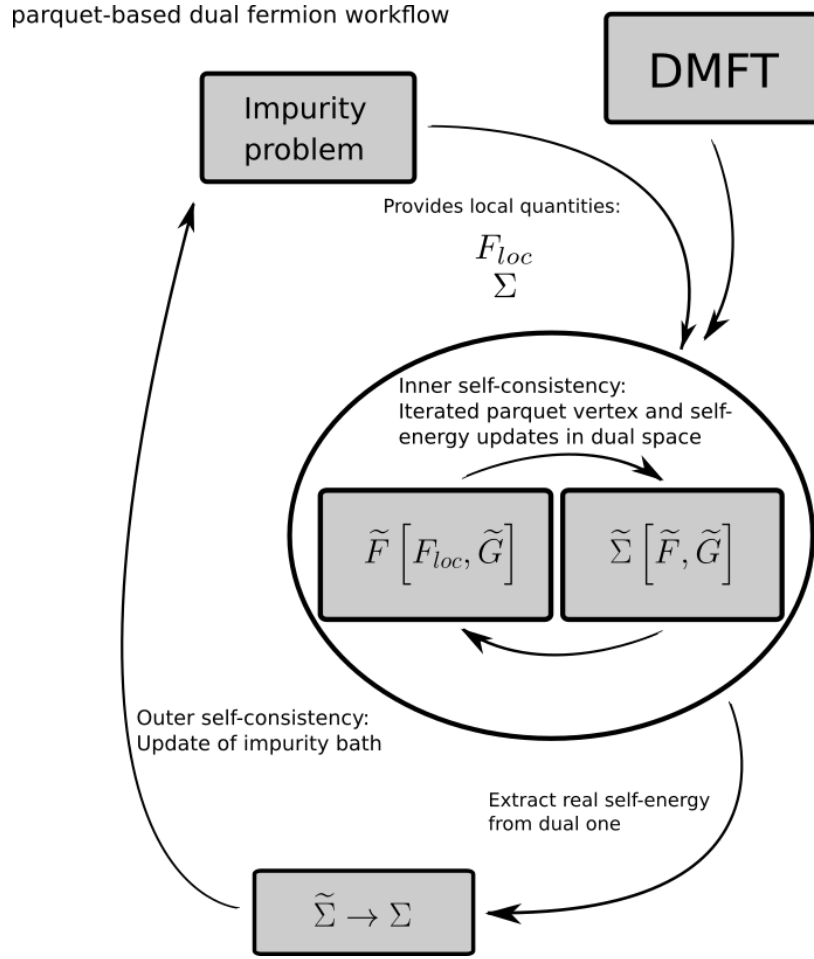

parquet-based dual fermion workflow

Figure 45: Workflow of a combined DMFT and dual parquet approach starting from a DMFT impurity. Two self-consistency loops need to converge. An inner one, for the behaviour of the dual fermions for a given impurity problem and an outer one for the underlying impurity problem.

Unfortunately, while iterating the procedure until self-consistency sounds simple in theory, it becomes a challenge in practice. An obvious issue is the required computational power. For the Falicov-Kimball model, the computational effort can be scaled down compared to the Hubbard model for two main reasons; first, there is only a single spin channel, which needs to be taken into account and second, even more importantly the vertices have a reduced frequency structure, which can be taken advantage of. Storage of the k-resolved vertices remains the most serious issue, with only one frequency argument being possible to omit. There is also some freedom in how to alternate between vertex and self-energy calculations. Updating the self-energy after each update of the full vertex seems prudent since it is computationally quite inexpensive compared to a vertex update and the updates are highly interdependent. Anyhow, for low enough temperatures, where at least one Bethe-Salpeter equation becomes unstable, the procedure is not guaranteed to converge.

In the half-filled, particle-hole symmetric case, the system becomes prone towards oscillations, as depicted in figure 46. How this arises is easy to see. Starting from the bare dual propagators, when approaching a phase transition, the associated ladder starts diverging, which results in huge values for the full dual vertex. Since the dual self-energy is essentially calculated from contracting the dual vertex with the bare dual interaction (i.e. the full local DMFT vertex) via three dual propagators, the self-energy becomes huge as well. This in turn leads to the dual propagators being suppressed and the previously divergent ladder converging. The suppressed propagators are then used to calculate the self-energy from the convergent vertex, further surpressing the value of the new self energy. With a small self-energy however, the ladders diverge again. A possible countermeasure against these oscillations is using a weighted average of a newly calculated self-energy and the one from the previous iteration. Using converged self-energy results from

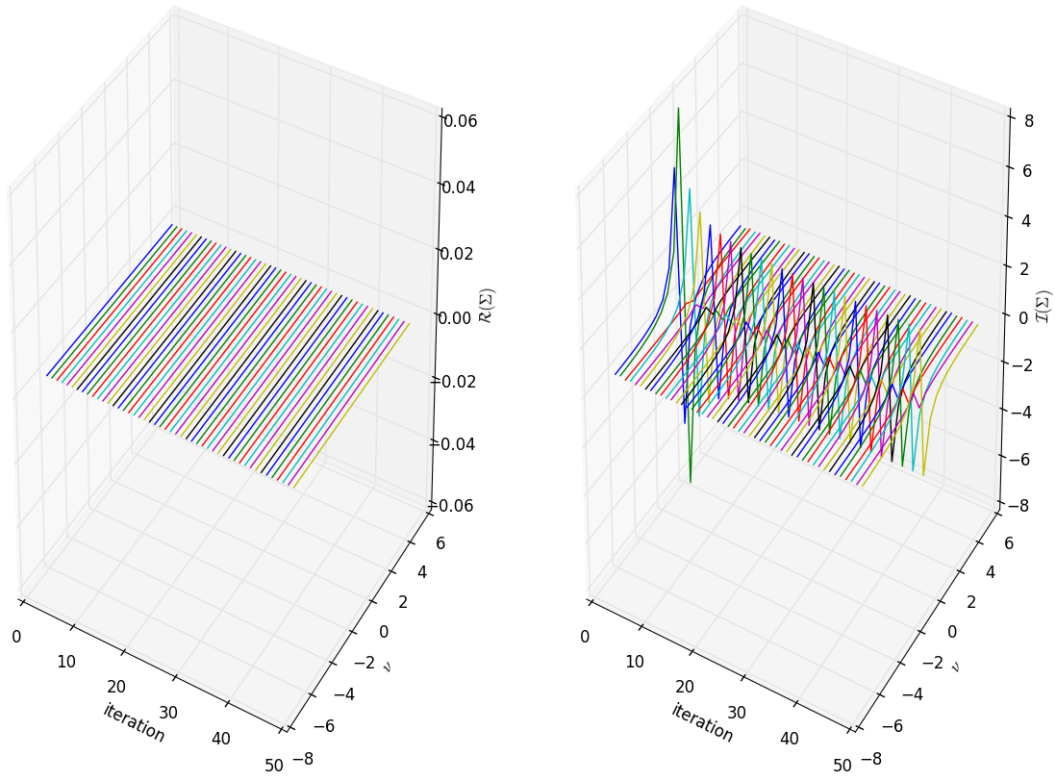higher temperatures also proved effective at surpressing these unwanted oscillations[1].

Figure 46: Exemplary plots of the real (left) and imaginary (right) part of the dual self-energy within the dual-fermion parquet approach as a function of the Matsubara frequency and inner self-consistency iteration. Note how the imaginary part starts oscillating between two configurations, while the real one remains 0 due to symmetries.

In our approach, the Bethe-Salpeter equations were solved iteratively, not by inverting them, but by building up reducible vertices step by step and updating the dual self-energy corrections in every step. This allowed us to use the behaviour of the dual self-energy as a convergence criterion as well, since it is the quantity we are actually interested in when evaluating the results.

10.2. Problems arising from finite frequency boxes

As has already been mentioned, the parquet equations (24), (25) and (28) require the evaluation of vertices from larger frequency boxes to generate new vertices. An important aspect in understanding the origin of these problems is the frequency structure of two-particle vertices. Two-particle vertices are usually treated as three-frequency objects. Connecting two entering and two leaving particles, they should have four independent variables (frequencies as well as k-vectors). Conservation of energy and momentum reduces the numbers by one. Within ph-notation, the frequencies of the particles and holes are given by ν, ν', $\nu + \omega$ and $\nu' + \omega$. In figure 47, the simplest frequency box which–in principle–can be used is given. The frequency-cube is quite arbitrary; it restricts the infinity norm of the vector $(\nu, \nu', \omega)^2$. Unfortunately, the decomposition is not unique, and for example in pp-notation, ω carries a different meaning. Nevertheless, this choice is extremely convenient for pragmatic reasons. The BS equation in the ph channel is diagonal in ω_{ph}. Allocating and accessing memory is straightforward computationally and the equations look completely equal analytically and in the progammatic implementation. The ease of use comes at a price however: Let us now investigate what happens to the frequency-box when we apply an exchange of two outer legs: $\nu \to \nu$, $\nu' \to \nu + \omega$ and $\omega \to \nu' - \nu$. (cf. fig. 5 and 6) We will see that the volume element looks completely different, despite necessarily describing exactly the same physics[3]. The transformed volume element is depicted in

---

[1] The dual self-energies calculated for slightly higher temperatures were simply used for initialisation without any compensation for the change of the Matsubara frequencies with temperature.

[2] Note that our cut-off therefore depends on the choice of notational convention. This amounts to an approximation explicitly dependent on the choice of coordinatisation.

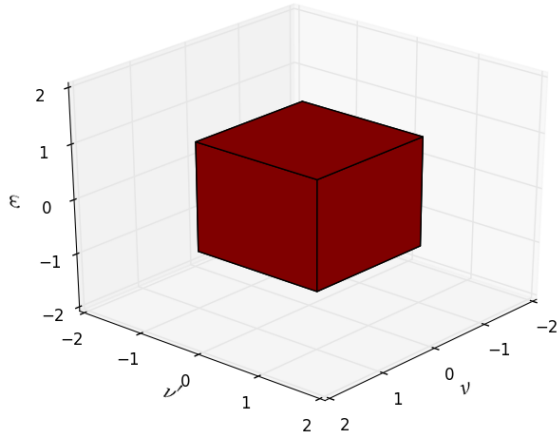[3] Two fermions have been swapped, which should only change an overall sign.

Figure 47: Box depicting the part of frequency space covered by a simple restriction of the absolute values of ν, ν' and ω. The scales of the axes are to be understood schematically.
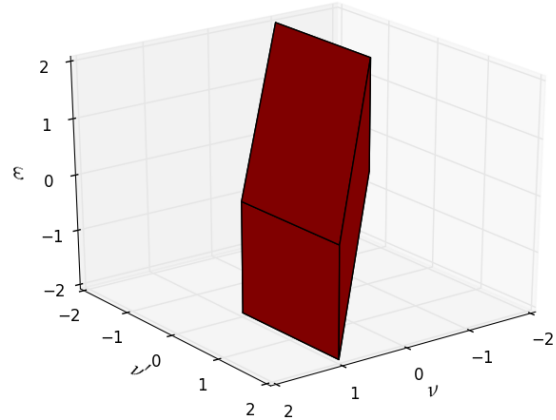

Figure 48: Same frequency box as in fig. 47, but transformed as $\nu \to \nu$, $\nu' \to \nu + \omega$ and $\omega \to \nu' - \nu$.
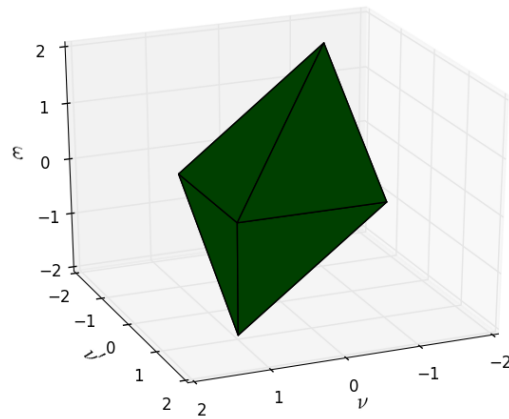

Figure 49: Box depicting the part of frequency space covered by a simple restriction of the absolute values of ν, ν', $\nu + \omega$ and $\nu' + \omega$. The scales of the axes are to be understood schematically.

figure 48. There is one more frequency substitution which only exchanges two legs: $\nu \to \nu' + \omega$, $\nu' \to \nu'$ and $\omega \to \nu - \nu'$. It distorts the form of the frequency box in a similar fashion, which is not explicitely shown. The substitution $\nu \to \nu' + \omega$, $\nu' \to \nu + \omega$ and $\omega \to -\omega$, which exchanges both pairs of external legs is also not depicted explicitely, again showing similar distortions. One can recognise the same problem in figure 32, where the main features of the $\nu = \nu'$ plane are not properly centered within the frequency box. Our restriction to some elements of the vertices only is not a controlled approximation in this case, as elements which are inherently equivalent (except for exchanging two fermions) are not treated on equal footing. Having identified this issue, we need to somehow remedy it. In fact, the idea of applying the infinity norm is a good one, we just need a physically unambigous vector to apply it to. The four-dimensional frequency-vector $(\nu, \nu' + \omega, \nu', \nu + \omega)$ (denoted in ph-notation) is invariant under the transformations discussed above. Additionally, parquet equations for constructing a vertex within such a frequency box do not "reach out". Both of the constituent vertices connected by Green's functions are simultanously either within or outside the new frequency box. The form of the resulting volume element in ph-notation is given in figure 49. When investigating the Falicov-Kimball model, implementing this type of frequency box is simplified, since all the reducible and irreducible local vertices V can be written as:

$$V(\nu, \nu', \omega) = \delta_{\omega,0}\overline{V}(\nu, \nu') - \delta_{\nu,\nu'}\underline{V}(\nu, \nu + \omega). \tag{206}$$

Any vertex built by means of iterated Bethe-Salpeter equations out of such local vertices inherits the frequency structure, even though a dependency on k-vectors arises when applying Parquet-based expansions. Then, the k-resolved vertices are of the structure

$$V(\nu, k, \nu', k', \omega, q) = \delta_{\omega,0}\overline{V}(\nu, \nu', k, k', q) - \delta_{\nu,\nu'}\underline{V}(\nu, \nu + \omega, k, k', q). \tag{207}$$

For the variables k, k' and q we have periodic boundary conditions and they can be distributed evenly in the Brillouin zone. Simple frequency boxes in the variables ν, ν' for $\overline{V}$ and $\nu, \nu + \omega$ for $\underline{V}$ can be employed. Thus, one frequency variable can be ommited. Saving the vertices in this form also allows for some simplifications in evaluating Bethe-Salpeter equations.

10.3. Updating the DMFT bath

Assuming one was able to calculate a stable dual self-energy from the parquet approach for dual fermions, the issue of updating the DMFT problem based on the results remains. For practical reasons, vertices can only be evaluated for quite coarse k-grids within a parquet-based calculation. Typically, resolutions of $8 \cdot 8$ k-points are already quite formidable. Assuming a moderate frequency box of 20 (10 positive) distinct Matsubara frequencies, a single vertex for the Falicov-Kimball model requires 209715200 complex numbers to be saved. Further assuming 16-byte complex numbers, this sums up to 3355443200 byte or ≈ 3.1 Gb of RAM required. On the other hand, using a k-mesh of $64 \cdot 64$ points for updating the hybridisation function from the dispersion relation is a non-issue and migitates problems arising from discretisation.

Specifically, a too coarse k-grid leads to a disproportionate amount of points of high symmetry being included on the grid. To be able to work with different k-meshes for different parts of the calculation, a mapping between them needs to be established. Arguably, the simplest such mapping is a partitioning of the Brillouin zone and utilisation of the closest point on the coarse grid as it was done for cluster extensions of DMFT before [45]. Assuming k-resolved corrections to the DMFT self-energy are known on a coarse grid, they need to be incorporated into the DMFT iteration scheme. This means that when updating the local Green's function from a k-sum over the dense DMFT-grid, the k-resolved self-energy corrections will also be required for vectors where it was not calculated in the first place. The simplest method of aquiring this value is depicted in figure 50, simply taking the value of the closest k-point where it was calculated.

This method of updating the local Green's function, while simple, has a few disadvantages. First, the employed self-energy is a discontinuous function in k-space. Also, typically the coarse meshes include a disproportionate amount of "special" points like Γ. Using the self-energy corrections for these points for extended areas of the Brillouin zone can lead to an inflated influence on the overall system. An additional possible issue can be seen in figure 50; If the sizes of the two grids are chosen in an unfortunate fashion, not every coarse section of the Brillouin zone contains the same amount of points of the denser mesh, arbitrarily increasing the influence of some k-points on the coarse grid. This specific problem can be circumvented by choosing the number of k points of the dense mesh per direction, N_i, as a multiple of the number of k-points on the coarse grid n_i:

$$N_i = l \cdot n_i \mid l \in \mathbb{N} \tag{208}$$

For this work, a linear interpolation scheme was employed. Figure 51 shows how the values on the dense mesh are calculated from the coarse one. The four points of the coarse grid surrounding the point of interest
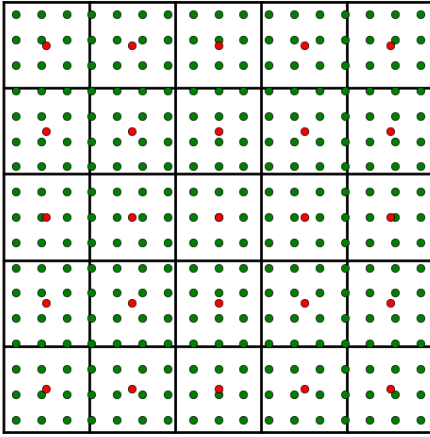
Figure 50: A simple partitioning of a Brillouin zone into a coarse mesh (red points) used for the parquet and BSE and a dense mesh (green points) used for impurity updates. To map from the coarse to the dense mesh, the variable of interest is simply evaluated at the nearest red point. The areas associated with each red point are separated by black lines.
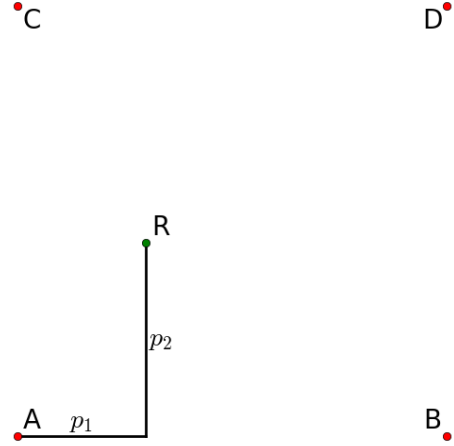
Figure 51: Schematic representation of a mapping from a coarse to a dense mesh by linear interpolation. The value of the variable at the green point R is determinded from the values of the four surrounding points of the coarse grid A, B, C and D.

on the dense mesh are interpolated as follows: p_1 gives the ratio of the distance between the green point R in k_x-direction from A and the step size of the coarse grid. p_2 is defined similarily for the k_y-direction. the value of the self-energy, R at the point of interest is then calculated as

$$R = (1 - p_1)(1 - p_2)A + p_1(1 - p_2)B + (1 - p_1)p_2C + p_1p_2D. \tag{209}$$

This method was chosen because it is guaranteed to generate a continous self-energy with respect to the k-vector within the Brillouin zone. It does come with some perils however. One can easily see that a k-point with an extremal value for Σ will generate a sharply pointed peak in the interpolated function, while the actual physical self-energy is expected to behave paraboloidically around an extremal value.

11. Dynamical mean field theory on the real axis

Many of the analytical results derived so far are based on a converged DMFT calculation for the Falicov-Kimball model. For other models this would typically restrict the applicability to the imaginary frequency axis as DMFT calculations on the real frequency axis encounter difficulties, although they are not unheard of [72], especially for the Falicov-Kimball model [73]. Fortunately, the Falicov-Kimball model does not require a local DMFT solver and can therefore be treated on the real axis without any complications. This means that many of the results obtained so far can be straightforwardly applied on the real frequency axis without having to burden oneself with methods for analytic continuation of functions like the notorious Padé-fit.

In this section, real-frequency DMFT results will be given and discussed at half filling as well as away from it. These results will act as the basis for and be followed up by application of different vertex-based expansions of DMFT. While applying such methods to other problems would be computationally prohibitively expensive for the Hubbard model on the real frequency axis, the reduced structure of the problem for the Falicov-Kimball model and the availability of analytical expressions for certain correction terms makes such an endeavour feasible for the Falicov-Kimball model.

11.1. DMFT iteration scheme

To take maximum advantage of the availability of analytical expressions for the Falicov-Kimball model, as much of the actual calculation as possible has to be performed on the Matsubara axis, where the limited number of Matsubara frequencies which have to be taken into account compared to a dense real-frequency mesh reduce the computational time immensely. In practice, this means that it is advantageous to perform a DMFT calculation on the Matsubara axis first, converge the occupation of f-electrons, and then calculate the real-frequency data for the c-electrons. Otherwise, the standard DMFT iteration procedure applies, albeit with an algebraic expression instead of a local solver.

11.2. Numerical results for half-filling

At half-filling ($\mu = U/2$), the Falicov-Kimball DMFT result is temperature-independent. For a fixed particle-hole symmetric non-interacting density of states, the local behaviour of the c-electrons depends on the interaction strength only. Also, the real and imaginary parts of the calculated functions (Σ, Δ, G) have to be even or odd functions due to particle-hole symmetry. First, data for the square lattice will be presented, showing the formation of a gap in the spectrum and the divergence of the self-energy. The hopping integral t is set to a value 0.25, fixing the bandwidth to 2. DMFT is able to describe the transition to an insulating state, tough it is a quantum-critical phase transition with respect to variation of the interaction parameter U, since the result is temperature-independent. A short recapitulation of what DMFT can and cannot describe is in order here. It performs well at capturing purely local correlations between particles, but fails at describing non-local correlations. The metal-insulator transition seen in the spectral function is a consequence of purely local repulsion. The probability of states with energies around 0 existing decreases as U is increased for random configurations of f-electrons. For an example of gap formation at arbitrarily small values of U, for an admittedly very specific configuration of f-electrons, see appendix G. DMFT does not describe the correlations between f-electrons on different sites at all, in a sense, it produces an effective model for all the different possible configurations of them on a lattice. In figure 52, the formation of the gap in the imaginary part of the local Green's function can be witnessed as U is increased. In the high-U regime, two Hubbard-like bands are observed, each one reminiscent of the density of states of the non-interacting problem and with a relative shift of U.
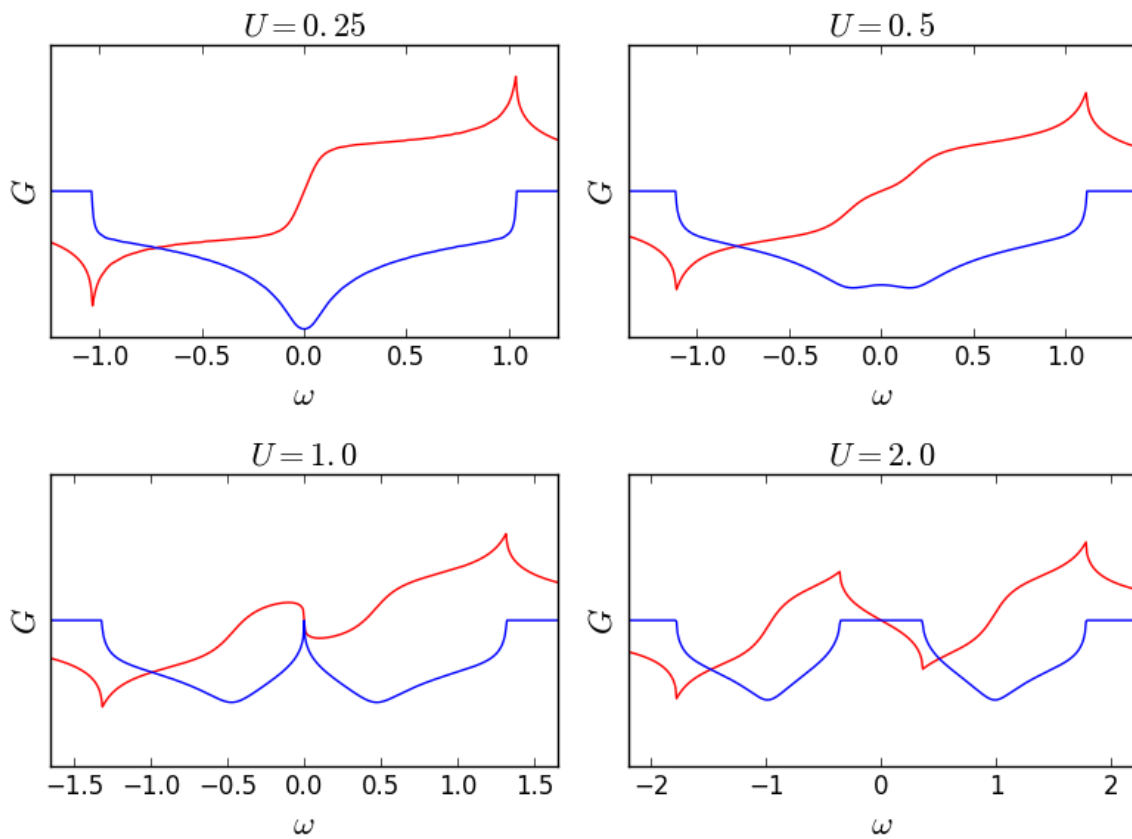
Figure 52: Real (red) and imaginary (blue) part of the local Green's function G_{loc} for the Falicov-Kimball model on the real frequency axis for different values of U.
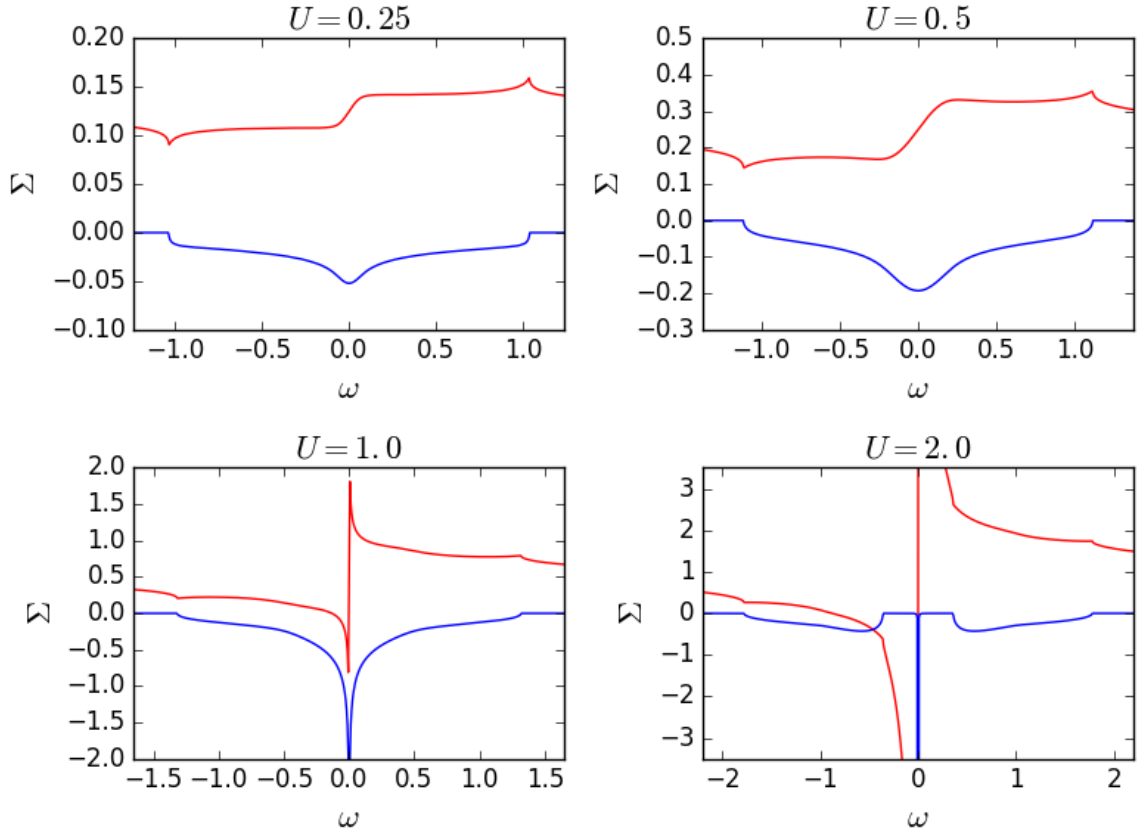
Figure 53: Real (red) and imaginary (blue) part of the local self-energy Σ on the real frequency axis for different values of U.

11.2.1. Stability of the particle-hole symmetric case

It is known that the f-electron occupation within DMFT is stationary at half-filling. Anyhow, the important question of stability remains. In [29], the quadratic nature of the action for c-electrons for the two DMFT-sub-problems is pointed out, allowing for a direct calculation of the partition functions. Thus, the f-electron occupation can be calculated by comparing the partition functions of the f-occupied and non-occupied impurities. From this, we can investigate how the system reacts to small perturbations of the f-occupation p_1. To do so, DMFT calculations were performed at different starting values of p_1 for systems otherwise fullfilling the requirements of half filling ($\mu = U/2$) at different temperatures and different U values. First, the c-part of the DMFT was converged for the original value of p_1 and then p_1 was updated. The results are given in figure 54. It should be noted, that DMFT as a mean field theory will overestimate the ordering temperature, especially for ferromagnetic order.
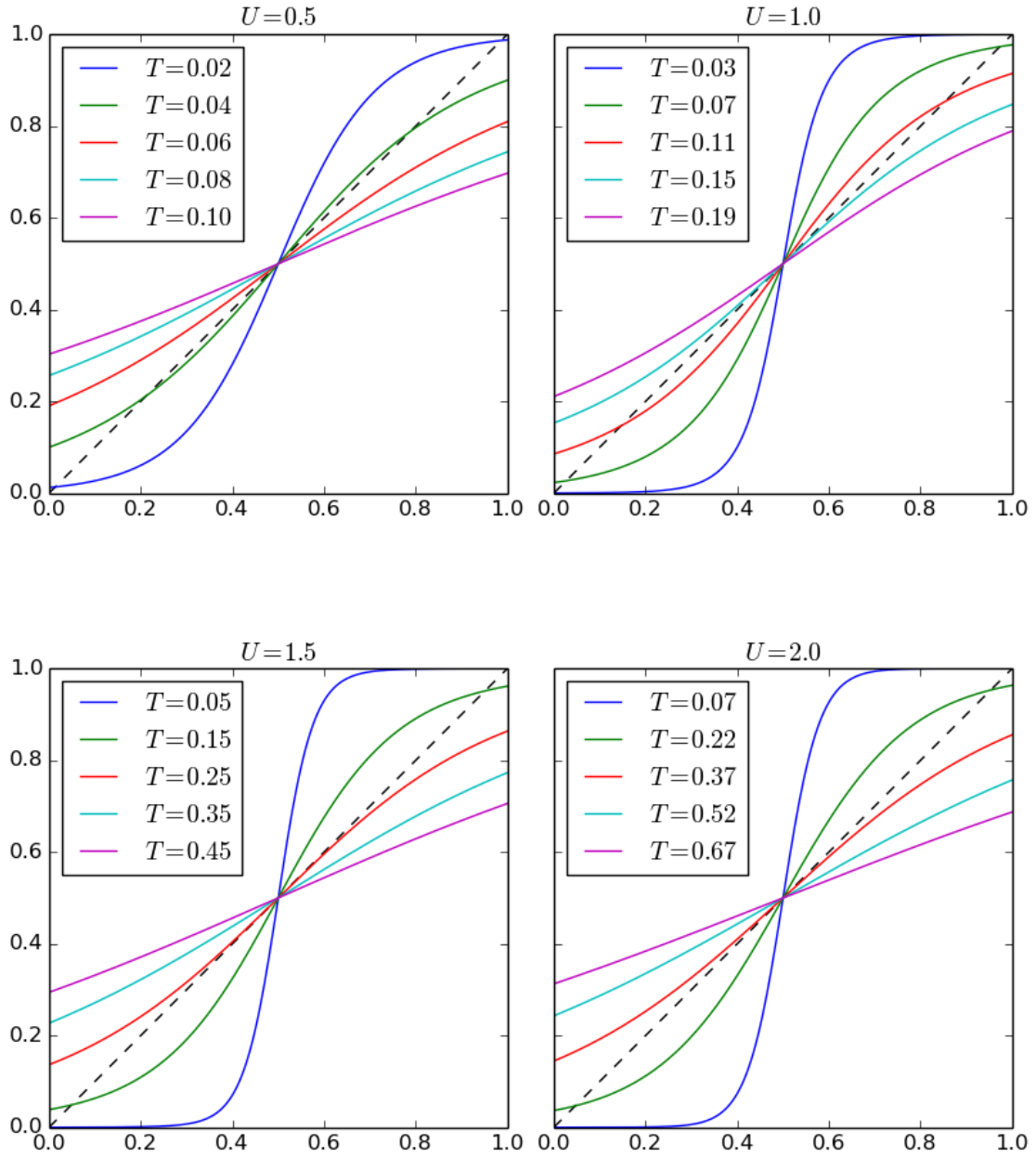
Figure 54: Updated value of p_1 as a function of the original value for different values of U and temperatures T. To identify fixed points, the main diagonal is plotted as a dashed line. Intersections of the curves with the dashed line give fixed points, but only intersections which are locally contractions (absolute value of the derivative ≤ 1, the diagonal is steeper than the function) are stable.

11.2.2. Vertex quantities

Unlike the vertices on the Matsubara axis, the corresponding real-frequency objects are not purely real in the half-filled case. Anyhow, the analytic continuation of the vertices is straightforward as they are expressed in closed form in terms of one-particle quantities, for which the continuation is already known. The most basic building block is the function a appearing as a factor of the local full vertex. Numeric data for a is given in figure 55. The factor $\sqrt{\beta}$ was omitted to make the result temperature-independent.
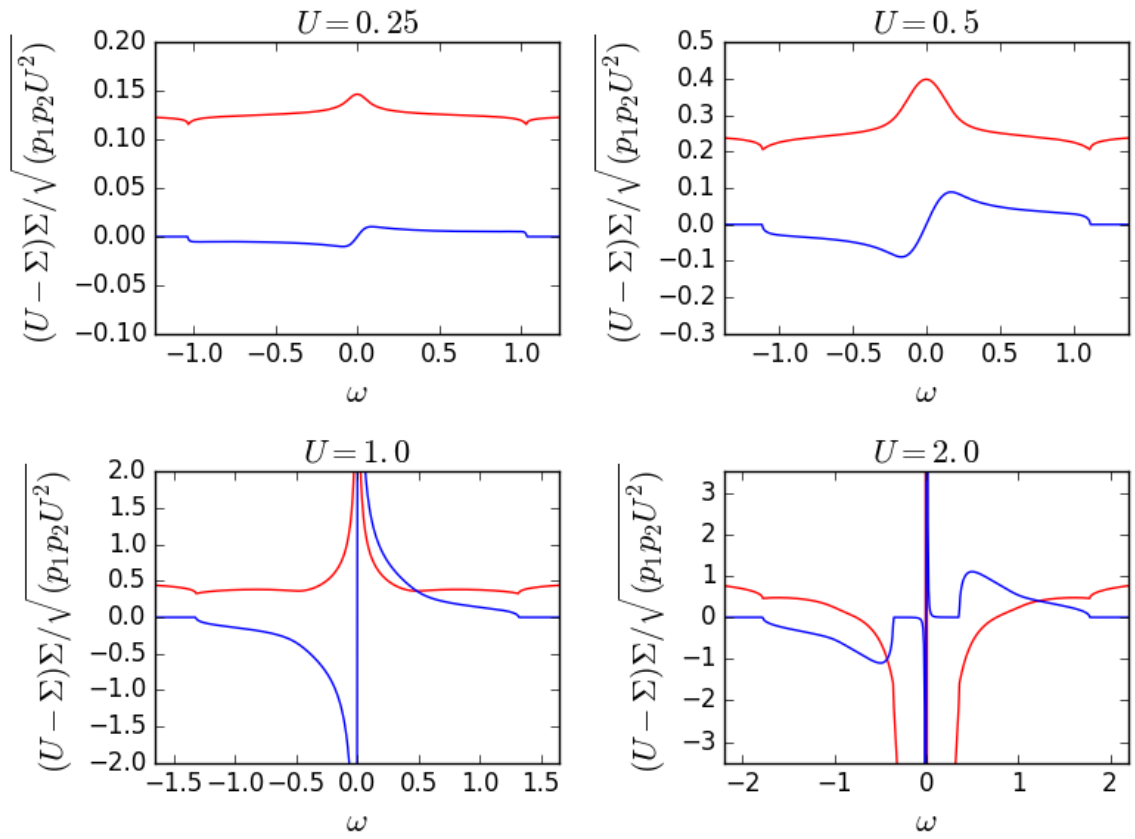
Figure 55: Real (red) and imaginary (blue) part of $(U - \Sigma)\Sigma/\sqrt{(p_1 p_2 U^2)}$ on the real frequency axis for different values of U on a square lattice.
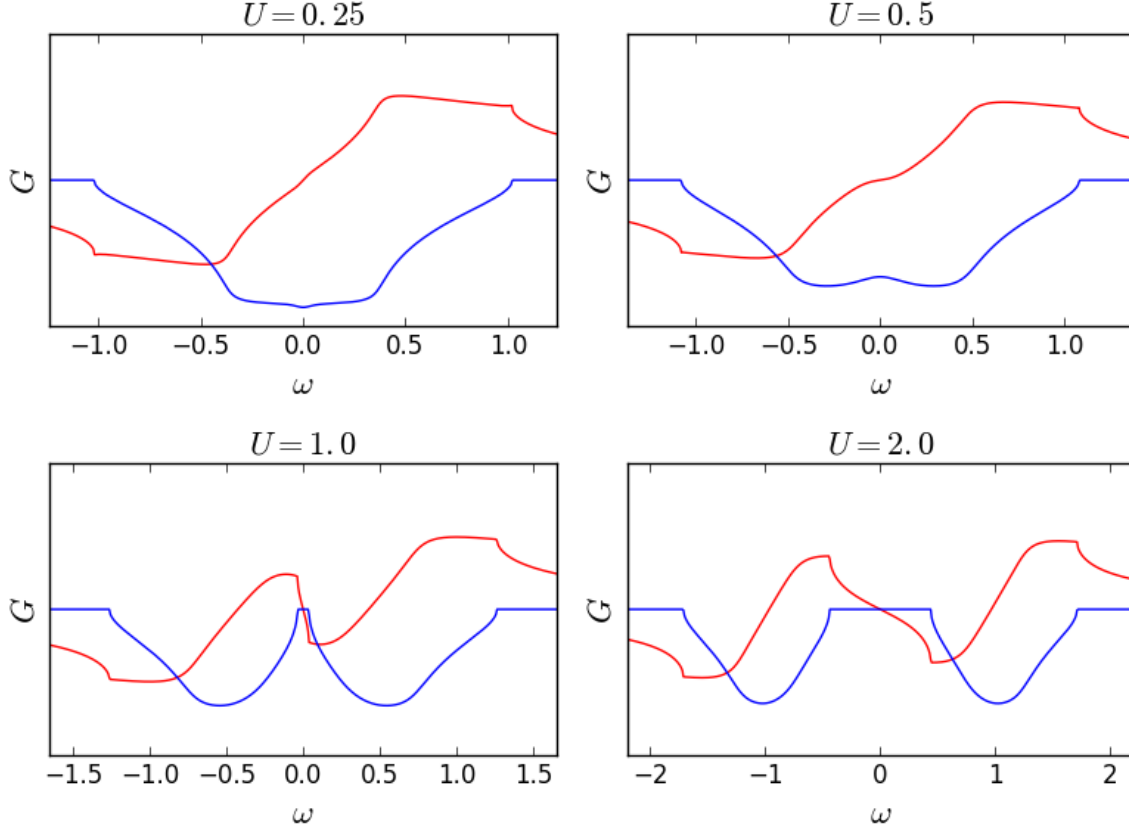
Figure 56: Real (red) and imaginary (blue) part of the local Green's function G_{loc} on the real frequency axis for different values of U on a cubic lattice.

11.2.3. Results on a cubic lattice

While one is often interested in the two-dimensional case when investigating interacting lattice systems like the Hubbard model or the FKM, with the interest raised by physical systems such as cuprates which are effectively two-dimensional and practical considerations about the available computational power, a short investigation of the three-dimensional case is in order here. To make the comparison with the quadratic case simpler, the hopping amplitude was fixed to a value of $t = 1/6$. This means the bandwidth of the non-interacting case is held constant, which corresponds to a scaling of $t \sim 1/Z$ with the number of nearest neighbours Z[1]. The critical value of U where a band separation occurs is thus set to $\sqrt{(2/3)}$. The same plots as for the two-dimensional case are given. Qualitatively, there is not a lot of difference between the two cases, with the 3D-results having slightly less pronounced features since the underlying non-interacting density of states does not show a peak in the center. On the other hand, the divergence of Σ at sufficiently large values for U does not vanish with the more regular density of states.

11.3. Results away from half-filling

Two things have to be realised when leaving the symmetric half-filled case, the first one being that for any set of parameters, a converged f-occupation p_1 exists. For this fixed occupation, the c-electrons "do not know" about the on-site f-energy. Also, for a given f-occupation and converged c-electron DMFT calculation, ϵ_f can be adjusted so that p_1 becomes stationary. Thus, the calculation can be performed by choosing occupations first and then adjusting the parameters until they fit the desired occupations. This procedure is bound to generate a set of parameters that are stationary, but does not guarantee a stable solution. To provide an idea of the behaviour of the local systems, plots for the spectral function on the real axis are given for different values of U and p_1 on a square lattice. Also given is the integral of the spectral functions in question.

When p_1 comes close to either 0 or 1 for smaller values of U, problems with discretisation arise. If p_1

---

[1] Note that a scaling required to obtain a non-trivial limit when letting $Z \to \infty$ is $t \sim 1/\sqrt{Z}$
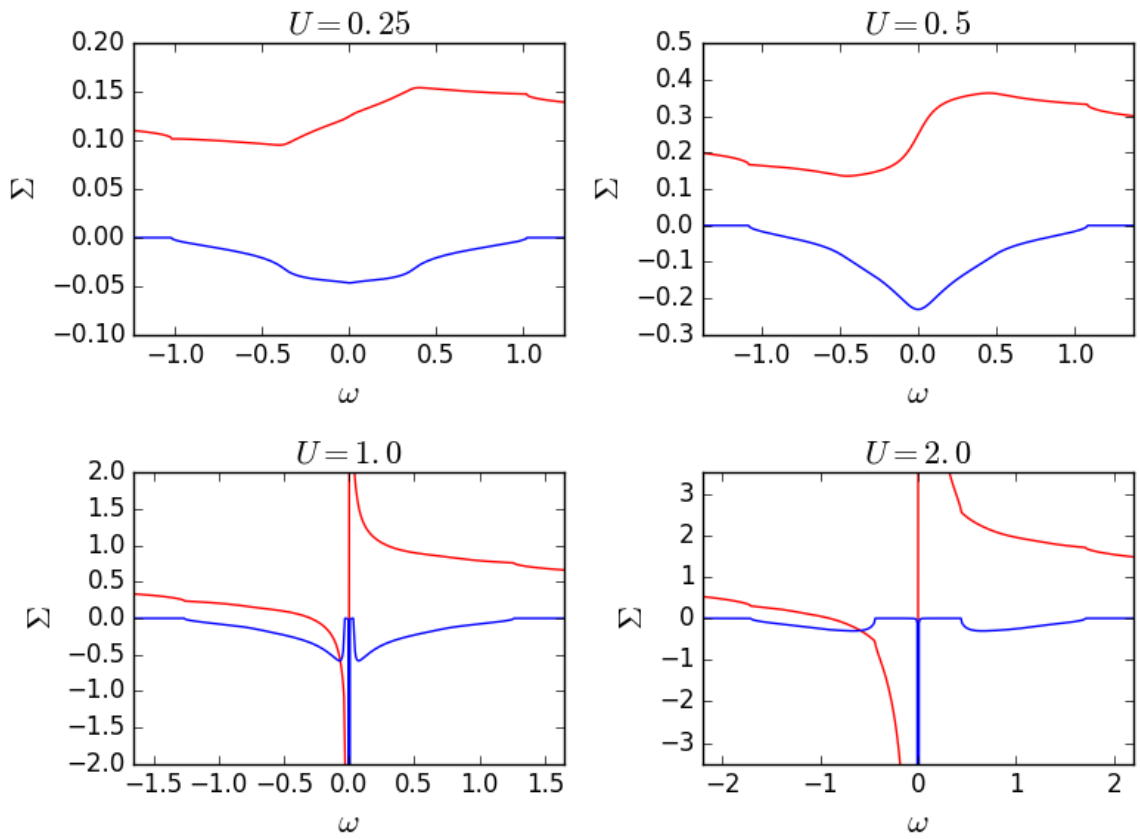
Figure 57: Real (red) and imaginary (blue) part of the local self Energy Σ on the real frequency axis for different values of U on a cubic lattice.
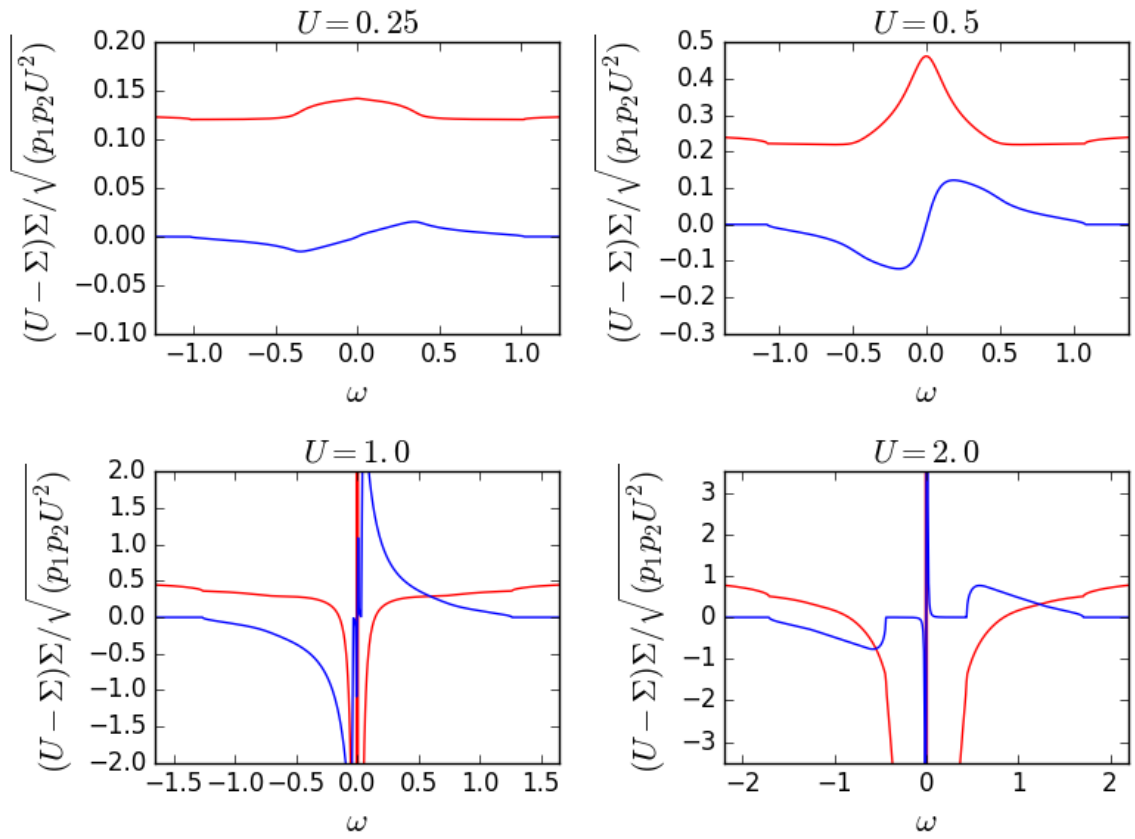
Figure 58: Real (red) and imaginary (blue) part of $(U - \Sigma)\Sigma/\sqrt{(p_1 p_2 U^2)}$ on the real frequency axis for different values of U on a cubic lattice.
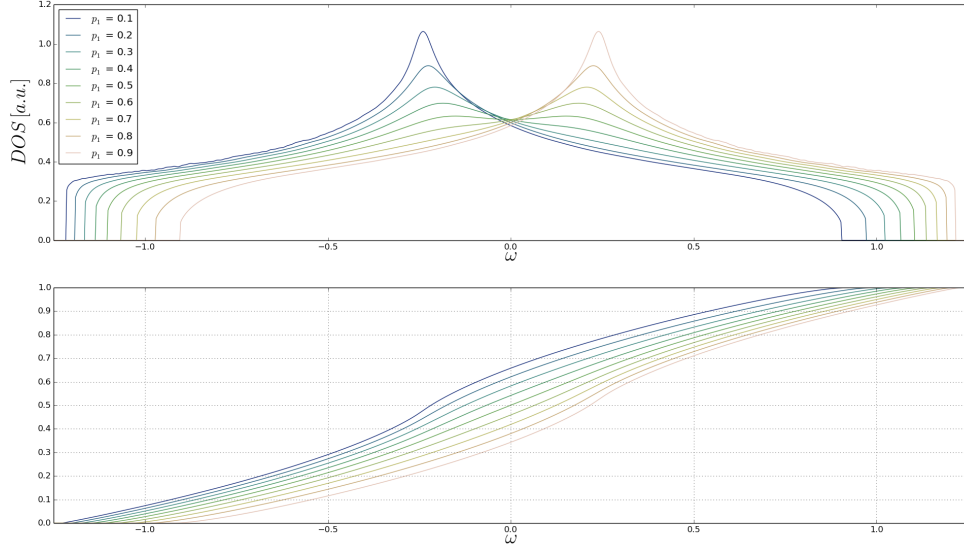
Figure 60: Spectral function and integral of the spectral function of the Falicov-Kimball model on a square lattice for different values of p_1 at $U = 0.5$ and $\mu = U/2$. Due to problems with the discretisation, noise became a problem for the spectral functions with p_1 close to 0 or 1. Thus, a low pass filter was applied to the spectral functions.

approaches these values, the system becomes more and more similar to a non-interacting system and the imaginary part of Σ becomes small, so the features of the utilised k-mesh become apparent. For the corresponding plots provided here, a simple low-pass filter was applied to the spectral function to remove the noise.
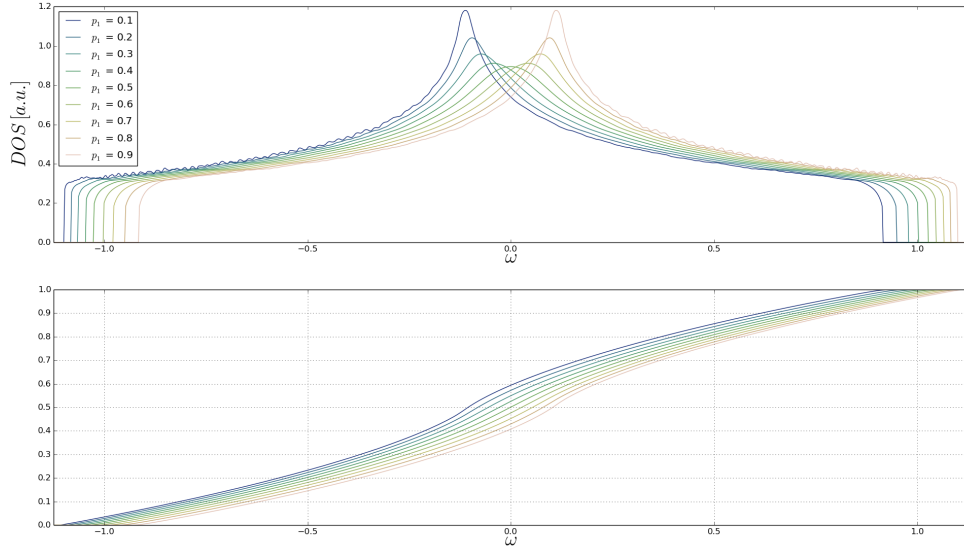

Figure 59: Spectral function and integral of the spectral function of the Falicov-Kimball model on a square lattice for different values of p_1 at $U = 0.25$ and $\mu = U/2$. Due to problems with the k-point discretisation, noise became a problem for the spectral functions with p_1 close to 0 or 1. Thus, a low pass filter was applied to the spectral functions.
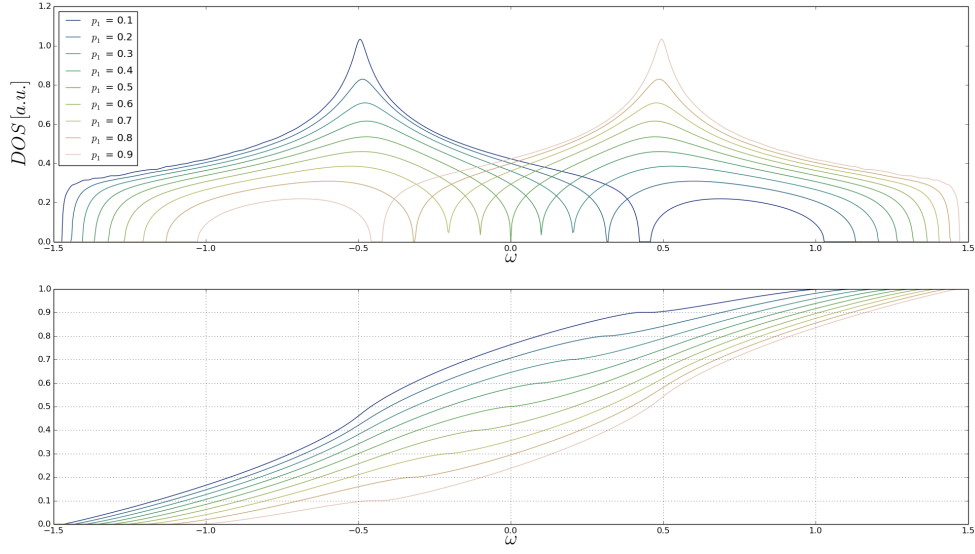
Figure 61: Spectral function and integral of the spectral function of the Falicov-Kimball model on a square lattice for different values of p_1 at $U = 1$ and $\mu = U/2$.
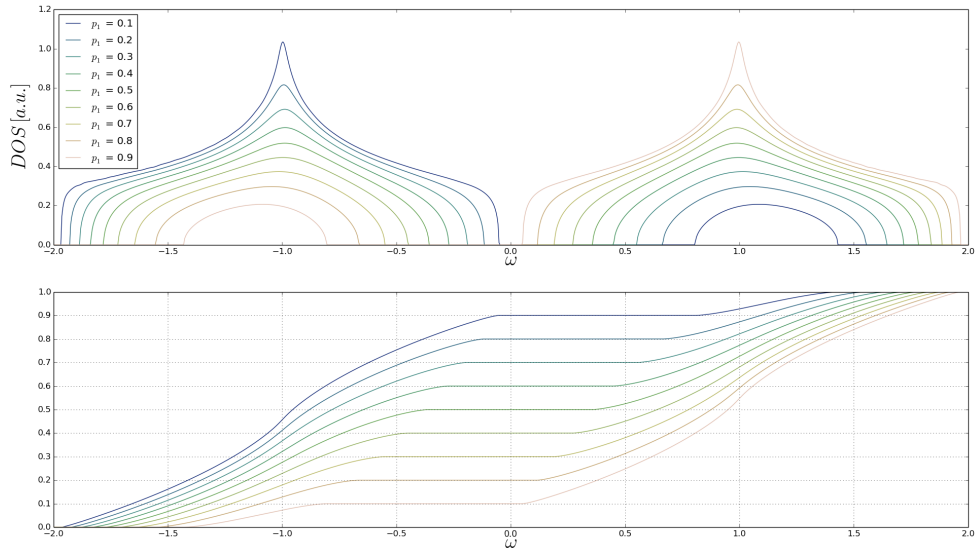

Figure 62: Spectral function and integral of the spectral function of the Falicov-Kimball model on a square lattice for different values of p_1 at $U = 2$ and $\mu = U/2$. Note how the gap in the spectral function leads to the appeareance of a plateau in the integrated intgral.

11.4. Physical observables on the real axis

Due to closed form expressions for many physical observables being available for the Falicov-Kimball model, they can be easily continued analytically from the Matsubara to the real frequency axis. This offers two interesting opportunities, the obvious one being the calculation of physical observable on the real frequency axis, extracting easily interpretable results. On the other hand, it is also possible to use the real frequency data as a benchmark to estimate the quality of analytic continuations from purely numerical solution methods for interacting quantum lattice systems, by applying them to the Falicov-Kimball model and performing an analytical continuation of the obtained data, then comparing the results.

Typical candidates for functions where it would be beneficial to know their value on the real frequency axis include susceptibilities. The scheme for analytically continuing them will be explained for the purely local DMFT case. The connected contribution to the purely local DMFT charge-charge correlator on the Matsubara axis is given by

$$\chi_{\rho,\rho}(\omega) = \beta^{-3} \sum_{\nu,\nu'} G(\nu)G(\nu'+\omega)F^{\nu,\nu',\omega}G(\nu+\omega)G(\nu'). \tag{210}$$

Which is known analytically to be

$$\chi_{\rho,\rho}(\omega) = \delta_{\omega,0}\beta^{-2}\left(\sum_\nu G^2(\nu)a(\nu)\right)^2 - \beta^{-2}\sum_\nu G^2(\nu)a(\nu)G^2(\nu+\omega)a(\nu+\omega). \tag{211}$$

Apart from the $\delta_{\omega,0}$ contribution, which already gives a term for the real frequency axis, the continuation for the second sum needs to be figured out. Luckily, $a(\nu)$ can be expressed in terms of Σ and nothing is to stop us from calculating DMFT values for G and Σ for a mixed frequency, having a real as well as an imaginary part. Normally, extreme caution with respect to the limits taken is necessary for calculating real-frequency data, especially concerning small imaginary parts of frequencies and their signs. Fortunately, this becomes a non-issue due to the Matsubara-frequencies involved. The scheme for calculating the value of

$$\sum_\nu G^2(\nu)a(\nu)G^2(\nu+\omega)a(\nu+\omega) = \sum_\nu \mathcal{F}(\nu)\mathcal{F}(\nu+\omega) \tag{212}$$

numerically for real frequencies ω starts from converged DMFT-values for G and a for a sufficient number of Matsubara frequencies. For any real value of ω, the sum in equation (212) is absolutely convergent. For any Matsubara frequency ν, $-\nu$ is also included in the summation. Since the sum is absolutely convergent, terms can be liberally rearranged, so we combine the contributions from $\pm\nu$.

$$\mathcal{F}(\nu)\mathcal{F}(\nu+\omega) = (\mathcal{F}(-\nu)\mathcal{F}(-\nu+\omega))^\dagger \tag{213}$$

Thus χ is real since the imaginary contributions exactly cancel. This leaves

$$\sum_\nu \mathcal{F}(\nu)\mathcal{F}(\nu+\omega) = 2\sum_{\nu_+} \mathcal{R}\left(\mathcal{F}(\nu)\mathcal{F}(\nu+\omega)\right), \tag{214}$$

with $\mathcal{R}$ denoting the real part and ν_+ the positive (imaginary) Matsubara frequencies. The real frequencies for which the susceptibility is to be calculated are selected and an array is prepared to hold it. Typically, one would select positive as well as negative frequencies in equal numbers. To speed up the convergence and thus the calculation, the known $G(\nu)$ and $a(\nu)$ for each Matsubara frequency are used as initialisation values for $G(\nu+\omega)$ and $a(\nu+\omega)$ and $\omega=0$, then, ω is changed by small increments δ, always using the converged value for $G(\nu+\omega_1)$ as initialisation for calculating $G(\nu+\omega_1+\delta)$. Obviously, a can be calculated from G, so all summands can be expressed and the summation performed. This approach works because different frequencies decouple for the FKM within DMFT.

In a cooperation with Patrik Gunacker, the quality of analytic continuations from the Matsubara to the real frequency axis was investigated. The original data was calculated by continuous-time quatum-Monte-Carlo (CTQMC), specifically using the W2Dynamics code [43]. CTQMC data is always noisy, which increases the difficulty of achieving a reasonable continuation. Using the expressions described above, the self-energy on the real axis was calculated and used as a reference for a desireable result. The results are summarised in figures 63 and 64. The methods of continuation that were considered were a Padé fit [74] and a MaxEnt approach [75].
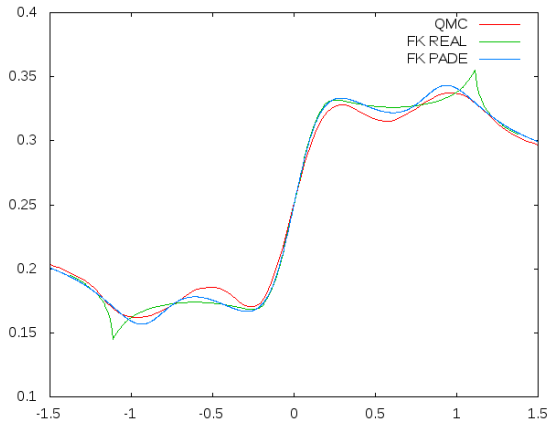
Figure 63: Real part of the DMFT-self energy on the real frequency axis as extracted from a maximum entropy approach based on the CTQMC data (QMC), from a Padé-fit of the exact Matsubara-frequency data (FK PADE) and calculated directly (FK REAL)
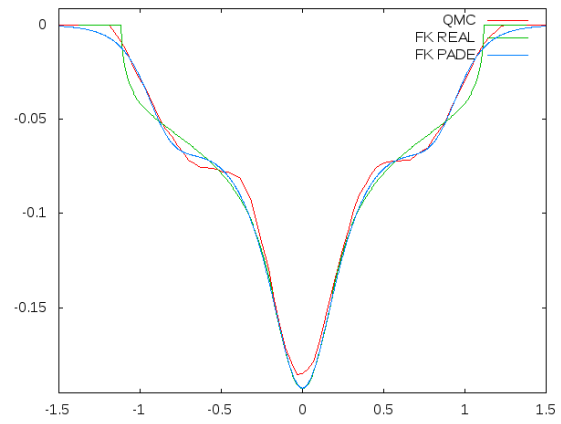
Figure 64: Imaginary part of the DMFT-self energy on the real frequency axis as extracted from a maximum entropy approach based on the CTQMC data (QMC), from a Padé-fit of the exact Matsubara-frequency data (FK PADE) and calculated directly (FK REAL)
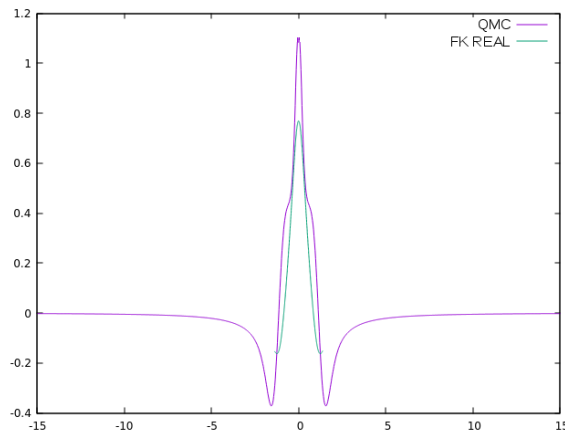

Figure 65: Density-density correlation function as extracted from a maximum entropy approach based on CTQMC data (QMC) and calculated directly (FK REAL).

The advantages of the calculation actually conducted on the real frequency axis are obvious. Sharp features such as edges of bands cannot be reproduced by fited functions. This is a consequence of our restriction to relatively few basis functions. Also, for the density-density correlation function, the fit fails to describe the features from the direct calculation.

12. Effect of the outer self-consistency within the dual fermion approach for the Hubbard model

In principle, the choice of hybridisation function that one employs for deriving the dual fermion approach is completely arbitrary. The DMFT hybridisation function makes the bare dual propagator completely non-local, but this property is lost upon including dual self-energies. The question about the best hybridisation function remains. Preferably, it should encode as much of the physics of the underlying system as possible. In this section, the influence of updating the underlying impurity system with results from dual fermion calculations is investigated.

12.1. Choice of outer self-consistency condition

There are two prominent outer self-consistency conditions for the dual fermion approach [36]. The first one is based on the non-locality of the dual fermions and demands that the hybridisation function be chosen in a way that makes the full dual propagator, including dual self-energy diagrams, non-local [23, 76]. Algebraically this condition is given by

$$\sum_{\mathbf{k}} \left(\widetilde{G}_0^{-1} - \widetilde{\Sigma} \right)^{-1} = 0. \tag{215}$$

Here, $\mathbf{k}$ denotes the inverse lattice vectors. Another possible outer self-consistency condition, more in the spirit of DMFT, is to require consistency between the local Green's function from the impurity model and the one calculated as the sum of of all k-Green's functions including corrections to the self-energy from DF. This can be written as

$$\sum_{\mathbf{k}} \left[\left(G_{\mathbf{k}}^{-1} - \Delta\Sigma_{\mathbf{k}} \right)^{-1} - G^{(1)} \right] = 0. \tag{216}$$

Here, the correction to the ($\mathbf{k}$-resolved) self-energy was denoted as $\Delta\Sigma_k$ and it was intentionally not specified how to extract this quantity (see section 5.2.1 for a discussion). One can see that both conditions become equivalent, not just to each other, but also to the DMFT condition, in the limit of weak correlation, where $\widetilde{\Sigma} \to 0$ and therefore $\Delta\Sigma_k \to 0$. In the following, the second condition will be employed, while we find that the first only causes minimal changes to the underlying impurity model. This condition has not been investigated closely, but there are two recent studies [77, 78] employing it.

12.2. Introduction of the employed methodology

The half-filled Hubbard model on a square lattice with nearest neighbour hopping t was investigated. The half-bandwidth was used as unit of energy: $4t \equiv 1$. The results presented later in this section were obtained based on CT-QMC [33, 43] one- and two-particle quantities which were provided by Patrik Gunacker. For the dual-fermion calculation, a self-consistent ph-ladder approximation was employed. The dual expansion was truncated on the two-particle vertex level[1]. The ladder approach reduces the strain on computational memory, allowing for a reasonable $64 \cdot 64$ point k-grid to be treated easily. The dual self-energy was calculated in accordance with the standard expression [23, 31]. The dual self energy was not modified to account for real fermion reducibility (c.f. 5.2.1). That is the dual self-energy was directly employed as a self-energy correction, without applying a mapping.

12.3. Results

12.3.1. $U = 1, \beta = 8$

For such small interaction values and high temperatures, only small corrections to the converged DMFT solution are expected from non-local correlation effects. Indeed, the dual self-energies, as well as the resulting corrections to the k-resolved self-energies are quite small compared to DMFT as can be seen in figure 67. If the self-energy corrections are included in calculating the updated local Green's function, there is only a minor change relative to the DMFT solution as can be seen in figure 68. While the resulting change in the hybridisation function in figure 69 is more noticeable, an outer self-consistency update was deemed unnecessary and the investigation shifted towards lower temperatures and higher interaction values.

---

[1] The calculations were done with the same program also used for the three-particle calculations in [31]. However, multiple calculations and updates of three-particle vertices on a huge frequency mesh (because the asymptotics need to be extracted) exceded the computational ressources available, making the truncation necessary.
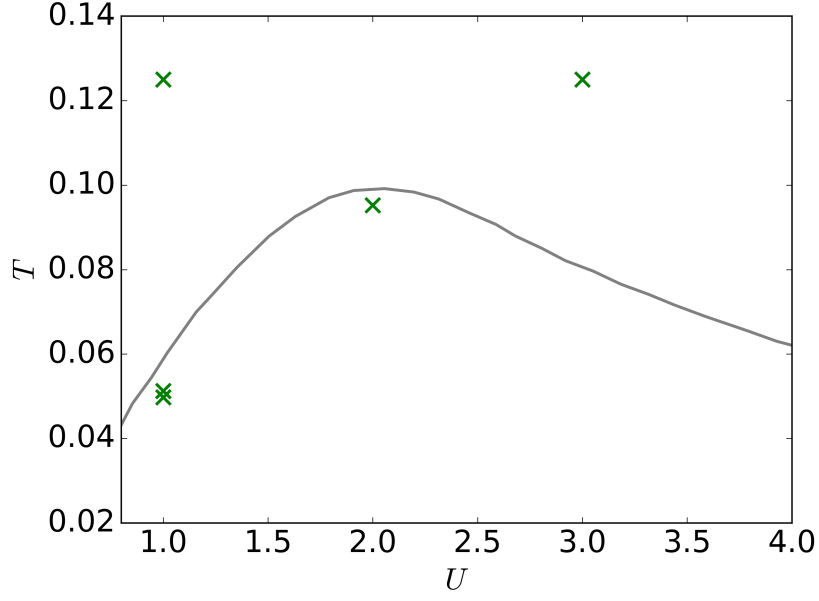
Figure 66: Overview of the investigated points in the phase diagram, including data for the DMFT Néel temperature from [79].
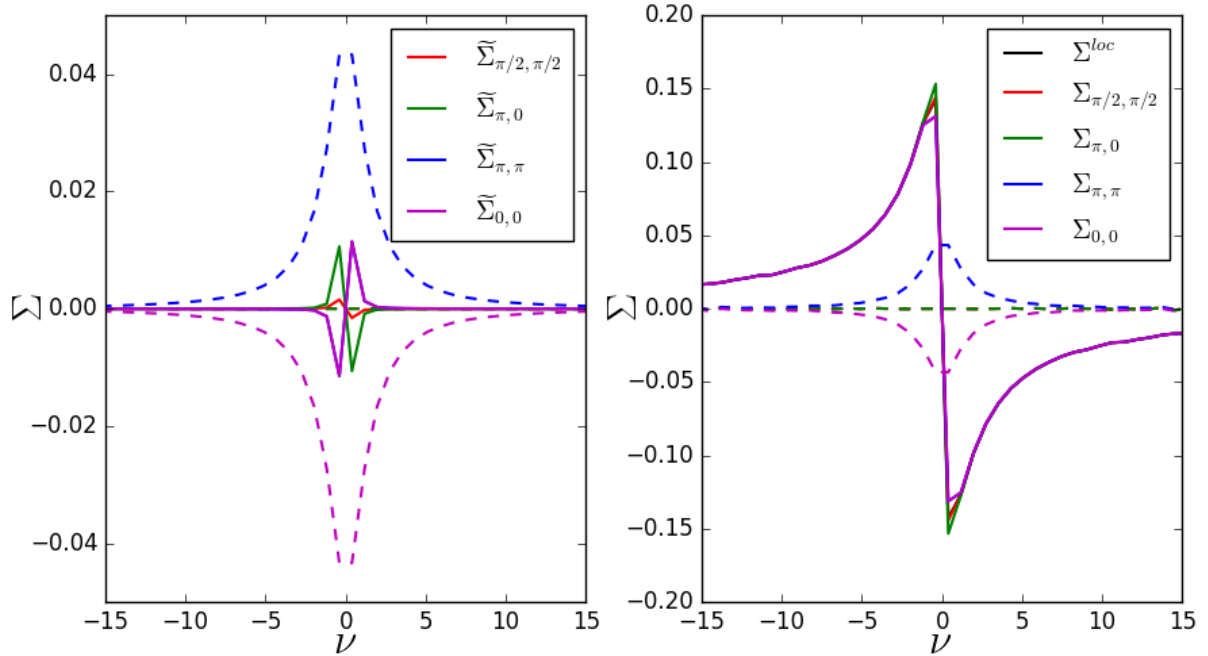

Figure 67: Dual self-energies (left) and physical self-energies (right) for the Hubbard model as a function of Matsubara frequency for different k-points for $U = 1$ and $\beta = 8$. Real parts are depicted as dashed lines and imaginary parts as full lines.
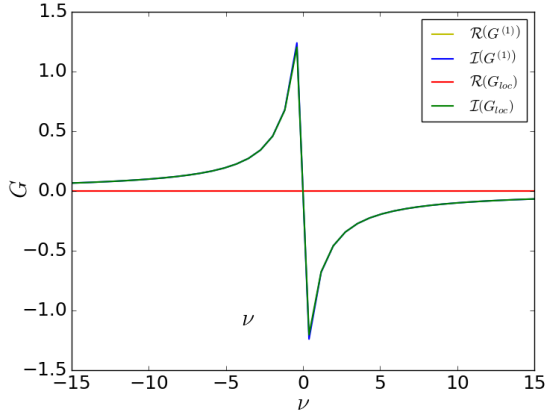
Figure 68: Local DMFT Green's function $G^{(1)}$ and local Green's function calculated from the sum of all lattice Green's functions, including DF self-energy corrections G_{loc} for $U = 1$ and $\beta = 8$.
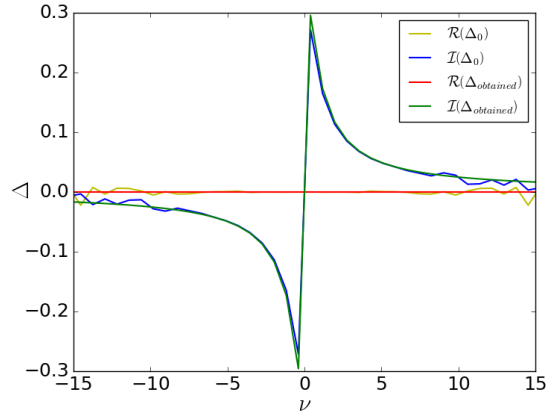
Figure 69: DMFT hybridisation function Δ_0 and hybridisation function obtained when including self-energy corrections from DF $\Delta_{obtained}$ for $U = 1$ and $\beta = 8$.

12.3.2. $U = 1, \beta = 19.5$

To see the effect of the outer self-consistency, the temperature was lowered, approaching the divergence of the antiferromagnetic susceptibility within DMFT [79]. Consequently, the self-energy corrections from the dual fermion approach also become larger as depicted in figure 70. We can see that the local Green's function is slightly suppressed by the outer self-consistency condition in figure 71. This means that spectral weight is removed from the Fermi edge by the non-local correlation effects. Note that the hybridisation is enhanced at low Matsubara frequencies as seen in figure 72[1] Since the change of hybridisation is sizeable, an outer self-consistency iteration was pursued for this data point. The resulting self-energies are documented in Figure 73. One can see that the self-energy corrections become smaller in comparison to fig. 70 (note the absolute scales). This is a consequence of the reduced weight for states near the Fermi-edge[2]. The resulting Green's functions after the outer self-consistency iteration are very much consistent for the impurity and when calculated as the sum of lattice Green's functions as can be seen in Figure 74, leading to a very small change in the hybridisation function (See Figure 75). Therefore, one outer self-consistency step was deemed sufficient for this parameter set.

12.3.3. $U = 1, \beta = 20.1$

This parameter set is interesting, as we find that the inner self-consistency loop of the dual fermion calculation would not converge when using DMFT-impurity quantities as input. When investigating the behaviour more closely, an oscillation between two configurations was found, with smaller and larger dual self-energies alternating. This is typical for the half-filled Hubbard model and can sometimes be remedied by introducing a mixing factor for the self-energy. However, we find that the two configurations slowly drift apart as the number of iterations is increased[3]. Nonetheless, it was possible to extract a set of dual self-energies with the qualitative behaviour observed at higher temperatures. With these, the hybridisation function was updated and a dual fermion calculation based on the new impurity was performed, which now did converge. The resulting self-energies are plotted in figure 76 and are quite similar to the ones obtained at the slightly higher temperature for $\beta = 19.5$ in fig. 73. The local Green's function (figure 77) and hybridisation function (figure 78) are also found to change very little. This implies that the DMFT impurity problem is not necessarily the best starting point for pursuing this type of dual fermion calculation. Additionally, since the breakdown of ph-ladder dual fermion calculations is associated with a divergence of the ph-ladder and antiferromagnetic susceptibility, shifting it to lower temperatures also postpones the antiferromagnetic transition which should

---

[1] For discrete bath sites this means the addition of bath states at low energies to the impurity problem with respect to DMFT.

[2] Stronger hybridisation and weaker correlation effects can be interpreted in a consistent fashion. DMFT seems to overestimate correlations between electrons, but they become weaker once more possibilities to evade each other (via low-energy non-interacting bath states) are offered to the electrons.

[3] In this situation, using a mixing factor can be dangerous, as it can stabilise a fixed point which would be unstable otherwise.
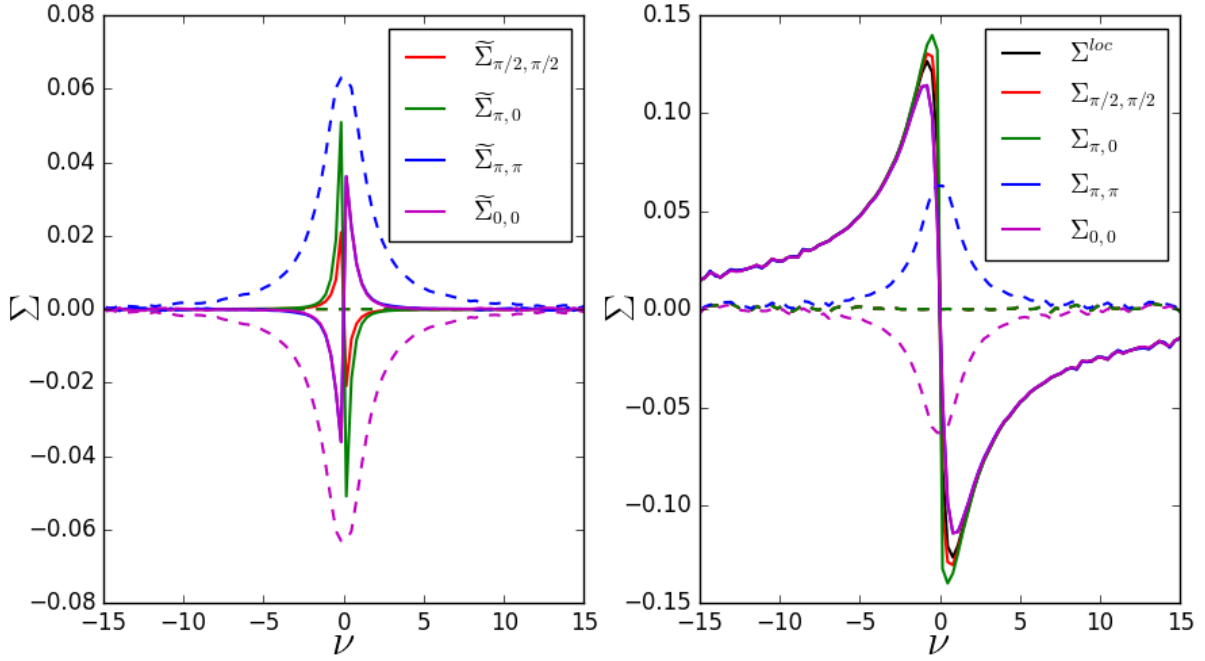
Figure 70: Same as fig. 67 but for $U = 1$ and $\beta = 19.5$.
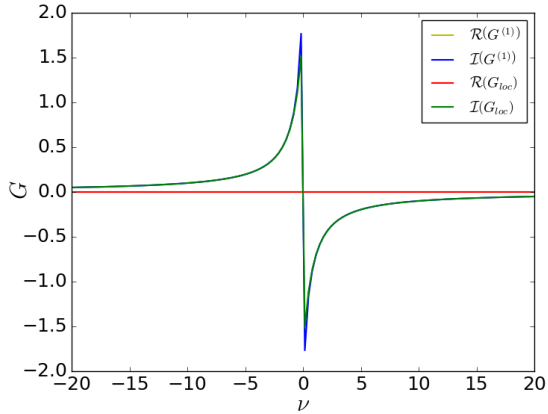

Figure 71: Local DMFT Green's function $G^{(1)}$ and local Green's function calculated from the sum of all lattice Green's functions, including DF self-energy corrections G_{loc} for $U = 1$ and $\beta = 19.5$.

Figure 72: DMFT hybridisation function Δ_0 and hybridisation function obtained when including self-energy corrections $\Delta_{obtained}$ for $U = 1$ and $\beta = 19.5$.

Figure 73: Same as fig. 67 but for $U = 1$ and $\beta = 19.5$ after the first outer self-consistency iteration.

Figure 74: Local impurity Green's function $G^{(1)}$ and local Green's function calculated from the sum of all lattice Green's functions, including DF self-energy corrections G_{loc} for $U = 1$ and $\beta = 19.5$ after the first outer self-consistency iteration.
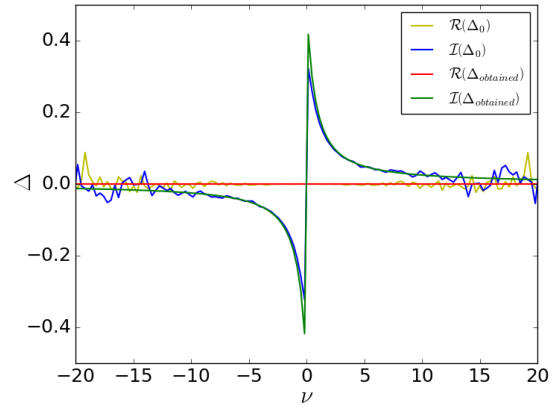
Figure 75: Impurity hybridisation function Δ_0 and hybridisation function obtained when including self-energy corrections $\Delta_{obtained}$ for $U = 1$ and $\beta = 19.5$ after the first outer self-consistency iteration.
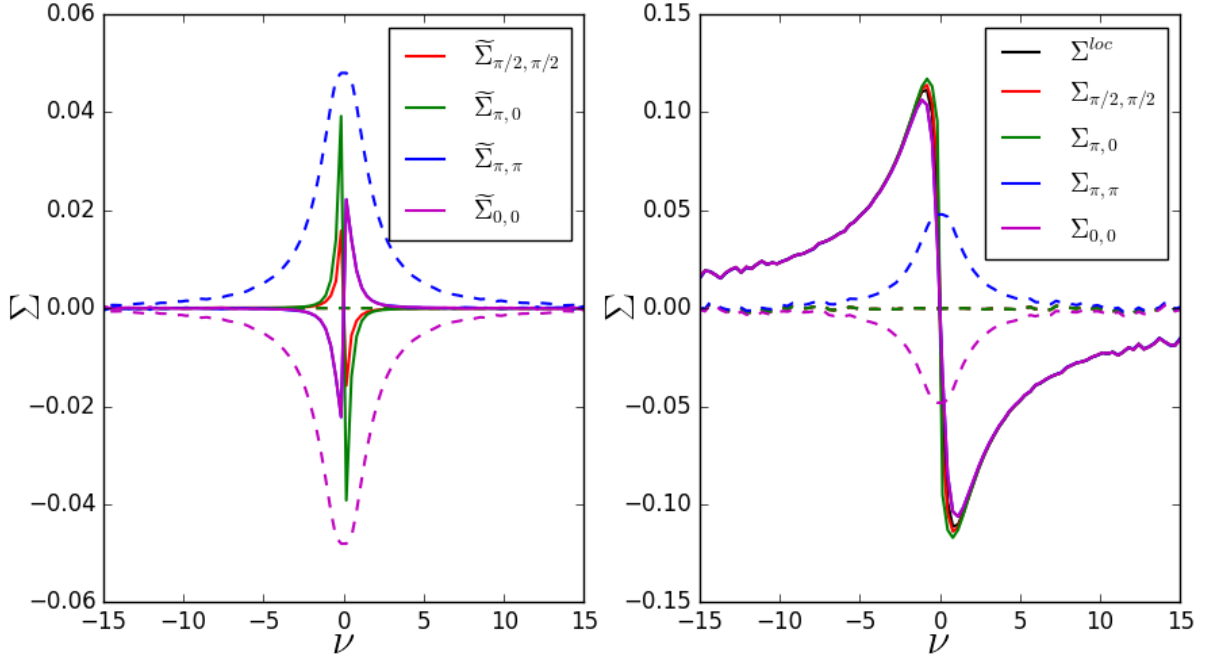
Figure 76: Same as fig. 67 but for $U = 1$ and $\beta = 20.1$ based on an already modified DMFT impurity problem.

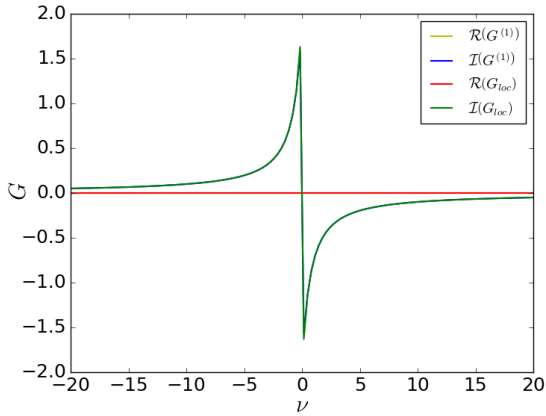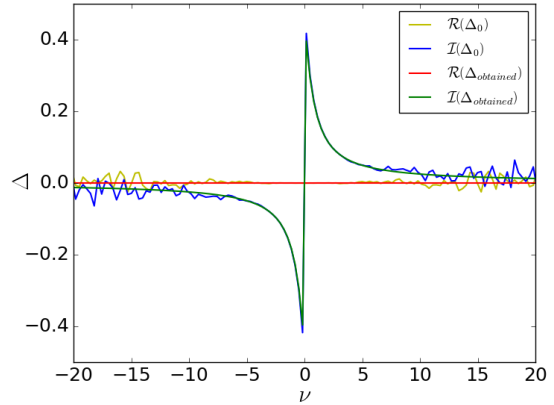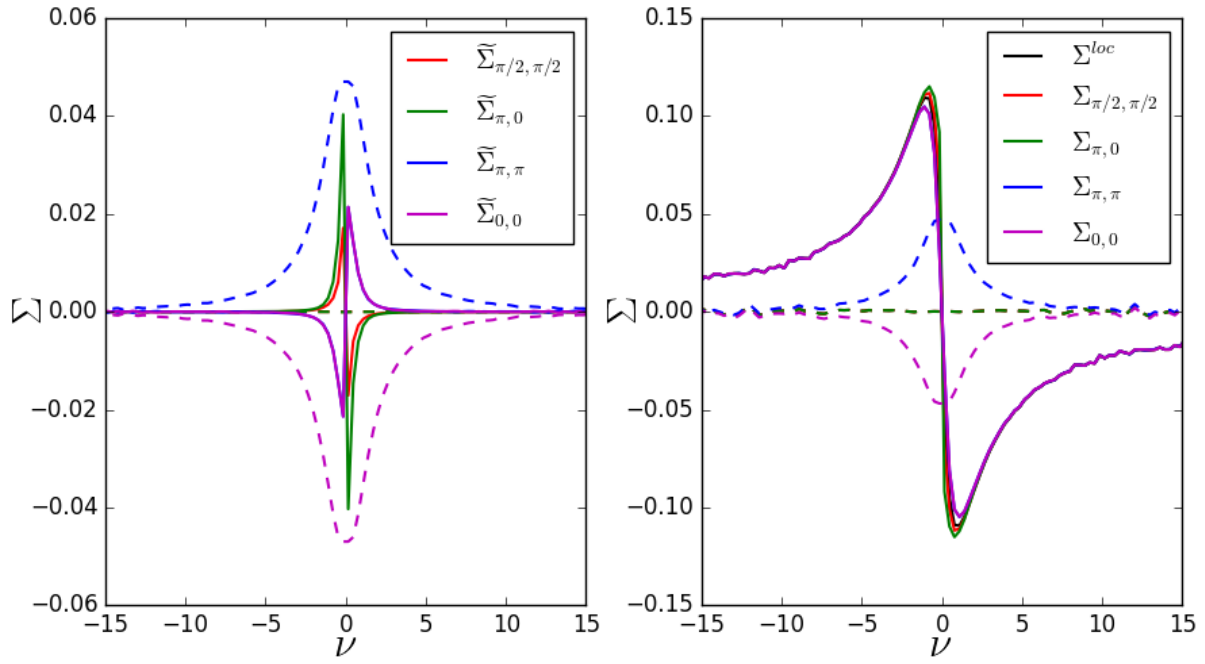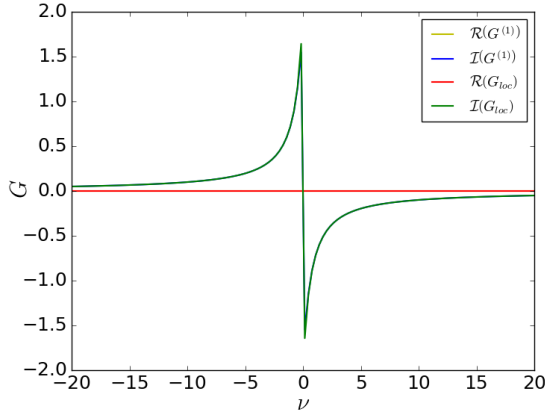be forbidden by the Mermin-Wagner theorem [80], and is thus desireable.

Figure 77: Local impurity Green's function $G^{(1)}$ and local Green's function calculated from the sum of all lattice Green's functions, including DF self-energy corrections G_{loc} for $U = 1$ and $\beta = 20.1$.
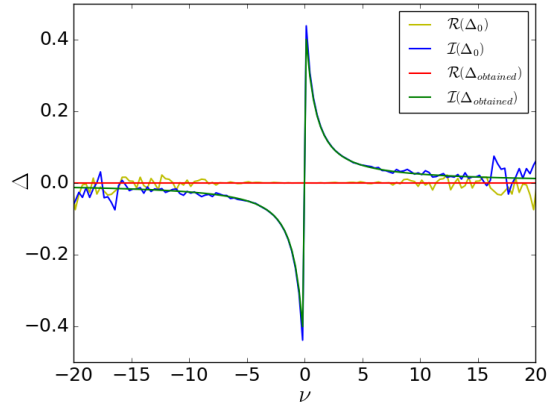

Figure 78: Impurity hybridisation function Δ_0 and hybridisation function obtained when including the resulting self-energy corrections $\Delta_{obtained}$ for $U = 1$ and $\beta = 20.1$.

12.3.4. $U = 2, \beta = 10.5$

Around $U = 2$, the DMFT Néel temperature reaches its maximum, so it is to be expected that antiferromagnetic correlations become especially important for this intermediate interaction value. Due to the stronger correlations, the dual fermion corrections based on DMFT-impurity quantities as seen in figure 79 become much larger than for $U = 1$. When outer self-consistency is enforced, the dual self-energies become smaller, but the self-energy changes drastically (see figure 80). While the direct effect of the self-energy corrections is small, it does influence the underlying impurity enough to have a huge effect, similar to the flap of a butterfly deciding on the formation of a storm [81, 82]. The physical self-energy in figure 80 is reduced by roughly a factor 3 for the real part and a factor 2 for the imaginary part compared to inner self-consistency based on DMFT only (figure 80).

The effect of the outer self-consistency on the underlying impurity is consistent with the $U = 1$ case, in that an impurity with smaller self-energy and Green's function (imaginary parts respectively) is generated, achieving these seemingly contradictory properties by means of an amplified hybridisation function at low Matsubara frequencies. Since the imaginary parts of the self-energy become smaller across the whole Brillouin zone, the reduced local weight has to be a consequence of the real parts. States with positive energies relative to the Fermi energy pick up a positive real part and vice versa, shifting extremal values outwards[1]. The change of the local physical Green's function and hybridisation function throughout the outer self-consistency iterations is documented in figs. 81 and 82.

12.3.5. $U = 3, \beta = 8$

With the rather high interaction value $U = 3$, the dual self-energies become very large. Dual self-energies after inner self-consistency, based on the DMFT impurity problem are given in figure 83, next to the resulting self-energies for the real fermions. One can see the huge effect the outer self-consistency iteration has for this parameter set in on the local impurity Green's function and hybridisation function in figures 85 and 86. Unlike the calculations at lower interaction values, the outer self-consistency convergence happens in a non-oscillating fashion after the first iteration. Starting from the DMFT impurity solution, the hybridisation function is first strongly enhanced and then decreases again. Note that in such a case, a mixing factor would have slowed down the convergence of the system in the later iterations. The dual self-energies are much smaller for the system once outer self-consistency was achieved than for the calculation based on the DMFT impurity, as documented in figures 83 and 84. The effect of the outer self-consistency is surprisingly large when considering the high temperature. The high number of outer self-consistency iterations is symptomatic of high interaction values and $\beta = 8$ was the lowest of the investigated temperatures where outer self-consistency could be achieved without resorting to additional ad-hoc methods to ensure convergence.

---

[1]This is consistent with the qualitative behaviour of second order perturbation theory.

Figure 79: Same as fig. 67 but for $U = 2$ and $\beta = 10.5$ based on the DMFT impurity problem.
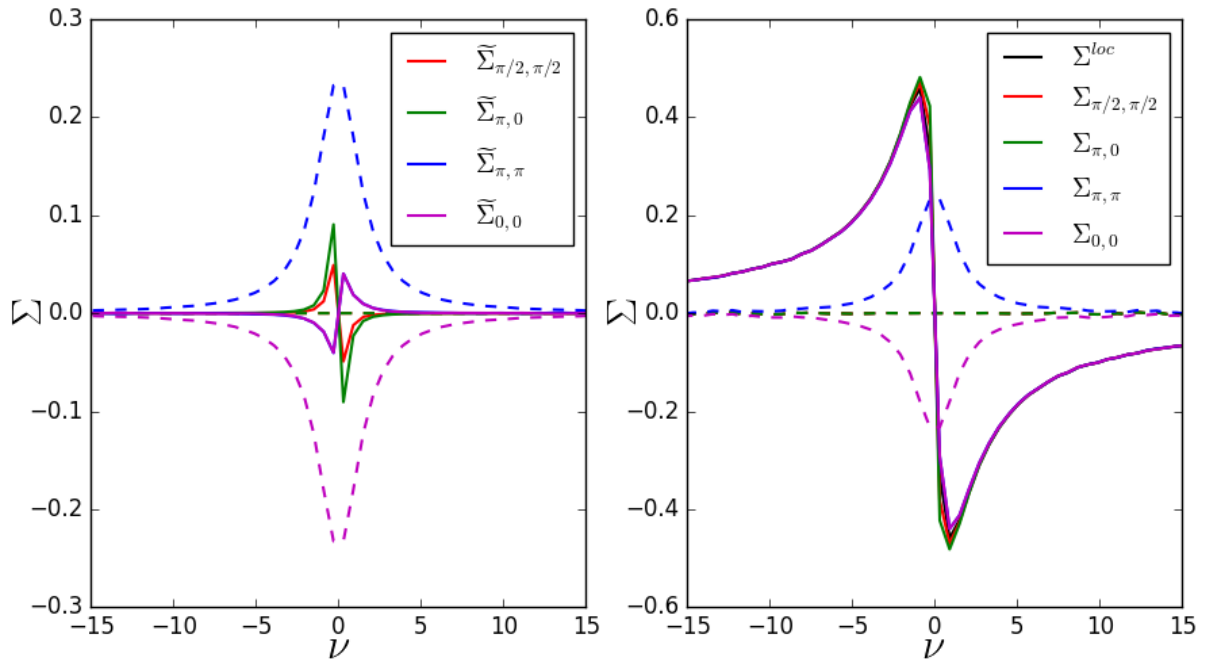
Figure 80: Dual self-energies (left) and self-energies (right) as a function of Matsubara frequency for different k-points for $U = 2$ and $\beta = 10.5$ when outer self-consistency is achieved. Real parts are depicted as dashed lines and imaginary parts as full lines.
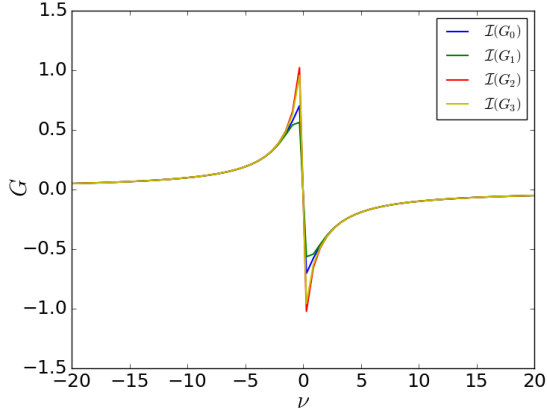
Figure 81: Imaginary part of the local Green's function dependant on outer self-consisteny iteration for $U = 2$ and $\beta = 10.5$. G_0 is the DMFT Green's function, G_1 the Green's function after one outer self-consistency step etc..
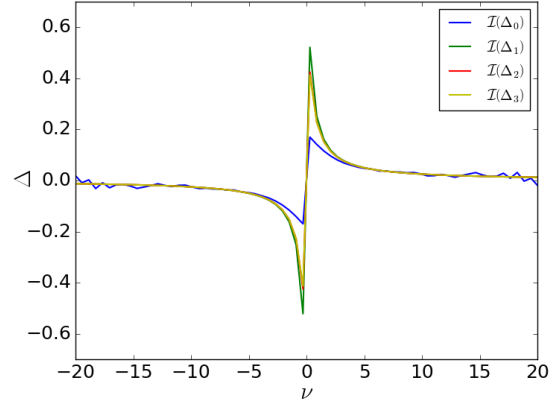
Figure 82: Imaginary part of the hybridisation function dependant on outer self-consistency iteration for $U = 2$ and $\beta = 10.5$. Δ_0 is the DMFT hybridisation function, Δ_1 the hybridisation function after one outer self-consistency step etc..
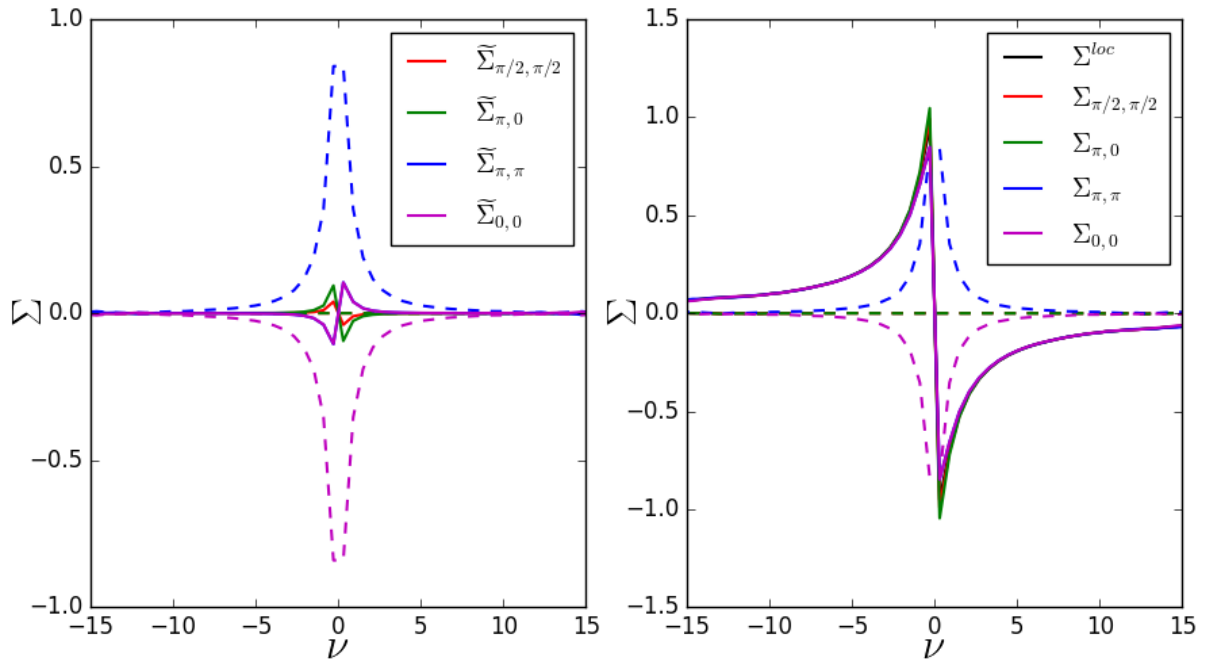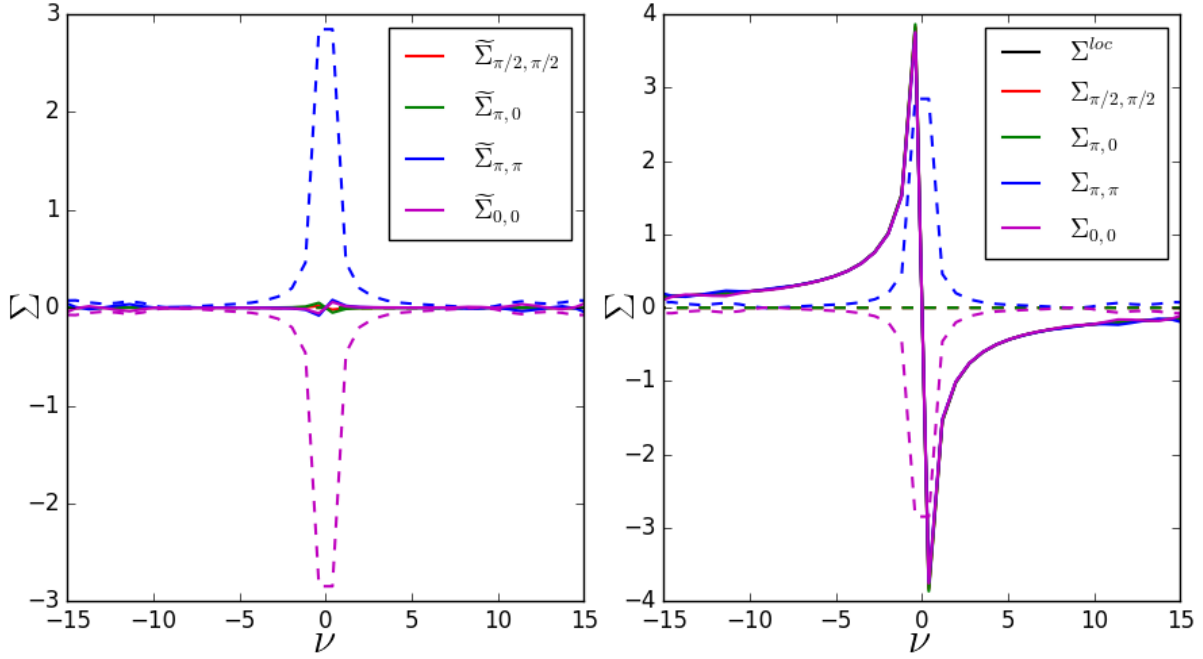

Figure 83: Same as fig. 67 but for $U = 3$ and $\beta = 8$ based on the DMFT impurity problem.
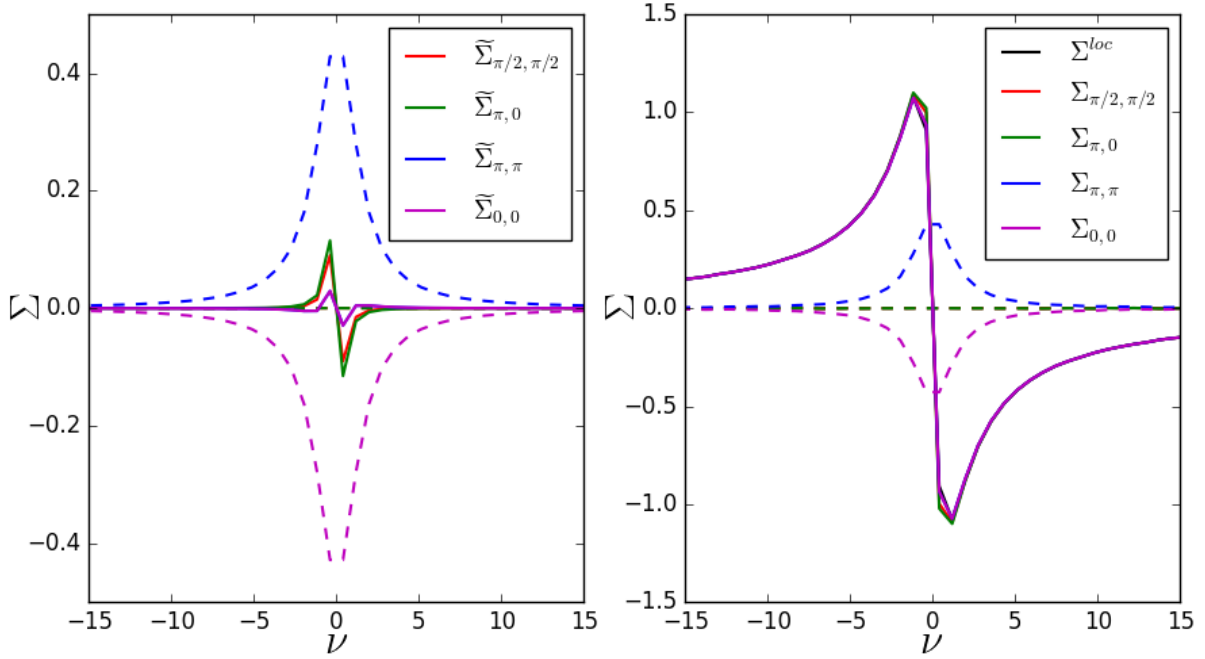
Figure 84: Dual self-energies (left) and self-energies (right) as a function of Matsubara frequency for different k-points for $U = 3$ and $\beta = 8$.
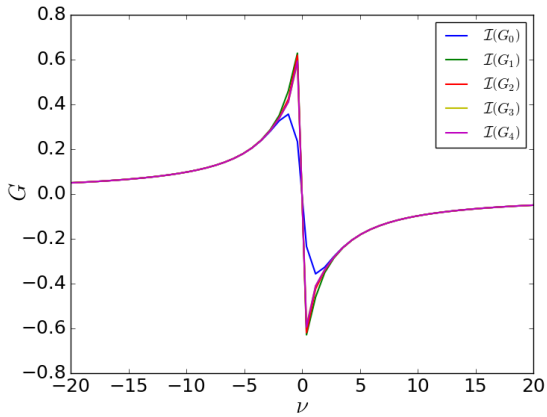
Figure 85: Local DMFT Green's function $G^{(1)}$ and local Green's function calculated from the sum of all lattice Green's functions, including DF self-energy corrections G_{loc} for $U = 3$ and $\beta = 8$.
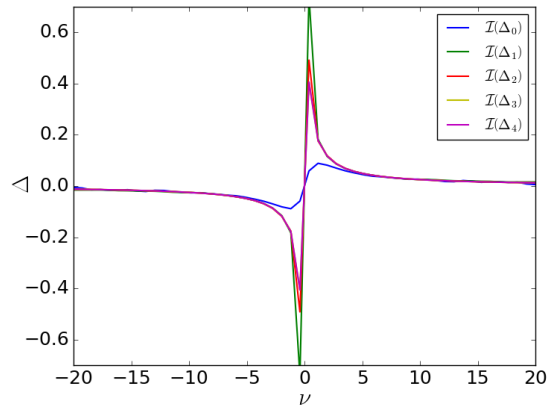
Figure 86: DMFT hybridisation function Δ_0 and hybridisation function obtained when including self-energy corrections $\Delta_{obtained}$ for $U = 3$ and $\beta = 8$.
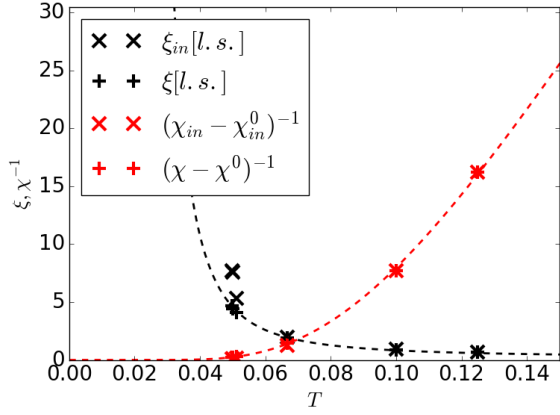
Figure 87: Correlation length ξ (measured in lattice spacings) and inverse connected contribution to the antiferromagnetic susceptibility as a function of the temperature T for the Hubbard model when employing a dual fermion ph-ladder approximation with inner and outer self-consistency for $U = 1$ at half-filling. The dashed lines give fits of exponential functions to the data, obtained via a least square fit.
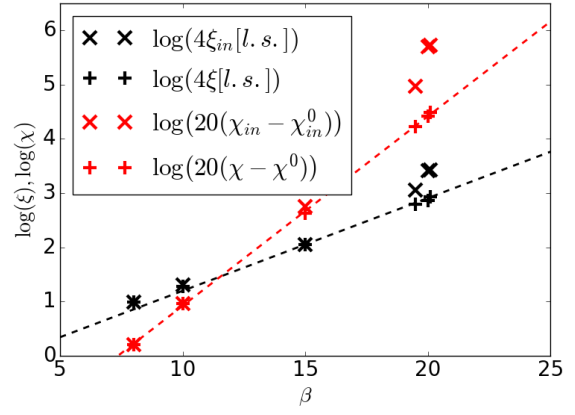
Figure 88: Logarithm of the correlation length ξ (measured in lattice spacings) and logarithm of the connected contribution to the antiferromagnetic susceptibility as a function of the inverse temperature β for the Hubbard model when employing a dual fermion ph-ladder approximation with inner and outer self-consistency for $U = 1$ at half-filling. In the logarithmic plot, the exponential fits from figure 87 become linear functions, again depicted as dashed lines.

12.3.6. Susceptibilities and correlation lengths

Aside from self-energy corrections, it is also possible to extract anti-ferromagnetic susceptibilities and correlation lengths from the dual fermion calculations. For $U = 1$ and $U = 2$, these quantities are documented as functions of temperature T and inverse temperature β respectively in figures 87 through 90. The connected contributions to the susceptibilities can be directly calculated from the dual fermion ladder already used for extracting dual self-energies. The correlation lengths are extracted from a parobolic fit of the inverse susceptibility in q-space.

As the temperature is decreased, the suceptibility increases. While the dual fermion calculation and the outer self-consistency condition stabilise some data points which already yield unphysical results within a DMFT approximation, converging the calculations becomes successively harder for lower temperatures. The correlation lengths remain smaller than the linear dimension 64 used as a mesh for the calculation.

Plotting the logarithm of the susceptibility as a function of the inverse temperature shows a clear linear trend over the investigated range, possibly hinting at the presence of a transition with exponential decay, similar to Kosterlitz-Thouless-transition [83]. A similar picture emerges if the logarithm of the correlation length is plotted as a function of β.
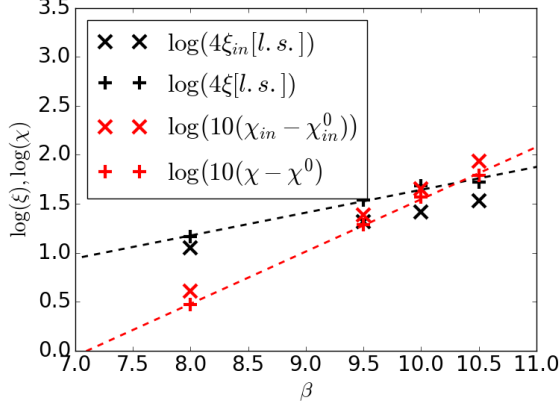
Figure 89: Same as figure 87, but for $U = 2$.
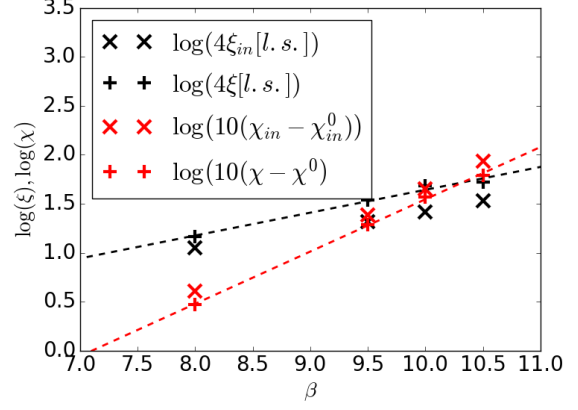
Figure 90: Same as figure 88, but for $U = 2$.

A. Derivation of the current operator on a lattice

In this section, a detailed derivation of the current density operator on a discrete lattice is given. The notation is chosen in accordance with section 2.6.2. The goal is to calculate an expression for macroscopic transport of charge in a system. We assume translational invariance and are only interested in $q = 0$ currents. For homogeneous currents in homogeneous systems, writing a volume-integrated current operator $\mathcal{I}$, basically the current monopole, as:

$$\mathcal{I} \propto iq_c \left\langle \sum_j (r_j - r_i) \left(t_{i,j} c_i^\dagger c_j - t_{j,i} c_j^\dagger c_i \right) \right\rangle \tag{217}$$

is promising. The resulting quantity is a vector (because of $(r_j - r_i)$ appearing in the sum), and it can be easily derived from the charge transported through a plane, as will be discussed in the following. It describes the macroscopic transport of charge[1] in the system and has the dimension of current times length. We start by investigating the current in three spatial dimensions in direction of one of the basis vectors of the dual lattice. This has the advantage that two of the real-space basis vectors are then aligned with the plane through which we want to calculate the charge transport, which in turn simplifies the calculations. All the currents which transport charge through the plane need to be added to arrive at the total current. As long as our assumptions about the infinity and translational invariance of the system and the current hold, the currents $I_{i,j}$ transporting charge from lattice site j to i are only functions of $\Delta = i - j$, the distance between the two sites. The remaining question is: for a given Δ, how many times does $I(\Delta)$ contribute to the total current through the plane? The total current through the selected plane, say an $y - z$ plane can be written as

$$I = \sum_{i,j \mid i_x \geq 0, j_x < 0} I_{i,j} \tag{218}$$

with i going over all sites on one side of the plane and j going over all sites on the other side. Currents which move charge only on one side of the plane without transporting it across are of no interest to us and therefore not summed. Now we decompose i and j into their components along the plane and the third coordinate i_x and j_x. Thus, which side of the plane a site is on depends only on the coordinate i_x or j_x and there are no conditions on the ranges for $i_{y,z}$ or $j_{y,z}$.

$$I = \sum_{i_{y,z}, j_{y,z}} \sum_{i_x = 0,1,2...} \sum_{j_x = -1,-2...} I_{i,j} \tag{219}$$

For translationally invariant systems, the current $I_{i,j}$ depends on the difference of the positions i and j only.

$$I = \sum_{i_{y,z}, j_{y,z}} \sum_{i_x = 0,1,2...} \sum_{j_x = -1,-2...} I(i - j) \tag{220}$$

We are interested in current densities $\vec{j}$, so we divide I by by the surface we are calculating the flow through, A, which can also be represented as

$$A = \sum_{i_{y,z}} A_{yz} \tag{221}$$

---

[1] Note that a current is only a meaningful quantity if the surface it flows through is indicated.

with A_{yz} being the surface area of the parallelogram spanned by the two lattice basis vectors within the plane. From our calculation, we got the current through the yz-plane, i.e. the surface-integrated projection of the current density onto the normal to the surface. The normal to the yz-plane is given by the dual x-basis vector $\vec{d}_x$. We introduce $\vec{e}_x$, the unit vector in the direction of the lattice vector x.

$$\frac{I}{A}\vec{e}_x = \vec{j} = \frac{1}{A_{yz}\cos\theta}\sum_{j_{y,z}}\sum_{i_x=0,1,2...}\sum_{j_x=-1,-2...} I(i-j)\vec{e}_x. \tag{222}$$

Here, $i_{y,z}$ can be chosen arbitrarily. θ is the angle between $\vec{e}_x$ and $\vec{d}_x$. As next step, we rewrite the summations in terms of the vector between the sites i and j, $\Delta = i - j$. Also, introducing the lattice vector in x-direction $\vec{b}_x$ and its length l_x and employing that the unit cell volume V is given by

$$V = A_{yz}l_x\cos\theta, \tag{223}$$

we can write

$$\vec{j} = \frac{1}{V}\sum_{\Delta_{y,z},\Delta_x>0} I(\Delta)\mathcal{C}(\Delta)\vec{b}_x, \tag{224}$$

where the factor $\mathcal{C}(\Delta)$ describes how many times $I(\Delta)$ contributes to the flow of charge through the plane. It turns out that the factor depends only on the difference of coordinates in x-direction and is 1 for nearest-neighbour hopping, 2 for second-nearest-neighbour hopping etc. (only taking into account the value of Δ_x for defining the distance). Thus, we can write the final expression for the current density in lattice-x direction

$$\vec{j} = \frac{1}{2V}\sum_\Delta I(\Delta)\Delta_x \cdot \vec{b}_x. \tag{225}$$

A factor $1/2$ appears due to the removal of the condition $\delta_{r,x} > 0$ which caused double-counting. The same derivation holds for the other directions, allowing to reconstruct the current density as a vectorial quantity:

$$\vec{j} = \frac{1}{2V}\sum_\Delta I(\Delta)\left(\Delta \cdot \vec{b}\right) = iq_c\sum_j t_{0,j}c_0^\dagger c_j\, r_j. \tag{226}$$

Note that this expression is closely related to equation (217). It is worth mentioning that this derivation can be performed more economically by taking the time derivative of the lattice dipole moment D,

$$D(t) = \sum_i r_i q(r_i, t) \tag{227}$$

which gives the same expression for the current density.

B. Decomposing a general action in terms of Green's functions

This appendix is intended to provide a derivation on how to express an exponential of an action S in terms of the exact n-particle Green's functions of the system. The starting point are the functional integral representations of the (grand-canonical) partition function Z and n-particle Green's functions:

$$Z = \int \mathcal{D}\left[c^\dagger; c\right] e^{-S[c^\dagger, c]} \tag{228}$$

$$G^{(n)}\left(\alpha, \ldots, \omega\right) = \frac{1}{Z} \int \mathcal{D}\left[c^\dagger; c\right] \left(c_\alpha^\dagger \ldots c_\omega\right) e^{-S_l[c^\dagger, c]} \tag{229}$$

Here, the indices $\alpha \ldots \omega$ are general indices encompassing all degrees of freedom of a system. The Grassmann-integration is performed over all of the system's degrees of freedom as well. From this, it is immediately clear that all the terms occuring in the expansion of e^{-S} which contain all Grassmann variables-except for the ones associated with the Green's function, $c_\alpha^\dagger \ldots c_\omega$-have to have a numerical prefactor of $Z \cdot G^{(n)}(\alpha, \ldots, \omega)$ if summed up.

Considering all possible Green's functions, as well as the partition function itself, we can express the expansion of the exponent of the action:

$$e^{-S[c^\dagger, c]} = Z \cdot \left[1 + \sum_{n=1}^\infty \frac{1}{(n!)^2} \sum_{\alpha \ldots \omega} G^{(n)}\left(\alpha, \ldots, \omega\right) \delta_\omega \ldots \delta_\alpha^\dagger\right] \prod_\alpha c_\alpha^\dagger c_\alpha. \tag{230}$$

In this expansion, Z ensures normalisation, $1/(n!)^2$ accounts for overcounting due to exchangeability of entering and leaving lines and the product over all $c_\alpha^\dagger c_\alpha$ gives a baseline expression which integrates to 1. The variational operators $\delta_\alpha^{(\dagger)}$ denote functional derivation with respect to $c_\alpha^{(\dagger)}$ and their order was chosen in a way which ensures the correct sign. One can easily verify that this form for e^{-S} satisfies equations (228) and (229).

Now, the connected and disconnected parts of the Green's functions are systematically seperated. The sum of all full Green's functions can be written as an exponential of fully connected Green's functions $G_C^{(n)}$.

$$\left[1 + \sum_{n=1}^\infty \frac{1}{(n!)^2} \sum_{\alpha \ldots \omega} G^{(n)}\left(\alpha, \ldots, \omega\right) \delta_\omega \ldots \delta_\alpha^\dagger\right] = \exp\left[\sum_{n=1}^\infty \frac{1}{(n!)^2} \sum_{\alpha \ldots \omega} G_C^{(n)}\left(\alpha, \ldots, \omega\right) \delta_\omega \ldots \delta_\alpha^\dagger\right] \tag{231}$$

While deriving this equation is not trivial, proving it to be correct is much simpler. Consider any summand on the left hand side of equation (231). For any n-particle Green's function term, there are $(n!)^2$ equivalent ones with only the order of the Grassmann operators exchanged, nicely canceling the denominator $1/(n!)^2$. We now discuss the corresponding terms on the right hand side. Obviously there is a connected n-particle term which stems from the first order expansion of the exponential. This term appears $(n!)^2$ times, but also comes with a denominator of $1/(n!)^2$. Disconnected contributions to the n-particle Green's function are generated from higher expansion orders of the exponential. Consider a disconnected term consisting of a product of l connected parts. Obviously, $l \leq n$ must hold. If the connected terms are mutually distinct, there are $l!$ permutations of them and all of them appear in the expansion of the exponential, nicely cancelling the $1/l!$ factor from the l-th order expansion of the exponent. Terms with two identical factors (or even sharing a single index $\alpha, \beta, \ldots$) evaluate to zero, because a functional derivation of appears twice.

Obviously, we can only rarely evaluate n-particle Green's functions, limiting the practical utility of the decomposition above. It does however play an important role in rewriting solved (impurity) problems into an expoential form, allowing for an interpretation as an effective action, specifically in the context of effective diagrammatic methods based on DMFT.

C. Alternative derivation of the fully connected n-particle propagator for the Falicov-Kimball model

Here, an alternative derivation to the one given in section 8 for the fully connected, n-particle propagator for the Falicov-Kimball model within DMFT will be pursued. We will use the expression we derived to rewrite the Green's function in equation (183). We also need an expression for the fully connected propagator. This we will extract from a path integral expression using generating functionals. The original idea to offer this alternative version of the proof was put forward by Georg Rohringer. An early version of this section was used as a draft for writing the corresponding section in [30].

C.1. General subtraction scheme for the fully connected propagator

In a path integral representation, Green's functions are calculated by evaluating expectation values of partial derivatives of the partition function with regard to some external fields which couple to the fermionic fields in question, evaluated at a value of 0 for those external fields. The fully connected propagator is given not by the derivative of the partition function, but its logarithm's. In equation (179), we already established that it is possible to write the full local n-particle Green's function as

$$G^{(n)}(a, b, c, \dots, d, e, f, \dots) = \delta_{def\dots}^{abc\dots} \left[p_1 \left(\overline{G}(a)\overline{G}(b)\overline{G}(c) \dots \right) + p_2 \left(\underline{G}(a)\underline{G}(b)\underline{G}(c) \dots \right) \right]. \tag{232}$$

We note that the special δ-structure of the propagator allows us to restrict ourselves only to cases where the incoming and outgoing frequencies are permutations of each other. When two or more pairs of frequencies are the same, everything is 0. With regard to derivations, this allows us to group the operators. The definition of the Green's function in terms of partial derivatives of the partition function Z by the source fields ζ and $\zeta^\dagger$ is given by:

$$G^{(n)}(a, b, c, \dots, d, e, f, \dots) = \frac{1}{Z} \delta_{\zeta_a^\dagger} \delta_{\zeta_d} \delta_{\zeta_b^\dagger} \delta_{\zeta_e} \delta_{\zeta_c^\dagger} \delta_{\zeta_f} \dots (Z) \tag{233}$$

We already know that the Green's function can only be non-zero if the incoming and outgoing frequencies are a permutation of each other. Thus we choose a specific permutation $a = d$, $b = e$... and redefine our derivation operators:

$$\delta_a = \delta_{\zeta_a^\dagger} \delta_{\zeta_a} \tag{234}$$

We grouped the two necessary derivation operators together into the new composite operator δ_a. This new operator retains some of its fermionic properties, while attaining bosonic behaviour under permutations:

$$\delta_a \delta_a = \quad 0 \tag{235}$$
$$\delta_a \delta_b = \quad \delta_b \delta_a \tag{236}$$

We note that it is possible to write

$$G^{(n)}(a, b, c, \dots, d, e, f, \dots) = \frac{1}{Z} \delta_{def\dots}^{abc\dots} \delta_a \delta_b \delta_c \dots (Z). \tag{237}$$

Now we derive the fully connected propagator. in terms of derivatives it can be written as:

$$G_{con}^{(n)}(a, b, c, \dots, d, e, f, \dots) = \delta_{\zeta_a^\dagger} \delta_{\zeta_d} \delta_{\zeta_b^\dagger} \delta_{\zeta_e} \delta_{\zeta_c^\dagger} \delta_{\zeta_f} \dots (\ln Z). \tag{238}$$

When applying the derivation, one arrives at a sum of many different terms with all possible combinations of the derivations acting on different Z (with the multiple derived Z originating from the derivations acting on the fractions $1/Z^l$ appearing after the first derivation acting on $\ln Z$). We already know that for a term to have a non-zero contribution, a pair of derivations $\delta_{\zeta_a^\dagger} \delta_{\zeta_a}$ has to act on the same Z. This motivates rewriting equation (238) as

$$G_{con}^{(n)}(a, b, c, \dots, d, e, f, \dots) = \delta_{def\dots}^{abc\dots} \delta_a \delta_b \delta_c \dots (\ln Z). \tag{239}$$

Now we want to establish a relation between the full propagator and the fully connected one. As a start, let us consider the frequency a as a reference. The part of the propagator containing the outer legs with frequency a can be fully connected to any number l of other frequencies between 0 and $n-1$ for any given diagram. There are $n_p(l, n)$ combinations of l out of $n-1$ frequencies,

$$n_p(l, n) = \binom{n-1}{l}. \tag{240}$$

Each diagram has a unique set of frequencies which are fully connected to a. This motivates subtracting the disconnected diagrams by orders of "connectedness" to a. Let us write down:

$$G_{con}^{(n)} = G^{(n)} - \sum_{l=0}^{n-2} \binom{n-1}{l} G_{con}^{(l+1)} G^{(n-l-1)} \tag{241}$$

Where the binomial coefficient actually represents the sum over all the possible permutations of l frequencies which are fully connected to the frequency a. We now want to prove that equation (241) actually holds. On the two-particle level, $n = 2$, this is trivially easy to check:

$$G_{con}^{(2)} = G^{(2)} - G_{con}^{(1)} G^{(1)} \tag{242}$$

We now want to conduct a proof by induction. To do so, we start from equation (241) and insert the expressions (237) and (239) for G and G_{con}. For all $\delta_{def...}^{abc...}$ we choose the trivial permutation

$$a, b, c, \,... \, = d, e, f, \, ... \,, \tag{243}$$

which sets all Kronecker deltas equal to 1. This yields

$$\delta_a \delta_b \delta_c... \, (\ln Z) = \frac{1}{Z} \delta_a \delta_b \delta_c... \, (Z) - \sum_{l=0}^{n-2} \binom{n-1}{l} (\delta_i)^{"l"} \delta_a (\ln Z) \frac{1}{Z} (\delta_i)^{"n-l-1"} (Z) \tag{244}$$

Where the binomial coefficients again denote all possible permutations of frequencies relative to a. The index i is used as a placeholder, but will become important later on. We will now apply another derivation on the whole equation, trying to recover the same expression for $n + 1$. We will use f as index for this derivation.

$$\delta_f \left(\delta_a \delta_b \delta_c... \, (\ln Z) = \frac{1}{Z} \left(\delta_a \delta_b \delta_c... \, (Z) - \sum_{l=0}^{n-2} \binom{n-1}{l} (\delta_i)^{"l"} \delta_a (\ln Z)(\delta_i)^{"n-l-1"} (Z) \right) \right) \tag{245}$$

$$\delta_a \delta_b \delta_c...\delta_f \, (\ln Z) = -\frac{1}{Z^2} \delta_f(Z) \left(\delta_a \delta_b \delta_c... \, (Z) - \sum_{l=0}^{n-2} \binom{n-1}{l} (\delta_i)^{"l"} \delta_a (\ln Z)(\delta_i)^{"n-l-1"} (Z) \right)$$
$$+ \frac{1}{Z} \left(\delta_a \delta_b \delta_c...\delta_f \, (Z) - \sum_{l=0}^{n-2} \binom{n-1}{l} (\delta_i)^{"l"} \delta_f \delta_a (\ln Z)(\delta_i)^{"n-l-1"} (Z) \right.$$
$$\left. - \sum_{l=0}^{n-2} \binom{n-1}{l} (\delta_i)^{"l"} \delta_a (\ln Z)(\delta_i)^{"n-l-1"} \delta_f(Z) \right) \tag{246}$$

Note that the product rule is applicable to our composite operators because any term where the composite operators separate immediately becomes 0. When taking a look at the term on the right hand side of the first line of equation (246), we can identify it as

$$-\frac{1}{Z} \delta_f(Z) \delta_a \delta_b \delta_c... \, (\ln Z) = -\frac{1}{Z} \delta_f(Z) \frac{1}{Z} \left(\delta_a \delta_b \delta_c... \, (Z) - \sum_{l=0}^{n-2} \binom{n-1}{l} (\delta_i)^{"l"} \delta_a (\ln Z)(\delta_i)^{"n-l-1"} (Z) \right) \tag{247}$$

by multiplying equation (244) by $-1/Z \delta_f(Z)$. Inserting this expression back into equation (246), we recover:

$$\delta_a \delta_b \delta_c...\delta_f \, \ln Z = -\frac{1}{Z} \delta_f(Z) \delta_a \delta_b \delta_c... \, \ln Z$$
$$+ \frac{1}{Z} \left(\delta_a \delta_b \delta_c...\delta_f \, Z - \sum_{l=0}^{n-2} \binom{n-1}{l} (\delta_i)^{"l"} \delta_f \delta_a (\ln Z)(\delta_i)^{"n-l-1"} (Z) \right.$$
$$\left. - \sum_{l=0}^{n-2} \binom{n-1}{l} (\delta_i)^{"l"} \delta_a (\ln Z)(\delta_i)^{"n-l-1"} \delta_f(Z) \right) \tag{248}$$

As next step, we want to combine both sums on the right hand side into one. To do so, we first align the terms by orders of derivations acting on $\ln Z$ and Z.

$$\sum_{l=0}^{n-2}\binom{n-1}{l}(\delta_i)^{"l"}\delta_f\delta_a(\ln Z)(\delta_i)^{"n-l-1"}(Z) + \sum_{l=0}^{n-2}\binom{n-1}{l}(\delta_i)^{"l"}\delta_a(\ln Z)(\delta_i)^{"n-l-1"}\delta_f(Z) =$$

$$\delta_a(\ln Z)(\delta_i)^{"n-1"}\delta_f(Z) + \sum_{l=1}^{n-2}\binom{n-1}{l}(\delta_i)^{"l"}\delta_a(\ln Z)(\delta_i)^{"n-l-1"}\delta_f(Z)$$

$$+ \binom{n-1}{n-2}(\delta_i)^{"n-2"}\delta_f\delta_a(\ln Z)(\delta_i)^{"1"}(Z) + \sum_{l=0}^{n-3}\binom{n-1}{l}(\delta_i)^{"l"}\delta_f\delta_a(\ln Z)(\delta_i)^{"n-l-1"}(Z). \quad (249)$$

We perform an index shift in the second sum:

$$\sum_{l=0}^{n-3}\binom{n-1}{l}(\delta_i)^{"l"}\delta_f\delta_a(\ln Z)(\delta_i)^{"n-l-1"}(Z) = \sum_{l=1}^{n-2}\binom{n-1}{l-1}(\delta_i)^{"l-1"}\delta_f\delta_a(\ln Z)(\delta_i)^{"n-l"}(Z) \quad (250)$$

and establish that now all permutations of l derivations in addition to δ_a acting on $\ln Z$ are included in both sums. The first one includes all the terms where δ_f is not acting on the logarithm while the second one includes all the ones where it is. We arrive at:

$$\sum_{l=1}^{n-2}\binom{n-1}{l}(\delta_i)^{"l"}\delta_a(\ln Z)(\delta_i)^{"n-l-1"}\delta_f(Z) + \sum_{l=1}^{n-2}\binom{n-1}{l-1}(\delta_i)^{"l-1"}\delta_f\delta_a(\ln Z)(\delta_i)^{"n-l"}(Z) =$$

$$\sum_{l=1}^{n-2}\binom{n}{l}(\delta_j)^{"l"}\delta_a(\ln Z)(\delta_j)^{"n-l"}(Z), \quad (251)$$

where f is now included in the possible indices for j. Note that

$$\binom{n-1}{l} + \binom{n-1}{l-1} = \binom{n}{l}. \quad (252)$$

The number of possible choices of l out of $n-1$ plus the number of possible choices of $l-1$ out of $n-1$ is the number of choices l out of n. It is easy to understand: Take a reference element out of the n elements and call it f. Now if selecting l of the n elements all the choices where f is included ($l-1$ out of the remaining $n-1$) or is not included (l out of the remaining $n-1$) are the total number of choices for l elements. We reinsert the expression in equation (251) into equation (247).

$$\delta_a\delta_b\delta_c...\delta_f\,(\ln Z) = -\frac{1}{Z}\delta_f(Z)\delta_a\delta_b\delta_c...\,(\ln Z)$$

$$+ \frac{1}{Z}\left(\delta_a\delta_b\delta_c...\delta_f\,(Z) - \sum_{l=1}^{n-2}\binom{n}{l}(\delta_j)^{"l"}\delta_a(\ln Z)(\delta_j)^{"n-l"}(Z)\right.$$

$$\left. - \delta_a(\ln Z)(\delta_i)^{"n-1"}\delta_f(Z) - \binom{n-1}{n-2}(\delta_i)^{"n-2"}\delta_f\delta_a(\ln Z)(\delta_i)^{"1"}(Z)\right). \quad (253)$$

The term where no derivations except for δ_a act on $\ln Z$ can be simply replaced:

$$\delta_a(\ln Z)(\delta_i)^{"n-1"}\delta_f(Z) = \delta_a(\ln Z)(\delta_j)^{"n"}(Z), \quad (254)$$

with the index j including f as a candidate again. The contribution

$$\frac{1}{Z}\binom{n-1}{n-2}(\delta_i)^{"n-2"}\delta_f\delta_a(\ln Z)(\delta_i)^{"1"}(Z) \quad (255)$$

is the sum of all diagrams where a is fully connected to all but one frequencies, excluding f as the disconnected one. There are $n-1$ terms of this kind. Luckily,

$$\frac{1}{Z}\delta_f(Z)\delta_a\delta_b\delta_c...\,(\ln Z) \quad (256)$$

is exactly the missing term, allowing us to rewrite

$$\frac{1}{Z}\binom{n-1}{n-2}(\delta_i)^{"n-2"}\delta_f\delta_a(\ln Z)(\delta_i)^{"1"}(Z) + \frac{1}{Z}\delta_f(Z)\delta_a\delta_b\delta_c...(\ln Z)$$
$$= \frac{1}{Z}\binom{n}{n-1}(\delta_j)^{"n-1"}\delta_a(\ln Z)(\delta_j)^{"1"}(Z). \quad (257)$$

In total, we arrive at:

$$\delta_a\delta_b\delta_c...\delta_f(\ln Z) = \frac{1}{Z}\delta_a\delta_b\delta_c...\delta_f(Z) - \sum_{l=0}^{(n+1)-2}\binom{(n+1)-1}{l}(\delta_j)^{"l"}\delta_a(\ln Z)\frac{1}{Z}(\delta_j)^{"(n+1)-l-1"}(Z), \quad (258)$$

which is exactly the expression we started with except for n being replaced by $n+1$. Thus our inductive proof is complete and equation (241) is actually fulfilled. Let us note at this point that apart from the grouping of derivations, up to this point nothing Falicov-Kimball-specific was done.

C.2. Calculation of the local fully-connected propagator for the Falicov-Kimball model

The next step is to employ equation (241) for calculating the fully connected local FK n-particle vertex. We start from the known expression for the n-particle Green's function in equation (183). Also, we make an Ansatz for the fully connected propagator.

$$G_{con}^{(n)} = \begin{cases} G^{(1)} & | \; n = 1 \\ \mathcal{C}_n(\overline{G} - \underline{G})^{"n"} & | \; n > 1 \end{cases} \quad (259)$$

We have to show the consistency of (259) as well as express $\mathcal{C}_n$. For completeness' sake, equation (183) is repeated here:

$$G^{(n)} = \sum_{l=0}^{n}\binom{n}{l}\mathcal{F}_l(\overline{G} - \underline{G})^{"l"}G^{(1)"n-l"}.$$

Explicit evaluation gives:

$$\mathcal{C}_n(\overline{G} - \underline{G})^{"n"} = \sum_{l=0}^{n}\binom{n}{l}\mathcal{F}_l(\overline{G} - \underline{G})^{"l"}G^{(1)"n-l"} - G^{(1)}\sum_{l=0}^{n-1}\binom{n-1}{l}\mathcal{F}_l(\overline{G} - \underline{G})^{"l"}G^{(1)"n-1-l"}$$
$$- \sum_{m=1}^{n-2}\binom{n-1}{m}\mathcal{C}_{m+1}(\overline{G} - \underline{G})^{"m+1"}\sum_{u=0}^{n-m-1}\binom{n-m-1}{u}\mathcal{F}_u(\overline{G} - \underline{G})^{"u"}G^{(1)"n-m-1-u"} \quad (260)$$

A short discussion of the frequency structure of the terms is in order here. The left hand side of the equation is not problematic, as it is simply a product of n similar terms and a constant factor. The sum originating from $G^{(n)}$ always contains all possible permutations of frequencies. The term

$$G^{(1)}\sum_{l=0}^{n-1}\binom{n-1}{l}\mathcal{F}_l(\overline{G} - \underline{G})^{"l"}G^{(1)"n-1-l"} \quad (261)$$

always contains the referential frequency a in the first $G^{(1)}$ factor, but otherwise contains all possible permutations of the remaining frequencies. The most involved term,

$$\sum_{m=1}^{n-2}\binom{n-1}{m}\mathcal{C}_{m+1}(\overline{G} - \underline{G})^{"m+1"}\sum_{u=0}^{n-m-1}\binom{n-m-1}{u}\mathcal{F}_u(\overline{G} - \underline{G})^{"u"}G^{(1)"n-m-1-u"} \quad (262)$$

always has the referential frequency in one of the $(\overline{G} - \underline{G})$ factors from the Ansatz for the fully connected propagator. The difference of the first two terms can be easily evaluated. It contains all the permutations of frequencies where a is not associated with a $G^{(1)}$ term. The first term includes all permutations while the second one includes all the ones where a appears in a $G^{(1)}$ factor. We can write:

$$\sum_{l=0}^{n}\binom{n}{l}\mathcal{F}_l(\overline{G} - \underline{G})^{"l"}G^{(1)"n-l"} - G^{(1)}\sum_{l=0}^{n-1}\binom{n-1}{l}\mathcal{F}_l(\overline{G} - \underline{G})^{"l"}G^{(1)"n-1-l"} =$$
$$(\overline{G} - \underline{G})\sum_{v=0}^{n-1}\binom{n-1}{v}\mathcal{F}_{v+1}(\overline{G} - \underline{G})^{"v"}G^{(1)"n-v-1"}, \quad (263)$$

106

where the first factor on the right hand side always belongs to the frequency a. Since $\mathcal{F}_1 = 0$, we can drop the first summand ($v = 0$) on the right hand side. Now we will use the expression we just recovered and insert it into equation (260), at the same time rearranging the term in (262).

$$\mathcal{C}_n(\overline{G} - \underline{G})^{"n"} = (\overline{G} - \underline{G}) \sum_{v=1}^{n-1} \binom{n-1}{v} \mathcal{F}_{v+1} (\overline{G} - \underline{G})^{"v"} G^{(1)"n-v-1"}$$
$$- \sum_{m=1}^{n-2} \sum_{u=0}^{n-m-1} \binom{n-1}{m+u} \binom{m+u}{u} \mathcal{C}_{m+1}(\overline{G} - \underline{G})^{"m+1"} \mathcal{F}_u (\overline{G} - \underline{G})^{"u"} G^{(1)"n-m-1-u"} \quad (264)$$

The summations were taken over all terms, changing the structure of the binomial coefficients at the same time. Before, we first chose m frequencies out of the $n-1$ available, followed by a choice of u out of the $n-m-1$ remaining ones. This was replaced by a selection of $u+m$ out of $n-1$ with u out of the $u+m$ being selected afterwards. As a next step, we will reorganise the summations.

$$\sum_{m=1}^{n-2} \sum_{u=0}^{n-m-1} \rightarrow \sum_{l=1}^{n-2} \sum_{u=0}^{l-2} + \sum_{l=n-1}^{n-2} \sum_{u=1}, \quad (265)$$

where $l = m + u$ was introduced as an independent variable.

$$\mathcal{C}_n(\overline{G} - \underline{G})^{"n"} = (\overline{G} - \underline{G}) \sum_{v=1}^{n-1} \binom{n-1}{v} \mathcal{F}_{v+1} (\overline{G} - \underline{G})^{"v"} G^{(1)"n-v-1"}$$
$$- (\overline{G} - \underline{G}) \sum_{l=1}^{n-2} \sum_{u=0}^{l-1} \binom{n-1}{l} \binom{l}{u} \mathcal{C}_{l+1-u} \mathcal{F}_u (\overline{G} - \underline{G})^{"l"} G^{(1)"n-l-1"}$$
$$- \sum_{u=1}^{n-2} \binom{n-1}{u} \mathcal{C}_{n-u} \mathcal{F}_u (\overline{G} - \underline{G})^{"n"} \quad (266)$$

Now we group the summations according to the first selection of frequencies.

$$\mathcal{C}_n(\overline{G} - \underline{G})^{"n"} = \left(\mathcal{F}_n - \sum_{u=1}^{n-2} \binom{n-1}{u} \mathcal{C}_{n-u} \mathcal{F}_u \right) (\overline{G} - \underline{G})^{"n"}$$
$$+ (\overline{G} - \underline{G}) \sum_{v=1}^{n-2} \binom{n-1}{v} (\overline{G} - \underline{G})^{"v"} G^{(1)"n-v-1"} \left(\mathcal{F}_{v+1} - \sum_{u=0}^{v-1} \binom{v}{u} \mathcal{C}_{v+1-u} \mathcal{F}_u \right) \quad (267)$$

Let us take a closer look at the second term on the right hand side, specifically at the factor

$$\left(\mathcal{F}_{v+1} - \sum_{u=0}^{v-1} \binom{v}{u} \mathcal{C}_{v+1-u} \mathcal{F}_u \right) = \mathcal{F}_{v+1} - \sum_{u=1}^{v-1} \binom{v}{u} \mathcal{C}_{v+1-u} \mathcal{F}_u - \mathcal{C}_{v+1}. \quad (268)$$

If

$$\mathcal{C}_m = \mathcal{F}_m - \sum_{u=1}^{m-2} \binom{m-1}{u} \mathcal{C}_{m-u} \mathcal{F}_u \quad (269)$$

holds for all $m < n$, then all these factors become exactly 0 and what remains of equation (267) is:

$$\mathcal{C}_n(\overline{G} - \underline{G})^{"n"} = \left(\mathcal{F}_n - \sum_{u=1}^{n-2} \binom{n-1}{u} \mathcal{C}_{n-u} \mathcal{F}_u \right) (\overline{G} - \underline{G})^{"n"} \quad (270)$$

We can get rid of the factors $(\overline{G} - \underline{G})$ and recover

$$\mathcal{C}_n = \mathcal{F}_n - \sum_{u=1}^{n-2} \binom{n-1}{u} \mathcal{C}_{n-u} \mathcal{F}_u \quad (271)$$

Thus we have an inductive proof for the structure of $G_{con}^{(n)}$ based on all lower orders $m < n$.

D. Deriving the local one-particle irreducible three-particle vertex for the Falicov-Kimball model

In the following, the one-particle-irreducible part of the local three-particle vertex of the Falicov-Kimball model within DMFT will be calculated. This local $1PI$ vertex can serve as a starting point for future $1PI$ calculations on the three-particle as discussed in section 5.3. We already know that the connected part of the three particle propagator factorises from section 8. The connected three-particle propagator $G_C^{(3)}$ is given by:

$$G_C^{(3)}(a, b, c, d, e, f) = \mathcal{C}_3\, \delta_{def}^{abc}\, \left(\overline{G}(a) - \underline{G}(a)\right) \left(\overline{G}(b) - \underline{G}(b)\right) \left(\overline{G}(c) - \underline{G}(c)\right). \tag{272}$$

We can amputate the outer legs of the connected propagator to arrive at the vertex, defining the new quantity γ:

$$\gamma(a) = \frac{\left(\overline{G}(a) - \underline{G}(a)\right)}{\left(G^{(1)}(a)\right)^2}, \tag{273}$$

we can express the three-particle Vertex $F^{(3)}$ as

$$F^{(3)}(a, b, c, d, e, f) = \mathcal{C}_3\, \delta_{def}^{abc}\, \gamma(a)\gamma(b)\gamma(c). \tag{274}$$

While we absorbed the factor $\mathcal{C}_3$ into the definition of the factors φ in section E and F, we will keep track of it explicitly here. Following this convention, the two-particle vertex is given by

$$F^{(2)}(a, b, c, d) = \mathcal{C}_2\, \delta_{cd}^{ab}\, \gamma(a)\gamma(b). \tag{275}$$

The constants $\mathcal{C}_2$ and $\mathcal{C}_3$ are given by

$$\mathcal{C}_2 = p_1 p_2 \tag{276}$$

and

$$\mathcal{C}_3 = p_1 p_2 \left(1 - 2p_1\right). \tag{277}$$

We will investigate how the one-particle-reducible contributions influence the value of the three particle vertex for a specific permutation of frequencies $a = d, b = e, c = f$ and then generalise the result. For this specific choice of frequencies, only six out of the nine channels of one-particle reducible diagrams contribute. They are depicted diagrammatically in figure 91.
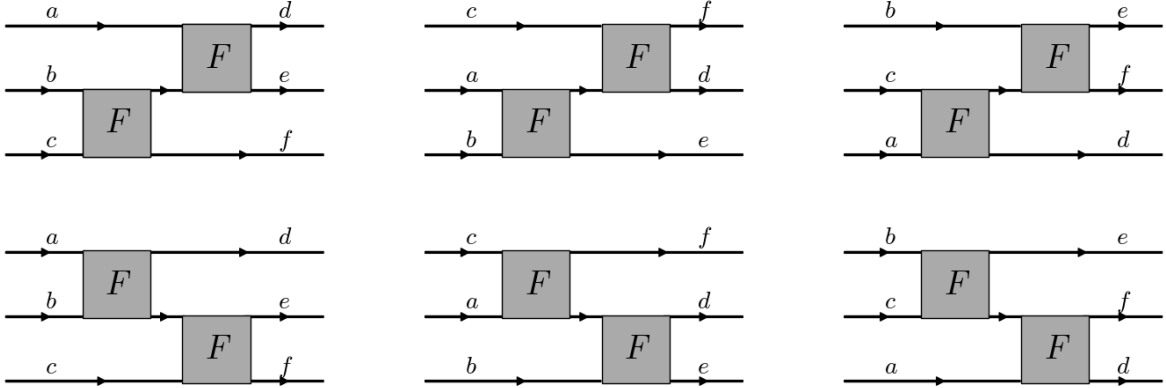
Figure 91: Diagrammatic representation of the six classes of one-particle-reducible diagrams contributing to the three-particle vertex when $a = d, b = e$ and $c = f$. Note that the other three channels of one-particle-reducibility do not contribute due to the special frequency-structure of vertices for the Falicov-Kimball model. The outer legs of the diagrams are depicted for reasons of clarity of notation and are not considered a part of the vertex.

The contributions of the 1PR diagram in the upper left corner of figure 91 can be written algebraically as

$$\sum_k F^{(2)}(b, c, k, f) G^{(1)}(k) F^{(2)}(a, k, d, e). \tag{278}$$

Since we already know which frequency permutation we are investigating, we can perform the summation and set $k = b$, yielding

$$\mathcal{C}_2^2\, \gamma(a)\gamma(b) G^{(1)}(b)\gamma(b)\gamma(c) \tag{279}$$

upon explicit evaluation. The diagram in the lower left corner of figure 91 gives the same algebraic contribution. The other diagrams can be evaluated analogously. Note that that the frequency labels in figure 91 were assigned in a way that ensures that all diagrams have a positive sign when contributing to the three-particle propagator. This implies that we have to subtract them from the full three-particle vertex to arrive at the one-particle-irreducible one. We evaluate explicitely:

$$
F_{1PI}^{(3)}(a, b, c, a, b, c) = p_1 p_2 \left(1 - 2p_1\right) \gamma(a)\gamma(b)\gamma(c) - 2(p_1 p_2)^2 \cdot
$$
$$
\left(\gamma(a)\gamma(b)G^{(1)}(b)\gamma(b)\gamma(c) + \gamma(b)\gamma(a)G^{(1)}(a)\gamma(a)\gamma(c) + \gamma(a)\gamma(c)G^{(1)}(c)\gamma(c)\gamma(b) \right). \quad (280)
$$

We can simplify this expression:

$$
F_{1PI}^{(3)}(a, b, c, a, b, c) = p_1 p_2 \, \gamma(a)\gamma(b)\gamma(c) \cdot
$$
$$
\left[1 - 2p_1 - 2p_1 p_2 \left(\gamma(a)G^{(1)}(a) + \gamma(b)G^{(1)}(b) + \gamma(c)G^{(1)}(c) \right) \right]. \quad (281)
$$

For the general case, one can show that $F_{1PI}^{(3)}$ can be written as:

$$
F_{1PI}^{(3)}(a, b, c, d, e, f) = \delta_{def}^{abc} \, F_{1PI}^{(3)}(a, b, c, a, b, c). \quad (282)
$$

E. Solving the Bethe-Salpeter-like equations for the three-particle Falicov-Kimball vertex

In the following, algebraic solutions to the Bethe-Salpeter-like equations (BSLE) for the three particle case when neglecting two-particle reducibility will be given. There are two independent equations to be solved: the one for the ppp-like channel and one for the remaining 9, equivalent, pph or phh-like channels. We will start with the ppp-like channel, where all the reducible contributions are given by the diagrams depicted in figure 92.
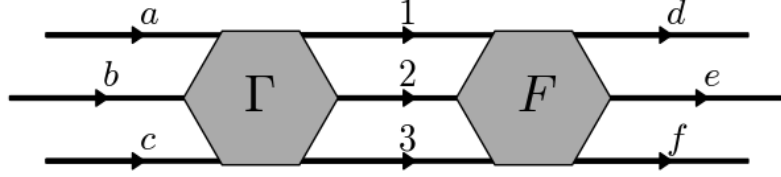
Figure 92: All diagrams reducible in the channel separating a, b, c from d, e, f. The variables 1, 2 and 3 are to be summed over and a factor $1/6$ is required to avoid overcounting.

We will adopt a notation for writing the variables of a vertex as a matrix, which will be useful in treating the pph-channel. The entering lines are written in the upper row and the leaving ones in the lower row of the variable matrix. In this notation, our BSLE for the ppp-channel can be written as[1]:

$$F \begin{pmatrix} a & b & c \\ d & e & f \end{pmatrix} = \Gamma \begin{pmatrix} a & b & c \\ d & e & f \end{pmatrix} + \frac{1}{6} \sum_{1,2,3} \Gamma \begin{pmatrix} a & b & c \\ 1 & 2 & 3 \end{pmatrix} G(1)G(2)G(3)\, F \begin{pmatrix} 1 & 2 & 3 \\ d & e & f \end{pmatrix}. \tag{283}$$

We already know that F can be written as

$$F \begin{pmatrix} a & b & c \\ d & e & f \end{pmatrix} = \delta_{def}^{abc} \varphi(a)\varphi(b)\varphi(c). \tag{284}$$

Here, we assume that for arriving at φ the factorised, connected propagator from section 8 had its outer legs amputated and that the factor $\mathcal{C}_3$ was already absorbed into φ as well. We can insert this expression as well as the explicit form for δ_{def}^{123}:

$$\delta_{def}^{123} = \delta_d^1 \delta_e^2 \delta_f^3 + \delta_e^1 \delta_f^2 \delta_d^3 + \delta_f^1 \delta_d^2 \delta_e^3 - \delta_f^1 \delta_e^2 \delta_d^3 - \delta_e^1 \delta_d^2 \delta_f^3 - \delta_d^1 \delta_f^2 \delta_e^3, \tag{285}$$

into equation (283) allowing us to evaluate the sum over 1, 2 and 3:

$$F \begin{pmatrix} a & b & c \\ d & e & f \end{pmatrix} = \Gamma \begin{pmatrix} a & b & c \\ d & e & f \end{pmatrix} + \frac{1}{6} G(d)\varphi(d)G(e)\varphi(e)G(f)\varphi(f) \cdot$$
$$\left(\Gamma \begin{pmatrix} a & b & c \\ d & e & f \end{pmatrix} + \Gamma \begin{pmatrix} a & b & c \\ e & f & d \end{pmatrix} + \Gamma \begin{pmatrix} a & b & c \\ f & d & e \end{pmatrix} \right.$$
$$\left. - \Gamma \begin{pmatrix} a & b & c \\ f & e & d \end{pmatrix} - \Gamma \begin{pmatrix} a & b & c \\ e & d & f \end{pmatrix} - \Gamma \begin{pmatrix} a & b & c \\ d & f & e \end{pmatrix} \right). \tag{286}$$

---

[1]Here, terms stemming from two-particle reducibility were neglected for the sake of readability. They can be reincluded on the r.h.s. of equation (283) without changing the qualitative structure of the derivation, but in the end change the denominator in equation (288) to $1 + G(a)\varphi(a)G(b)\varphi(b)G(c)\varphi(c) + G(a)\varphi(a)G(b)\varphi(b) + G(a)\varphi(a)G(c)\varphi(c) + G(b)\varphi(b)G(c)\varphi(c)$.

Since Γ changes its sign under exchange of any two entering or leaving lines, we can sum up the terms on the right hand side of equation (286).

$$\delta^{abc}_{def}\varphi(a)\varphi(b)\varphi(c). = \Gamma\begin{pmatrix} a & b & c \\ d & e & f \end{pmatrix} + G(a)\varphi(a)G(b)\varphi(b)G(c)\varphi(c)\cdot\Gamma\begin{pmatrix} a & b & c \\ d & e & f \end{pmatrix}. \tag{287}$$

Also the arguments d, e, f of G and φ were replaced by a, b, c since they have to be permutations of each other. We end up with an expression for the ppp-irreducible vertex very much reminescent of the pp-irreducible two-particle vertex:

$$\Gamma\begin{pmatrix} a & b & c \\ d & e & f \end{pmatrix} = \frac{\delta^{abc}_{def}\varphi(a)\varphi(b)\varphi(c)}{1 + G(a)\varphi(a)G(b)\varphi(b)G(c)\varphi(c)}. \tag{288}$$

Having calculated the ppp-irreducible vertex, we turn our attention towards a specific pph-channel, separating a, e, f from b, c, d. The contribution to the three-particle vertex reducible in this channel is depicted in figure 93.
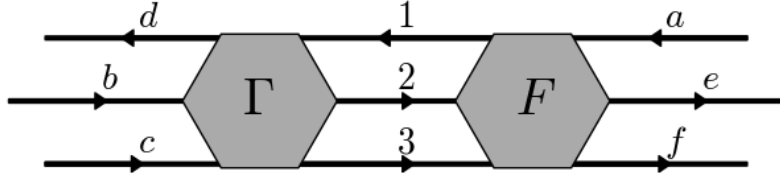

Figure 93: All diagrams reducible in the channel separating a, e, f from b, c, d. The variables 1, 2 and 3 are to be summed over and a factor $1/2$ is required to avoid overcounting.

The corresponding BSLE is given by[1]

$$F\begin{pmatrix} a & b & c \\ d & e & f \end{pmatrix} = \Gamma\begin{pmatrix} a & b & c \\ d & e & f \end{pmatrix} + \frac{1}{2}\sum_{1,2,3}\Gamma\begin{pmatrix} 1 & b & c \\ d & 2 & 3 \end{pmatrix}G(1)G(2)G(3)\,F\begin{pmatrix} a & 2 & 3 \\ 1 & e & f \end{pmatrix}. \tag{289}$$

Again, we insert the explicit expression (284) for F, allowing us to simplify the summations.

$$\delta^{abc}_{def}\varphi(a)\varphi(b)\varphi(c) = \Gamma\begin{pmatrix} a & b & c \\ d & e & f \end{pmatrix} + \frac{1}{2}\Bigg(G(a)\varphi(a)G(e)\varphi(e)G(f)\varphi(f)\Gamma\begin{pmatrix} a & b & c \\ d & e & f \end{pmatrix} -$$

$$G(a)\varphi(a)G(e)\varphi(e)G(f)\varphi(f)\Gamma\begin{pmatrix} a & b & c \\ d & f & e \end{pmatrix}\Bigg) + \sum_1\frac{1}{2}\Bigg($$

$$\delta^a_e G(a)\varphi(a)G(f)\varphi(f)G(1)\varphi(1)\Gamma\begin{pmatrix} 1 & b & c \\ d & f & 1 \end{pmatrix} - \delta^a_e G(a)\varphi(a)G(f)\varphi(f)G(1)\varphi(1)\Gamma\begin{pmatrix} 1 & b & c \\ d & 1 & f \end{pmatrix} +$$

$$\delta^a_f G(a)\varphi(a)G(e)\varphi(e)G(1)\varphi(1)\Gamma\begin{pmatrix} 1 & b & c \\ d & 1 & e \end{pmatrix} - \delta^a_f G(a)\varphi(a)G(e)\varphi(e)G(1)\varphi(1)\Gamma\begin{pmatrix} 1 & b & c \\ d & e & 1 \end{pmatrix}\Bigg) \tag{290}$$

While Γ does not show full crossing symmetry under exchange of any two entering or leaving lines, we can exchange equivalent ones (i.e. 2 and 3 or b and c in the BSLE above).

$$\Gamma\begin{pmatrix} a & b & c \\ d & e & f \end{pmatrix} = -\Gamma\begin{pmatrix} a & b & c \\ d & f & e \end{pmatrix} = \Gamma\begin{pmatrix} a & c & b \\ d & f & e \end{pmatrix} = -\Gamma\begin{pmatrix} a & c & b \\ d & e & f \end{pmatrix}. \tag{291}$$

---

[1]Again, terms accounting for two-particle reducible diagrams were neglected. Also, the one-particle reducible contributions of F were not properly accounted for. In principle, this can be accounted for, but at the cost of massively increased algebraic verbosity.

But we cannot exchange the leftmost arguments, since they are distinguishable by having a different orientation within the BSLE. Using these crossing relations, we can simplify equation (290):

$$\delta_{def}^{abc}\varphi(a)\varphi(b)\varphi(c) = \Gamma\begin{pmatrix} a & b & c \\ d & e & f \end{pmatrix} + G(a)\varphi(a)G(e)\varphi(e)G(f)\varphi(f)\Gamma\begin{pmatrix} a & b & c \\ d & e & f \end{pmatrix} + \sum_1 \Bigg($$

$$\delta_e^a G(a)\varphi(a)G(f)\varphi(f)G(1)\varphi(1)\Gamma\begin{pmatrix} 1 & b & c \\ d & f & 1 \end{pmatrix} + \delta_f^a G(a)\varphi(a)G(e)\varphi(e)G(1)\varphi(1)\Gamma\begin{pmatrix} 1 & b & c \\ d & 1 & e \end{pmatrix}\Bigg) \quad (292)$$

We can immediately see that for the case $a \neq e$ and $a \neq f$, essentially equivalent to $a = d$ if we require a non-vanishing contribution, the sums vanish. In such a case, we recover an expression similar to the ppp-case:

$$\Gamma\begin{pmatrix} a & b & c \\ d & e & f \end{pmatrix} = \frac{\delta_{def}^{abc}\varphi(a)\varphi(b)\varphi(c)}{1 + G(a)\varphi(a)G(e)\varphi(e)G(f)\varphi(f)} \quad (293)$$

Without loss of generality, we can therefore write:

$$\Gamma\begin{pmatrix} a & b & c \\ d & e & f \end{pmatrix} = \frac{\delta_{def}^{abc}\varphi(a)\varphi(b)\varphi(c)}{1 + G(a)\varphi(a)G(e)\varphi(e)G(f)\varphi(f)} + \delta_e^a \Delta_1 \begin{pmatrix} a & b & c \\ d & e & f \end{pmatrix} + \delta_f^a \Delta_2 \begin{pmatrix} a & b & c \\ d & e & f \end{pmatrix}, \quad (294)$$

with Δ_1 and Δ_2 being arbitrary functions for the moment. Employing the crossing symmetry

$$\Gamma\begin{pmatrix} a & b & c \\ d & e & f \end{pmatrix} = -\Gamma\begin{pmatrix} a & b & c \\ d & f & e \end{pmatrix}, \quad (295)$$

we can establish a relation between them:

$$\Delta_1 \begin{pmatrix} a & b & c \\ d & e & f \end{pmatrix} = -\Delta_2 \begin{pmatrix} a & b & c \\ d & f & e \end{pmatrix}. \quad (296)$$

From here on, we will call Δ_1 just Δ and express Δ_2 in terms of it. As a next step, we need to insert this expression for Γ into our BSLE.

$$\delta_{def}^{abc}\varphi(a)\varphi(b)\varphi(c) = (1 + G(a)\varphi(a)G(e)\varphi(e)G(f)\varphi(f))\Bigg(\frac{\delta_{def}^{abc}\varphi(a)\varphi(b)\varphi(c)}{1 + G(a)\varphi(a)G(e)\varphi(e)G(f)\varphi(f)}+$$

$$\delta_e^a \Delta\begin{pmatrix} a & b & c \\ d & a & f \end{pmatrix} - \delta_f^a \Delta\begin{pmatrix} a & b & c \\ d & a & e \end{pmatrix}\Bigg) + \sum_1 \Bigg($$

$$\delta_e^a G(a)\varphi(a)G(f)\varphi(f)G(1)\varphi(1)\cdot$$

$$\Bigg(\frac{\delta_{df1}^{1bc}\varphi(1)\varphi(b)\varphi(c)}{1 + G(1)\varphi(1)G(f)\varphi(f)G(1)\varphi(1)} + \delta_f^1 \Delta\begin{pmatrix} 1 & b & c \\ d & f & 1 \end{pmatrix} - \delta_1^1 \Delta\begin{pmatrix} 1 & b & c \\ d & 1 & f \end{pmatrix}\Bigg)+$$

$$\delta_f^a G(a)\varphi(a)G(e)\varphi(e)G(1)\varphi(1)\cdot$$

$$\Bigg(\frac{\delta_{d1e}^{1bc}\varphi(1)\varphi(b)\varphi(c)}{1 + G(1)\varphi(1)G(e)\varphi(e)G(1)\varphi(1)} + \delta_1^1 \Delta\begin{pmatrix} 1 & b & c \\ d & 1 & e \end{pmatrix} - \delta_e^1 \Delta\begin{pmatrix} 1 & b & c \\ d & e & 1 \end{pmatrix}\Bigg)\Bigg) \quad (297)$$

The terms without δ_e^a or δ_f^a cancel exactly and the terms with either δ_e^1 or δ_f^1 contribute with exactly one sumand in the sum, leaving us with the following terms:

$$0 = (1 + G(a)\varphi(a)G(e)\varphi(e)G(f)\varphi(f))\Bigg(\delta_e^a \Delta\begin{pmatrix} a & b & c \\ d & a & f \end{pmatrix} - \delta_f^a \Delta\begin{pmatrix} a & b & c \\ d & a & e \end{pmatrix}\Bigg)+$$

$$\delta_e^a G(a)\varphi(a)G(f)\varphi(f)\cdot\Bigg(G(f)\varphi(f)\Delta\begin{pmatrix} f & b & c \\ d & f & f \end{pmatrix}+$$

$$\sum_1 G(1)\varphi(1)\Bigg(\frac{\delta_{df1}^{1bc}\varphi(1)\varphi(b)\varphi(c)}{1 + G(1)\varphi(1)G(f)\varphi(f)G(1)\varphi(1)} - \Delta\begin{pmatrix} 1 & b & c \\ d & 1 & f \end{pmatrix}\Bigg)\Bigg)+$$

$$\delta_f^a G(a)\varphi(a)G(e)\varphi(e)\cdot\Bigg(-G(e)\varphi(e)\Delta\begin{pmatrix} e & b & c \\ d & e & e \end{pmatrix}+$$

$$\sum_1 G(1)\varphi(1)\Bigg(\frac{\delta_{d1e}^{1bc}\varphi(1)\varphi(b)\varphi(c)}{1 + G(1)\varphi(1)G(e)\varphi(e)G(1)\varphi(1)} + \Delta\begin{pmatrix} 1 & b & c \\ d & 1 & e \end{pmatrix}\Bigg)\Bigg) \quad (298)$$

We now require the equation to be fulfilled for the terms containing δ_e^a and δ_f^a separately, yielding the two equations

$$0 = (1 + G(a)\varphi(a)G(a)\varphi(a)G(f)\varphi(f)) \, \Delta \begin{pmatrix} a & b & c \\ d & a & f \end{pmatrix} + G(a)\varphi(a)G(f)\varphi(f) \cdot$$

$$\left(G(f)\varphi(f)\Delta \begin{pmatrix} f & b & c \\ d & f & f \end{pmatrix} + \right.$$

$$\left. \sum_1 G(1)\varphi(1) \left(\frac{\delta_{df1}^{1bc}\varphi(1)\varphi(b)\varphi(c)}{1 + G(1)\varphi(1)G(f)\varphi(f)G(1)\varphi(1)} - \Delta \begin{pmatrix} 1 & b & c \\ d & 1 & f \end{pmatrix} \right) \right) \quad (299)$$

for δ_e^a and

$$0 = -(1 + G(a)\varphi(a)G(e)\varphi(e)G(a)\varphi(a)) \, \Delta \begin{pmatrix} a & b & c \\ d & a & e \end{pmatrix} + G(a)\varphi(a)G(e)\varphi(e) \cdot$$

$$\left(-G(e)\varphi(e)\Delta \begin{pmatrix} e & b & c \\ d & e & e \end{pmatrix} + \right.$$

$$\left. \sum_1 \left(\frac{\delta_{d1e}^{1bc}\varphi(1)\varphi(b)\varphi(c)}{1 + G(1)\varphi(1)G(e)\varphi(e)G(1)\varphi(1)} + \Delta \begin{pmatrix} 1 & b & c \\ d & 1 & e \end{pmatrix} \right) \right) \quad (300)$$

for δ_f^a. It can be easily verified, that apart from the roles of e and f being exchanged and an overall sign, the two equations are equivalent. For this reason, we will only investigate the first equation further. We will now reduce the number of variables Δ depends on to a more managable four independent ones. To this end, the first sumand is brought to the left hand side of the equation.

$$-(1 + G(a)\varphi(a)G(a)\varphi(a)G(f)\varphi(f)) \, \Delta \begin{pmatrix} a & b & c \\ d & a & f \end{pmatrix} = G(a)\varphi(a)G(f)\varphi(f) \cdot$$

$$\left(G(f)\varphi(f)\Delta \begin{pmatrix} f & b & c \\ d & f & f \end{pmatrix} + \right.$$

$$\left. \sum_1 G(1)\varphi(1) \left(\frac{\delta_{df1}^{1bc}\varphi(1)\varphi(b)\varphi(c)}{1 + G(1)\varphi(1)G(f)\varphi(f)G(1)\varphi(1)} - \Delta \begin{pmatrix} 1 & b & c \\ d & 1 & f \end{pmatrix} \right) \right) \quad (301)$$

From here, one can divide by $G(a)\varphi(a)$, removing the dependence of the right hand side on the frequency a, implying that the left hand side be independent as well. We introduce a new quantity $\mathcal{U}$, which does not depend on a:

$$\frac{(1 + G(a)\varphi(a)G(a)\varphi(a)G(f)\varphi(f))}{G(a)\varphi(a)} \Delta \begin{pmatrix} a & b & c \\ d & a & f \end{pmatrix} = \mathcal{U} \begin{pmatrix} & b & c \\ d & & f \end{pmatrix} \quad (302)$$

$$\Delta \begin{pmatrix} a & b & c \\ d & a & f \end{pmatrix} = \mathcal{U} \begin{pmatrix} & b & c \\ d & & f \end{pmatrix} \frac{G(a)\varphi(a)}{(1 + G(a)\varphi(a)G(a)\varphi(a)G(f)\varphi(f))} \quad (303)$$

The blank spaces in the variable definitions of $\mathcal{U}$ were kept for aesthetic reasons and to preserve symmetry of the notation[1]. We insert the newly calculated expression for Δ into equation 301 and remove the known a-dependence.

$$-\mathcal{U} \begin{pmatrix} & b & c \\ d & & f \end{pmatrix} = G(f)\varphi(f) \cdot$$

$$\left(G(f)\varphi(f)\mathcal{U} \begin{pmatrix} & b & c \\ d & & f \end{pmatrix} \frac{G(f)\varphi(f)}{(1 + G(f)\varphi(f)G(f)\varphi(f)G(f)\varphi(f))} + \right.$$

$$\sum_1 G(1)\varphi(1) \left(\frac{\delta_{df1}^{1bc}\varphi(1)\varphi(b)\varphi(c)}{1 + G(1)\varphi(1)G(f)\varphi(f)G(1)\varphi(1)} - \right.$$

$$\left. \left. \mathcal{U} \begin{pmatrix} & b & c \\ d & & f \end{pmatrix} \frac{G(1)\varphi(1)}{(1 + G(1)\varphi(1)G(1)\varphi(1)G(f)\varphi(f))} \right) \right) \quad (304)$$

---

[1] Also, the blank spaces allowed me to preserve my own sanity when keeping track of the frequency indices, which seemed desireable.

$$\mathcal{U}\begin{pmatrix} & b & c \\ d & & f \end{pmatrix}\left(\sum_1 \frac{G(1)\varphi(1)G(1)\varphi(1)G(f)\varphi(f)}{(1+G(1)\varphi(1)G(1)\varphi(1)G(f)\varphi(f))}-\right.$$

$$\left.\frac{G(f)\varphi(f)G(f)\varphi(f)G(f)\varphi(f)}{(1+G(f)\varphi(f)G(f)\varphi(f)G(f)\varphi(f))}-1\right)=$$

$$G(f)\varphi(f)\sum_1 G(1)\varphi(1)\frac{\delta^{1bc}_{df1}\varphi(1)\varphi(b)\varphi(c)}{1+G(1)\varphi(1)G(f)\varphi(f)G(1)\varphi(1)}. \tag{305}$$

Evaluating the right hand side of above equation is straightforward, so we end up with a closed form expression for $\mathcal{U}$. We will now investigate the evaluation of the sum as well as the resulting features of Γ. Decomposing δ^{1bc}_{df1} again allows us to simplify the summations:

$$G(f)\varphi(f)\sum_1 G(1)\varphi(1)\frac{\delta^{1bc}_{df1}\varphi(1)\varphi(b)\varphi(c)}{1+G(1)\varphi(1)G(f)\varphi(f)G(1)\varphi(1)}=G(f)\varphi(f)\cdot\Bigg($$

$$\delta^b_f\delta^c_d\frac{G(d)\varphi^3(d)\varphi(f)}{1+(G(d)\varphi(d))^2 G(f)\varphi(f)}-\delta^c_f\delta^b_d\frac{G(d)\varphi^3(d)\varphi(f)}{1+(G(d)\varphi(d))^2 G(f)\varphi(f)}+$$

$$\delta^c_f\delta^b_d\sum_1\frac{G(1)\varphi^2(1)\varphi(d)\varphi(f)}{1+(G(1)\varphi(1))^2 G(f)\varphi(f)}-\delta^b_f\delta^c_d\sum_1\frac{G(1)\varphi^2(1)\varphi(d)\varphi(f)}{1+(G(1)\varphi(1))^2 G(f)\varphi(f)}+$$

$$\delta^b_f\delta^c_d\frac{G(f)\varphi^3(f)\varphi(d)}{1+(G(f)\varphi(f))^3}-\delta^c_f\delta^b_d\frac{G(f)\varphi^3(f)\varphi(d)}{1+(G(f)\varphi(f))^3}\Bigg) \tag{306}$$

If we define an auxiliary function F' depending on only the two variables d and f, we can write:

$$F'(d,f)=G(f)\varphi(f)\cdot$$
$$\left(\sum_1\frac{G(1)\varphi^2(1)\varphi(d)\varphi(f)}{1+(G(1)\varphi(1))^2 G(f)\varphi(f)}-\frac{G(d)\varphi^3(d)\varphi(f)}{1+(G(d)\varphi(d))^2 G(f)\varphi(f)}-\frac{G(f)\varphi^3(f)\varphi(d)}{1+(G(f)\varphi(f))^3}\right). \tag{307}$$

And the right hand side of equation (306) can be simplified to

$$\delta^{bc}_{df}F'(d,f). \tag{308}$$

and we can express $\mathcal{U}$ as:

$$\mathcal{U}\begin{pmatrix} & b & c \\ d & & f \end{pmatrix}=$$

$$\frac{\delta^{bc}_{df}F'(d,f)}{\left(\sum_1\frac{G(1)\varphi(1)G(1)\varphi(1)G(f)\varphi(f)}{(1+G(1)\varphi(1)G(1)\varphi(1)G(f)\varphi(f))}-\frac{G(f)\varphi(f)G(f)\varphi(f)G(f)\varphi(f)}{(1+G(f)\varphi(f)G(f)\varphi(f)G(f)\varphi(f))}-1\right)} \tag{309}$$

Or equivalently, by including the denominator into the definition of a new, two-variable $\mathcal{U}$:

$$\mathcal{U}\begin{pmatrix} & b & c \\ d & & f \end{pmatrix}=\delta^{bc}_{df}\mathcal{U}(d,f) \tag{310}$$

Note that, since the dependence of $\mathcal{U}(d,f)$ on d and f is not symmetric, we have

$$\mathcal{U}\begin{pmatrix} & b & c \\ d & & f \end{pmatrix}=-\mathcal{U}\begin{pmatrix} & c & b \\ d & & f \end{pmatrix}, \tag{311}$$

but not

$$\mathcal{U}\begin{pmatrix} & b & c \\ f & & d \end{pmatrix}=-\mathcal{U}\begin{pmatrix} & b & c \\ d & & f \end{pmatrix}. \tag{312}$$

If we also define a function $\beta(a,f)$:

$$\beta(a,f)=\frac{G(a)\varphi(a)}{(1+G(a)\varphi(a)G(a)\varphi(a)G(f)\varphi(f))}, \tag{313}$$

114

it is possible to write Δ as:

$$\Delta \begin{pmatrix} a & b & c \\ d & a & f \end{pmatrix} = \delta_{df}^{bc}\,\mathcal{U}(d,f)\cdot\beta(a,f),\tag{314}$$

and to finally express Γ for the *pph*-case as

$$\Gamma \begin{pmatrix} a & b & c \\ d & e & f \end{pmatrix} = \frac{\delta_{def}^{abc}\varphi(a)\varphi(b)\varphi(c)}{1+G(a)\varphi(a)G(e)\varphi(e)G(f)\varphi(f)} + \delta_e^a\delta_{df}^{bc}\mathcal{U}(d,f)\cdot\beta(a,f) - \delta_f^a\delta_{de}^{bc}\mathcal{U}(d,e)\cdot\beta(a,e),\quad\tag{315}$$

with $\mathcal{U}$ defined in equation (309). The crossing relations

$$\Gamma \begin{pmatrix} a & b & c \\ d & e & f \end{pmatrix} = -\Gamma \begin{pmatrix} a & c & b \\ d & e & f \end{pmatrix} = -\Gamma \begin{pmatrix} a & b & c \\ d & f & e \end{pmatrix}\tag{316}$$

are easily verified. Just as in the two-particle *ph* case, we can see that there is a term looking exactly like the *ppp*-irreducible vertex. This term describes the case when the distinguished particle running into the other direction within the BSLE has the same frequency on one end of the ladder as on the other, but no other frequencies are equal to it. Different contributions arise when either $a = e$ or $a = f$ (or equivalently $d = b$ or $d = c$), the possibility for the distinguished particle to "loop back" immediately arises and suddenly internal degrees of freedom within the BSLE need to be summed over. Unlike the two-particle case, there are two possibilities of such loops arising instead of one. Thus, there are also two additional terms; the δ_e^a and the δ_f^a one.

F. Ladder approximations on the three-particle level within the dual fermion approach for the Falicov-Kimball model

Since we know of instabilities of the FKM in the *ph*-channel, already on the two particle level, we want to investigate the effect of such instabilities on the self-energy of other electrons. To do so, we calculate the three-particle ladder approximations for the 9 *pph*- or *phh*-like channels within dual fermion theory. This section is quite similar to appendix E in that the same approaches are used to solve the algebraic equations, though to determine the full vertex from a irreducible one and not the other way round. Again, effects of two-particle reducibility are neglected. Our starting point is the Bethe-Salpeter-like equation (BSLE) within DF

$$
F_q \begin{pmatrix} a & b & c \\ d & e & f \end{pmatrix} = F^{(3)} \begin{pmatrix} a & b & c \\ d & e & f \end{pmatrix} +
$$
$$
\frac{1}{2} \sum_{1,2,3,k_1,k_2} F_q \begin{pmatrix} a & b & 3 \\ d & 1 & 2 \end{pmatrix} \widetilde{G}(1,k_1)\widetilde{G}(2,k_2)\widetilde{G}(3,q+k_1+k_2)\, F^{(3)} \begin{pmatrix} 1 & 2 & c \\ 3 & e & f \end{pmatrix}. \quad (317)
$$

Here, 1, 2 and 3 are frequencies to be summed over and q, k_1 and k_2 are vectors from the first Brillouin zone. $\widetilde{G}$ denotes dual (k-dependent) Green's functions. It is possible to define a three-particle susceptibility χ_q^0:

$$
\chi_q^0(1,2,3) = \sum_{k_1,k_2} \widetilde{G}(1,k_1)\widetilde{G}(2,k_2)\widetilde{G}(3,q+k_1+k_2). \quad (318)
$$

We insert the expression

$$
F^{(3)} \begin{pmatrix} a & b & c \\ d & e & f \end{pmatrix} = \delta_{def}^{abc}\, \varphi(a)\varphi(b)\varphi(c) \quad (319)
$$

for $F^{(3)}$, allowing us to evaluate the summation over the indices 1 and 2.

$$
F_q \begin{pmatrix} a & b & c \\ d & e & f \end{pmatrix} = \delta_{def}^{abc}\, \varphi(a)\varphi(b)\varphi(c) + \frac{1}{2}\Bigg\{ \sum_3 \Bigg[F_q \begin{pmatrix} a & b & 3 \\ d & 3 & e \end{pmatrix} \chi_q^0(3,e,3)\varphi(3)\varphi(e)\varphi(c)\delta_f^c -
$$
$$
F_q \begin{pmatrix} a & b & 3 \\ d & 3 & f \end{pmatrix} \chi_q^0(3,f,3)\varphi(3)\varphi(e)\varphi(f)\delta_e^c + F_q \begin{pmatrix} a & b & 3 \\ d & f & 3 \end{pmatrix} \chi_q^0(f,3,3)\varphi(3)\varphi(e)\varphi(f)\delta_e^c -
$$
$$
F_q \begin{pmatrix} a & b & 3 \\ d & e & 3 \end{pmatrix} \chi_q^0(e,3,3)\varphi(3)\varphi(e)\varphi(f)\delta_f^c \Bigg] + F_q \begin{pmatrix} a & b & c \\ d & e & f \end{pmatrix} \chi_q^0(e,f,c)\varphi(c)\varphi(e)\varphi(f) -
$$
$$
F_q \begin{pmatrix} a & b & c \\ d & f & e \end{pmatrix} \chi_q^0(f,e,c)\varphi(f)\varphi(e)\varphi(c) \Bigg\}. \quad (320)
$$

Using crossing relations, it is possible to form pairs of terms, absorbing the factor 1/2 on the right-hand side of above equation.

$$
F_q \begin{pmatrix} a & b & c \\ d & e & f \end{pmatrix} = \delta_{def}^{abc}\, \varphi(a)\varphi(b)\varphi(c) + F_q \begin{pmatrix} a & b & c \\ d & e & f \end{pmatrix} \chi_q^0(e,f,c)\varphi(e)\varphi(f)\varphi(c) +
$$
$$
\sum_3 \Bigg[\delta_f^c F_q \begin{pmatrix} a & b & 3 \\ d & 3 & e \end{pmatrix} \chi_q^0(e,3,3)\varphi(c)\varphi(e)\varphi(3) + \delta_e^c F_q \begin{pmatrix} a & b & 3 \\ d & f & 3 \end{pmatrix} \chi_q^0(f,3,3)\varphi(e)\varphi(f)\varphi(3) \Bigg]. \quad (321)
$$

When $c \neq e$ and $c \neq f$, we can solve the equation for F_q. For the general solution, we only need to add terms proportional to δ_f^c and δ_e^c. We thus make an Ansatz:

$$
F_q \begin{pmatrix} a & b & c \\ d & e & f \end{pmatrix} = \delta_{def}^{abc}\frac{\varphi(a)\varphi(b)\varphi(c)}{1-\chi_q^0(e,f,c)\varphi(e)\varphi(f)\varphi(c)} + \delta_f^c M_q \begin{pmatrix} a & b & c \\ d & e & f \end{pmatrix} + \delta_e^c M_q' \begin{pmatrix} a & b & c \\ d & e & f \end{pmatrix} \quad (322)
$$

From the crossing relation

$$
F_q \begin{pmatrix} a & b & c \\ d & e & f \end{pmatrix} = -F_q \begin{pmatrix} a & b & c \\ d & f & e \end{pmatrix}, \quad (323)
$$

we can infer

$$
M_q \begin{pmatrix} a & b & c \\ d & f & e \end{pmatrix} = -M_q' \begin{pmatrix} a & b & c \\ d & e & f \end{pmatrix}. \quad (324)
$$

116

Which allows us to simplify the expression for F_q further. We can also drop the dependency of M on f or e in the terms containing δ_f^c and δ_e^c respectively.

$$F_q \begin{pmatrix} a & b & c \\ d & e & f \end{pmatrix} = \delta_{def}^{abc} \frac{\varphi(a)\varphi(b)\varphi(c)}{1 - \chi_q^0(e,f,c)\varphi(e)\varphi(f)\varphi(c)} + \delta_f^c M_q \begin{pmatrix} a & b & c \\ d & e \end{pmatrix} - \delta_e^c M_q \begin{pmatrix} a & b & c \\ d & f \end{pmatrix}. \quad (325)$$

This expression for F_q can be inserted into equation (320), yielding

$$\left[\delta_{def}^{abc} \frac{\varphi(a)\varphi(b)\varphi(c)}{1 - \chi_q^0(e,f,c)\varphi(e)\varphi(f)\varphi(c)} + \delta_f^c M_q \begin{pmatrix} a & b & c \\ d & e \end{pmatrix} - \delta_e^c M_q \begin{pmatrix} a & b & c \\ d & f \end{pmatrix} \right] \cdot$$

$$(1 - \chi_q^0(e,f,c)\varphi(e)\varphi(f)\varphi(c)) = \delta_{def}^{abc}\varphi(a)\varphi(b)\varphi(c) +$$

$$\delta_f^c \left\{ \sum_3 \left[\delta_{d3e}^{ab3} \frac{\varphi(a)\varphi(b)\varphi(3)}{1 - \chi_q^0(e,3,3)\varphi(e)\varphi(3)\varphi(3)} + \delta_e^3 M_q \begin{pmatrix} a & b & 3 \\ d & 3 \end{pmatrix} - \delta_3^3 M_q \begin{pmatrix} a & b & 3 \\ d & e \end{pmatrix} \right] \cdot \right.$$

$$\left. \left[\chi_q^0(e,3,3)\varphi(c)\varphi(e)\varphi(3) \right] \right\} +$$

$$\delta_e^c \left\{ \sum_3 \left[\delta_{df3}^{ab3} \frac{\varphi(a)\varphi(b)\varphi(3)}{1 - \chi_q(f,3,3)\varphi(f)\varphi(3)\varphi(3)} + \delta_3^3 M_q \begin{pmatrix} a & b & 3 \\ d & f \end{pmatrix} - \delta_f^3 M_q \begin{pmatrix} a & b & 3 \\ d & 3 \end{pmatrix} \right] \cdot \right.$$

$$\left. \left[\chi_q(f,3,3)\varphi(c)\varphi(f)\varphi(3) \right] \right\}. \quad (326)$$

All terms containing δ_{def}^{abc} cancel exactly. Both sides of the equation separate into parts propartional to δ_f^c and δ_e^c, which are equivalent and necessarily fullfilled simultaneously. Thus, we only investigate the δ_f^c part explicitely.

$$M_q \begin{pmatrix} a & b & c \\ d & e \end{pmatrix} (1 - \chi_q^0(e,c,c)\varphi(e)\varphi(c)\varphi(c)) = M_q \begin{pmatrix} a & b & e \\ d & e \end{pmatrix} \chi_q^0(e,e,e)\varphi(c)\varphi(e)\varphi(e) +$$

$$\left\{ \sum_3 \left[\delta_{d3e}^{ab3} \frac{\varphi(a)\varphi(b)\varphi(3)}{1 - \chi_q^0(e,3,3)\varphi(e)\varphi(3)\varphi(3)} - M_q \begin{pmatrix} a & b & 3 \\ d & e \end{pmatrix} \right] \chi_q^0(e,3,3)\varphi(c)\varphi(e)\varphi(3) \right\}. \quad (327)$$

Note that the right hand side of the equation is proportional to $\varphi(c)$ and otherwise shows no dependency on the variable c. This implies that a factorisation property must hold:

$$M_q \begin{pmatrix} a & b & c \\ d & e \end{pmatrix} = N_q \begin{pmatrix} a & b \\ d & e \end{pmatrix} \frac{\varphi(c)}{1 - \chi_q^0(e,c,c)\varphi(e)\varphi(c)\varphi(c)} \quad (328)$$

with some general function N_q yet to be determined. By inserting (328) into (327), we arrive at

$$N_q \begin{pmatrix} a & b \\ d & e \end{pmatrix} = N_q \begin{pmatrix} a & b \\ d & e \end{pmatrix} \left(\frac{\chi_q^0(e,e,e)\varphi(e)\varphi(e)\varphi(e)}{1 - \chi_q^0(e,c,c)\varphi(e)\varphi(c)\varphi(c)} - \sum_3 \frac{\chi_q^0(e,3,3)\varphi(e)\varphi(3)\varphi(3)}{1 - \chi_q^0(e,3,3)\varphi(e)\varphi(3)\varphi(3)} \right) +$$

$$\sum_3 \delta_{d3e}^{ab3} \frac{\varphi(a)\varphi(b)\varphi(3)}{1 - \chi_q^0(e,3,3)\varphi(e)\varphi(3)\varphi(3)} \chi_q^0(e,3,3)\varphi(e)\varphi(3). \quad (329)$$

In the next step, we collect all terms containing N_q on the left hand side and evaluate δ_{d3e}^{ab3} as follows:

$$\delta_{d3e}^{ab3} = -\delta_3^3 \delta_{de}^{ab} + \delta_d^a \delta_3^b \delta_e^3 - \delta_3^a \delta_d^b \delta_e^3 + \delta_3^a \delta_e^b \delta_d^3 - \delta_e^a \delta_3^b \delta_d^3 = -\delta_3^3 \delta_{de}^{ab} + \delta_{de}^{ab} \delta_e^3 + \delta_{de}^{ab} \delta_d^3. \quad (330)$$

Which allows us to express N_q

$$N_q \begin{pmatrix} a & b \\ d & e \end{pmatrix} = \delta_{de}^{ab} \left(1 - \frac{\chi_q^0(e,e,e)\varphi(e)\varphi(e)\varphi(e)}{1 - \chi_q^0(e,c,c)\varphi(e)\varphi(c)\varphi(c)} + \sum_3 \frac{\chi_q^0(e,3,3)\varphi(e)\varphi(3)\varphi(3)}{1 - \chi_q^0(e,3,3)\varphi(e)\varphi(3)\varphi(3)} \right)^{-1} \cdot$$

$$\left(\frac{\chi_q^0(e,e,e)\varphi(d)\varphi(e)\varphi(e)\varphi(e)\varphi(e)}{1 - \chi_q^0(e,e,e)\varphi(e)\varphi(e)\varphi(e)} + \frac{\chi_q^0(e,d,d)\varphi(d)\varphi(d)\varphi(d)\varphi(e)\varphi(e)}{1 - \chi_q^0(e,d,d)\varphi(e)\varphi(d)\varphi(d)} - \right.$$

$$\left. \sum_3 \frac{\chi_q^0(e,3,3)\varphi(d)\varphi(e)\varphi(e)\varphi(3)\varphi(3)}{1 - \chi_q^0(e,3,3)\varphi(e)\varphi(3)\varphi(3)} \right). \quad (331)$$

G. Symmetry-broken mean-field treatment of the Falicov-Kimball model

The half-filled Falicov-Kimball model on a square lattice displays an instability towards checkerboard ordering. In an effort to further the understanding of this ordered phase, a simplicistic mean field model was developed and numerically investigated. To account for symmetry breaking, the unit cell was doubled, so as to include two lattice sites. This has the effect of breaking the Brillouin zone in half as well, at the same time introducing a second band for the c-electrons.

For a given interaction value and temperature, a square lattice with two distinct types of sites and nearest neighbour hopping t ($4t = 1$ was again chosen as the unit of energy) was investigated. The effect of the interaction was approximated as a mean field in the following form: For the two sublattices, the mean occupation by f-electrons on the respective types of site was multiplied by the interaction strength and added as an onsite-term for c-electrons. The relatively simple problem of diagonalising the resulting one-particle Hamiltonian for the c-electrons remained. From them, the mean occupation could be calculated as the Fermi function of the Eigenenergy multiplied by the absolute square of the amplitude on the respective type of site. The mean occupation of the c-electrons was in turn multipied by U and used as an onsite-potential for the f-electrons. The procedure was iterated until convergence was achieved[1].

Besides the (crude) prediction of the transition temperature, this approach also provides an approximative dispersion relation, as well as a density of states, for the c-electrons. The dispersion relation is interesting because the states at the former Fermi-edge split into states which are localised exclusively on one of the sublattices and separated by an effective interaction value $U_{eff} = U \cdot (p_{fA} - p_{fB})$ in energy, where p_{fA} and p_{fB} are the mean occupations of f-electrons on the sublattices. The resulting densities of state for different values of U_{eff} are documented in figure 94. The pronounced peaks at the inner edges of the bands provide a stark contrast to the smoother Hubbard-bands centered around a peak one obtains from DMFT. The resulting f and c-occupations on the f-dominated sublattice are given as false-colour plots in figure 95. The f-occupation is found to tip much easier, which is expected, as these electrons have no kinetic energy, which would tend to delocalise them. One the other hand, the c-electrons always have a finite weight on the f-dominated sublattice for finite values of U. Note the prediction of of an ordered phase at very high temperatures compared to the DMFT Néel temperature (cf. [79]). This is to be expected as mean-field theories favour ordering.

The numerical data was generated using a k-grid of $121 \cdot 121$ points with the f-occupations being initialised as $p_{fA} = 1$ and $p_{fB} = 0$, with a separate run starting with $p_{fA} = 0.55$ and $p_{fB} = 0.45$ showing consistent results[2].

---

[1]For the investigated particle-hole symmetric parameter sets, it is important to initialise the calculation with a slightly symmetry-broken initial state, as the exact particle-hole symmetry otherwise pins both c and f occupations to exactly 1/2.

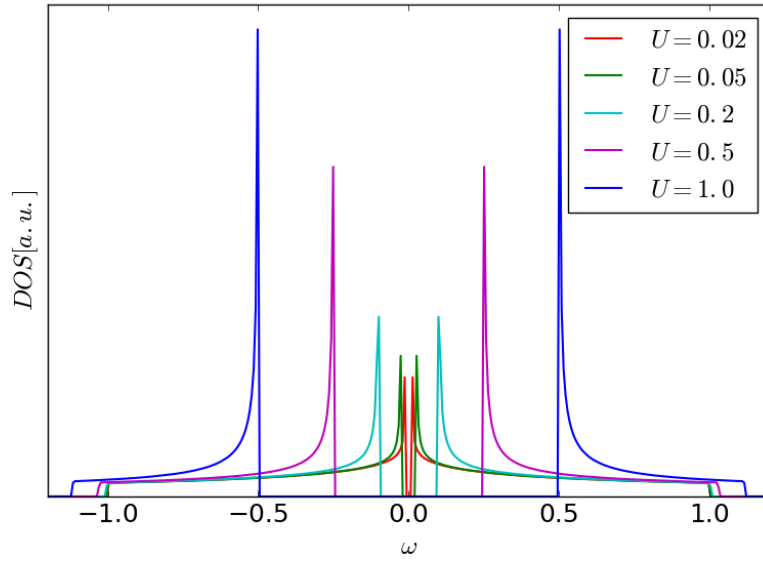[2]This implies that there are not two separate stable configurations.

Figure 94: Density of states for c-electrons when the system becomes fully checkerboard-ordered. (corresponds to $U_{eff} = U$)
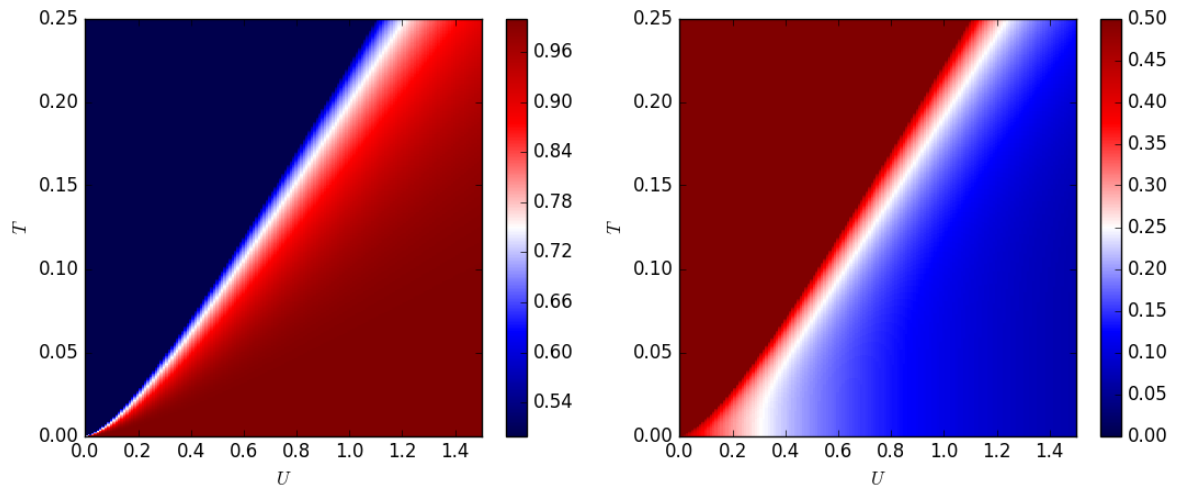

Figure 95: Occupation of one type of site by f-electrons (left) and c-electrons (right) as a function of interaction strength U and temperature T.

H. Summary of occassionally useful expressions

This section is dedicated to collecting equations which are frequently used for reference.

H.1. single-particle quantities

The probability of a site being occupied by an f-electron is called p_1.

$$p_1 = \langle f^\dagger f \rangle$$
$$p_2 = 1 - p_1$$

The c-electron Green's function within DMFT is called G, the Green's functions for sites occupied by an f-electron is called $\overline{G}$, the Green's function for sites without f-electron $\underline{G}$. They share a common hybridisation function Δ.

$$\underline{G}(\nu) = \frac{1}{i\nu - \Delta(\nu) + \mu},$$
$$\overline{G}(\nu) = \frac{1}{i\nu - \Delta(\nu) - U + \mu},$$
$$G(\nu) = p_1 \overline{G} + p_2 \underline{G}$$

The following identities hold:

$$\overline{G}(\nu) = \frac{G(\nu)\Sigma(\nu)}{p_1 U},$$
$$\underline{G}(\nu) = \frac{G(\nu)\left(U - \Sigma(\nu)\right)}{p_2 U},$$
$$\left(\Sigma(\nu) - p_1 U\right) = G(\nu)\left(U - \Sigma(\nu)\right)\Sigma(\nu).$$

H.2. two-particle quantities

To shorten expressions, the shorthand notation $\nu'' = \nu' + \omega$ is introduced. The full local c-electron vertex in ph-notation is given by:

$$F^{\nu\nu'\omega} = \beta(\delta_{\omega,0} - \delta_{\nu,\nu'})a(\nu)a(\nu''),$$
$$a(\nu) = \sqrt{1/p_1 p_2 U^2}(\Sigma(\nu) - U)\Sigma(\nu).$$

The local irreducible vertices (all in ph-notation) are given by

$$\Gamma_{pp}^{\nu\nu'\omega} = \beta(\delta_{\omega,0} - \delta_{\nu,\nu'})\frac{a(\nu)a(\nu'')}{1 + G(\nu)a(\nu)G(\nu'')a(\nu'')}$$

$$\Gamma_{ph}^{\nu\nu'\omega} = \beta\delta_{\omega,0}C^2\frac{a(\nu)a(\nu'')}{(1 + (G(\nu)a(\nu))^2)(1 + (G(\nu'')a(\nu''))^2)} - \beta\delta_{\nu,\nu'}\frac{a(\nu)a(\nu'')}{1 + G(\nu)a(\nu)G(\nu'')a(\nu'')}$$

$$\Gamma_{\overline{ph}}^{\nu\nu'\omega} = -\Gamma_{ph}^{\nu(\nu+\omega)(\nu'-\nu)}$$

$$\Lambda^{\nu\nu'\omega} = \beta(\delta_{\omega,0} - \delta_{\nu,\nu'})a(\nu)a(\nu'')\left(C^2\frac{1}{(1 + (G(\nu)a(\nu))^2)(1 + (G(\nu'')a(\nu''))^2)} + 2\frac{G(\nu)a(\nu)G(\nu'')a(\nu'')}{1 + G(\nu)a(\nu)G(\nu'')a(\nu'')}\right)$$

$$C^2 = \left(1 - \sum_{\nu_1}\frac{(G(\nu_1)a(\nu_1))^2}{1 + (G(\nu_1)a(\nu_1))^2}\right)^{-1}$$

H.3. n-particle quantities

The local n-particle Green's function for c-electrons is given by

$$G^{(n)}(a,b,c,\ldots,d,e,f,\ldots) = \delta_{def\ldots}^{abc\ldots}\left[p_1\left(\overline{G}(a)\overline{G}(b)\overline{G}(c)\ldots\right) + p_2\left(\underline{G}(a)\underline{G}(b)\underline{G}(c)\ldots\right)\right].$$

The one-particle connected contribution to the n-particle propagator is given by

$$T^{(n)}(a,b,c,\ldots,d,e,f,\ldots) = \delta_{def\ldots}^{abc\ldots}\mathcal{F}_n\left(\overline{G}(a) - \underline{G}(a)\right)\left(\overline{G}(b) - \underline{G}(b)\right)\left(\overline{G}(c) - \underline{G}(c)\right)\ldots,$$

with $\mathcal{F}_n$ given as:
$$\mathcal{F}_n = p_1(p_2)^n + p_2(-p_1)^n.$$
The fully connected contribution to the propagator $C^{(n)}$ is given by
$$C^{(n)}(a,b,c,...,d,e,f,...) = \delta_{def...}^{abc...}\mathcal{C}_n\big(\overline{G}(a) - \underline{G}(a)\big)\big(\overline{G}(b) - \underline{G}(b)\big)\big(\overline{G}(c) - \underline{G}(c)\big)... \, .$$

The factor $C^{(n)}$ being defined recursively as

$$\mathcal{C}_n = \mathcal{F}_n - \sum_{l=2}^{n-2}\binom{n-1}{l-1}\mathcal{C}_l\mathcal{F}_{n-l}.$$

The n-particle vertex $V^{(n)}$ function can be extracted by amputating the outer legs from the connected contribution to the propagator.

$$V^{(n)}(a,b,c,...,d,e,f,...) = \delta_{def...}^{abc...}\mathcal{C}_n\gamma(a)\gamma(b)\gamma(c)... \, ,$$

where γ is given by

$$\gamma(a) = \frac{\big(\overline{G}(a) - \underline{G}(a)\big)}{\big(G^{(1)}(a)\big)^2}.$$

References

[1] J. D. Hunter. Matplotlib: A 2D graphics environment. *Computing In Science & Engineering*, 2007.

[2] Faraday M. On conducting power generally. *Experimental Researches in Electricity. Royal Institution, London*, 1833.

[3] Braun F. Ueber die stromleitung durch schwefelmetalle. *Annalen der Physik und Chemie*, 1875.

[4] Lilienfeld J. E. Device for controlling electric current, 03 1928.

[5] Wilson A. H. The theory of electronic semi-conductors. *Proceedings of the Royal Society of London. Series A*, 1931.

[6] Bardeen J. and Brattain W. The transistor, a semi-conductor triode. *Physical Review*, 1948.

[7] Hartree D. R. The wave mechanics of an atom with a non-coulomb central field. *Proc. Cambr. Phil. Soc.*, 1928.

[8] Fock V. Näherungsmethode zur Lösung des quantenmechanischen Mehrkörperproblems. *Zeitschrift f. Physik*, 1930.

[9] Slater J. C. A simplification of the Hartree-Fock method. *Physical Review*, 1950.

[10] Bardeen J., Cooper L. N., and Schrieffer J. R. Theory of superconductivity. *Physical Review*, 1957.

[11] Hohenberg P. and Kohn W. Inhomogeneous electron gas. *Physical Review*, 1964.

[12] Kohn W. and Sham L. J. Self-consistent equations including exchange and correlation effects. *Physical Review*, 1965.

[13] Kohn W. Electronic structure of matter—wave functions and density functionals. *Rev. Mod. Phys.*, 1999.

[14] Capelle K. A bird's-eye view of density-functional theory. *arXiv:1611.07523*, 2002.

[15] Hubbard J. Electron correlations in narrow energy bands. *Proc. Phys. Soc. London*, 1963.

[16] Lieb E. H. and Wu F. Y. Absence of mott transition in an exact solution of the short-range, one-band model in one dimension. *Phys. Rev. Let.*, 1968.

[17] Yang C. N. η pairing and off-diagonal long-range order in a hubbard model. *Phys. Rev. Let.*, 1989.

[18] Essler F. H. L., Frahm H., Göhmann F., Klümper A., and Korepin V. E. *The One-Dimensional Hubbard Model*. Cambridge U.P., 2005.

[19] Metzner W. and Vollhardt D. Correlated lattice fermions in $d = \infty$ dimensions. *Phys. Rev. Lett.*, 1989.

[20] Anisimimov V. I., Poteryaev A. I., Korotin M. A., Anokhin A. O., and Kotliar G. First-principles calculations of the electronic structure and spectra of strongly correlated systems: dynamical mean-field theory. *J. Phys: Condens. Matter*, 1997.

[21] Lichtenstein A. I. and Katsnelson M. I. Ab initio calculations of quasiparticle band structure in correlated systems: LDA++ approach. *Phys. Rev. B*, 1998.

[22] Toschi A., Katanin A. A., and Held K. Dynamical vertex approximation: A step beyond dynamical mean-field theory. *Phys. Rev. B*, 2007.

[23] Rubtsov A. N., Katsnelson M. I., and Lichtenstein A. I. Dual fermion approach to nonlocal correlations in the Hubbard model. *Phys. Rev. B*, 2008.

[24] Rubtsov A. N., Katsnelson M. I., and Lichtenstein A. I. Dual boson approach to collective excitations in correlated fermionic systems. *Annals of Physics*, 2012.

[25] Katanin A. A. The effect of six-point one-particle reducible local interactions in the dual fermion approach. *J. Phys. A*, 2013.

[26] Ayral T. and Parcollet O. Mott physics and spin fluctuations: A unified framework. *Phys. Rev. B*, 2015.

[27] Ayral T. and Parcollet O. Mott physics and collective modes: An atomic approximation of the four-particle irreducible functional. *Phys. Rev. B*, 2016.

[28] Falicov L. M. and Kimball J. C. Simple model for semiconductor-metal transistions: SmB_6 and transition-metal oxides. *Phys. Rev. Lett.*, 1969.

[29] Freericks J.K. and Zlatić V. Exact dynamical mean-field theory of the Falicov-Kimball model. *Rev. Mod. Phys.*, 2003.

[30] Ribic T., Rohringer G., and Held K. Local correlation functions of arbitrary order for the Falicov-Kimball model. *Phys. Rev. B*, 2017.

[31] Ribic T., Gunacker P., Iskakov S., Wallerberger M., Rohringer G., Rubtsov A. N., Gull E., and Held K. Role of three-particle vertex within dual fermion calculations. *Phys. Rev. B*, 2017.

[32] Gunacker P., Wallerberger M., Gull E., Hausoel A., Sangiovanni G., and Held K. Continuous-time quantum monte carlo using worm sampling. *Phys. Rev. B*, 2015.

[33] Gunacker P., Wallerberger M., Ribic T., Hausoel A., Sangiovanni G., and Held K. Worm-improved estimators in continuous-time quantum monte carlo. *Phys. Rev. B*, 2016.

[34] Abrikosov A., Gorkov L., and Dzyaloshinsky. *Methods of Quantum Field Theory in Statistical Physics*. Dover, 1975.

[35] Rohringer G. *New routes towards a theoretical treatment of nonlocal electronic correlations*. PhD thesis, TU Wien, 2013.

[36] Rohringer G., Hafermann H., Toschi A., Katanin A. A., Antipov A. E., Katsnelson M. I., Lichtenstein A. I., Rubtsov A. N., and Held K. Diagrammatic routes to nonlocal correlations beyond dynamical mean field theory. *Rev. Mod. Phys.*, 2018.

[37] Kubo R. Statistical-mechanical theory of irreversible processes. I. general theory and simple applications to magnetic and conduction problems. *J. Phys. Soc. Jpn.*, 1957.

[38] Held K. Electronic structure calculations using dynamical mean field theory. *Advances in Physics*, 2007.

[39] Müller-Hartmann E. The hubbard model at high dimensions: some exact results and weak coupling theory. *Z. Phys. B*, 1989.

[40] Georges A. and Kotliar G. Hubbard model in infinite dimensions. *Phys. Rev. B*, 1992.

[41] Georges A., Kotliar G., Krauth W., and Rozenberg M. J. Dynamical mean-field theory of strongly correlated fermion systems and the limit of infinite dimensions. *Rev. Mod. Phys.*, 1996.

[42] Jarrel M. Hubbard model in infinite dimensions: A quantum monte carlo study. *Phys. Rev. Lett.*, 1992.

[43] Parragh N., Toschi A., Held K., and Sangiovanni G. Conserved quantities of $SU(2)$-invariant interactions for correlated fermions and the advantages for quantum monte carlo simulations. *Phys. Rev. B*, 2012.

[44] Kotliar G., Savrasov S. Y., Haule K., Oudovenko V. S., Parcollet O., and Marianetti C. A. Electronic structure calculations with dynamical mean-field theory. *Rev. Mod. Phys.*, 2006.

[45] Maier T., Jarrel M., Pruschke T., and Hettler M. H. Quantum cluster theories. *Rev. Mod. Phys.*, 2005.

[46] Herrmann A. J., Tsuji N., Eckstein M., and Werner P. Nonequilibrium dynamical cluster approximation study of the Falicov-Kimball model. *Phys. Rev. B*, 2016.

[47] Hassan S. R. and Krishnamurthy H. R. Spectral properties in the charge-density-wave phase of the half-filled falicov-kimball model. *Phys. Rev. B*, 2007.

[48] Hettler M. H., Tahvildar-Zadeh, Jarrel M., Pruschke T., and Krishnamurthy H. R. Nonlocal dynamical correlations of strongly interacting electron systems. *Phys. Rev. B*, 1998.

[49] Li G. Hidden physics in the dual-fermion approach - a special case of a non-local expansion scheme. *Phys. Rev. B*, 2015.

[50] Wentzell N., Li G., Tagliavini A., Taranto C., Rohringer G., Held K., Toschi A., and Andergassen S. High-frequency asymptotics of the vertex function: diagrammatic parametrization and algorithmic implementation. *arXiv:1610.06520*, 2016.

[51] Li G., Wentzell N., Pudleiner P., Thunström P., and Held K. Efficient implementation of the parquet equations: Role of the reducible vertex function and its kernel approximation. *Phys. Rev. B*, 2016.

[52] Rohringer G., Valli A., and Toschi A. Local electronic correlation at the two-particle level. *Phys. Rev. B*, 2012.

[53] Faddeev L. D. Scattering theory for a three-particle system. *J. Exp. Theor. Phys.*, 1960.

[54] De Dominicis C. and Martin P. C. Stationary entropy principle and renormalization in normal and superfluid systems. *Journal of mathematical Physics*, 1964.

[55] Hafermann H., Li G., Rubtsov A. N., Katsnelson M. I., Lichtenstein A. I., and Monien H. Efficient perturbation theory for quantum lattice models. *Phys. Rev. Lett.*, 2009.

[56] Gukelberger J., Kozik E., and Hafermann H. Diagrammatic monte carlo approach for diagrammatic extensions of dynamical mean-field theory: Convergence analysis of the dual fermion technique. *Phys. Rev. B*, 2017.

[57] Maśka M. M. and Czajka K. Thermodynamics of the two-dimensional falicov-kimball model: A classical monte carlo study. *Phys. Rev. B*, 2006.

[58] Žonda M., Farkašovský P., and Čenčariková H. Phase transitions in the three-dimensional falicov–kimball model. *Sol. State Comm.*, 2009.

[59] Kennedy T. and Lieb E. An itinerant electron model with crystalline or magnetic long range order. *Physica A*, 1986.

[60] Kennedy T. Some rigorous results on the ground states of the falicov-kimball model. *Rev. Math. Phys.*, 1994.

[61] Brandt U. and Schmidt R. Exact results for the distribution of the f-level ground state occupation in the spinless Falicov-Kimball model. *Zeitschrift f. Physik B*, 1986.

[62] Brandt U. and Schmidt R. Ground state properties of a spinless Falicov-Kimball model. *Zeitschrift f. Physik B*, 1987.

[63] Antipov A. E., Gull E., and Kirchner S. Critical exponents of strongly correlated fermion systems from diagrammatic multiscale methods. *Phys. Rev. Lett.*, 2014.

[64] Ribic T., Rohringer G., and Held K. Nonlocal correlations and spectral properties of the Falicov-Kimball model. *Phys. Rev. B*, 2016.

[65] Hettler M. H., Tahvildar-Zadeh A. N., Jarrel M., Pruschke T., and Krishnamurthy H. R. Nonlocal dynamical correlations of strongly interacting electron systems. *Phys. Rev. B*, 1998.

[66] Hettler M. H., Mukherjee M., Jarrel M., Pruschke T., and Krishnamurthy H. R. The dynamical cluster approximation: Non–local dynamics o f correlated electron systems. *Phys. Rev. B*, 2000.

[67] Ribic T. Vertex extensions of the dynamical mean field theory for the Falicov-Kimball model. Master's thesis, TU Wien, 2015.

[68] Shvaika A. M. Dynamical susceptibilities in strong coupling approach. *Physica C*, 2000.

[69] Schäfer T., Rohringer G., Gunnarsson O., Ciuchi S., Sangiovanni G., and Toschi A. Divergent precursors of the Mott-Hubbard transition at the two-particle level. *Phys. Rev. Lett.*, 2013.

[70] Schäfer T., Ciuchi S., Wallerberger M., Thunström P., Gunnarsson O., Sangiovanni G., Rohringer G., and Toschi A. Non-perturbative landscape of the mott-hubbard transition: Multiple divergence lines around the critical endpoint. *Phys. Rev. B*, 2016.

[71] Metzner W., Salmhofer M., Honerkamp C., Meden V., and Schönhammer K. Functional renormalization group approach to correlated fermion systems. *Rev. Mod. Phys. B*, 2012.

[72] Lu Y., Höppner M., Gunnarsson O., and Haverkort M. W. Efficient real-frequency solver for dynamical mean-field theory. *Phys. Rev. B*, 2014.

[73] Janis V. and Pokorny V. Critical metal-insulator transition and divergence in a two-particle irreducible vertex in disordered and interacting electron systems. *Phys. Rev. B*, 2014.

[74] Baker G. A. and Graves-Morris P. *Padé approximants*. Cambridge U.P., 1996.

[75] Jarrel M. and Gubernatis J. E. Bayesian inference and the analytic continuation of imaginary-time quantum monte carlo data. *Physics Reports*, 1996.

[76] Li G., Lee H., and Monien H. Determination of the lattice susceptibility within the dual fermion method. *Phys. Rev. B*, 2008.

[77] van Loon E. G. C. P., Katsnelson M. I., and Hafermann H. Second-order dual fermion approach to the mott transition in the two-dimensional hubbard model. *arXiv:1805.08572*, 2018.

[78] Ribic. T, Gunacker P., and Held K. Impact of self-consistency in dual fermion calculations. *arXiv:1805.10996*, 2018.

[79] Kuneš J. Efficient treatment of two-particle vertices in dynamical mean-field theory. *Phys. Rev. B*, 2011.

[80] Mermin N. D. and Wagner H. Absence of ferromagnetism or antiferromagnetism in one- or two-dimensional isotropic Heisenberg models. *Phys. Rev. Lett*, 1966.

[81] Lorenz E. N. *The Essence of Chaos*. CRC Press, 1995.

[82] Pratchett Sir T. D. J. *Interesting Times*. Corgi Books, 1998.

[83] Kosterlitz J. M. and Thouless D. J. Ordering, metastability and phase transitions in two-dimensional systems. *J. Phys. C*, 1973.

I. Curriculum Vitae

Name	Tin Ribic
Geboren	August 11, 1991
Geburtsort	Wien, Österreich
Staatsbürgerschaft	Österreich
Familienstand	ledig

Ausbildung

1997-2001	Volksschule Alt-Erlaa
2001-2003	GRG23
2003-2006	GRG12 Zweig Realgymnasium
2006-2009	RG3 Zweig Realgymnasium mit Schwerpunkt darstellende Geometrie; Matura mit Auszeichnung
2009-2012	TU Wien Bachelorstudium der Technischen Physik, Abschluss mit Auszeichnung
2012-2015	TU Wien Masterstudium der Technischen Physik, Abschluss mit Auszeichnung, Diplomarbeitspreis der Stadt Wien
2015-2018	TU Wien Doktoratsstudium der Technischen Physik

Berufliche Erfahrungen

2011-2014	Tutorentätigkeit an der TU Wien, Schwerpunkt mathematische und theoretische Physik
Jul-Sep 2014	Projektassistent am Institut für Festkörperphysik, TU Wien
2015-2018	Projektassistent am Institut für Festkörperphysik, TU Wien
2015-2017	Entwicklungsingenieur technische Optik, IN-VISION Guntramsdorf

Ausbildung

Deutsch und Englisch in Wort und Schrift. Grundkenntnisse Kroatisch und Französisch

Publikationsliste

- T. RIBIC, P. GUNACKER, AND K. HELD, *Impact of self-consistency in dual fermion calculations.* arXiv, 1805.10996 (2018).
- T. RIBIC, P. GUNACKER, S. ISKAKOV, M. WALLERBERGER, G. ROHRINGER, A.N. RUBTSOV, E. GULL AND K. HELD, *Role of three-particle vertex within dual fermion calculations .* Phys. Rev. B **96**, 135127 (2017).
- T. RIBIC, G. ROHRINGER, AND K. HELD, *Local correlation functions of arbitrary order for the Falicov-Kimball model.* Phys. Rev. B **95**, 155130 (2017).
- P. GUNACKER, M. WALLERBERGER, T. RIBIC, A. HAUSOEL, G. SANGIOVANNI, AND K. HELD, *Worm-improved estimators in continuous-time quantum Monte Carlo.* Phys. Rev. B **94**, 125153 (2016).
- T. RIBIC, G. ROHRINGER, AND K. HELD, *Nonlocal correlations and spectral properties of the Falicov-Kimball model.* Phys. Rev. B **93**, 195105 (2016).
- T. RIBIC, E. ASSMANN, A. TÓTH, AND K. HELD, *Cubic interaction parameters for t_{2g} Wannier orbitals.* Phys. Rev. B **90**, 165105 (2014).